Thermal Design and Analysis of a Passively Cooled, Low Temperature Cryogenic Astrophysical Observatory in Low Earth Orbit

By

Bradley Moore

A dissertation submitted in partial fulfillment of

the requirements for the degree of

Doctor of Philosophy

(Mechanical Engineering)

at the

UNIVERSITY OF WISCONSIN-MADISON

2025

Date of final oral examination: 10/08/2025

The dissertation is approved by the following members of the Final Oral Committee:

Franklin Miller, Associate Professor, Mechanical Engineering
Gregory Nellis, Professor, Mechanical Engineering
Allison Mahvi, Assistant Professor, Mechanical Engineering
Eric Tervo, Assistant Professor, Electrical and Computer Engineering
Peter Timbie, Professor, Physics
Warren Holmes, Engineer, JPL/Caltech

Abstract

The Spectro-Photometer for the History of the Universe, Epoch of Reionization, and Ices Explorer (SPHEREx) is a NASA Medium-class Explorer mission conducting a 26-month all-sky survey from low Earth orbit. This dissertation documents the development, correlation, and on-orbit performance of SPHEREx's passive cryogenic thermal system. The work begins with detailed modelling of key thermophysical and thermo-optical properties of the payload, including honeycomb photon shields, V-grooves, and detector harnessing. Temperature- and wavelength-dependent emissivity, ice contamination effects, and optical constants of coatings are incorporated through a combination of literature data, first-principles derivations, and custom MATLAB tools. Ground testing of subcomponents, composite conductance, paint emissivity, and detector power dissipation provide anchor points for model calibration.

A comprehensive Thermal Desktop® model was developed with Monte-Carlo radiation analysis, environmental load estimators, and sensitivity studies covering emissivity, specularity, transmissivity, tip-over angle, and structural support geometry. Novel tools were created to translate spacecraft attitude into environmental heat-load predictions, enabling rapid assessment of seasonal trends and pointing maneuvers. On-orbit telemetry collected since the successful launch in March 2025 demonstrates that the MWIR and SWIR focal plane assemblies reached their 45 K and 62 K setpoints faster than predicted (13 days versus 13.7 days) and have maintained stable control with margins exceeding 150 % relative to requirement temperatures. Model correlation with in-flight data reduced discrepancies in stage loads to below 5–10 %, validated contamination-control strategies, and identified likely mechanisms for gradual emissivity changes such as UV darkening and ice accumulation.

Beyond verifying SPHEREx's thermal performance, the methods employed in this work are transferable to future cryogenic missions, including fundamental optical properties and ice emissivity, contamination management, and automated environmental-load mapping from flight telemetry. Together these techniques expand what is considered feasible for entirely passive cryogenic cooling in low Earth orbit and provide a roadmap for designing, testing, and correlating next-generation space observatories.

Acknowledgements

I'd like to thank my wonderful and supportive wife, who I met at the beginning of this endeavor and has seen me through every high and low of it. Franklin Miller, my advisor, and Greg Nellis, my co-advisor, for their support, accommodation, and understanding. My family for their support from afar. JPL for the financial support and being a fantastic place to work even in trying times. The entire SPHEREx team, of which I was only a small part, for building a spectacular observatory that will change our understanding of the Cosmos.

The research was carried out at the Jet Propulsion Laboratory, California Institute of Technology, under a contract with the National Aeronautics and Space Administration (80NM0018D0004).

Contents

List of Tables

List of Figures

List of Symbols

Symbol	Definition	Units
$\varepsilon_{\lambda,\parallel}$	Spectral emissivity at wavelength λ for parallel polarization	–
$\varepsilon_{\lambda,\perp}$	Spectral emissivity at wavelength λ for perpendicular polarization	–
ε_{λ}	Average (unpolarized) spectral emissivity at wavelength λ	–
ε(T)	Total emissivity as a function of temperature	–
α	Absorptivity	–
ρe	Electrical resistivity	Ω·cm
σ	Stefan–Boltzmann constant (5.670×10^{-8})	$W \cdot m^{-2} \cdot K^{-4}$
λ	Wavelength	μm
θ	Angle of incidence (to surface normal)	deg or rad
n	Real part of refractive index	–
k	Extinction coefficient (imaginary part of refractive index)	–
ω	Angular frequency of EM wave	$rad \cdot s^{-1}$
ωp	Plasma frequency	$rad \cdot s^{-1}$
ζ	Damping coefficient (Drude model)	$rad \cdot s^{-1}$
μ0	Magnetic permeability of free space ($4\pi \times 10^{-7}$)	$H \cdot m^{-1}$
c0	Speed of light in vacuum (3.00×10^{8})	$m \cdot s^{-1}$
NA	Avogadro's number (6.022×10^{23})	mol^{-1}
A	Atomic or molar mass	$kg \cdot mol^{-1}$
ρm	Mass density	$kg \cdot m^{-3}$
e	Elementary charge (1.602×10^{-19})	C
ε0	Vacuum permittivity (8.854×10^{-12})	$F \cdot m^{-1}$
me	Electron mass (9.109×10^{-31})	kg
Bij	Radiation exchange factor from surface I to j	–
Ai	Surface area of element i	m^2
Ti, Tj	Temperature of surfaces I and j	K
Qrad,ij	Radiative heat transfer between surfaces I and j	W
Φ	Phase function (Lambertian)	–
f	Illumination fraction (lit vs dark side)	–
Teff,moon	Effective blackbody temperature of Moon IR	K
Hlmoon,IR	Lunar IR heat load	$W \cdot m^{-2}$
Hlmoon,alb	Lunar albedo (reflected solar) heat load	$W \cdot m^{-2}$
Rmoon	Moon radius	m
DistSC,moon	Distance from spacecraft to Moon	m
τ	Thermal time constant	min
cp	Specific heat capacity	$J \cdot kg^{-1} \cdot K^{-1}$

List of Acronyms

Acronym	Definition
AO	Atomic Oxygen
BOL	Beginning of Life
CBE	Current Best Estimate
CERES	Clouds and the Earth's Radiant Energy System
ESH	Equivalent Sun Hours
FPA	Focal Plane Assembly
IOC	In-Orbit Checkout
IR	Infrared
LDEF	Long Duration Exposure Facility
MMOD	Micro-Meteorite and Orbital Debris)
MWIR	Mid-Wave Infrared
PM/SM/TM	Primary, Secondary, and Tertiary Mirror
RRR	Residual Resistivity Ratio
S-13G	White silicone paint used on SPHEREx shields
SCTC	Spacecraft Thermal Control (Handbook)
SINDA	Systems Improved Numerical Differencing Analyzer (thermal solver)
SPHEREx	Spectro-Photometer for the History of the Universe, Epoch of Reionization and Ices Explorer
STOP	Structural-Thermal-Optical Performance
SWIR	Short-Wave Infrared
TVAC	Thermal Vacuum (test)
VDA	Vacuum-Deposited Aluminum coating
V-groove	V-shaped passive radiator

1 Introduction

Cryogenic cooling has long been critical for space-based astrophysical missions. It is essential for reducing thermal emissions from the instrument itself, this can be likened to turning out the lights to see out a window at night. In addition to reducing the thermal self-emission, low temperatures also enable greatly increased sensitivity in detectors by reducing the energy level of the detector itself thereby increasing its sensitivity to low energy light from distant cosmic sources. The unique physics of some materials can also be leveraged below specific temperatures, such as superconducting transitions, to enhance their capability as detectors. Ross (2007) compiled a reference of the typical detector architecture given the desired wavelength ranges and the required operating temperature, shown in Table 1.

Table 1 Detector temperatures required relative to wavelengths of interest (R. Ross 2007)

Radiation Type	Wavelength (microns)	Blackbody Temp. (K)	Detector Technology	Detector Temp. (K)
γ-rays	10^{-5}	3×10^{8} K	Ge Diodes	80 K
γ-rays	10^{-4}	3×10^{7} K	Ge Diodes	80 K
x-rays	10^{-3}	3×10^{6} K	Microcalorimeters	0.05 K
x-rays	10^{-2}	3×10^{5} K	CCD/CMOS	0.05 K
UV	0.1	30,000 K	CCD/CMOS	200-300 K
visible	1	3000 K	HgCdTe	200-300 K
IR	2	1500 K	HgCdTe	80-130 K
IR	5	600 K	HgCdTe	80-120 K
LWIR	10	300 K	HgCdTe	35-80 K
LWIR	15	200 K	Si:As	35-60 K
LWIR	20	150 K	Ge:Ga	7-10 K
LWIR	50	60 K	Ge:Ga	2 K
LWIR/microwaves	100	30 K	Bolometers	1.5 K
microwaves	200	15 K	Bolometers	0.1 K
microwaves	500	6 K	Bolometers	0.1 K

Of specific interest in this research is the infrared (IR) to “short” longwave infrared (LWIR) and the HgCdTe detectors that measure in this range. SpectroPhotometer for the History of the universe, Epoch of Reionization and ices Explorer (SPHEREx) is an upcoming MIDEX (Medium class explorer) NASA mission to conduct an all-sky spectral survey from 0.75um-5um using two Teledyne H2RG™ (HgCdTe) detectors requiring cooling temperatures of 55K and 80K respectively. This mission hopes to

"Probe the origin and destiny of our Universe", "Explore whether planets around other stars could harbor life", and "Explore the origin and evolution of galaxies" (Korngut, et al. 2018). The mission is managed by JPL with contributions from Caltech, UC-Berkley, and BAe (British Aerospace – formerly Ball Aerospace) and was launched on Wednesday, March 12, 2025 at 3:10AM UTC and has a planned duration of 26 months. The insertion successfully entered a 6AM-6PM Sun-Synchronous Low Earth orbit (LEO) with an average altitude of 658km.

The telescope and two detectors are the only instruments in the mission and require no moving parts, such as filter wheels or scan mirrors, to scan the entire sky. With a large instantaneous Field of View (FOV) of 11.3°x3.5° and planned along track slew of +/-38deg[1], multiple passes on a given patch of the sky over the mission build an all-sky survey. An animation of this can be found on the SPHEREx website: https://spherex.caltech.edu/ (JPL/Caltech 2024). The spectroscopic component of the survey is accomplished by a linear variable filter. As an object in the sky moves down the filter gradient selected wavelengths illuminate specific pixels. Post processing stitches together precise knowledge of the spacecraft pointing with these measurements to build up the spectroscopic image. The interleaving of multiple sequential images to build up the data set drives very tight thermal stability requirements for the optics and telescope over the short span (<150s) of a slew. And the multiple passes of a given portion of the sky over the whole mission requires well controlled long duration stability. (Crill, et al. 2020)

The agility of the spacecraft in low earth orbit with heat sources from the Earth, Sun and even the Moon, produces a particularly challenging thermal environment. Given the very low temperatures of the coldest components, direct illumination from the Earth can have a large impact on absolute temperature and temperature stability with any illumination from the Sun a catastrophic impact. A balance must be struck between allowable pointing and protection from these environmental loads.

This report will focus on the passive cryogenic system required to support the SPHEREx observatory, which achieves less than 55K on the coldest radiator and protects sensitive optical

[1] After launch, there was a modification of this slew as will be discussed in more detail in later sections

components from perturbations across large slews. The main components and contributors are shown in Figure 1. Though there are multiple contributors, the overall thermal architecture and analysis of the full system, as well as the detailed thermal design and specifications of all JPL and Caltech contributions, was the responsibility of this author and will be discussed.

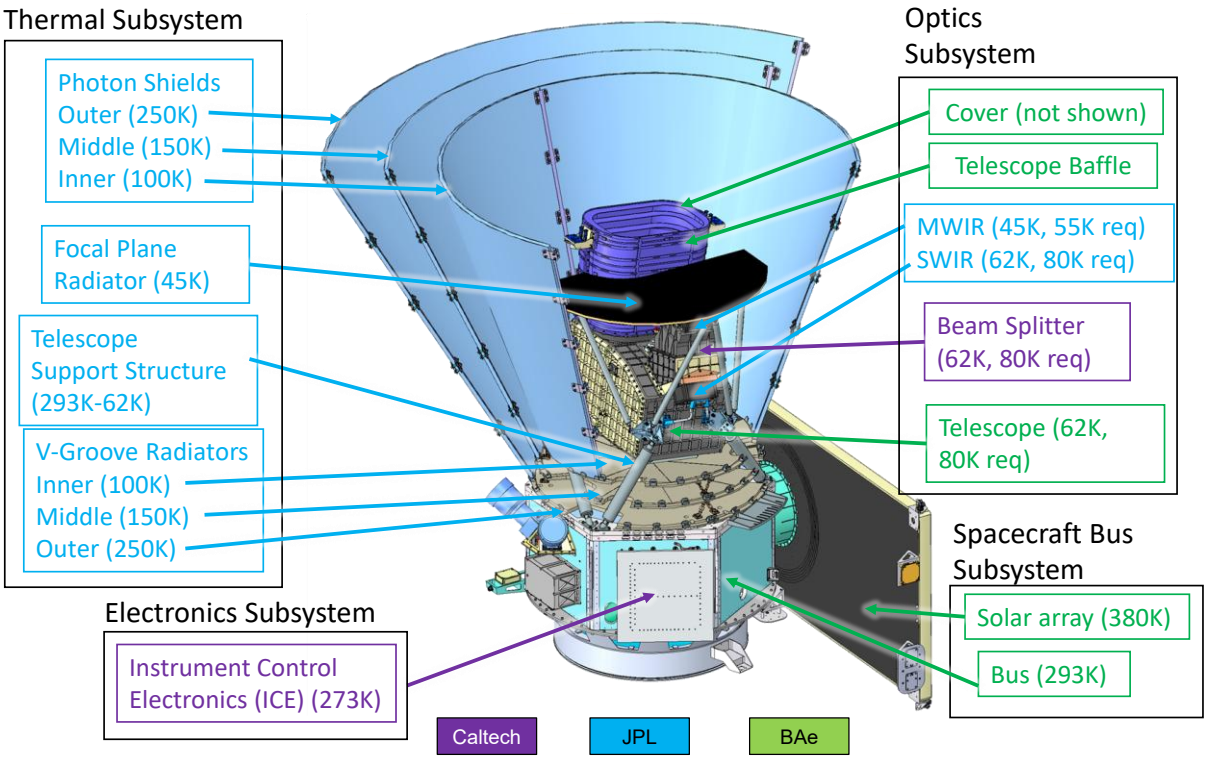

Figure 1 Main components of the SPHEREx Observatory and the contributors with approximate operational temperatures

The Focal Plane Radiator is the coldest component on the observatory and is a dedicated radiator stage for the Mid-Wave Infrared (MWIR) focal plane, which requires <55K cooling. Often this is simply referred to at the MWIR radiator for clarity. This radiator is mounted via thermally isolating struts to the telescope, which is cooled to <80K and serves as the radiator stage for the Short-Wave Infrared (SWIR) detector. A telescope cover, not shown in the image, is present only for launch to mitigate particulate contamination on the optics and was ejected before final cooldown and operations. Thermally isolating struts attach the telescope to the Spacecraft Bus top deck. To intercept radiative and environmental heat loads and dissipate them to space a 3-layer V-groove system surrounds the telescope and FPA radiator. In

the diagram this is comprised of “Photon Shields” and “V-grooves”, the nomenclature is distinct given that they are different components and construction. The Photon Shields are primarily used to block environmental loads, while the V-grooves block radiation from the spacecraft. However, the full assembly acts as a singular V-groove system with the aperture at the top of the Photon Shields.

Although this text focuses on a single mission, the principles and approaches described are applicable to any space mission requiring cryogenic temperatures. The integration of mission requirements, detailed thermal design, and comprehensive analysis demonstrates the feasibility of achieving temperatures previously considered unattainable through passive cooling. This thesis is organized into two main components: (1) pre-launch work establishing that SPHEREx would perform as intended on-orbit, and (2) actual on-orbit performance and correlation.

2 Literature review and Prior Work

The first question to ask when assessing this approach to meet the goal of achieving <55K and <80K in Low-Earth Orbit is: “What other cooling technologies could achieve this?”

Ross (Ross Jr, Refrigeration systems for achieving cryogenic temperatures 2016), Donebedian (Donabedian, Spacecraft thermal control handbook, volume II: cryogenics 2004), Chen (Chen, McKinley and Moore 2024), Collaudin (Collaudin and Rando 2000) all provide very complete discussions of refrigeration systems for achieving cryogenic temperatures in space. Of the technologies that are currently available, liquid cryogens, solid cryogens, cryocoolers, and passive systems can all reach the temperatures required for SPHEREx. Figure 2 shows the relative heat load and temperature regime used for cooling in space. Of note is the fact that passive radiators are indicated only above 60K. This chapter was written before some recent missions that achieved cooling below 60K with the passive component of their cooling chains. However, this illustrates the challenge in building a passive only system to achieve 55K.

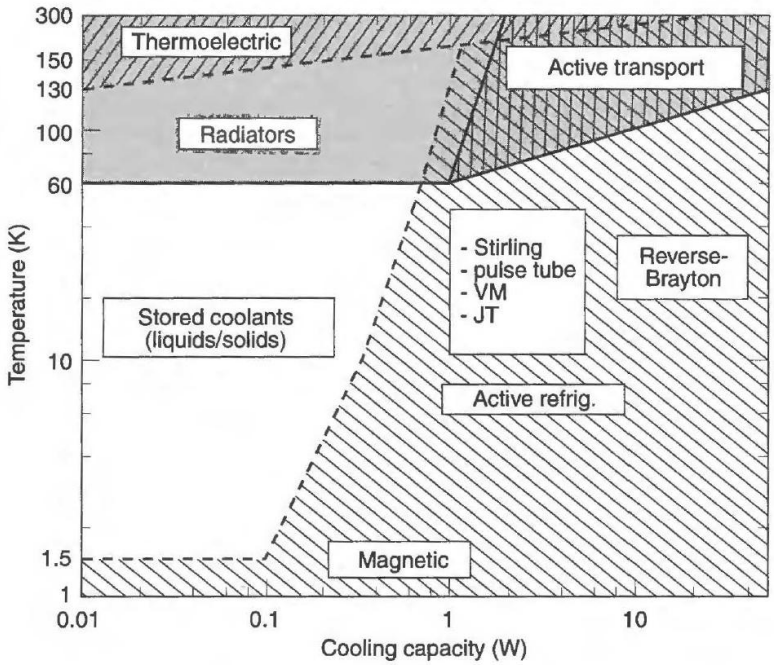

Figure 2 Typical operating regimes of different cryogenic refrigeration technologies for Space (Donabedian, Spacecraft thermal control handbook, volume II: cryogenics 2004)

All these references discuss the architectural considerations for each of these methods. But Ross also provides a method for estimating conducted heat loads into a cryogenic system. More detail on this

approach is documented in another paper by the same author (Ross Jr, Estimation of thermal conduction loads for structural supports of cryogenic spacecraft assemblies 2004). The key equation is shown in 1

$$Q = \mathcal{A} * k * m^{0.66} * \Delta T \quad (1)$$

where Q is the heat load in Watts, k is the conductance of the material in W/m-K, m is the supported mass in kg, and ΔT is the temperature difference across the structure in Kelvin. $\boldsymbol{A}$ is an empirical scaling factor ranging from ~2.0E-4 to 2.7E-3 m/kg$^{0.66}$, with lower numbers signifying higher structural efficiency. For a simple heat load assessment, assuming the full telescope mass of ~70kg telescope must be held at 55K off of a 293K bus with ~0.5W/m-K conductance S-glass struts. There is a larger discussion on comparing the structural figure of merit of different materials and how the specific materials used on SPHEREx were selected, but S-glass was used for the primary telescope support struts. Larger masses (>>1kg) tend to be more structurally efficient, thus an $\boldsymbol{A}$ of 2E-4 m/kg$^{0.66}$ can be used. Thus for comparing different cooling methods, the total load at 55K should be on the order of ~400mW. This only includes conductive loads, so a conservative estimate is to double this number to include radiative loads. For the HgCdTe detectors used on SPHEREx, detector dissipation is negligible at this fidelity.

A relative comparison of the cooling methods presented can be conducted for the specific operating conditions of SPHEREx using the estimated 800mW of load at 55K for a 26 month mission. Note that the "mass at launch" is purely the mass of the component that provides the cooling (compressor and coldhead, cryogen, or radiator), an extensive passive thermal shielding system is assumed for all of these options.

Table 2 Comparison of cooling methods applicable to the SPHEREx mission

Cooling method	Mass at launch (kg)	Power on-orbit (W)	System robustness	System cost	Test complexity
Liquid O2	1819	0	Low	Medium	High
Solid CO (O2, Ar, and N2 other options)	222	0	Low	Medium	High
Cryocooler – reference AIRS cooler (JPL/Caltech n.d.)	37	53	Medium	High	Low
Passive radiator (e= .9, 1.7 m,^2, 2mm thick Al)	9.25	0	High	Low	High

*mass usage computed with internal properties of EES (Klein 2022)

System robustness is defined here as a combination of the ability to handle higher than expected loads, as well as how quickly a system loses cooling capability in the case of a failure.

Crycoolers have very high reliability but if the electronics driving the cooler stop functioning or the helium charge leaks out, the loss of cooling can be complete, which lowers the system robustness. Additionally, if loads greatly exceed the cooling capacity, most coolers have ~T^1 relationship between temperature and cooling capacity; as a result much greater loads can result in much higher temperatures. As Chen discusses, active cooling systems with significant flight heritage can be substantially cheaper than a custom alternative. However, while there are many low cost cryocooler options for >60K operation with >~1W of cooling, at the time of the SPHEREx mission planning, there were no low cost and high reliability options available for the <55K and >~1W of cooling.

Cryogens present the problem that once the stored mass is consumed all cooling power is lost, and if loads are higher than expected then the mission ends early. For a survey plan that requires the full 26 month mission to complete an all sky survey this was a substantial risk. Additionally, the lowest mass of cryogen required is ~3X the mass of the telescope itself.

Passive coolers have an intrinsic “stiffness” given the T^4 charactristics of lift; there will never be run-away warming of the system. However, this same relationship makes it progressively more difficult to reach very low temperatures. It also becomes difficult to accurately test a passive low temperature cryogenic radiator. Therefore, these coolers must rely heavily on analysis and extrapolation of both test data and on-orbit environments.

For a multiyear cost-capped mission such as SPHEREx, the choice of passive cooling was driven primarily by the cost and potential complexity of accomodating a cryocooler. Since much of the same shielding would be required for both a passive or an active system the cost of a cryocooler would be essentially in addition to the costs required for a passive system. The successful development of a passive system at the required temperatures in LEO has never been done before and is contingent on the development of a very accurate thermal model to ensure the low required temperatures are met. This

model needs to provide both a clear correlation with ground test data and provide estimates of the operating temperatures across the entire mission.

Given that SPHEREx is an all-passive mission, comparisons to the state of the art are made only with other flown passive systems. Drawing on Chen, Ross, and Donebian, along with additional references from missions not included in those papers, Figure 3 compiles examples of passive cooling in space (this list is not exhaustive). Numerous missions now operate passively below 200 K without published detector temperatures or cooling powers, as reaching such temperatures passively has become routine. Several upcoming missions also plan hybrid or fully passive systems—including NEOS (39 K planned), Roman (94 K), Athena (50 K), and PRIMA (45 K)—but these are not included in the figure. One mission did technically meet the <55 K requirement: after its helium charge was depleted, COBE warmed to approximately 43 K ± 5 K (plotted here as 48 K) and was warming very slowly. Volz and Dipirro theorized this might never exceed 50 K, but no public records document its eventual steady-state temperature. As discussed later, SPHEREx achieves substantially improved science return at its 45 K operating setpoint and is currently maintaining that temperature with significant control authority. If control heat were minimized, SPHEREx could operate detectors at <40K. To the best of publicly available knowledge, SPHEREx may therefore be the coldest passively cooled, fully operational instrument in LEO.

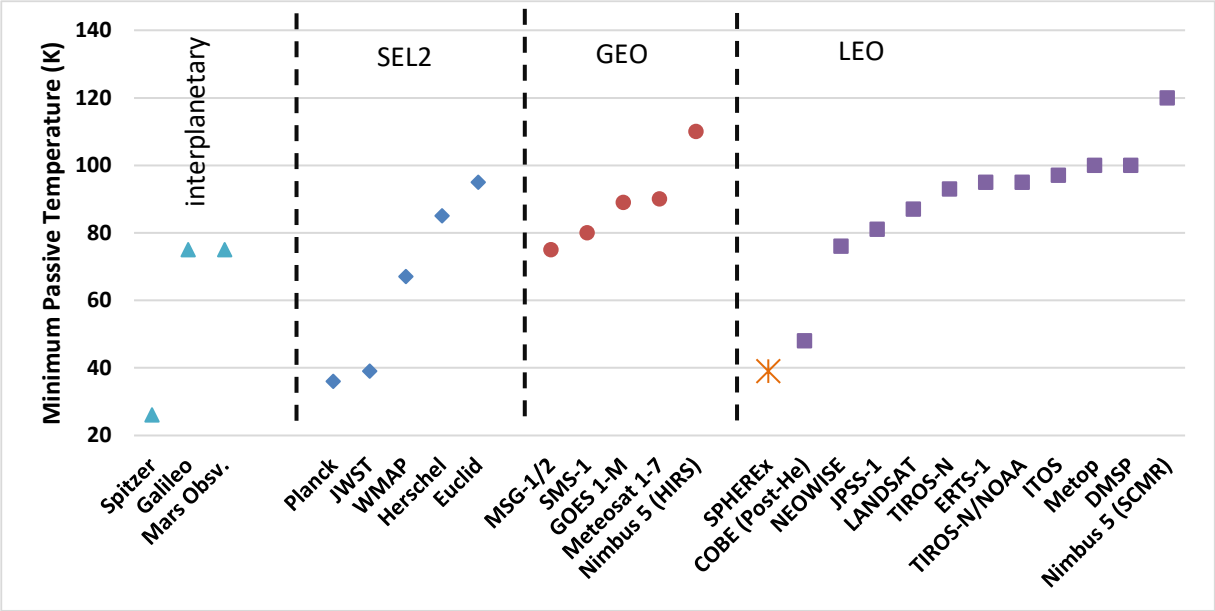

Figure 3 Passive cooling temperature of various flight missions. SEL2 (Sun-Earth Lagrange 2) ~1.5M km altitude, GEO (Geosynchronous Earth Orbit) ~36K km altitude, LEO (Low Earth Orbit)<2K km altitude. References: (Ade, et al. 2011) (Chen, McKinley and Moore 2024) (Collaudin and Rando 2000) (Donabedian, Spacecraft thermal control handbook, volume II: cryogenics 2004) (Mainzer, et al. 2014) (Pilbratt, et al. 2010) (Ross Jr, Refrigeration systems for achieving cryogenic temperatures 2016) (L3Harris 2020) (Glazer, et al. 2003) (Boggess, et al. 1992) (Volz and DiPirro 1992) (Cao, et al. 2013)

To achieve these temperatures in LEO, the SPHEREx thermal system combines isolating structures, low-conductance harnesses, V-groove radiators, and highly black cryogenic radiating surfaces. While conductive isolation and high-emissivity radiators are nearly as old as thermodynamics itself, V-groove radiators are relatively recent innovations. The first published staged radiator relying on specular reflections was proposed by Hulett and Zierman (Hulett and Zierman 1970), but it was not until 1984 that a full V-groove with a direct view to space from the aperture was built (Bard 1984). As explained by Bhandari (Bhandari, et al. 2020), the basic concept is to angle multiple high-reflectance, specular shield layers relative to each other, tuning their angle relative to shield length to achieve the desired temperature. To first order, V-groove performance is governed mainly by the view factor to space. Bhandari and Moore used this simple approach to analyze a set of three V-grooves in approximately the SPHEREx geometry, although this simplified model shows a much steeper response to angle than a detailed Monte-Carlo ray-tracing radiation analysis that includes specularity and multiple reflections.

Notable flight applications of V-grooves before SPHEREx include Planck, which achieved a baffle temperature of ~36 K, and JWST (James Webb Space Telescope), which reached an optical bench

temperature of ~39 K. Both missions operated at SEL2, a significantly more benign thermal environment. Blocking both Earth and Sun while maintaining a large field of view is far easier at ~1.5 million km, where the Earth and Sun are mostly aligned. Planck's configuration is similar to SPHEREx, with rigid aluminum shields and three stages. Its survey geometry and Earth/Sun angle allowed the system to use the solar panel on the bottom as a Sun blocker and permitted relatively large inter-shield angles of ~5° with a ~2.1 m radius (ESA 2024). This high view factor to deep space, combined with a large black-painted baffle directly coupled to the upper V-groove, enabled the low temperatures achieved. JWST, by contrast, employed much shallower angles (~2°), a much larger V-groove system (~22 m × ~10 m), and five layers. Its sunshield layers are Kapton membranes deployed and tensioned to improve specularity. Given the relative fragility of any single layer, additional layers were used to ensure robustness against micrometeoroid damage; these extra layers enabled the relatively shallow ~2° geometry. (Fellini and Kropp 2008) (Arenberg, et al. 2016).

A recent mission similar to Planck is the ESA ARIEL mission, which will operate a 60 K telescope and a subset of 42 K detectors in an L2 orbit, with launch planned for 2028. The mission is expected to achieve in-flight temperatures similar to those already demonstrated by SPHEREx but will employ a neon Joule–Thomson cooler for the 42 K stage. To illustrate how this compares to SPHEREx, if the total 42 K cooling load from the ARIEL design (approximately 40 mW) is combined with the intrinsic load of the SPHEREx MWIR FPA radiator (approximately 12 mW) and compared with the measured lift of the SPHEREx MWIR FPA radiator at 42 K (84.6 mW), the resulting thermal margin would be approximately 62% in flight. Additional details regarding the SPHEREx thermal loads and their conversion to margin will be provided later. (Morgante, et al. 2022)

Although passive cooling below 55 K has been achieved in previous space missions using the same basic approaches as SPHEREx, no prior mission has relied entirely on passive cooling to these temperatures within the challenging environment of LEO. This work therefore pushes the limits of cryogenic design, testing, and model correlation to ensure that SPHEREx achieves and maintains its required operating temperatures on-orbit, enabling its ground-breaking science goals. Furthermore, the

mission's long duration and stringent stability requirements demand a well-understood thermal model to track any potential degradation or unexpected performance differences throughout its lifetime. The lessons learned from this work may inform future missions on the capabilities of passive cooling and enable its selection in temperature ranges previously reserved for active cooling.

3 Pre-Launch Analysis

3.1 Requirements

As discussed previously, the primary temperature requirements for SPHEREx are 55 K for the MWIR detector and 80 K for the SWIR detector. These are maximum limits; science return improves at lower temperatures. The dominant benefit below requirement is a reduction in dark current. Although each H2RG is somewhat unique (necessitating unit-specific down-selection and calibration), an example of H2RG dark-current sensitivity to temperature is shown in Figure 4 (Regan and Bergeron 2020) There is substantial advantage to cooling below 50 K, with diminishing returns below ~45 K. Comparing this trend with the simulated sky images in in (Crill, et al. 2020), shows clear benefit when a significant fraction of pixels achieve dark current below 10^{-1} (bottom of the image scale).

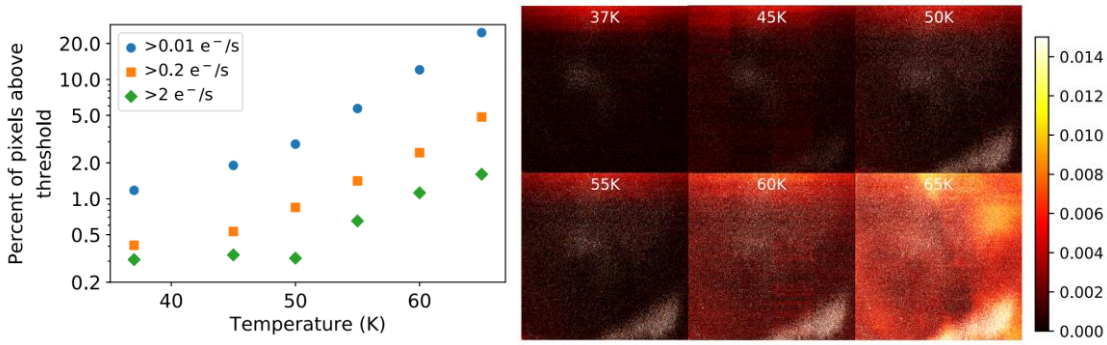

Figure 4 H2RG detector dark current vs temperature (Regan and Bergeron 2020)

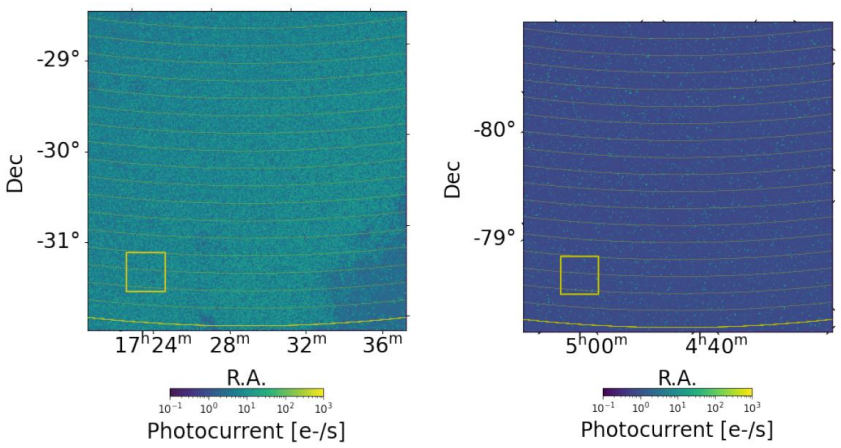

Figure 5 Simulated sky images generated by SPHEREx: (Left) galactic bulge, (Right) high ecliptic latitude (Crill, et al. 2020)

In addition to improved science returns, JPL mission design principals require margin against the requirement temperatures/heat loads. Throughout the following sections, margin is used as a convenient relative measure of system-level performance under various design choices and effects. Typical JPL thresholds vary by phase: 45% at preliminary design review, 35% at critical design (start of build), and 25% at final qualification/acceptance test. This margin is defined by equation 2.

$$Margin = 100\% * (\frac{System\ Heat\ Load\ Capacity}{CBE\ Heat\ Load} - 1) \quad (2)$$

Here, the CBE (Current Best Estimate) Heat-Load is the total cryogenic load including active dissipations (e.g., detectors, mechanisms) and passive parasitics. Environmental loads are typically excluded (and were excluded for SPHEREx) because the cryogenic radiators do not typically receive direct environmental irradiance; as shown later, the small reflected component is negligible, and environmental effects appear primarily through elevated Photon-Shield temperatures that manifest within the CBE term.

"System Heat-Load Capacity" is defined as the maximum load that can be applied at the radiator while still maintaining the detector temperature requirement. This capacity can be demonstrated in several ways; for example, a load may be incrementally applied at the radiator until the detector just reaches its

maximum allowable temperature. For SPHEREx, the capacity was instead computed from the thermal model as the net coupling of the radiator stage to space, shown in equation 3.

$$\mathrm{Q}_{\mathrm{capac}ity} = A * e * VF_{rad-space} * \sigma * \left(\left(T_{req} - \Delta T_{strap}\right)^4 - T_{space}^4\right) \quad (3)$$

In this expression, $A \cdot \varepsilon \cdot VF_{rad\text{-}space}$ (radiating area, emissivity, and view factor to space) are provided by the model; $\sigma = 5.670 \times 10{-}8$ $W \cdot m^{-2} \cdot K^{-4}$ is the Stefan–Boltzmann constant; T_{req} and T_{space} are the detector requirement temperature and the space sink temperature, respectively. The assumed radiator-to-detector temperature drop, ΔT_{strap}, was used to preserve flexibility in the thermal-link design while minimally affecting margin reporting. Based on initial load estimates and anticipated low-resistance links, ΔT_{strap} =2 K was adopted for the SWIR stage and ΔT_{strap} =1 K for the MWIR stage.

Consistent definition of the radiator stage is critical for margin assessment with this method. The MWIR radiator is straightforward, as it is a stand-alone element. The SWIR detector, however, is cooled by the telescope, which comprises the primary structure, mirrors, and a baffle. For consistency, the main telescope body was designated as the radiator surface, with the baffle and mirrors excluded. The mirrors have negligible impact on margin because they are low-emissivity and recessed within the telescope. The baffle provides additional cooling but also receives additional load; its net effect is included in the total CBE heat-load roll-up, whereas excluding its area from the capacity term removes additional cooling power from the “capacity” side of the ratio. At the time of model inception, the baffle geometry (length and diameter) had not been finalized; exclusion of its area therefore maintained consistency and provided a conservative margin assessment. The radiating surfaces used for margin are illustrated in Figure 6.

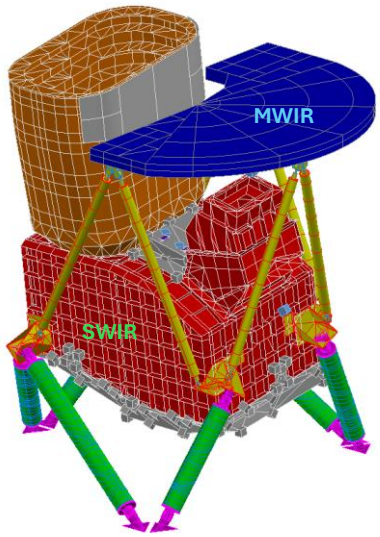

Figure 6 Radiating surfaces for each detector. SWIR radiating surfaces are shown in red and MWIR radiating surfaces are shown in blue.

Although JPL design principles specify a minimum thermal margin of 25% at launch, the much lower operating temperatures of SPHEREx relative to typical passive systems—and the greater performance degradation that can arise at such temperatures from effects negligible at higher cryogenic levels—led the project to establish a goal of 100% thermal margin at launch.

Driven by detector sensitivity and the objective of robust margins, the design was developed to achieve end-of-life (EOL) minimum temperatures of 41.8 K for the MWIR detector and 60.4 K for the SWIR detector.

In addition to absolute temperature requirements, stringent stability criteria were imposed. These are divided into (i) structural stability (thermoelastic distortions) and (ii) detector temperature stability, each with thresholds defined over specific timescales Table 3. All values are specified as changes over the indicated interval—for example, structural stability is assessed relative to pointing changes during the mission, not the total change from initial cooldown.

To satisfy these requirements, active thermal-control heaters were incorporated to trim the focal planes to a higher, tightly controlled temperature.

Table 3 Structural and detector stability requirements relative to timespans

Timespan	Detector thermal stability	Structural stability – rotation about [Δx, Δy, Δz]
150s (an exposure)	0.67μK/s average slope	[0.14, 0.14, 0.50] arcsec 1sigma
8 min (series of exposures)	2mK pk-pk	-
6 months	100mK pk-pk	-
1 year	200mK pk-pk	-
Full mission	-	[6.35, 15.70, 19.8] arcsec pk-to-pk

3.2 Overall Analysis approach

Much of the thermal analysis for SPHEREx was performed using Thermal Desktop® 6.3 together with its supplemental solvers RadCAD® and SINDA® from C&R Technologies® (now owned by Ansys). Thermal Desktop functions as a combined finite-element and finite-difference solver that is particularly well suited to aerospace thermal analysis. The model is constructed within a three-dimensional modeling environment provided as a plug-in to Autodesk® AutoCAD®. Numerous thermal-specific logic objects are available, including PID controllers for arbitrary process variables, multiple heater implementations, surface contactors, and interpolated temperature sensors.

Model geometry can be generated using traditional finite-element meshing or by employing built-in geometric “primitives” such as cylinders, spheres, and cones. These primitives can be discretized with either edge-based or body-centered nodalizations, and their parameters can be controlled programmatically. This capability allows optimization and makes thermal models readily adaptable to design changes without the need to re-import CAD files for each iteration.

Thermal Desktop is particularly effective for radiation calculations and orbital heating-rate predictions. Several methods are available, including progressive radiosity and view-factor calculations, but the most commonly used for SPHEREx was Monte-Carlo ray tracing. This approach was applied both to determine surface-to-surface view factors and to compute views from spacecraft surfaces to planetary bodies or the Sun. Ray impacts are translated into “RadKs” (radiation conductances), which are then solved together with the linear conductances of the thermal network. Importantly, RadKs are evaluated with T^4 on both source and sink surfaces; no effective linearized resistance with T^3 or other approximations is used in the solution.

Another useful feature of Thermal Desktop is its capability for orbital heating-rate calculations. Heat inputs from the Sun and planets can be specified through direct vector inputs, simple circular-orbit definitions at a given altitude with beta angle/inclination, or full Keplerian orbital elements. For SPHEREx, the Keplerian input form was employed.

Additional analysis was performed using MATLAB, Excel, and EES. MATLAB was employed to derive optical properties, generate orbits, and post-process results. EES was used for simple hand-calculation checks of the thermal model and to access its extensive library of material properties. Excel was used in the final stage of post-processing to compile results into a format suitable for distribution.

The overall approach for building and validating the thermal model was as follows:

1. Build the Thermal Desktop geometry, apply thermal properties from the literature, and model expected Thermo-optical properties.
2. Develop bounding orbits, orientations, and environments.
3. Generate preliminary temperature results in parallel with the design and conduct optimization and sensitivity studies.
4. Measure specific thermal and optical material properties.
5. Correlate conductive interfaces during instrument-level TVAC (thermal vacuum) testing.
6. Correlate radiative interfaces during observatory-level TVAC testing.
7. Produce final on-orbit predictions, including guidance for maneuvers and flight thermal setpoints.
8. Correlate on-orbit predictions and adjust thermal setpoints as required.

The first four steps were performed in parallel, with design changes and test/modeling results iteratively informing one another.

3.3 Bounding Environments

SPHEREx is injected into a polar, 6 AM–6 PM sun-synchronous orbit at an altitude of approximately 650 km and with low eccentricity, rendering the orbit nearly circular. Orientation constraints limit the permissible angles to the Earth, Sun, and Moon. No direct sunlight is permitted to

enter any region inboard of the outer shield; compliance is ensured by maintaining a Z-axis–to–Sun angle greater than 90 degrees.

Immediately after launch, SPHEREx operates in an inertial-pointing mode (Figure 7, left), which allows the telescope and MWIR radiator to have an unobstructed view of Earth during part of each orbit. During nominal operations, the spacecraft is pointed toward deep space (Figure 7, right), and limits are imposed on the allowable Earth angle. Although Earthshine can illuminate the inner Photon Shield, direct illumination of the telescope or MWIR FPA radiator is not allowed.

The primary sources of environmental-load variation over the mission timeline are gradual altitude degradation and variation of the β-angle, defined as the tilt of the orbital plane relative to the Sun. During the SPHEREx mission, the β-angle varies between approximately −89.4 degrees (nearly perpendicular to the Sun) and −58.58 degrees. The sign of the β-angle indicates the Sun's position relative to the orbital plane, with negative values indicating that the Sun lies south of the plane. Figure 9: isometric views of high- and low-β SPHEREx orbits.

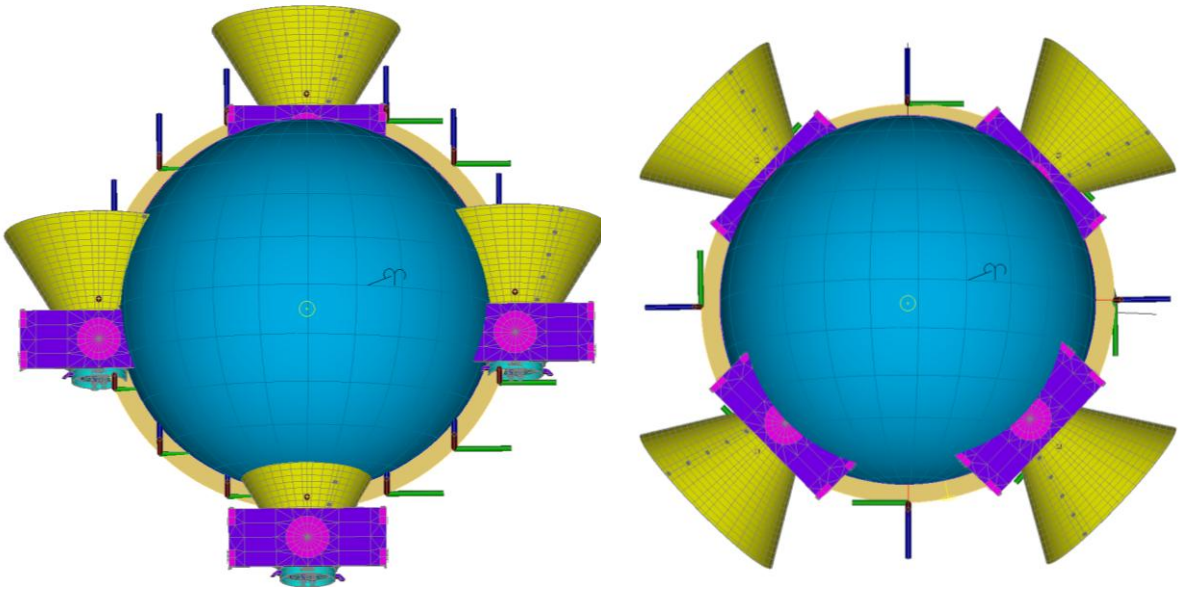

Figure 7 Relative orientations of SPHEREx in orbit: (left) inertial pointing; (right) zenith pointing

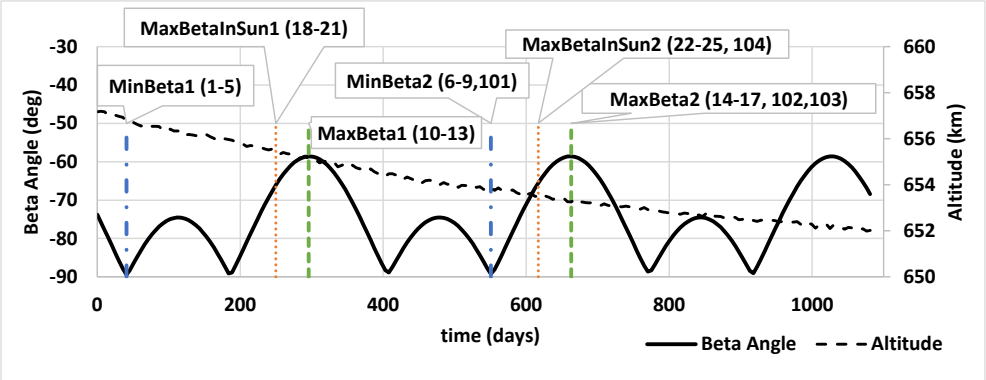

Figure 8 Beta and altitude variation across planned SPHEREx mission. The vertical lines correspond with orientation goals and case numbers discussed later.

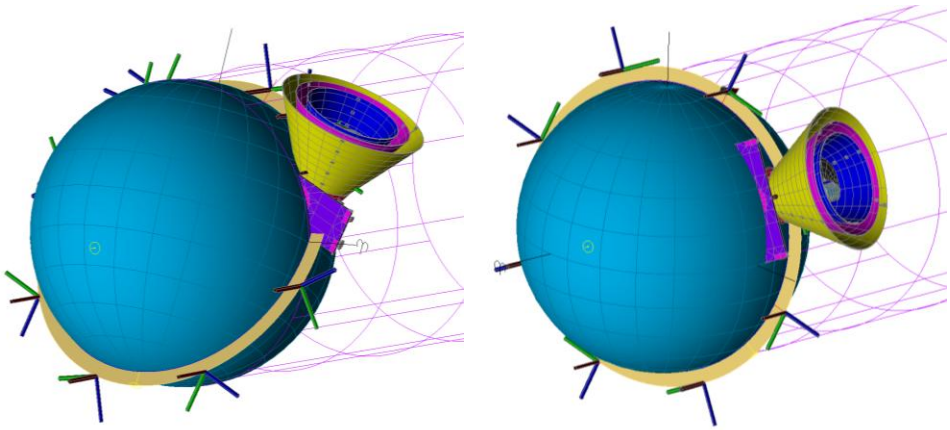

Figure 9 (Left) High-β-angle orbit with SPHEREx tipped to the maximum allowed within constraints. (Right) Orbit at the lowest β-angle with SPHEREx at minimum Earth exposure. The gold disc represents the orbital path; the yellow arrow pointing to the center of the sphere representing Earth is the Sun vector; and the purple grid cylinder represents Earth's shadow cone. SPHEREx is scale-enlarged for clarity, but the orbital path relative to the shadow cone is shown at 1:1 scale.

A distinctive aspect of the SPHEREx thermal analysis is that spacecraft pointing was derived independently from observational constraints and only later compared to a tentative survey plan. In typical practice, a thermal engineer collaborates with a navigation engineer to select a few "bounding" orientations based on constraints and engineering judgment. For a highly sensitive mission such as SPHEREx, this guess-based worst-case approach can be unreliable because environmental load exposure across an orbit varies non-linearly with both β-angle and MLTAN (Mean Local Time of the Ascending Node). Many missions discover late in the design phase that their assumed worst case was not actually bounding. By constructing a full "box" around all limiting combinations of orbit and orientation, this outcome was avoided.

A somewhat unique approach in thermal analysis on SPHEREx is that the spacecraft pointing is derived independently based on observational constraints and only later compared to a tentative survey plan. Typically, a thermal engineer would have to work with a navigation engineer to try to guess a few orientations that seem they would be bounding based on the constraints and "engineering judgement". The basic guessing of the worst-case approach can be fraught for a very sensitive mission such as SPHEREx, where the albedo exposure across an orbit can be non-linear due to constraints coupled with both Beta angle and MLTAN (Mean Local Time of the Ascending Node) variation. Often, missions will only find much later in the design phase that this guess is actually not the worst case. By building a full "box" around all limiting combinations of orbit and orientation, this surprise was avoided.

The constraints for SPHEREx are graphically illustrated in Figure 11. An important thing to remember with the relative Earth angle is that the Earth limb must be accounted for. If Earth were a completely flat plane, then any tip greater than 0 deg would result in some view from the inner Photon Shield to Earth, whereas if Earth were a point source only pointing directly down (Nadir) would result in a view to Earth. Instead, it's common knowledge that Earth is not a flat plate. This means that depending on the orbital height the SPHEREx Z-axis can tip relative to the Earth vector (Zenith) by up to the Earth limb before illumination of the inner Photon Shield. Beyond this tip, angles at which critical items are illuminated is shown in Figure 10. Adding the relevant angles (such as angle to illuminate the baffle) to the Earth limb, gives the max Z-Zenith angle that SPHEREx can tip to before illuminating a given component. The Earth limb angle (θ_{el}) is calculated from equation 4. For SPHEREx, using the radius of Earth (6,371km) and an end of mission altitude of 652km, a limb angle of 24.87° results.

$$\theta_{el} = \arccos\left(\frac{Radius_{earth}}{Radius_{earth} + altitude}\right) \tag{4}$$

For SPHEREx, using $Radius_{earth}$= 6,371km and an end-of-mission altitude of 652 km yields θ_{el}= 24.87°

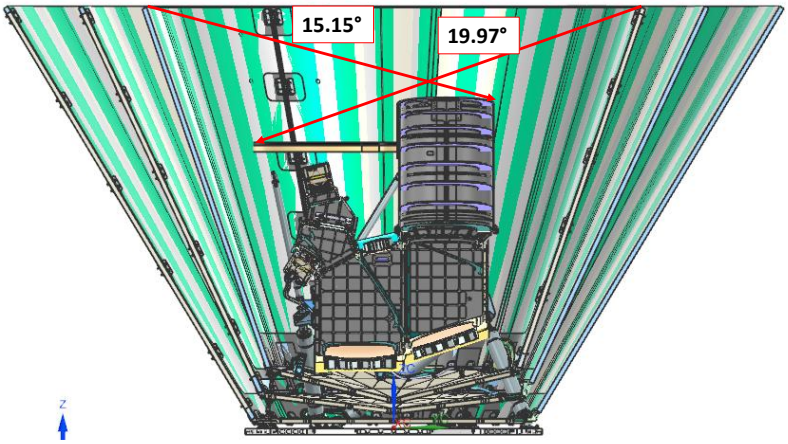

Figure 10 Angles relative to the top plane of the Photon Shield at which the telescope baffle and FPA radiator are illuminated. View is from the Sun vector with a cutaway to show the interior.

For the derivation of spacecraft orientations based on the defined constraints, the mean Keplerian orbital elements for the entire mission were supplied by the mission planning team. These mean elements defined the orbit but did not provide attitude (orientation) information.

A MATLAB script was developed to generate the necessary inputs for Thermal Desktop using the mission plan, planetary positions, and orientation constraints. Six points across the mission were selected (indicated in Figure 8): three β-angles near the beginning of the mission and three near the end. These β-angles corresponded to (i) the minimum value, (ii) the maximum value while remaining continuously sunlit over the entire orbit, and (iii) the absolute maximum value. At this maximum β-angle, the spacecraft passed through eclipse for part of each orbit.

At each selected point, rotation matrices were generated to maintain the payload at the maximum permissible limit of a given constraint throughout an orbit by tipping, tilting, or twisting as required (see Figure 11). Rotation matrices were used rather than quaternions because they can be more easily translated into the Cartesian rotations accepted by Thermal Desktop. The constraints incorporated Earth and Sun avoidance criteria as well as the minimum solar-array–to–Sun angle averaged over an orbit. A case was also defined in which the spacecraft minimized all environmental loads.

Combining four orientations with six times across the mission yielded a total of 24 “steady-state” orbits, which bounded the hot and cold conditions achievable if survey constraints were driven to their

limits. In addition, three short-timescale transient orbits were derived. Rather than maintaining a maximum or minimum environmental load across the entire orbit, these transients transitioned from maximum to minimum load within a single orbit. Because the orbit-averaged load from Moonshine was relatively small—approximately 2 mW on the FPA radiator and 5 mW on the telescope—it was included only in bounding transient cases during pre-launch analysis (later added more broadly post-launch). For cases that included Moonshine, the Moon was held at a fixed point and allowed to pass directly over the Z-axis to simplify the analysis (rather than maintaining the 30° requirement).

A complete listing of the thermal cases and corresponding orbits is provided in Table 4. Building orbits using this technique also permitted visual inspection with the built-in orbital visualization tools in Thermal Desktop, thereby reducing the likelihood of error. All cases were then executed and assessed for thermal margin and structural–optical–thermal (STOP) performance. As the project progressed, some orbits consistently proved worse for thermal margin, whereas others bounded structural distortion, demonstrating the value of this comprehensive approach. The derived orbits were ultimately compared with the survey plan and verified to encompass all planned orientations across the mission. This comparison is shown in Figure 12.

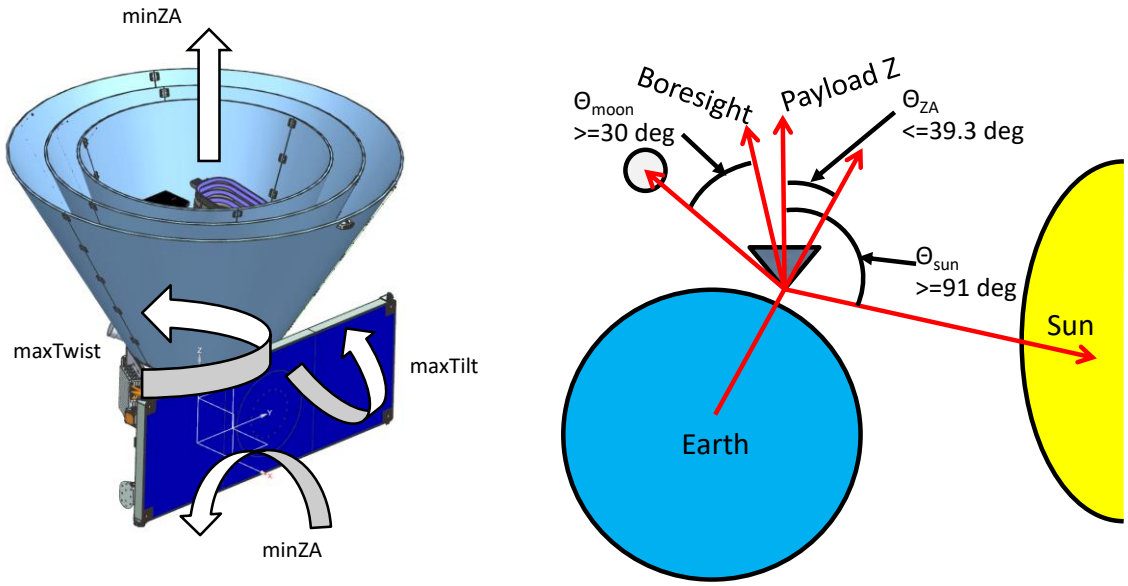

Figure 11 (Left) axis of rotation associated with various orientation goals (Right) SPHEREx constraints relative to Earth, Sun and Moon vectors.

Table 4 Listing of reference steady state and transient cases and associated orbits.

#	Case name	Type	Orbit Description	Sun	Earth	Moon	Optic props
1	SS_BOL_CBE_minBeta1_minZA	Steady state	Min Beta angle at beginning of mission, minimized Earth angle (~-90°)	>91° Z (varied)	Min	None	BOL
2	SS_BOL_minBeta1_minZA	Steady state	Min Beta angle at beginning of mission, minimized Earth angle	>91° Z (varied)	Min	None	BOL
3	SS_BOL_minBeta1_maxZA	Steady state	Min Beta angle at beginning of mission, max Earth angle	91° Z	39.3° Z	None	BOL
4	SS_BOL_minBeta1_maxTilt	Steady state	Min Beta angle at beginning of mission, max tilt maintaining solar array angle	20° X avg	<39.3° Z (varied)	None	BOL
5	SS_BOL_minBeta1_maxTwist	Steady state	Min Beta angle at beginning of mission, max twist maintaining solar array angle	20° X avg	<39.3° Z (varied)	None	BOL
6	SS_EOL_minBeta2_minZA	Steady state	Min Beta angle at end of mission, minimized Earth angle	>91° Z (varied)	Min	None	EOL
7	SS_EOL_minBeta2_maxZA	Steady state	Min Beta angle at end of mission, max Earth angle	91° Z	39.3° Z	None	EOL
8	SS_EOL_minBeta2_maxTilt	Steady state	Min Beta angle at end of mission, max tilt maintaining solar array angle	20° X avg	<39.3° Z (varied)	None	EOL
9	SS_EOL_minBeta2_maxTwist	Steady state	Min Beta angle at end of mission, max twist maintaining solar array angle	20° X avg	<39.3° Z (varied)	None	EOL
10	SS_BOL_maxBeta1_minZA	Steady state	Max Beta angle at beginning of mission, minimized Earth angle (~=-57°)	>91° Z (varied)	Min	None	BOL
11	SS_BOL_maxBeta1_maxZA	Steady state	Max Beta angle at beginning of mission, max Earth angle	91° Z	39.3° Z	None	BOL

#	Case name	Type	Orbit Description	Sun	Earth	Moon	Optic props
12	SS_BOL_maxBeta1_maxTilt	Steady state	Max Beta angle at beginning of mission, max tilt maintaining solar array angle	20° X avg	<39.3° Z (varied)	None	BOL
13	SS_BOL_maxBeta1_maxTwist	Steady state	Max Beta angle at beginning of mission, max twist maintaining solar array angle	20° X avg	<39.3° Z (varied)	None	BOL
14	SS_EOL_maxBeta2_minZA	Steady state	Max Beta angle at end of mission, minimized Earth angle (~=-57°)	>91° Z (varied)	Min	None	EOL
15	SS_EOL_maxBeta2_maxZA	Steady state	Max Beta angle at end of mission, max Earth angle	91° Z	39.3° Z	None	EOL
16	SS_EOL_maxBeta2_maxTilt	Steady state	Max Beta angle at end of mission, max tilt maintaining solar array angle	20° X avg	<39.3° Z (varied)	None	EOL
17	SS_EOL_maxBeta2_maxTwist	Steady state	Max Beta angle at end of mission, max twist maintaining solar array angle	20° X avg	<39.3° Z (varied)	None	EOL
18	SS_BOL_maxBetaInSun1_minZA	Steady state	Max Beta angle with no eclipse at beginning of mission, minimized Earth angle (~=-57°)	>91° Z (varied)	Min	None	BOL
19	SS_BOL_maxBetaInSun1_maxZA	Steady state	Max Beta angle with no eclipse at beginning of mission, max Earth angle	91° Z	39.3° Z	None	BOL
20	SS_BOL_maxBetaInSun1_maxTilt	Steady state	Max Beta angle with no eclipse at beginning of mission, max tilt maintaining solar array angle	20° X avg	<39.3° Z (varied)	None	BOL
21	SS_BOL_maxBetaInSun1_maxTwist	Steady state	Max Beta angle with no eclipse at beginning of mission, max twist maintaining solar array angle	20° X avg	<39.3° Z (varied)	None	BOL
22	SS_EOL_maxBetaInSun2_minZA	Steady state	Max Beta angle with no eclipse at end of mission, minimized Earth angle (~=-57°)	>91° Z (varied)	Min	None	EOL
23	SS_EOL_maxBetaInSun2_maxZA	Steady state	Max Beta with no eclipse angle at end of mission, max Earth angle	91° Z	39.3° Z	None	EOL
24	SS_EOL_maxBetaInSun2_maxTilt	Steady state	Max Beta angle with no eclipse at end of mission, max tilt maintaining solar array angle	20° X avg	<39.3° Z (varied)	None	EOL
25	SS_EOL_maxBetaInSun2_maxTwist	Steady state	Max Beta angle with no eclipse at end of mission, max twist maintaining solar array angle	20° X avg	<39.3° Z (varied)	None	EOL
101	TR_EOL_minBeta2_maxDeltaZA	Transient	min Beta angle at end of mission	>91° Z (varied)	0-39.3° Z	Max	EOL
102	TR_EOL_maxBeta2_maxDeltaZA	Transient	Max Beta angle at end of mission	>91° Z (varied)	0-39.3° Z	Max	EOL
104	TR_EOL_maxBetaInSun1_maxDeltaTiltTwist	Transient	Max Beta angle at end of mission while still in Sun	>91° Z (varied)	0-39.3° Z	Max	EOL

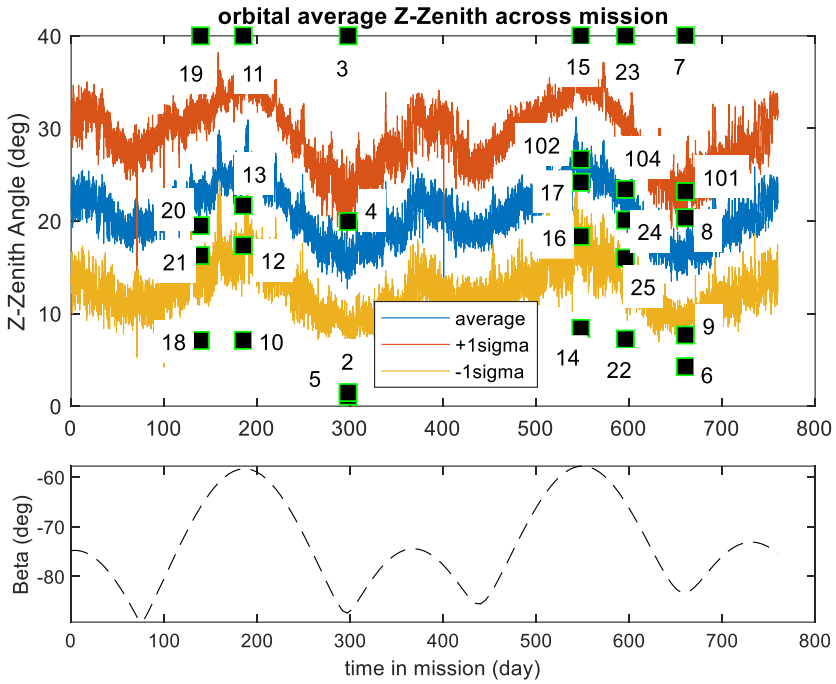

Figure 12 Comparison of orbit Z-Zenith (Earth angle) from survey plan to Thermal Desktop orbits

While the orbit and orientation define the positions of the Earth, Sun, and Moon relative to the SPHEREx mission plan, the actual heat flux from these sources is the critical driver of thermal performance. To fully bound this performance, the minimum expected values of Earth infrared (IR), albedo, and solar flux at the beginning of the mission were combined with BOL optical properties, and the maximum expected values of these parameters were combined with EOL optical properties.

This approach does not represent a physically continuous phenomenon, because environmental loads vary cyclically with the time of year and Earth's orbital position, and the degradation from BOL to EOL optical properties is gradual rather than a step change between the two cases. However, this method completely bounds the range of variation across the mission and ensures that temperature requirements are satisfied. Additional work is needed to establish a more accurate time-correlated model of these parameters rather than relying solely on bounding values.

For SPHEREx, the solar flux was fixed at 1323 $W \cdot m^{-2}$ for the minimum case and 1414 $W \cdot m^{-2}$ for the maximum case. Earth IR and albedo were treated as latitude dependent, as shown in Figure 13. The

reference for these values is the JPL internal environment-definition document D-8160 (Clawson unpublished).

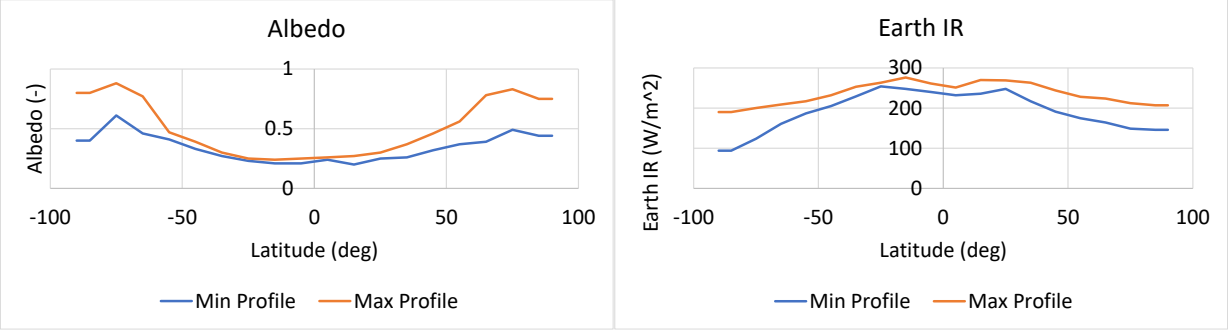

Figure 13 (Left) latitude dependent albedo (Right) latitude dependent Earth IR

3.4 Thermal Model and Component Descriptions

The pre-flight thermal model consisted of 11928 nodes, 7467 two-dimensional finite elements, 814 three-dimensional finite elements, and 9043 Thermal Desktop primitives (2-D and 3-D). After modifications for on-orbit correlation, the model expanded to 14516 nodes. Figure 14 shows the principal components and contributors of the thermal model.

As discussed previously, although multiple organizations contributed, the combined model was assembled and managed at JPL. Responsibility for integrating all sub-models, defining the environments, auditing properties, and managing the top-level payload thermal-performance requirements, together with detailed modeling of the FPAs and the thermal subsystem, rested with the author.

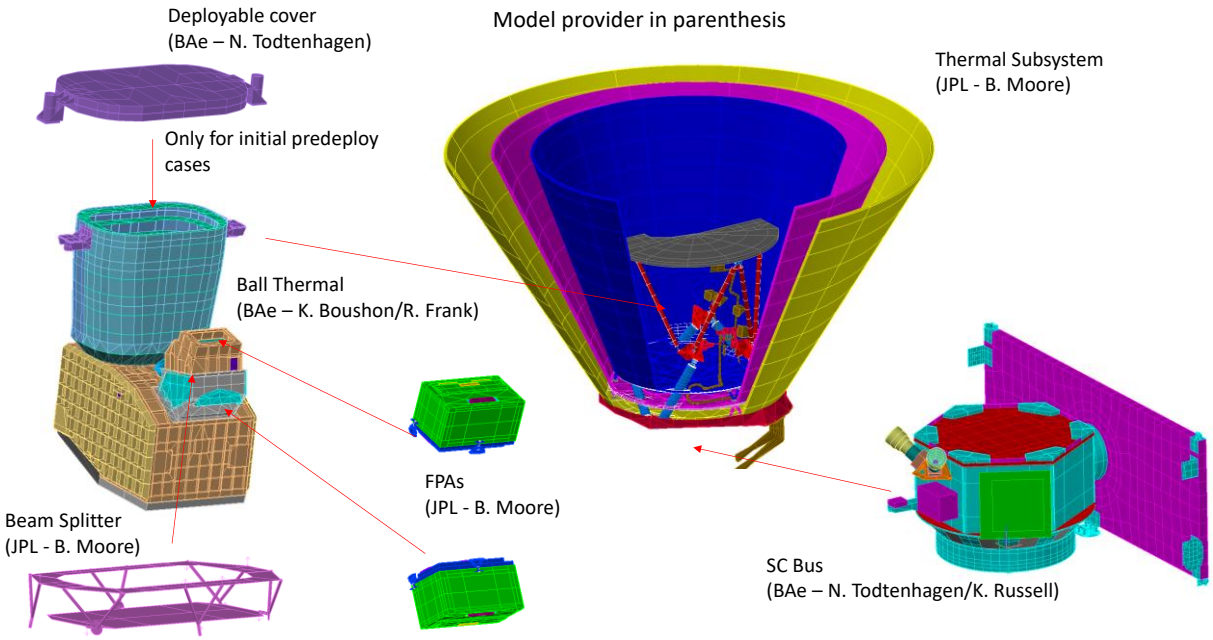

Figure 14 SPHEREx Thermal model main components and owners

3.4.1 Photon Shields and V-grooves

The Photon Shields and V-grooves function together as an integrated "V-groove radiator" system designed to direct thermal radiation to deep space through specular, low-emittance surfaces at a prescribed spread angle. The overall geometry of the SPHEREx system was selected after evaluating 41 discrete configurations and comparing the resulting thermal margins against the moment of inertia, which is a driving constraint for slew time and, consequently, survey completeness. These geometries were constrained by requirements to block direct Earth illumination of the telescope or FPA radiator for Z-axis tips up to approximately 40 degrees from zenith and to prevent direct re-reflection of Earthshine onto the telescope. Physical limits were also imposed by the launch-vehicle fairing diameter, which constrained the absolute outer diameter, while the inner Photon Shield and V-groove dimensions were limited by the telescope geometry. Figure 15 presents the scatter of acceptable geometries, with inter-shield angles ranging from 4 to 7 degrees and varied diameters within these physical constraints. The right side of Figure 15 illustrates the angles that provided the best balance of thermal margin relative to moment of inertia.

The Photon Shields are fabricated from ¾-inch-thick, 2.1-pcf Flex-Core® aluminum honeycomb (HexWeb Flex-Core CR-III-5056-F40-2.1) with 0.008-inch-thick 2024-aluminum face sheets clad with high-purity aluminum in accordance with AMS-QQ-A-250/5 (AMS-QQ-A-250/5: Aluminum Alloy Alclad Sheet and Plate 2017). The inner surfaces of the face sheets are polished, while the outer surfaces of the outer Photon Shield are primed and coated with S13G white paint to withstand direct solar heating. The Flex-Core® enables the conical form of the Photon Shield, as shown Figure 19. The high-purity cladding enhances thermo-optical performance compared with standard polished aluminum alloys.

The V-grooves are machined from 6061 aluminum with lightweighting pockets on the underside. These pockets are covered with 0.02-inch-thick polished 2024-aluminum face sheets also clad with high-purity aluminum. The internal rib detail is shown in the thermal desktop representation in Figure 17. Sheets of 0.02” thick high purity clad 2024 aluminum sheets cover the rib structure for the inner and middle V-grooves and an MLI blanket covers the outer V-groove. The V-grooves incorporate 3-D-printed Ultem closeouts with VDA Kapton coverings around the telescope-support strut penetrations. Flexible, overlapping VDA Kapton “fingers” intermesh around the support struts to create a compliant light seal without structural coupling between the V-grooves and the optical assembly. The integrity of these closeouts was verified after assembly by illuminating the system with a high-powered flashlight in a dark chamber; the assumption was that if visible light could penetrate, then thermal IR could also penetrate. Although a few small pinholes approximately 0.005 inch in diameter were detected in the prototype (Figure 18), no evidence of light penetration was observed when the full V-groove system underwent the same test. A conservative analysis assuming 1% transmissivity (~40 × 0.005-inch holes) showed negligible effect on thermal performance, and transmissivity was removed from future analyses.

In addition to the closeouts around the bipods, further VDA tape was applied to cover 3-D-printed components, and VDA Kapton tape was used to close out any remaining light gaps between the Photon Shields and V-grooves. Aluminum strips were installed over the seams between Photon Shields to join them. Even the visible A286 fasteners were enclosed within small SLI boxes to reduce unpredictable stray light and improve thermal performance.

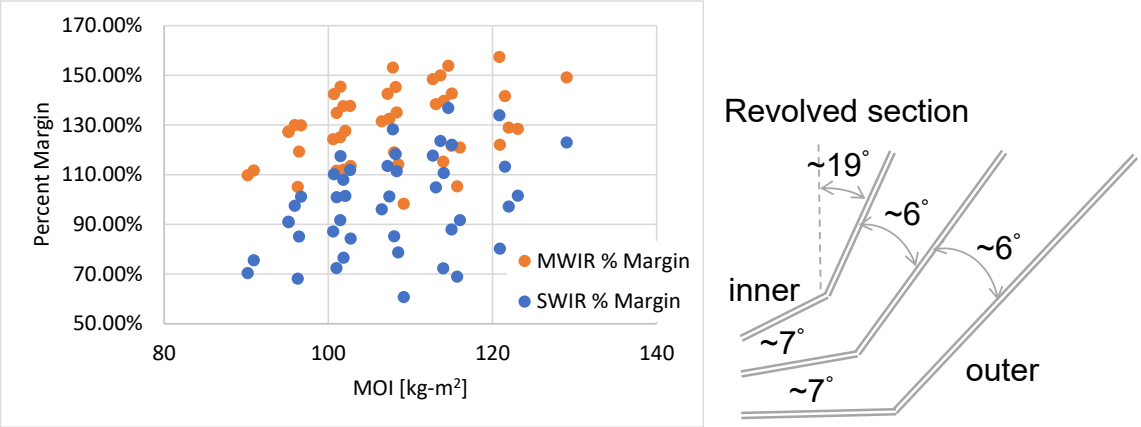

Figure 15 (Left) Moment of inertia vs thermal margin geometric trade. (Right) Approximate Photon Shield and V-groove angles used for final design

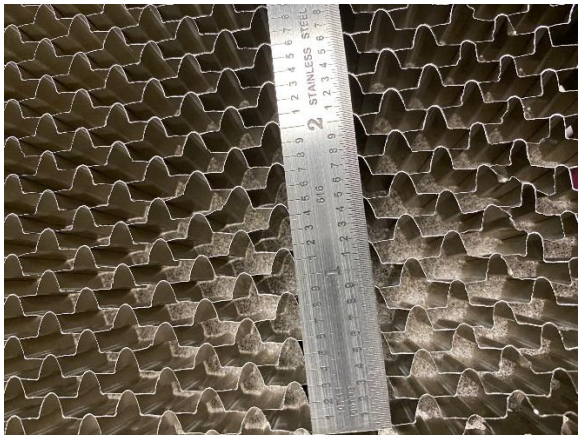

Figure 16 Photon Shield HexWeb Flex-Core CR-III-5056-F40-2.1 with an inch scale for reference

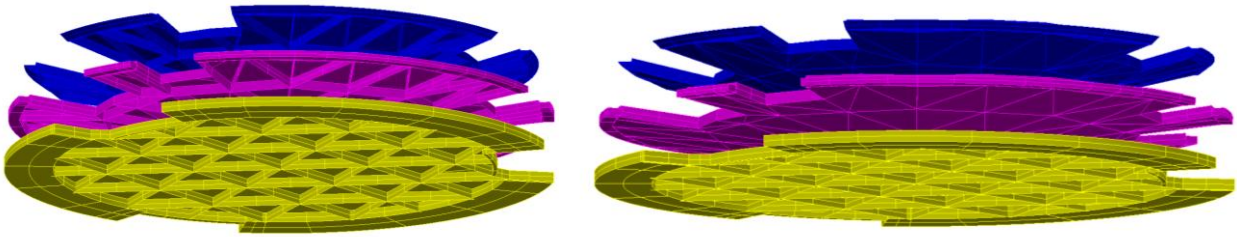

Figure 17 Thermal desktop representation of the V-groove radiators: (right) with ribs showing; (left) with ribs covered

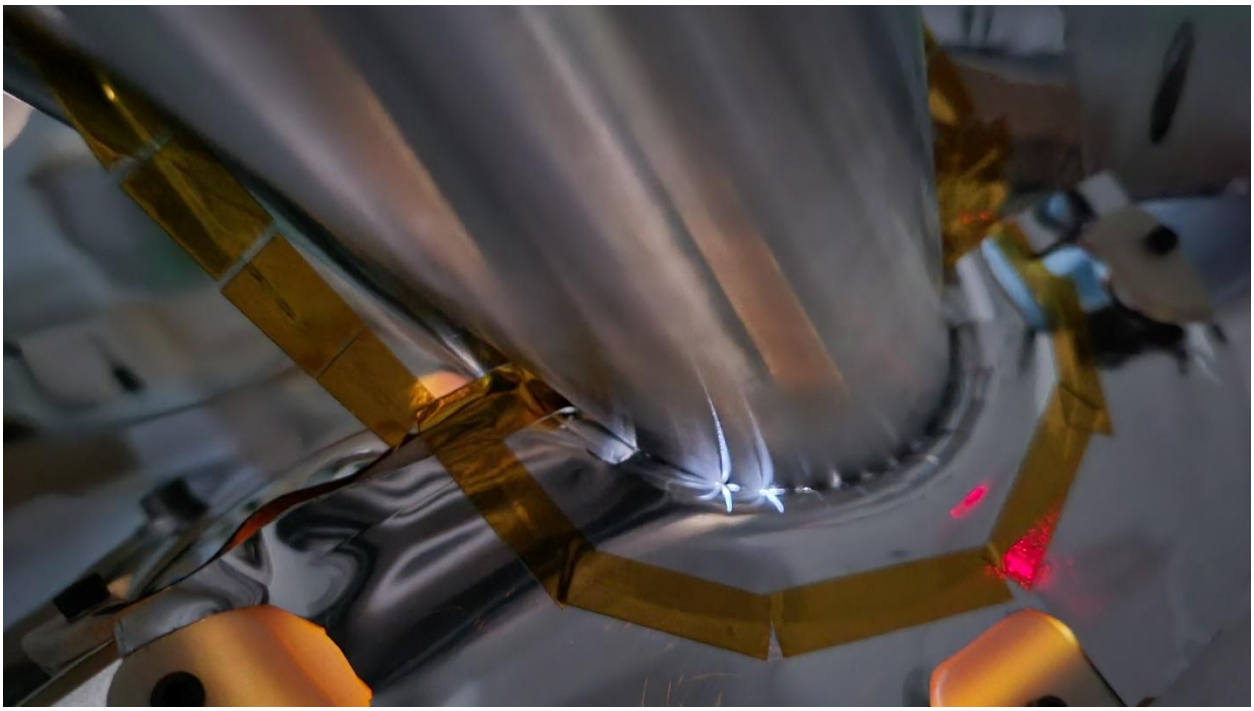

Figure 18 Close up view of the prototype main telescope support strut V-groove closeouts. A bright light is shining from behind to show the small penetrations.

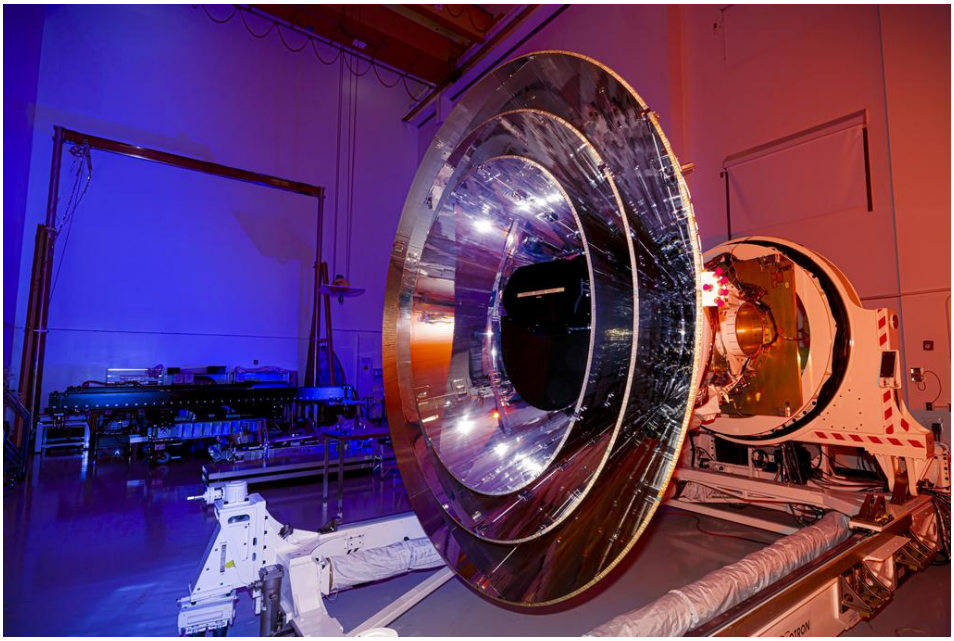

Figure 19 Image of SPHEREx fully assembled with Photon Shields (JPL/Caltech 2024)

3.4.2 Isolating structures

The largest and most critical isolating structures are the telescope support struts. These struts are arranged in a semi-kinematic hexapod configuration that supports the telescope from the spacecraft's top

deck. They are fabricated from S-glass tubes with a 60 mm outer diameter and a 2.2 mm wall thickness, using a cyanate ester resin. To enhance radiative coupling to deep space, the tubes are wrapped in black Kapton to increase emissivity. Titanium 6Al-4V end fittings incorporating reentrant flexures are bonded to the composite struts using 3M 2216 epoxy. The reentrant flexures provide a compact means of introducing compliance and additional thermal isolation and are shown in Figure 20.

Because the telescope support struts are large in diameter, down-tube radiative heat exchange constitutes a significant contributor to the overall heat transfer. The preliminary flight design incorporated a VDA-Kapton baffle structure consisting of multiple levels of disks to block this radiation. Additionally, the original flight design was coated with Z307 paint, which has a higher emissivity than black Kapton. However, testing demonstrated that this coating introduced a problematic conductive path to ground for the sensitive FPA and instrument control electronics. Earlier strut iterations fabricated for testing lacked black paint or baffles; the Kapton wrapping was subsequently added to improve thermal emissivity and to suppress transmitted infrared radiation through the tube wall.

The FPA radiator struts are similar to the telescope support struts but feature a slightly different composite layup reflecting their smaller size and lower structural loads. These struts consist of S-glass tubes with a 30 mm outer diameter and a 1.5 mm wall thickness, using the same cyanate ester resin with titanium end fittings. Ball joints are employed as the final structural attachments to the telescope support brackets to accommodate alignment and thermal contraction.

Each successive layer of the V-groove/Photon Shield system is supported from the preceding layer by titanium flexures. These flexures are optimized to achieve a balance between stiffness, necessary to withstand launch-induced vibrations, and radial compliance, required to accommodate differential thermal contraction between thermal zones.

Figure 20 Telescope support strut reentrant end flexure

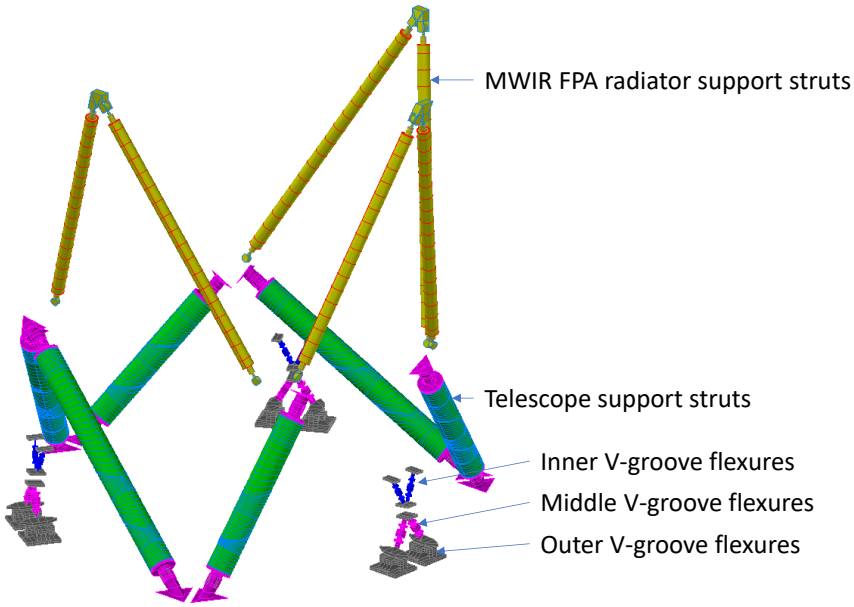

Figure 21 Thermal desktop representation of isolating structures on SPHEREx

3.4.3 Radiating surfaces – FPA Radiator and Telescope

At the core of the SPHEREx payload are the coldest radiating surfaces: the telescope and the FPA radiator. These surfaces achieve ultimate operating temperatures of < 80 K and < 55 K, respectively. Because they are nested within the Photon Shields, the key performance metric for these components is not simply their area but the product of area, emissivity, and view factor to space ($A \times \varepsilon \times VF$), as referenced in equation 3.

The telescope cools both the optical system and the short-wave infrared (SWIR) detector. It is a machined aluminum structure with an $A \times \varepsilon \times VF$ to space of 0.34 m^2. This value excludes the fore baffle—a barrel-like structure at the entrance pupil of the telescope—since the baffle is not counted as part of the radiator area. External lightweighting was incorporated to increase the effective emissivity and radiating area and is coated with Aeroglaze Z307 black paint. The Thermal Desktop model of the telescope is shown in Figure 23. A large number of nodes was allocated to this component in order to accurately capture the external lightweighting geometry and associated shading effects.

The telescope cover, provided by Ball Aerospace (now BAe), is a simple chromated aluminum cap. Detailed thermal modeling was not pursued beyond establishing its temperature bounds, because the cover deploys before final cooldown and operational phases. Nevertheless, it was included in the model to account for its influence on initial cooldown temperatures early in the mission.

The FPA radiator cools only the MWIR FPA and its parasitic loads. It consists of an open-cell aluminum honeycomb panel supported by a two-sided aluminum honeycomb sandwich. The underside of the panel is polished aluminum, while the open-cell upper surface is coated with Z307 black paint. An aspect ratio greater than 3:1 was selected to ensure each cell behaves as an essentially black cavity emitter. The representation in Thermal Desktop is shown in Figure 23. In contrast to the telescope, individual honeycomb cells were not explicitly modeled due to the prohibitive node count. The high aspect ratio permits internal cell shading to be treated as an effective surface property rather than a fully resolved geometric feature.

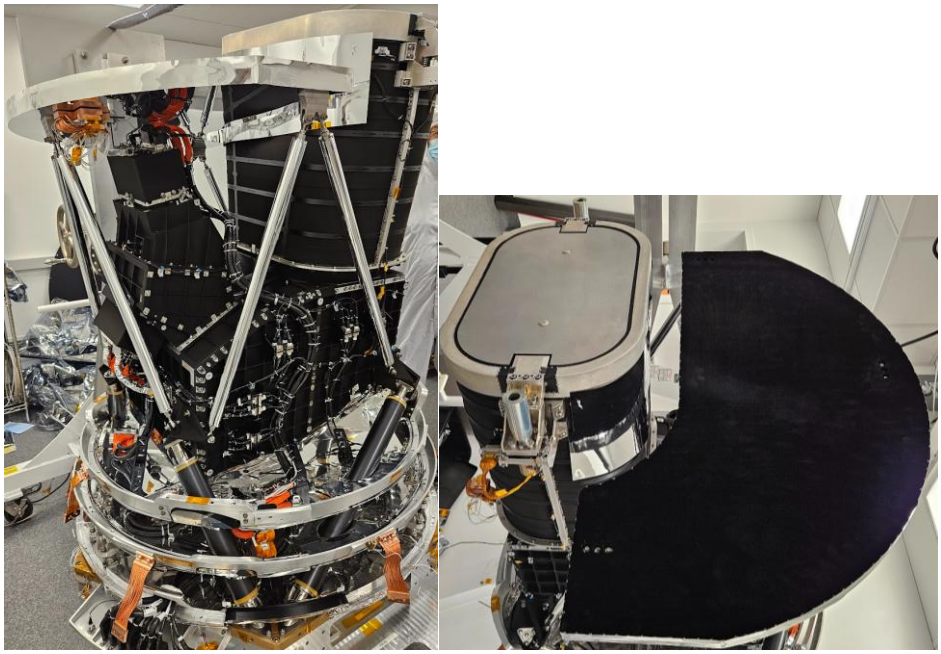

Figure 22 Assembled FPA radiator mounted on telescope

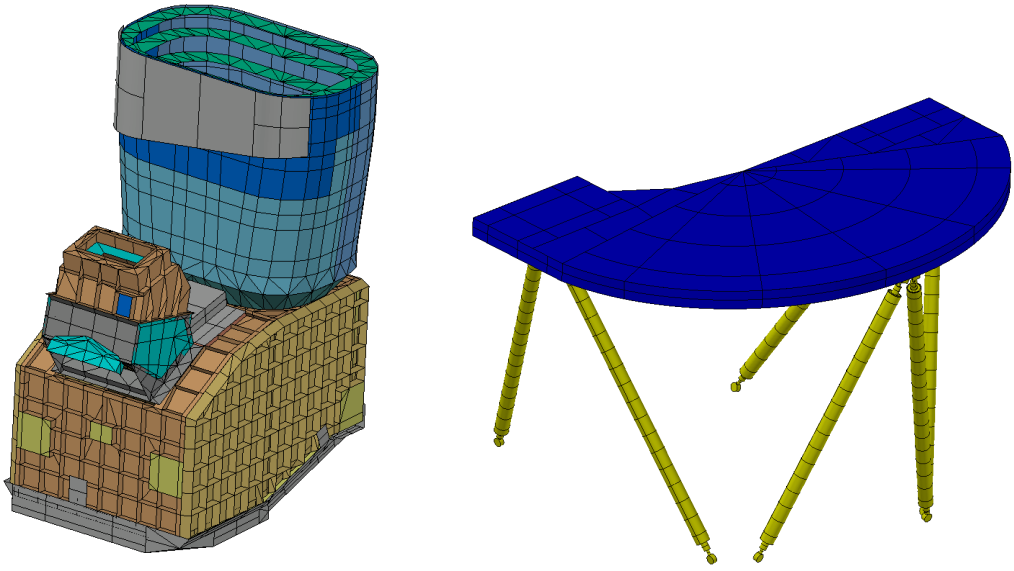

Figure 23 Thermal desktop representation of telescope (left) and MWIR FPA radiator (right)

3.4.4 Focal plane assemblies

Although they operate at different temperatures, the two focal plane assemblies (FPAs) are thermo-mechanically identical to reduce design time and cost. The MWIR focal plane requirements dictate the thermal isolation strategy because this assembly is mounted to the much warmer telescope. By contrast, the SWIR focal plane is cooled directly by the telescope; although thermal isolation is not

strictly necessary in this case, it improves both temperature stability and the control authority of the active temperature control system. Under nominal operation, both focal planes dissipate a total of 18 mW (6 mW per detector × 3 detectors).

An Image of the FPA Is shown In Figure 24, with selected detector details obscured. This image highlights the reentrant titanium bipod system serving as the primary FPA support, separate titanium bipods for an internal thermal strap support, and an external S-glass enclosure that blocks stray light and supports harnessing. The internal thermal strap contains all active thermal control components and provides a thermal link to the exterior of the enclosure while isolating the detector from FPA radiator motion during launch and subsequent thermo-mechanical distortion. External thermal straps (not shown) connect the two detectors to the FPA radiator and the telescope, respectively.

A simplified thermo-centric block diagram is presented in Figure 25, and the representation in Thermal Desktop is shown in Figure 26.

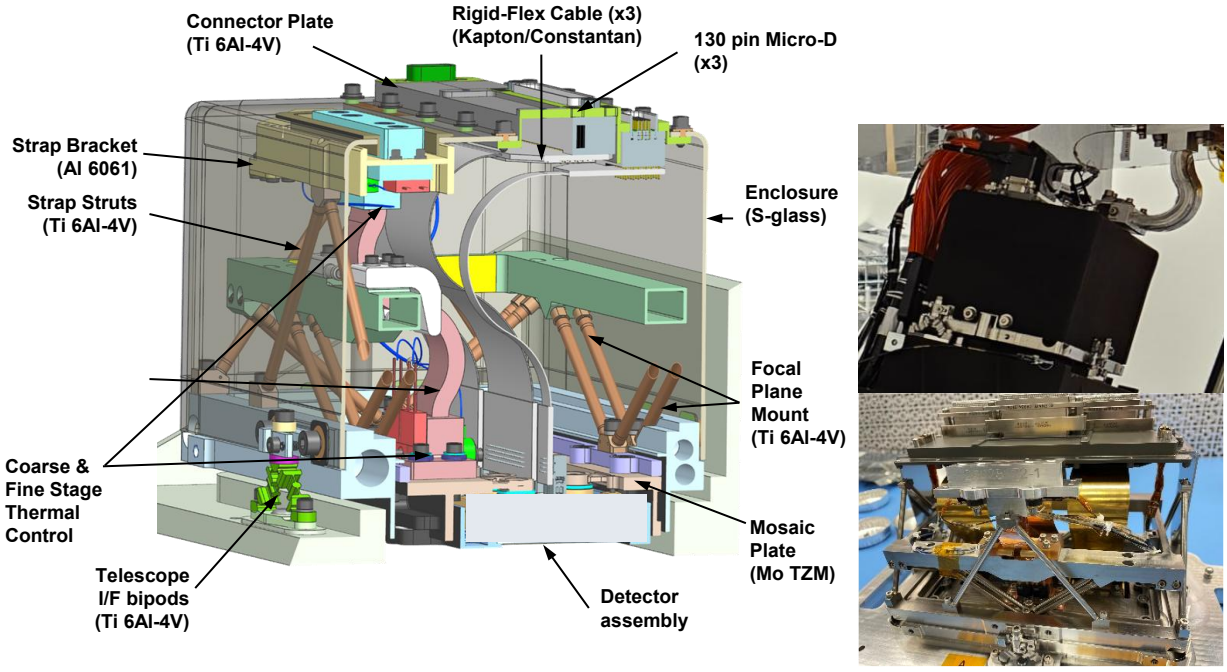

Figure 24. (left) SPHEREx FPA layout, detector details occluded due to export restrictions (right bottom) photo of FPA internal strap and supports during assembly. (right top) fully assembled MWIR FPA mounted to the telescope.

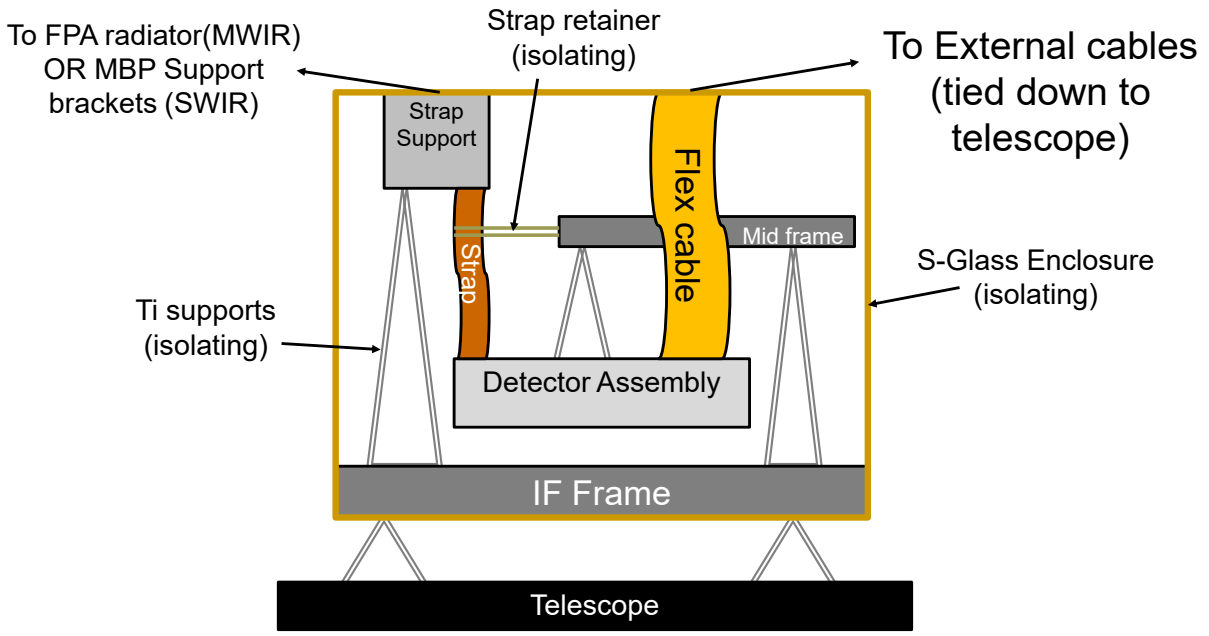

Figure 25 Thermal-centric block diagram of Focal Plane Assembly (FPA)

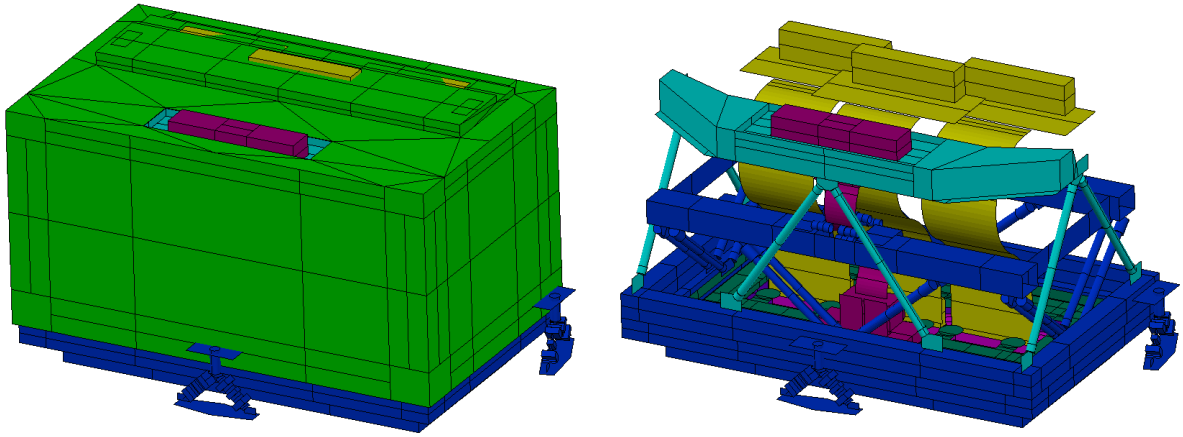

Figure 26 Thermal Desktop representation of FPA: (right) with enclosure (left) with enclosure removed

The S-glass enclosure employs varied layer configurations to maximize structural strength while minimizing conductive heat transfer to the cable bracket, as shown in Figure 27. The titanium bipods forming the main reentrant supports are extremely thin-walled, with dimensions of 0.15 mm thickness × 3.4 mm diameter, and are brazed into end fittings. The strap supports have similar dimensions (0.157 mm × 3.46 mm). The thermal strap consists of copper foils with a copper lower end block and an aluminum upper end block to reduce supported mass. The copper lower end block improves temperature control

performance by reducing thermal gradients and enabling the control point to more effectively intercept environmental loads that perturb the thermal strap.

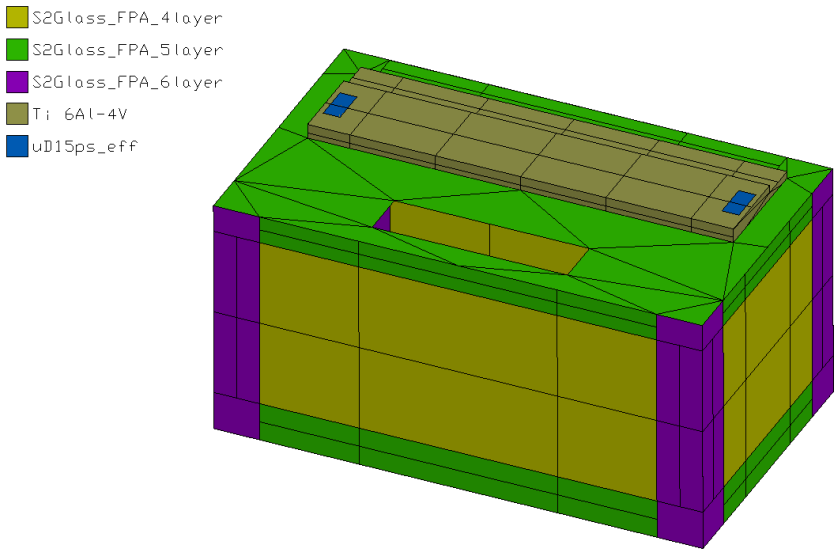

Figure 27 Focal plane enclosure showing number of S-glass mat layers

3.4.5 Cabling

Harness heat loads are typically significant contributors to parasitic heat loads in cryogenic instruments, and SPHEREx is no exception. The detector cables dominate the harness system, consisting of a total of 420 twisted pairs of 36 AWG manganin conductors (840 individual conductors) with stainless-steel shields. The stainless-steel shields employ a reduced optical density (~40%) to lower radiative loads. Additional phosphor-bronze shielded and unshielded harnesses are provided for temperature sensors and heaters. A table summarizing the number of conductors and their cross-sections is shown in Table 5.

Table 5 Listing of key harnesses, approximate cross section, and number of wires

Name	Wire spec	Materials	cross section per TP or TQ (m^2)	Number of TP or TQ between regions				
				SC to outer VG	Outer VG to middle VG	Middle VG to inner VG	Inner VG to tele	Tele to MWIR
MWIR detector harness	TP-0221009R0 – Wire, 36 AWG, Twisted Pair Shielded Jacket	SS 304 Manganin PTFE	2.23E-08 2.53E-08 1.50E-07	210	210	210	210	210
SWIR detector harness	TP-0221009R0 – Wire, 36 AWG, Twisted Pair Shielded Jacket	SS 304 Manganin PTFE	2.23E-08 2.53E-08 1.50E-07	210	210	210	210	210
FPA Temperature control Harness	TP-0821054R0 – Wire, 36 AWG, Twisted Pair Shielded Jacket	SS 304 PhBr PTFE	2.23E-08 5.08E-08 7.66E-07	16	16	16	16	8
Decon sensor harness	86127 – NASA TPJ 36 – Wire, 36 AWG, Twisted Pair Jacket, PhBr	PhBr PTFE	2.53E-08 1.41E-08	14	14	14	14	2
Decon heater harness	86128 – NASA TPJ 26 – Wire, 26 AWG, Twisted Pair Jacket, PhBr	PhBr PTFE	2.58E-07 3.89E-07	9	9	9	9	2
Science sensor harness	HC-1220053R0-1 – Wire, 36 AWG, Twisted Quad Shielded Jacket	SS 304 PhBr PTFE	2.23E-08 2.53E-08 3.83E-07	21	17	13	9	1
Cover mechanism harness	Lakeshore 32AWG PhBr twisted pair – DT-32 with PI	PhBr	6.41E-08	16	16	16	16	0
Grounding wire	Lakeshore 32AWG PhBr twisted pair – DT-32 with PI	PhBr	6.41E-08	16	16	16	16	0

To intercept these loads, a heat sink with bond channels accommodating clusters of one to four wires is bolted to the inner V-groove. Although studies were conducted on heat sinking at the middle and outer V-grooves, the achievable temperature and wire length between stages led to the decision to provide heat sinking only on the inner V-groove. Wires are laid into each channel and the channel is then filled with Stycast® 2850 epoxy. A close-up of this configuration is shown in Figure 29, depicting a four-twisted-pair bundle exiting a channel adjacent to a conceptual diagram of the approach. A detailed analysis was performed to determine the effective conductance per unit length and, consequently, the total

length of these heat sinks. The cables are wrapped in black Kapton tape to radiate heat directly to deep space. The cable surfaces are discretely modeled in Thermal Desktop with a very conservatively low radial conductance, treated as pure Teflon. Initially, the radius of the bundle was multiplied by two to approximate the constant cross-section with which Thermal Desktop represents insulation nodes; this parameter was later tuned based on thermal testing. Reference images of the installed cables with a heat sink, cable internals, and their representation in Thermal Desktop are shown in Figure 28.

Figure 28 (Left) Image of as-installed SWIR detector harness. (Center) Microscope image showing partial braid coverage. (Right) Representative surfaces in Thermal Desktop

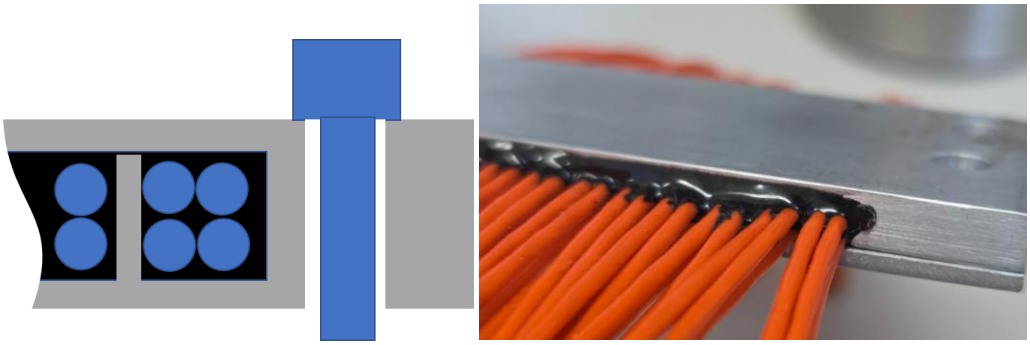

Figure 29 Harness heat sink detail: (left) cross section (right) close up of prototype

The flex cables inside the FPAs are also potential parasitic heat paths requiring special attention. They consist of constantan traces on polyimide substrates and are gold-coated to reduce radiative parasitic loads.

3.4.6 Sensors and Heaters

In total, SPHEREx includes 43 temperature sensors and 12 heater zones, including redundant sensors and heaters. It should be noted that some heater zones contain multiple elements wired in parallel.

During normal operation, only the active MWIR and SWIR FPA temperature-control heater zones are utilized (primary and redundant, fine and coarse control; four zones in total). A planned four zones of optical decontamination heaters are employed during controlled cooldown to maintain the optics at a temperature higher than that of the telescope housing, thereby reducing water ice accumulation. This process will be discussed in greater detail later. Both the decontamination and FPA control heaters are compact TO-220 package Vishay VPR220SZ devices.

Rosemount 118MM 2 kΩ PRTs are used to control the decontamination heaters. Their ~2 kΩ resistance at room temperature enables reasonable accuracy at cryogenic temperatures. A key consideration with this type of sensor is its ceramic packaging with very low coefficient of thermal expansion (CTE), which is susceptible to cracking if bonded directly to metallic or composite substrates. Consequently, these sensors were bonded to carriers made from Osprey CE7, a low-CTE silicon–aluminum alloy. The carriers can then be bolted to components as required. An image of a sensor bonded to a carrier is shown in Figure 30**.**

During testing, two Rosemount 118MM temperature sensors failed; although the root cause was undetermined, termination of the soft platinum leads was suspected. Two decontamination heaters also failed during testing—the MWIR primary heater (for which a redundant backup exists) and the SWIR heater (for which no backup is available).

The PRTs and decontamination heaters are both read and controlled by the spacecraft Integrated Avionics Unit (IAU). The total excitation current for each PRT is approximately 2 mA. Although this could represent a substantial instantaneous load even at the relatively low resistance of PRTs at cryogenic temperatures, the measurements are multiplexed across 32 channels. As a result, the time-averaged dissipation at 45 K (~111 Ω) is ~13.8 μW and at 62 K (~240 Ω) is 30 μW. At room temperature (~2.2 kΩ), the dissipation is ~275 μW, which remains negligible.

A potential concern was whether sensor dissipation could disturb FPA temperature stability. When requirements for multiplexing were generated, a simple test model was developed using the detailed FPA model. An impulse of 600 μW for 1/32 s was applied at the top of the thermal strap (where the PRT is

located), and the response at the base of the strap (where control is critical) was measured, shown in Figure 31. The top of the strap exhibited a periodic variation of 1 mK, which was attenuated to 10 μK at the bottom of the strap. The final multiplexing dwell time selected was 100 μs. Given the two orders of magnitude shorter dwell time and two orders of magnitude lower dissipation at critical temperatures, this effect was deemed negligible.

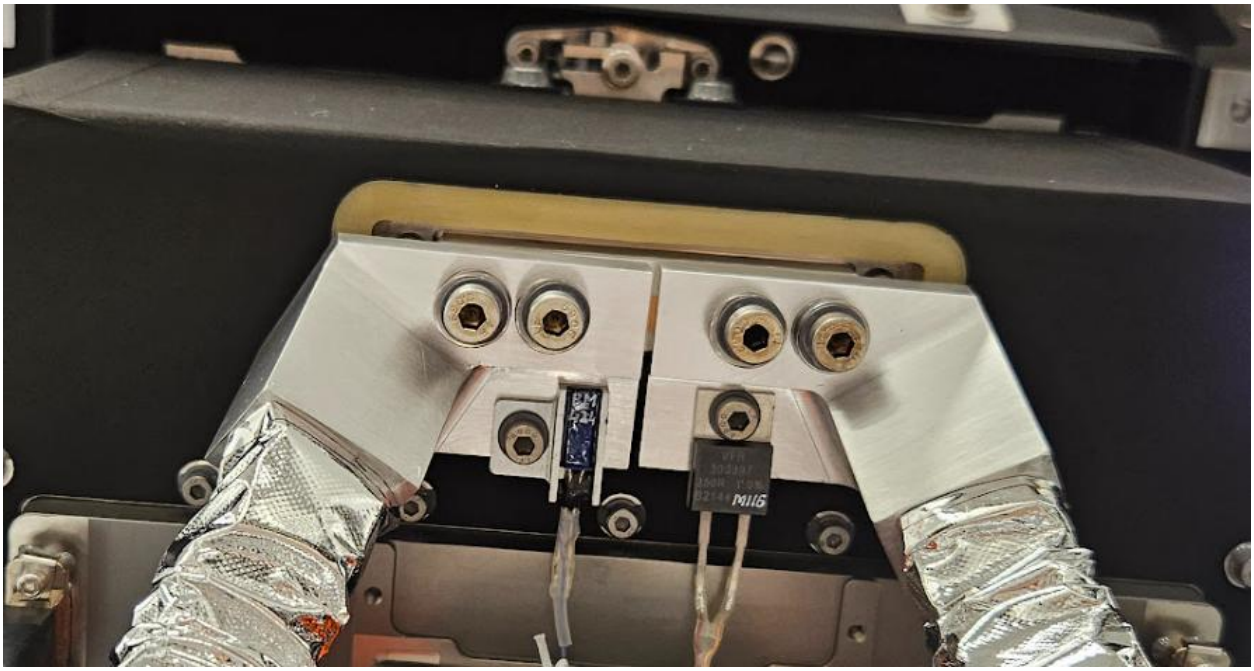

Figure 30 SWIR FPA interface showing Vishay VPR220SZ decontamination heater and 118MM PRT bonded into chassis

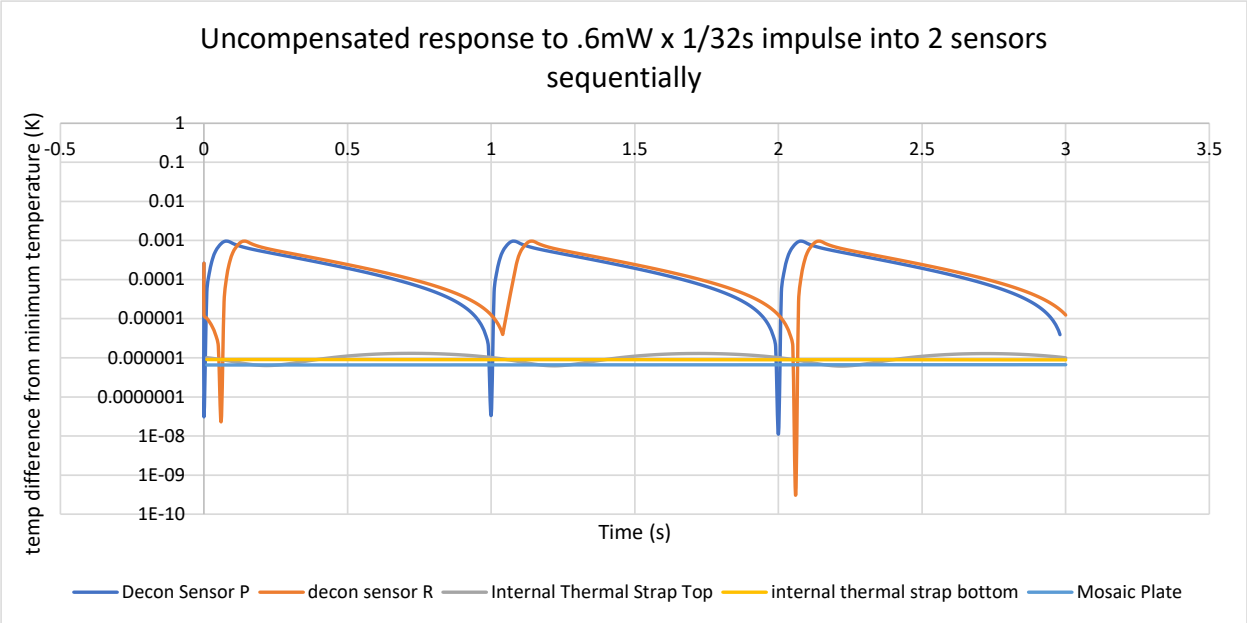

Figure 31 Maximum possible temperature fluctuations from extremely conservative estimate of temperature sensor dissipation and MUXing

The FPA temperature-control and science-telemetry temperature sensors are Lakeshore Cernox® CX-1080-CU devices, accurate from above room temperature down to 20 K. The outer photon shield and V-grooves use a high-temperature variant to accommodate the possible temperature ranges of those components. These sensors are semiconductor NTC (negative temperature coefficient) RTDs commonly used in cryogenics for their high dR/dT at cryogenic temperatures while maintaining sufficiently low total resistance to allow manageable excitation current, readout voltage, and dissipation. These sensors are read out by the instrument control electronics (ICE).

In laboratory settings, very low excitations are typically used—on the order of 10 mV, which would translate to ~50 nW (~5 µA) at 40 K for a typical Cernox 1080 resistance of 2 kΩ. The SPHEREx instrument control electronics use a much higher excitation of ~140 µA; however, at the lowest temperature of 45 K (~7 kΩ max, 4.5 kΩ typical) this yields 140 µW maximum dissipation, and at 62 K (6 kΩ max, 2.5 kΩ typical) only 20 µW. Because these are NTC devices, the dissipation decreases at higher temperatures. Based on the actual resistances of the sensors used, the dissipations were tabulated.

Combining the dissipation from all spacecraft-read PRTs and ICE-read Cernoxes at expected operational temperatures yields a total dissipation of approximately 0.42 mW on the 45 K MWIR stage

and ~1 mW on the SWIR stage. These contributions are not included in the thermal model but should be noted when comparing modeled versus measured results.

A table summarizing the temperature sensors and their required accuracies along with installation locations is shown in Appendix A. Appendix A also presents the locations of all installed sensors on the payload.

3.5 Thermal properties

3.5.1 Thermophysical Properties

The following section highlights key thermophysical properties within SPHEREx, with particular emphasis on thermal conductivity.

3.5.1.1 Photon shields

As previously discussed, the photon shields consist of ¾-inch-thick, 2.1 pcf Flex-Core® aluminum honeycomb with 0.008-inch-thick 2024 aluminum facesheets clad with high-purity aluminum. Care must be taken to correctly account for the effective thermal conductance of the honeycomb layup, both through-thickness and laterally. Correlations for regular honeycomb panels are available in standard references such as the *Spacecraft Thermal Control Handbook* (Donabedian, Spacecraft thermal control handbook, volume I: Fundamental Technologies 2002). However, these correlations are not directly applicable to Flex-Core® because of its asymmetric cell geometry.

In addition to the asymmetric honeycomb structure, the high-purity aluminum cladding can contribute significantly to the overall thermal conductivity at cryogenic temperatures. Explicitly modeling the internal geometry of the photon shields would require a prohibitive number of nodes; therefore, a detailed model was developed to derive an effective thermal conductivity. This effective property can then be applied to a two-dimensional surface of specified thickness within Thermal Desktop.

The facesheet specification is 0.008-inch total thickness AMS-QQ-A-250/5, which specifies 5% nominal and 4% minimum thickness of high-purity aluminum cladding over 2024 aluminum (AMS-QQ-A-250/5: Aluminum Alloy Alclad Sheet and Plate 2017). At the time this analysis was performed, the

cladding purity was assumed to be only 1%, and the analysis was not repeated after final material selection with a higher-purity cladding. Furthermore, inter-ribbon bonds were not represented in the detailed model; each layer was assumed to be in perfect contact. As will be discussed later in post-launch correlation, this analysis was subsequently reassessed.

The ribbons are 1.4-mil-thick 5056 aluminum. A "half-thickness" symmetry model was generated, as shown in Figure 32. A fixed temperature was applied at one side, and heat was applied to the opposing side in each principal direction; $Q/(A \cdot \Delta T)$ was then used to derive the effective conductivity. Radiation exchange was neglected. The preliminary effective conductance is presented in Figure 33. As will be discussed later in correlation, this model was subsequently improved based on on-orbit results.

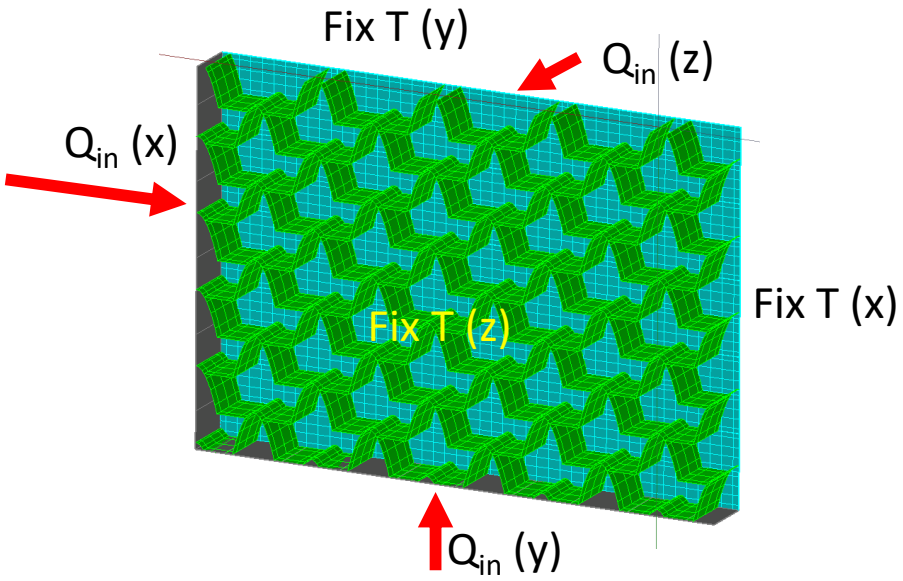

Figure 32 Half symmetry detailed thermal model of flex core honeycomb.

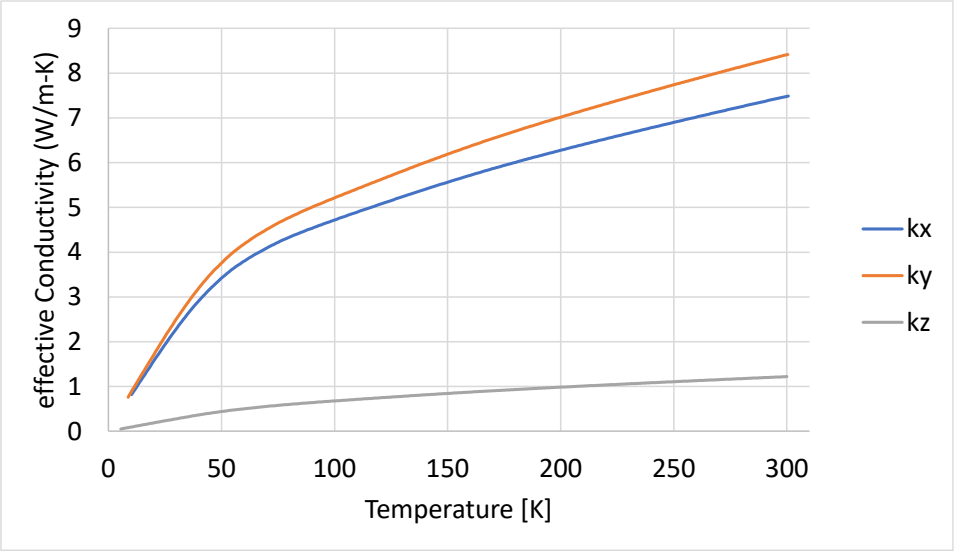

Figure 33 Effective photon shield conductance from half symmetry model with 0.008" thick facesheet, 1% high purity cladding, no inter-ribbon bonds, no radiation included

3.5.1.2 Thermal isolators

The Ti-6Al-4V alloy used for the V-groove flexures and S-glass strut ends is a well-characterized material with tabulated cryogenic properties (Bradley, Radebaugh and others 2013). By contrast, the thermal conductivity of S-glass/cyanate-ester composites depends strongly on fiber architecture, fiber volume fraction, constituent properties, and processing history. To reduce uncertainty, SPHEREx leveraged commonality across subsystems by using the same S2-glass fiber and cyanate-ester matrix for the FPA enclosure, telescope support struts, and FPA radiator support struts to fabricate flight-like uniaxial coupons. These coupons were characterized for conductivity both parallel and transverse to the fiber direction, and the results were mapped to the specific lay-ups employed. The FPA enclosure used a heavier-areal-weight fabric (≈300 g m^{-2}) than the ≈120 g m^{-2} fabric used in the radiator and telescope struts, introducing some extrapolation uncertainty; this risk was mitigated by an early standalone FPA thermal-balance test.

A custom apparatus was designed to minimize parasitic radiative and conductive heat leaks, following the general approach used at NASA Goddard for JWST materials (Tuttle, Canavan and Jahromi, Cryogenic thermal conductivity measurements on candidate materials for space missions 2017) but tailored to SPHEREx's small, flat coupons. As shown in Figure 34, the composite specimen was

bonded into copper end blocks whose temperatures were actively controlled and instrumented. Heat flow was introduced at the upper block and inferred from its electrical heater power. Effective conductance was determined from the measured heat flow, the temperature difference across the copper blocks, and the specimen geometry, with temperature sensing performed on the copper to avoid local gradients and contact perturbations on the composite. Bond-line contributions were analyzed and found to be smaller than the errors that would be introduced by mounting sensors directly on the coupon.

The specimen assembly and surrounding guard cylinder were housed within a shroud thermally referenced to the specimen's cold end so that the enclosure "floated" near the test temperature. A close-fitting stainless-steel inner shield reduced radiative view factors between the warm and cold ends; this shield terminated in a copper shield surrounding the hot end and was controlled to match the hot-block temperature, enforcing an axial shield gradient that mirrored the specimen gradient and thereby suppressing parasitic radiative exchange. Electrical leads were heat-sunk to the hot block to eliminate conducted parasitic loads. Recognizing that absolute diode readings carry offsets on the order of ±0.02 K (with comparable systematic noise), the procedure emphasized slope measurements. The heater power (and thus the hot-end temperature) was stepped through three levels while maintaining the same mean temperature at each point, and the $d(\Delta T)/dQ$ relation was used to extract conductance with reduced sensitivity to absolute calibration. A detailed thermal model—resolving heater geometry, sensor placement, bond-line thickness, and coupon dimensions—was developed to inform rig design and quantify residual setup error, shown in Figure 35 and Figure 36.

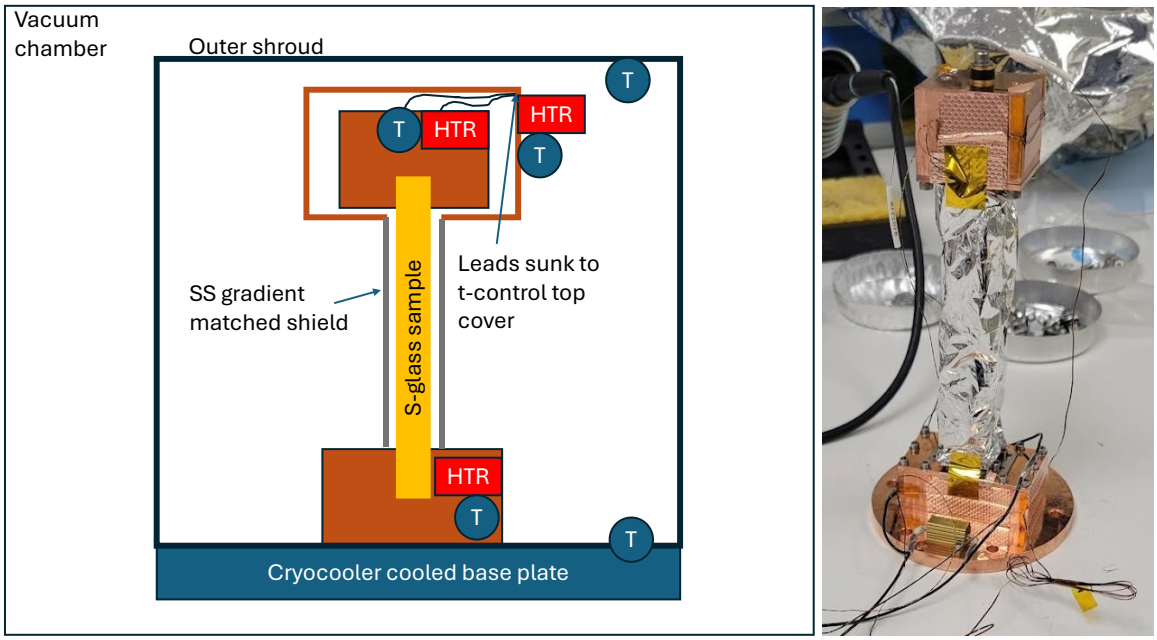

Figure 34 S-Glass conductivity measurement rig: (left) block diagram (right) assembled sample and shield

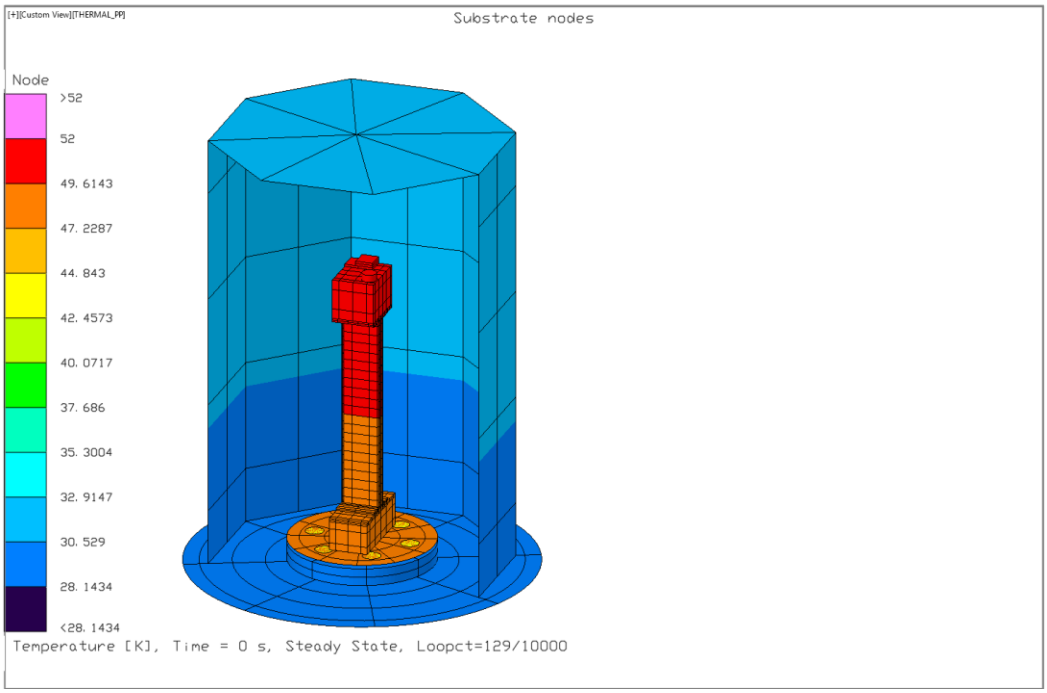

Figure 35 Thermal Desktop model of S-Glass conductivity measurement rig

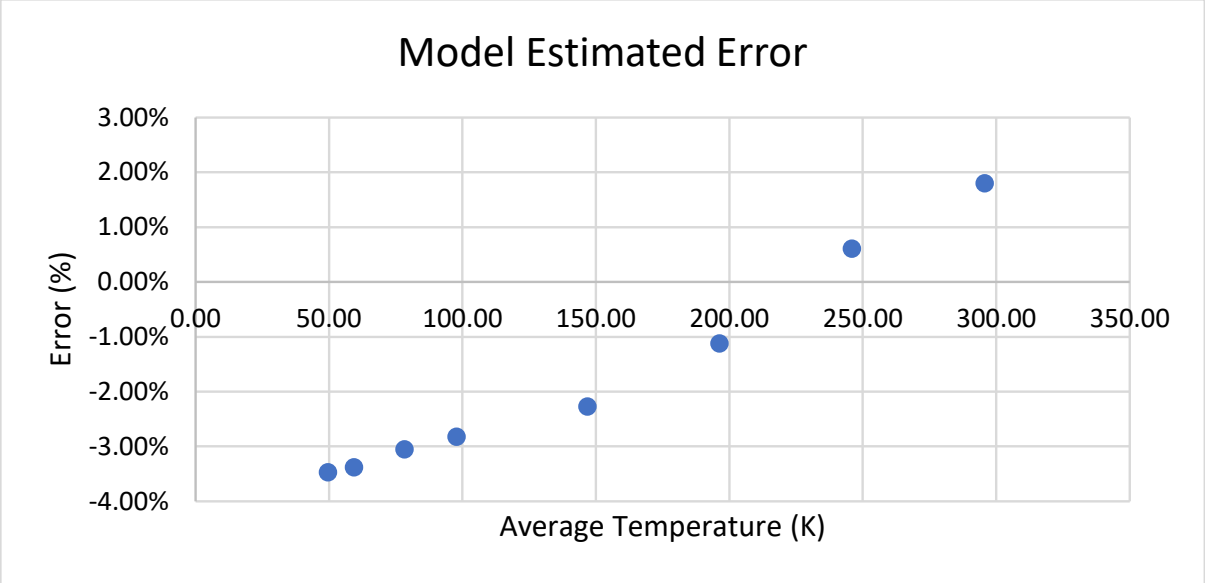

Figure 36 Model estimated error of S-Glass conductivity measurement

A scaling was then applied to convert these one-dimensional results to the planned lay-ups, as described in the literature (Kulkarni and Brady 1997). This was done by applying a simple geometric scaling, shown in equation 5 through equation 7, to derive the effective conductivity of the 45° layers (with the 0° and 90° layers taken directly from measurement). Here θ is the fiber orientation angle from the x-axis, k_1 is the along-fiber conductivity, and k_2 is the cross-fiber conductivity. It should be noted that the Kulkarni equation may appear slightly different from below since it is expressed in terms of magnitude rather than the full expansion. A thickness-weighted average of all layers was then used to produce the effective conductance. Each layer was assumed to have the same effective thickness so that the layers could be summed and divided by the total number of layers.

$$k_x = \frac{k_1 \cos^2(\theta)}{\sin^2(\theta) + \cos^2(\theta)} + \frac{k_2 \sin^2(\theta)}{\sin^2(\theta) + \cos^2(\theta)} \tag{5}$$

$$k_y = \frac{k_2 \cos^2(\theta)}{\sin^2(\theta) + \cos^2(\theta)} + \frac{k_1 \sin^2(\theta)}{\sin^2(\theta) + \cos^2(\theta)} \tag{6}$$

$$k_z = k_2 \ (out\ of\ plane) \tag{7}$$

The measurements compared to literature values (Tuttle, Canavan and Jahromi, Cryogenic thermal conductivity measurements on candidate materials for space missions 2017), (Hust 1984) are

shown in Figure 37. The SPHEREx samples show better performance (lower conductivity) at higher temperatures than other samples, which could be attributed to differences in fiber fill factors, epoxy, or lay-ups. At cryogenic temperatures, even a very thin (hundreds of angstroms) high-purity metal layer can have an appreciable effect on parasitic loads. Consequently, in the final inputs to the thermal model, the effective conduction of the Kapton blanketing was also included with the thin VDA layer for both the FPA radiator struts (double VDA Kapton), creating an effective aggregate material for the FPA radiator bipods. The telescope struts used a simple covering of thin adhesive black Kapton with conduction similar enough to the S-glass that a slight thickness adjustment could be made without needing an aggregate material.

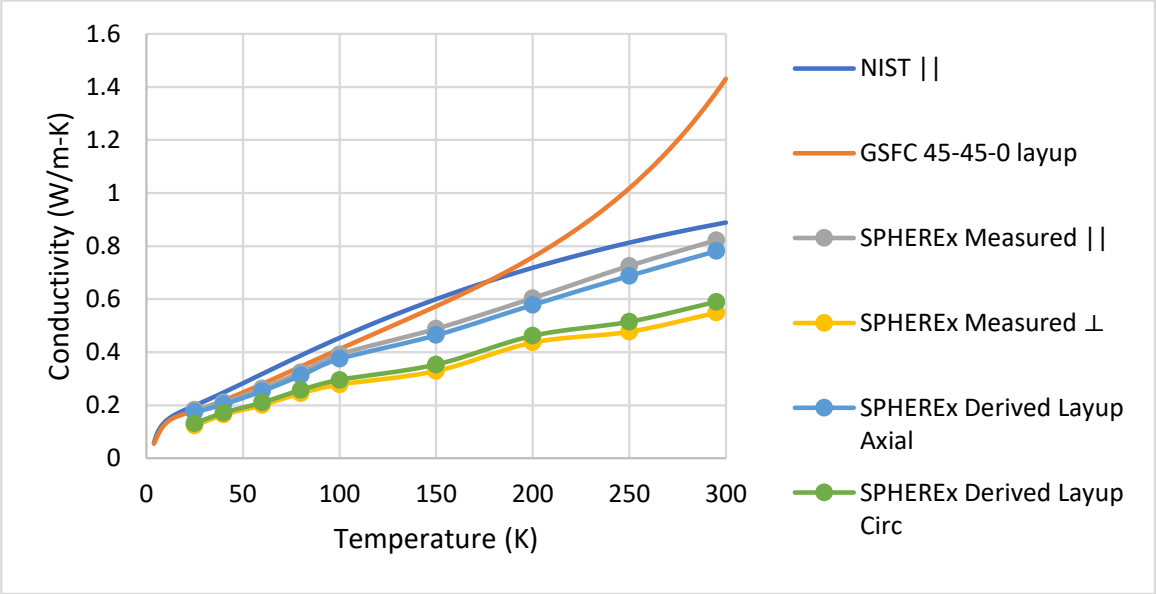

Figure 37 S-glass conductivity of SPHEREx samples relative to similar samples in literature.

For the V-groove supports and telescope support strut ends, although Ti-6Al-4V is a well-understood material, inaccuracies can still arise in model representation. Because Thermal Desktop is not ideal for extremely dense meshes due to radiation view-factor calculations, the minimum number of nodes was used for features such as the flexures. A much more detailed conduction-only model was therefore run to capture the net effect of fillets and more complex geometry. Heat was applied at one end with a boundary node at the other to measure the effective conductance relative to the simple model. This

produced effective multipliers for each set of V-groove flexures. An example for the middle V-groove to inner V-groove flexures is shown in Figure 38, and a table of the multipliers is provided in Table 6.

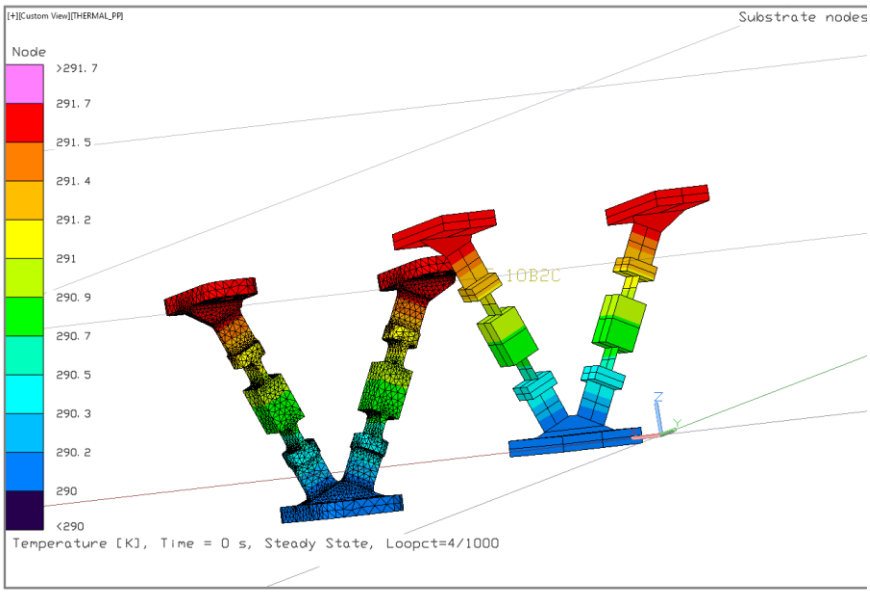

Figure 38 Detailed conduction only model of V-groove flexures next to simplified representation for main model

Table 6 Conductivity multipliers for flexures to match simplified model to detailed conduction only model

Component	Conductivity Multiplier
Telescope strut flexures	0.976
Spacecraft to outer v-groove flexures	0.99
Outer v-groove to middle v-groove flexures	0.988
Middle v-groove to inner v-groove flexures	1.015

3.5.1.3 Cables

The cross sections discussed in 3.4.5 are not sufficient to determine the actual conductance of the harnessing. All harnesses, even the unshielded ones, are configured as twisted pairs, and the shielding consists of a mesh weave. Because the detector readout harnesses dominate the harness cross section, particular emphasis was placed on deriving the effective conductance of the different components, explicitly accounting for the twist factor of the cables.

First, cables were dissected for visual measurement of the cable twist angle, as shown in Figure 39**.** This angle was used to apply a cosine knockdown factor to account for the extra effective length resulting from twisting, in conjunction with the specified cross section and number of conductors.

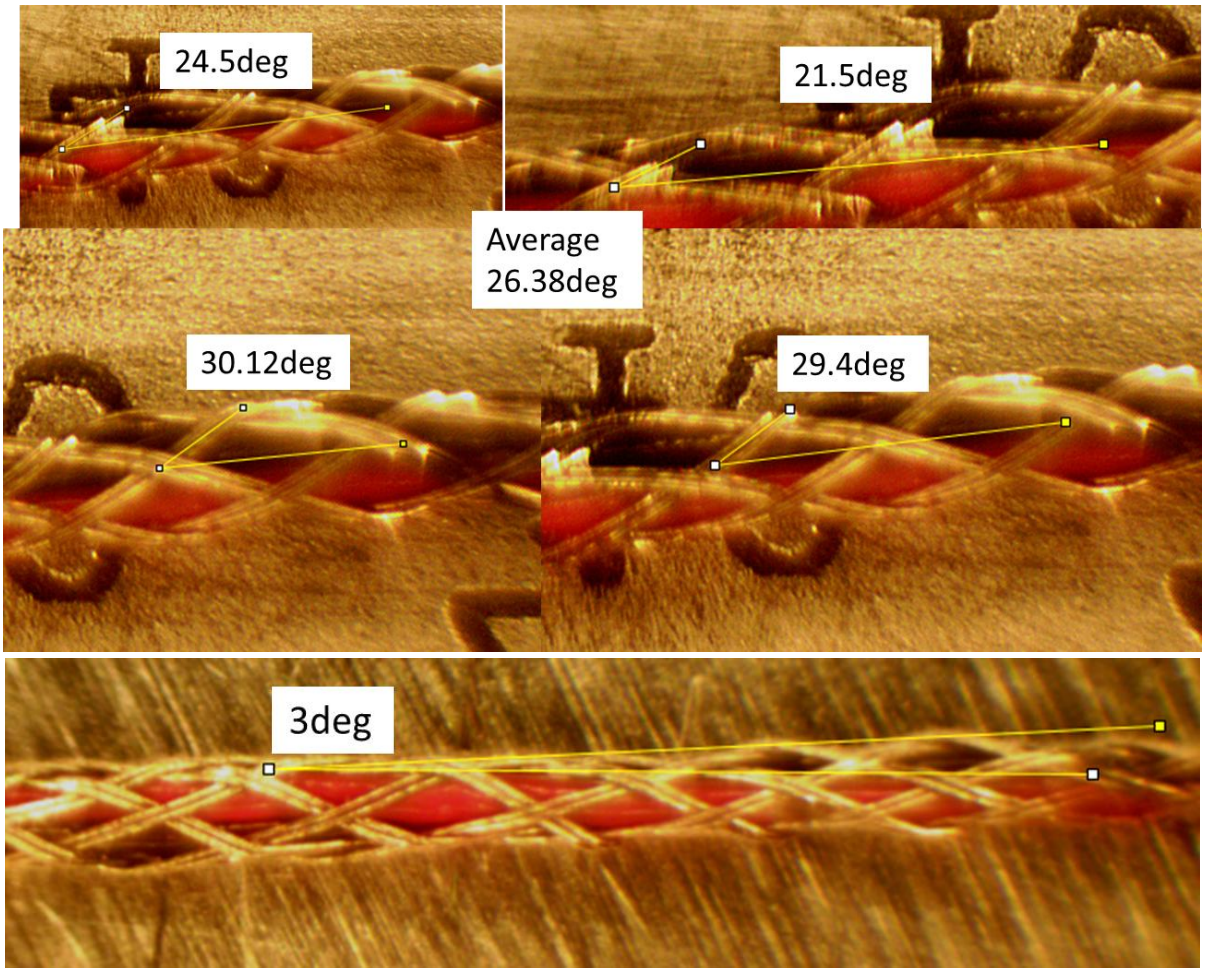

Figure 39 Close up images of detector harness with approximate twist angles. The top 4 images show the shield twist, the bottom image shows the main conductor

A second method was used to verify this approach, employing directly measured resistivity at room temperature and in liquid nitrogen, combined with the known length, to derive the effective cross section. This test setup is shown in Figure 40**.** The results from both the direct measurement and cosine knockdown are presented in Table 7**.** It should be noted that this test was performed with 40 AWG manganin; this was later changed to 36 AWG manganin, which employed the same stainless-steel braid. Therefore, the measured stainless-steel cross section was used in the final analysis, while the specified diameter of the 36 AWG manganin (0.127 mm) was adopted. The difference between the room-temperature and liquid-nitrogen measurements for stainless steel can be attributed to the stainless steel 304 being in a full-hard condition; different annealing processes affect resistivity as a function of temperature. The average effective cross section was used for the analysis.

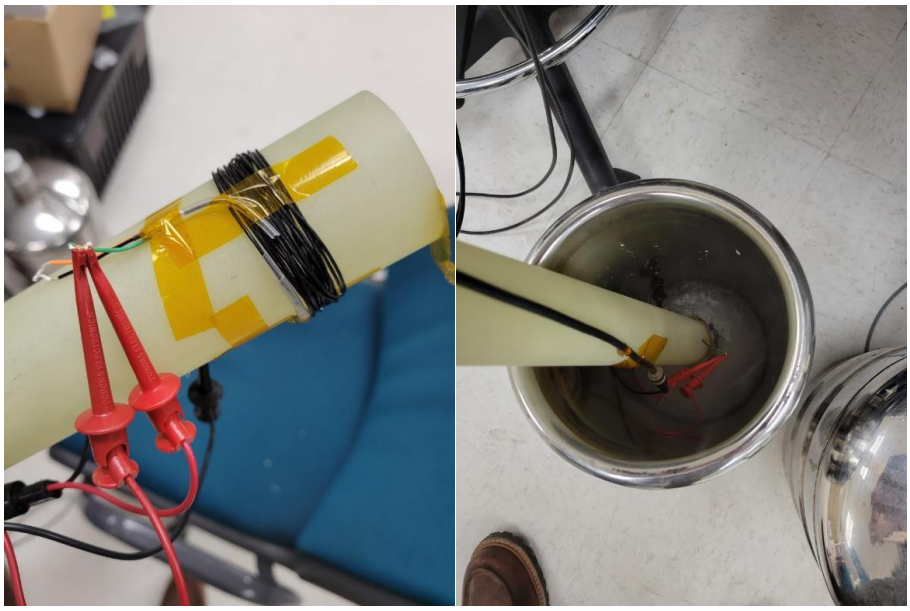

Figure 40 Images of the detector harness resistance measurement: (left) Room temperature; (right) Liquid Nitrogen temperature

Table 7 Measured and derived cross sectional areas of metallic components of the detector harness

	Effective A_c derived from RT R meas (m^2)	Effective A_c derived from LN2 R meas (m^2)	average A_c from R meas (m^2)	Percent diff RT to LN2 (%)	A_c from spec no knock-down (m^2)	A_c from spec with cos knock-down (m^2)	Percent diff spec to meas (%)
SS shield	2.42E-08	2.038E-08	2.229E-08	15.79	3.17E-8	2.85E-08	27.9
Manganin – Red	4.297E-09	4.279E-09	4.288E-09	0.42	4.56E-09	4.55E-09	6.1
Manganin – Black	4.295E-09	4.29E-09	4.2925E-09	0.12	4.56E-09	4.55E-09	6.1

For the remaining harnesses, the specified cross sections were used directly. Although this approach decreases accuracy, these harnesses constitute a smaller fraction of the overall harness loads, and the associated uncertainty was therefore considered acceptable.

For the harness heat sinks, a detailed half-symmetry cross-section model was developed for one-half of a single twisted pair in a bundle, as shown in Figure 41. The maximum and minimum conductance was derived based on two bounding assumptions: point contact between each component in the twisted pair versus complete contact. The results of this analysis are shown in Figure 42. It is important to note that although the units are expressed in W/m·K, this quantity represents an effective conductance per unit

length (hence the K·m expression). Multiplying by the actual length of the heat sinks yields a conductance in W/K.

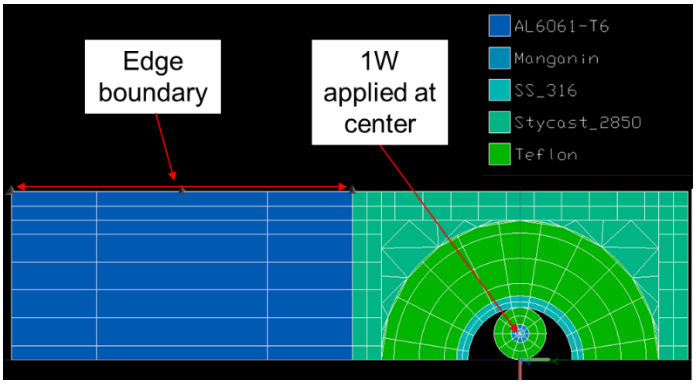

Figure 41 Detailed Thermal Desktop model of harness heat sink

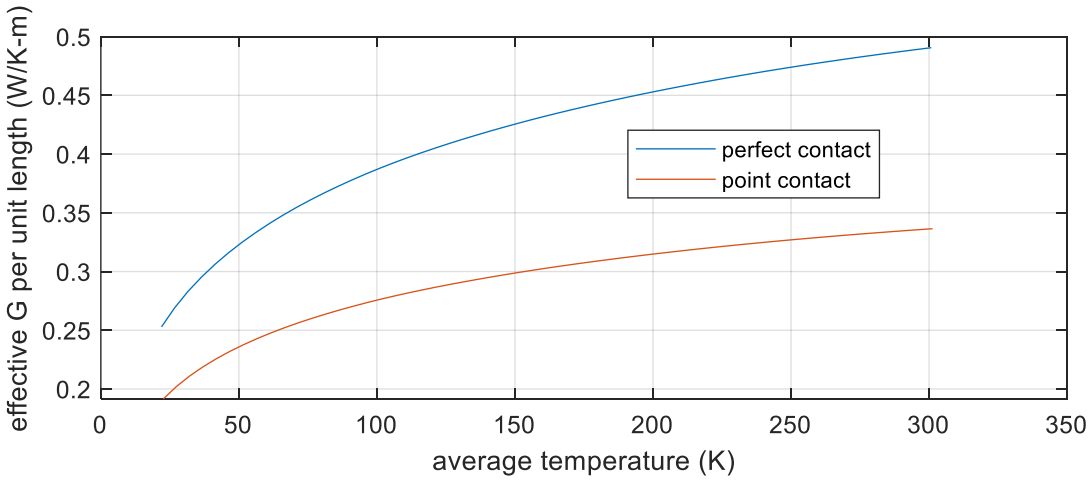

Figure 42 Harness heat sink modelled effective conductivity, best case and worst case

For all harnesses, the cross sections were combined with material properties to create an "aggregate" material in Thermal Desktop to represent the surfaces or conductors associated with the harnessing. The cable-sink effective conductance was derived using a detailed model bounded by these assumptions.

The FPA flex cable material was likewise represented as an aggregate material property based on the cross-sectional-area-weighted conductance of all its components. The relative fractions of each material in the flex cable cross section are: Constantan, 8.5%; PMMA, 52.3%; Gold, 0.005%; and Kapton (39.2% listed).

3.5.2 Optical properties

Given the very large temperature range of the SPHEREx instrument, the temperature dependence of thermo-optical properties must be accounted for. In addition to temperature dependence, Thermal Desktop can perform wavelength-dependent calculations. Ultimately, the goal is to include a first-principles estimate of the impact of water ice on the emissivity of the low-emissivity surfaces. More sophisticated formulations of this approach require wavelength-dependent optical constants.

It is considered best practice to run full temperature- and wavelength-based calculations, as discussed in the TFAWS 2014 short course (Bell, Panczak and Green 2014). In Thermal Desktop's RadCAD Monte Carlo method, each node emits a large number of rays representing photon bundles. As rays strike other surfaces, energy is absorbed (reduced by the surface absorptivity, which equals the emissivity per Kirchhoff's law), and the remaining fraction is reflected or transmitted according to the surface optical properties. By tracking all possible reflection paths, the fraction of the total energy originally emitted from surface *I* that is absorbed by surface *j* is tallied. This fraction is the radiation exchange factor, B_{ij}. The net heat transfer between surfaces is then calculated per equation 8, where σ is the Stefan–Boltzmann constant, ϵ_i is the emissivity of surface *I*, A_i is the emitting surface area, and $T_{i/j}$ are the emitting and receiving surface temperatures. The $\epsilon_i B_{ij} A_i$ term is called the RadK or radiation conductor; it is the quantity actually assembled into the thermal solution matrix, with an internal flag to indicate whether it is multiplied by σ and T^4 in computing a solution.

Given the very large temperature range of the SPHEREx instrument, temperature dependence must be accounted for in the thermo-optical properties used. In addition to temperature dependence, thermal desktop can conduct wavelength dependent calculations. Eventually the goal is to also include a first principles estimate of the impact of water ice on the emissivity of the low emissivity surfaces. More complicated formulations of the approach to derive this require wavelength dependent optical constants.

It Is considered best practice to run full temperature and wavelength-based calculations as discussed in the TFAWS 2014 short course on Non-Grey and Temperature Dependent Radiation Analysis Methods (Bell, Panczak and Green 2014). In Thermal Desktop's RadCAD Monte Carlo method, each

node emits a large number of rays that represent photon bundles. As rays strike other surfaces, energy is absorbed (reduced by the surface absorptivity which is the same as the emissivity per Kirchoff's law) and the remaining fraction is reflected or transmitted according to the surface optical properties. By tracking all possible reflection paths, the fraction of the total energy originally emitted from surface I that is absorbed by surface j is tallied. This fraction is the radiation exchange factor, Bij. The heat between the surfaces is then calculated per equation 8, where σ is the Stefan-Boltzmann constant, ϵ_i is the initial surface emissivity, A_i is the initial surface area, and $T_{i/j}$ are the emitting/receiving surface temperatures. The $\epsilon_i * B_{ij} * A_i$ term (RadK) is actually what goes into the thermal solution matrix with a flag as to whether it is multiplied by σ and T^4 is used in computing a solution.

$$Q_{rad,ij} = \sigma * \epsilon_i * B_{ij} * A_i * (T_i^4 - T_j^4) \tag{8}$$

If temperature-dependent values of emissivity are supplied, the emissivity is interpolated based on the surface's initial temperature, since the radiation calculations are performed separately and before the thermal solution.

For wavelength-dependent calculations, the user can specify a set of wavelength bins. For each bin, the emissivity is interpolated from a user-defined table of emissivity versus wavelength. Temperature dependence can be added as an additional dimension to this table.

For a grey analysis to hold, equation 9 must be satisfied. Thus, using a fixed, non-temperature- or non-wavelength-dependent (grey) emissivity becomes problematic for materials with strong temperature or wavelength dependence that are in radiative exchange across large temperature differences, such as the aluminum used for the photon shields.

$$\alpha_2(T_2)\epsilon_1(T_1) = \alpha_1(T_1)\epsilon_2(T_2) \tag{9}$$

However, computing a radiation solution with full temperature and wavelength dependence is very computationally intensive, since each wavelength bin requires a separate Monte Carlo simulation. The temperature solution is sequential to the radiation solution, and the two must be iterated to update emissivity values as the temperature solution progresses. Given the number of nodes involved, a Monte

Carlo simulation for a single wavelength bin takes approximately one hour of computation time. Even a relatively sparse bin count of ten would require ~10 hours for a single iteration. In addition to the time to compute the RadKs, this also generates an effective radiation conductor in each band and thus expands the thermal network matrix by the number of wavelength bands. Several iterations—conducting a radiation solution, then a temperature solution, and feeding the updated temperatures back into the next radiation iteration—are required to converge on the final temperature. This is tractable for a steady-state solution; however, for a transient solution the larger thermal network dramatically slows each timestep.

To perform multiple sensitivity studies and cooldown analyses, a compromise was required. For conservative pre-flight assessments, such as those used for margin calculations, a “hot-side” balance was employed. This approach is typically used when the hot surface is much warmer than the cold surface and thus dominates the energy exchange; for example, 300 K to 40 K (a factor of 3164 in energy). For SPHEREx, the temperature differences are large but not sufficient to make this assumption exact. From the outer shield (~250 K) to the middle shield (~150 K) the factor is only ~8×, and from the middle shield to the inner shield (~100 K) it is ~5×. However, emissivity decreases at lower temperatures, so a higher emissivity and thus higher radiation exchange is represented if the surface emissivity is taken at the hot-side temperature. This was verified with a time-consuming temperature and wavelength-dependent analysis on a single case. The comparison between the hot-side bias and full temperature and wavelength-dependent calculations, and its effect on the telescope and FPA radiator temperatures, is shown in Figure 43.

These emissivity values were then tuned in the model based on TVAC results to produce the values used for more accurate flight predictions and were further refined in flight as will be discussed later. Figure 44 and Figure 45 show the emissivity and absorptivity of all surfaces on SPHEREx, including the spacecraft bus, which is relevant due to potential coupling with the outer shields. Greater detail on this coupling is not explored further in this work.

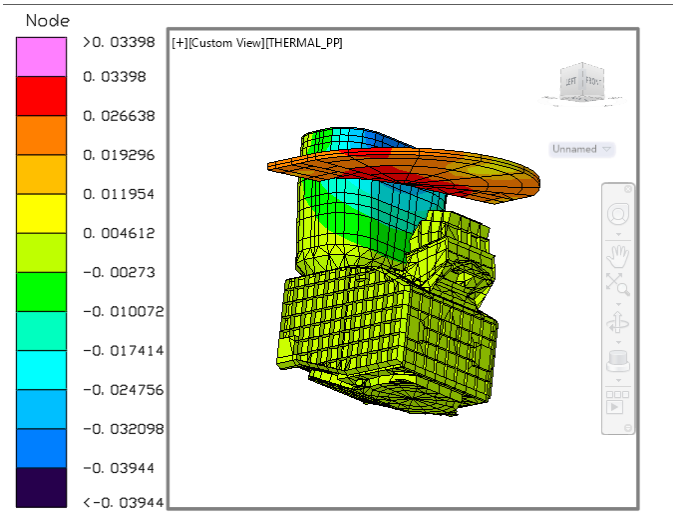

Figure 43 Temperature comparison of solution with temperature and wavelength dependent radiation calculations minus solution using hot side bias emissivity values

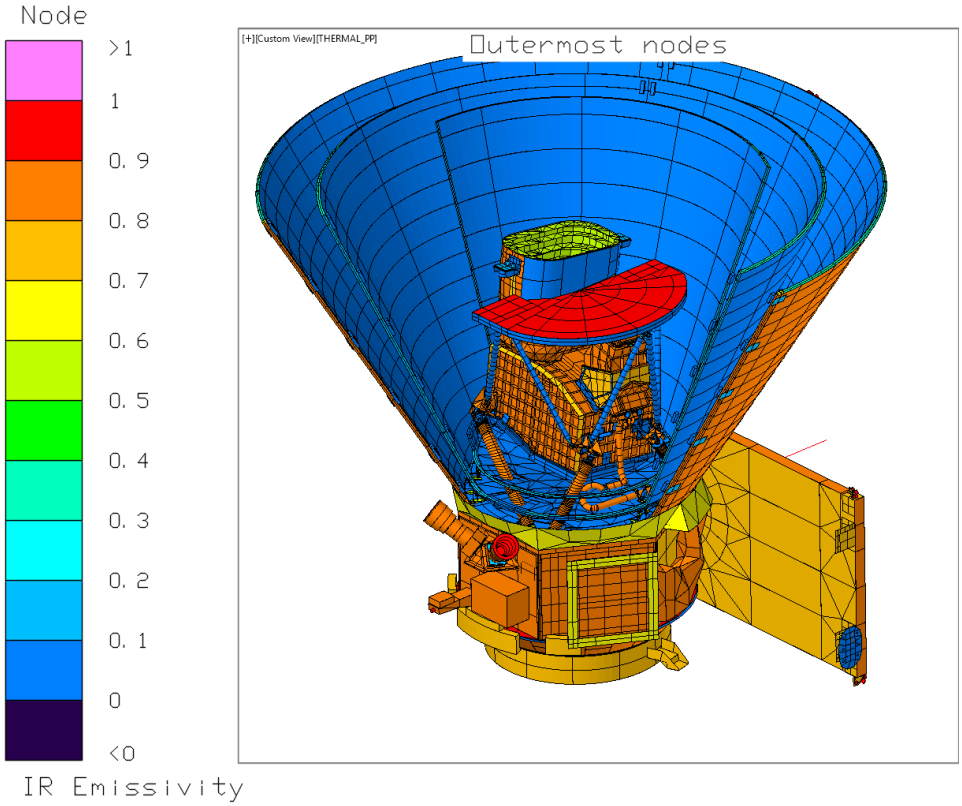

Figure 44 Infrared emissivity of all components on SPHEREx, photon shield sections removed for clarity

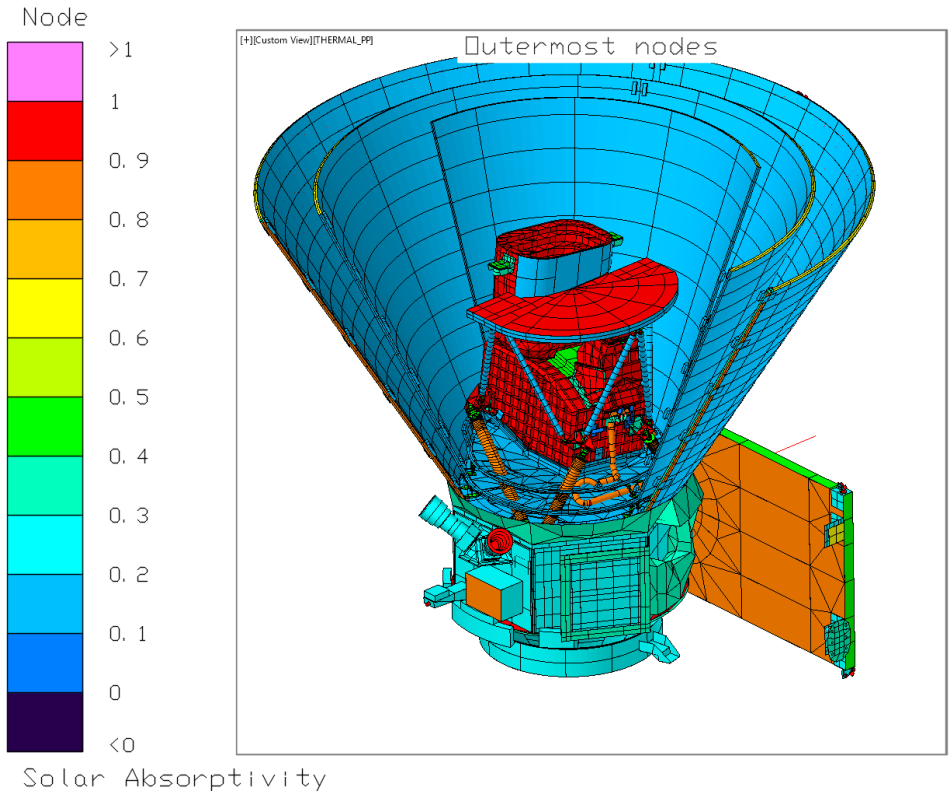

Figure 45 Solar absorptivity of all components on SPHEREx, photon shield sections removed for clarity

3.5.2.1 High emissivity surfaces

The high-emissivity surfaces of SPHEREx constitute the primary radiating surfaces. Even the most effective isolation and shielding can only achieve limited thermal control if there is not a surface with both a clear view to space and a high emissivity to dissipate unavoidable parasitic heat loads and detector dissipation.

The S-13G paint used for the outer photon shield was extensively qualified at JPL, including direct emissivity and absorptivity measurements. Pre-launch, these room-temperature emissivity measurements were used directly. However, temperature-dependent data are available from Kauder (Kauder 2005), shown in Figure 46.

For the telescope, samples painted by Ball Aerospace (now BAe) were sent to Goddard Space Flight Center, where their emissivity was verified to be consistent with the values used in the model and with samples measured previously using a specialized cryogenic emissivity test facility (Tuttle, Canavan and DiPirro, et al. 2014). These measurements are shown in Figure 46. All masked areas and fastener

heads were accounted for in effective knockdowns of the emissivity, assuming these surfaces have much lower emissivity than the paint. The different regions of this knock down are shown in Figure 47.

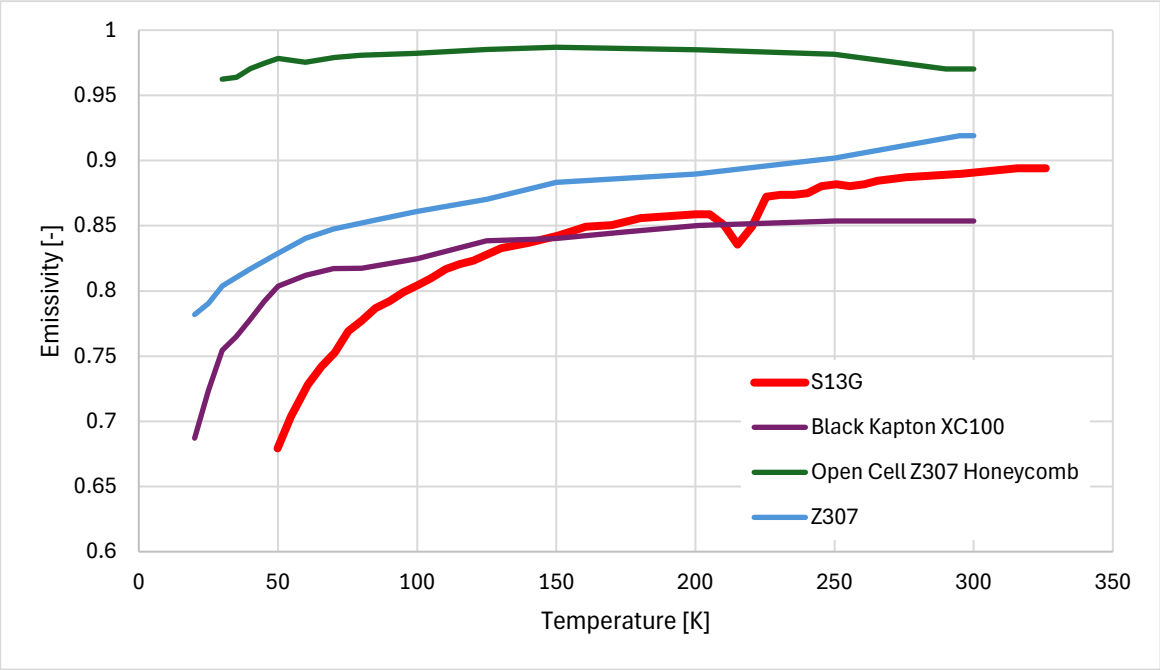

Figure 46 Total hemispherical emissivity vs temperature for key high emissivity surfaces

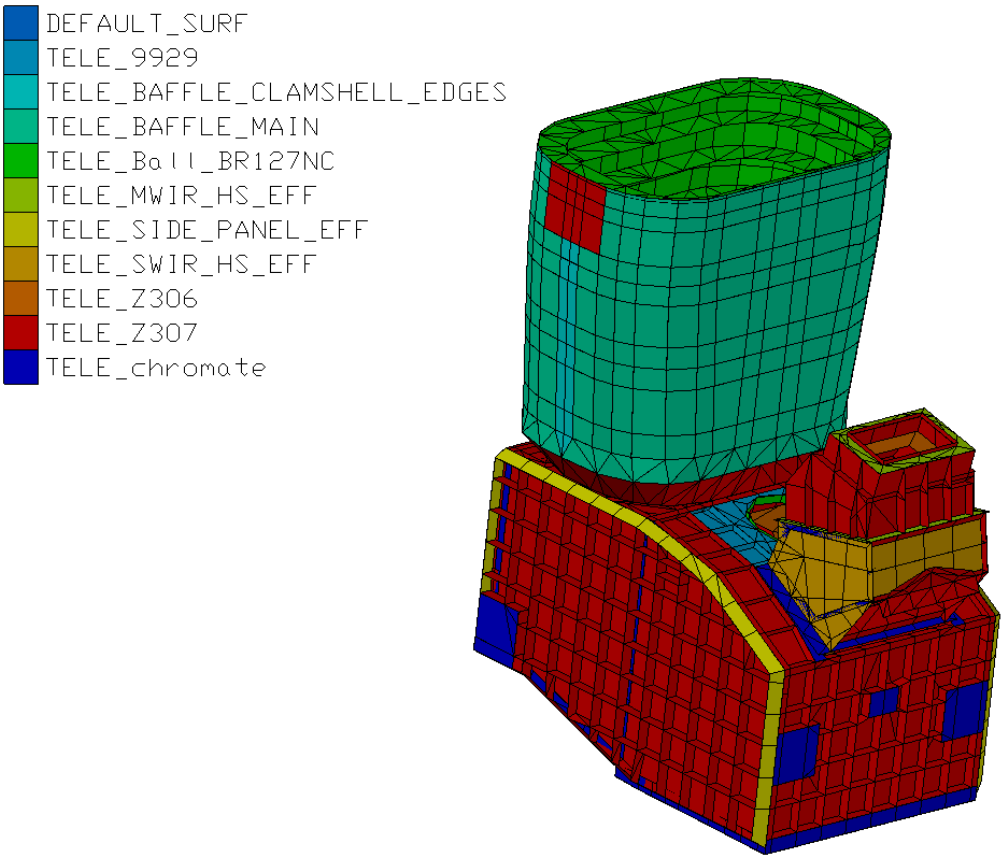

Figure 47 Regions of emissivity knock downs associated with fastener or masking coverage

The FPA radiator was not directly measured; however, its aspect ratio matches samples measured by Tuttle in the same 2014 paper, though with slightly larger honeycomb cells (3/16-inch diameter, ½-inch depth, L/R = 5), as shown in Figure 48. The cavity emittance can also be derived from first principles. Sparrow analyzed a hole of finite depth as a function of surface emissivity shown in Figure 49**.** Because the L/R ≈ 5 falls on the flat portion of the curve for essentially all reasonably high emissivities, a Z-307 emissivity of ~0.83 (measured at 45 K) yields a theoretical maximum hemispherical emissivity of 0.95, with a much higher normal emissivity of 0.99. The GSFC data shows a measured value of 0.974 at 45 K. Without intimate knowledge of the test setup, it is likely that the close spacing of the sample and the receiving honeycomb skew the data toward normal emittance rather than total hemispherical emittance. The initial value used for SPHEREx also included knockdowns for bolt holes, resulting in a lower value than both measurements; however, this is worth noting to interpret test and on-orbit data.

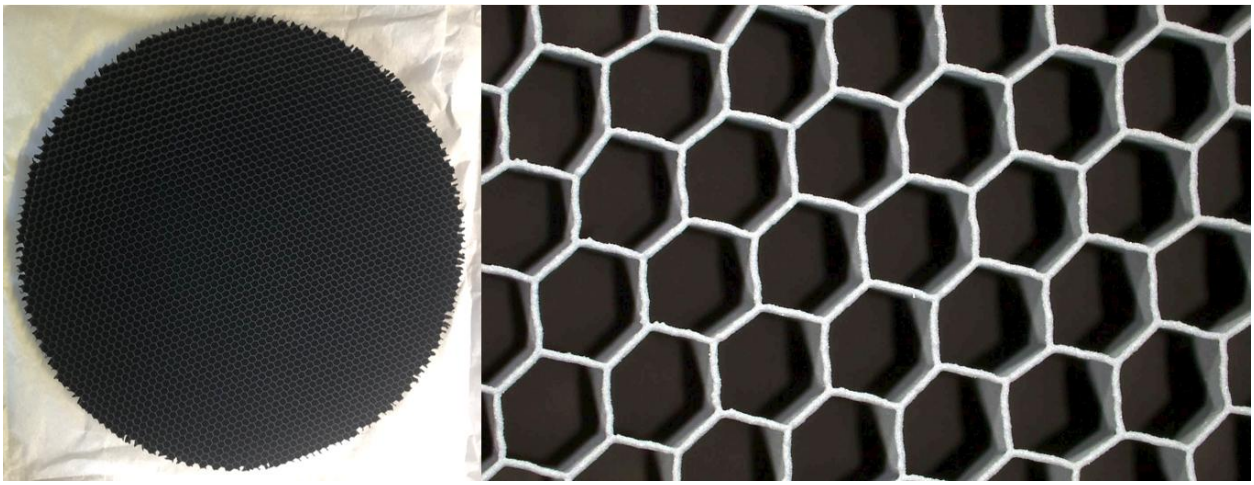

Figure 48 FPA radiator paint sample (left) with a zoom in and false contrast image of the honeycomb cells (right)

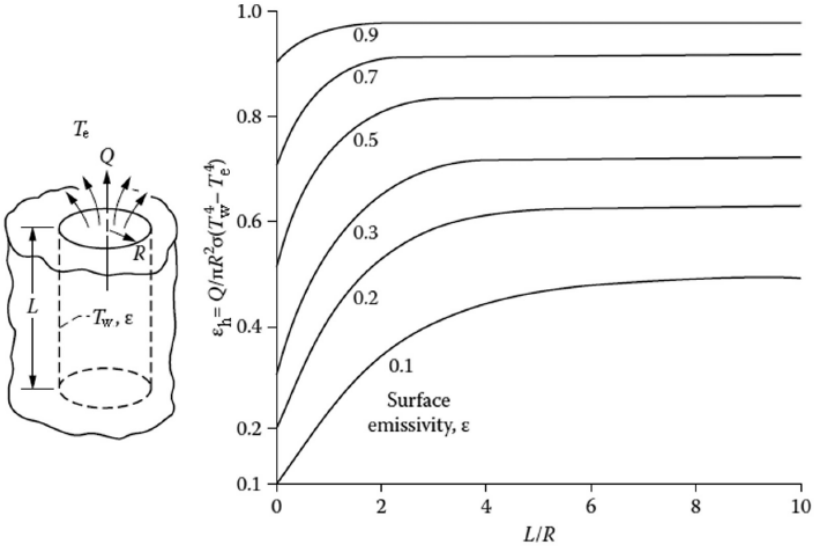

Figure 49 Theoretical emissivity of cylindrical cavity with different emissivities (Sparrow, Albers and Eckert 1962) reprinted in (Howell, et al. 2020)

Regarding specularity, Z-307 exhibits relatively high specularity in the infrared, especially in the far-infrared regime characteristic of the cryogenic telescope. The Goddard group measured the specularity of Z-307 as 98% at room temperature, increasing to >99% at 175 K and below (DiPirro, et al. 2012). By contrast, S-13G is quite diffuse; Kraus measured its BRDF as a broad peak (Krause, et al. 2002). Because there is very low sensitivity to specularity on the exterior of the outer shield, no effort was expended to convert the BRDF to a precise numerical value; for thermal modeling, a specularity value of 0.1 was used. The FPA radiator is assumed to be very diffuse with a specularity of 0.

3.5.2.2 Low emissivity surfaces

For metallic surfaces, several approaches are available for estimating emissivity, including direct measurements, theoretical derivations using the Hagen–Rubens relation, and derivations based on the Drude model. The simplest approach is to apply measured, temperature-dependent emissivity values such as those in the (Donabedian, Spacecraft thermal control handbook, volume II: cryogenics 2004) or in (Frolec, et al. 2019)**.** However, large variations can occur among samples due to surface defects, impurities, and specific alloy composition. In addition, modeling the thin-film effect required for water contamination demands optical constants: the refractive index n and the extinction coefficient k. Directly measured wavelength- and temperature-dependent optical constants across the very broad range required are seldom available. Typically, optical constants are tabulated only at room temperature, such as those at refractiveindex.info. This drives the need to employ more fundamental models for surface emissivity.

The derivation of emissivity from optical constants is well established. Although the reflectivity expressions derived from optical constants have a complicated general form, their derivations are presented in many optical texts, with the primary reference for this work being (Howell, et al. 2020). For metals, the formulation can be simplified because the extinction coefficient k is very large. Howell provides reflectivity equations that, combined with Kirchhoff's law, yield emissivity as shown in equations 10 through 12, where n and k are the real and imaginary components of the complex index of refraction at a given wavelength and θ is the angle of incidence

$$\epsilon_{\lambda,\parallel}(\theta) = 1 - \rho_{\lambda,\parallel}(\theta) = 1 - \frac{(n\cos(\theta) - 1)^2 + \left(k\cos(\theta)\right)^2}{(n\cos(\theta) + 1)^2 + \left(k\cos(\theta)\right)^2} \tag{10}$$

$$\epsilon_{\lambda,\perp}(\theta) = 1 - \rho_{\lambda,\perp}(\theta) = 1 - \frac{(n - \cos(\theta))^2 + \left(k\cos(\theta)\right)^2}{(n\cos(\theta) + 1)^2 + \left(k\cos(\theta)\right)^2} \tag{11}$$

$$\epsilon_{\lambda}(\theta) = 1 - \rho_{\lambda}(\theta) = 1 - \frac{\rho_{\lambda,\parallel}(\theta) + \rho_{\lambda,\perp}(\theta)}{2} \tag{12}$$

A fundamental theory for deriving the optical constants is the Drude model. Howell notes that it is particularly effective at approximating aluminum, which is key for SPHEREx. This theory delves more deeply into the electromagnetic physics driving reflectance. The complex dielectric constant is a function of the electromagnetic radiation frequency (ω), plasma frequency (ω_p), and damping coefficient (ζ), shown in equation 13. This dielectric constant relates back to n and k through equation 14 and 15.

$$\bar{\epsilon} = \epsilon_I + i\epsilon_{II} = 1 - \frac{\omega_p^2}{\omega^2 + i\zeta\omega} \tag{13}$$

$$n^2 = \frac{1}{2}\left(\epsilon_I + \sqrt{\epsilon_I^2 + \epsilon_{II}^2}\right) \tag{14}$$

$$k^2 = \frac{1}{2}\left(-\epsilon_I + \sqrt{\epsilon_I^2 + \epsilon_{II}^2}\right) \tag{15}$$

For application, the plasma frequency and damping coefficient must be related back to temperature-dependent, commonly measurable engineering properties as defined in equations 16 and 17. The plasma frequency is constant relative to temperature in this formulation with the physical constants N_A (Avogadro Constant= 6.022 E-23 mol^{-1}), A (molar mass), ρ_m (mass density), e (electron charge =1.6022e-19 Coulombs), ϵ_0 (vacuum permittivity=8.8542e-12 F/m), and m_e (electron mass=9.1094e-31 kg). The key to the temperature dependence of the Drude formula is the electrical resistivity of the damping coefficient (Wikipedia contributors 2025).

$$\omega_p = \sqrt{\left(\frac{N_A Z \rho_m}{A}\right) * \left(\frac{e^2}{\epsilon_0 m_e}\right)} \tag{16}$$

$$\zeta = \left(\frac{N_A Z \rho_m}{A}\right) * \frac{e^2}{m_e} * \rho_e \tag{17}$$

The Drude model can be simplified in cases with a highly conducting metal at longer wavelengths (>5 μm) using the Hagen–Rubens relation. This assumption allows n=k, which greatly simplifies downstream emissivity derivations. Howell provides the formulation for n and k, shown in equation 18, where λ_0 is the wavelength in μm and ρ_e is the resistivity in Ω·cm. The other constants are μ_0 (magnetic permeability) and c_0 (speed of light in a vacuum):

$$n = k = \sqrt{\frac{\lambda_0 \mu_0 c_0}{4\pi \rho_e}} = \sqrt{\frac{0.003\lambda_0}{\rho_e}} \tag{18}$$

In the scripts used for this work, n and k were inserted into equations 10 through 12. Since n=k, Howell simplified and integrated across all angles and wavelengths to yield an effective total emissivity as a function of temperature, shown in equation 19, where T is the temperature in K:

$$\epsilon(T) = 0.751\sqrt{\rho_e T} - 0.396\rho_e T \tag{19}$$

Finally, to apply these models in practice, a measured emissivity is used to tune the effective resistivity as a function of temperature. The physical resistivity is approximated from available data with a fixed offset solved to match the measured emissivity. The results of this scaling for the different Drude and Hagen–Rubens models are shown for the materials used on the photon shields and V-grooves in Figure 50, and compared to available data sources. The corrected emissivity from Hagen–Rubens drops off much more rapidly than Drude; therefore, Drude was adopted as the more conservative reference. The true curve for a perfect surface with the correct resistivity lies somewhere between these two models, but surface damage and contamination push the effective emissivity of any real surface well above both. The code used to generate these data expands on scripts found in Modest's Heat Transfer text. (Modest and Mazumder 2021)

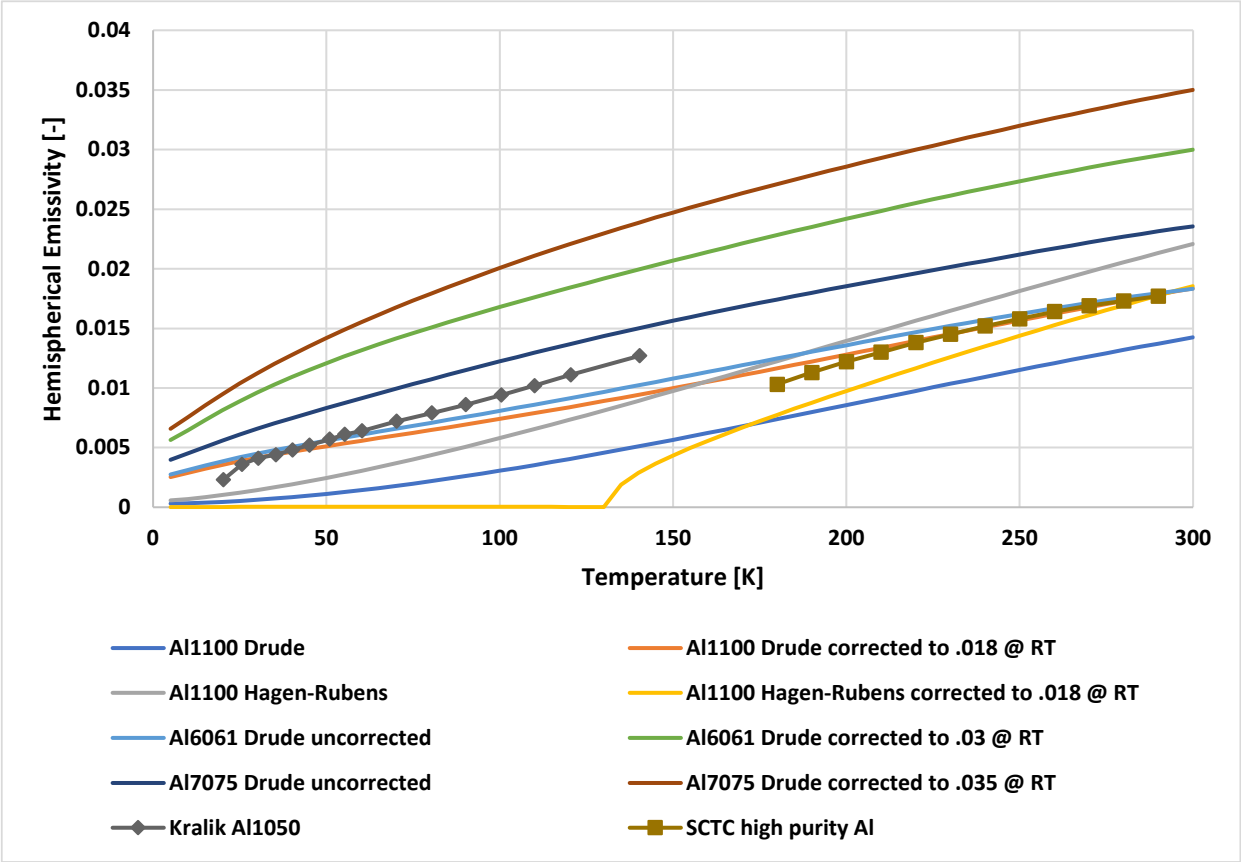

Figure 50 Modelled temperature dependent emissivity using corrected and uncorrected Drude and Hagen-Rubens approximations compared to measured data from Kralik and the Spacecraft Thermal Control Handbook (Frolec, et al. 2019) (Donabedian, Spacecraft thermal control handbook, volume II: cryogenics 2004)

For the VDA surfaces, a more advanced anomalous skin-effect correction must be added to the classical Drude model. Gilberd proposes such an approach (Gilberd, 1982). The primary use of VDA on SPHEREx is for the bottom of the telescope, the telescope baffle facing the MWIR radiator, the bipod/V-groove closeouts, and miscellaneous tape used to close out light gaps. Because these surfaces represent small fractions of the low-emissivity surfaces for SPHEREx, the full model was not developed. Instead, the correlation proposed in (Donabedian, Spacecraft thermal control handbook, volume II: cryogenics 2004) shown in equation 20 was used, where T is in Kelvins.

$$\epsilon(T) = (6.512E-4) * T^{0.667} \tag{20}$$

A final consideration is surface specularity. Perfectly polished aluminum exhibits a specularity close to 1. Measurements of the specular and hemispherical reflectance yielded a specularity of 0.998 for the photon-shield samples. This value was reduced to account for scratching and particulate

contamination. The exact reduction was not revisited given the relatively low sensitivity of thermal performance to reasonable changes in specularity, as will be seen later.

3.5.2.3 Ice accumulation and effect on emissivity

Ice accumulation is a persistent concern for cryogenic engineers, both on the ground and in space. Ice can reduce thermal performance by increasing the emissivity of shields and can also interfere with instrument measurements as seen recently for the Euclid mission (Jahnke 2024) (Schirmer, et al. 2023). The SPHEREx design intentionally avoids the use of multilayer insulation near critical cryogenic surfaces to minimize ice accumulation. The instrument's performance is particularly susceptible to throughput degradation caused by ice accumulation. As part of the theme "Explore whether planets around other stars could harbor life," SPHEREx measures extragalactic ice concentrations, which could be compromised by such contamination.

In general, contaminants such as ice are technically mobile to some degree and migrate to the coldest surface in line-of-sight via absorption and desorption. Much like radiation exchange, a Monte Carlo simulation can be used to model "reflection" and "absorption" of such molecules. The degree of mobility is temperature-dependent, and ice begins to accumulate on surfaces below approximately 180–200 K if there is a source of absorbed water (such as a polymer or composite). This behavior is governed by the vapor pressure of the accumulated contaminants, which can be derived from the Clausius–Clapeyron equation and is plotted in Figure 51. Below approximately 150 K, water molecules effectively become frozen in the contamination source because the vapor pressure falls below the ambient pressure in space. Consequently, controlling contamination is most critical when temperatures are between roughly 200 K and 150 K.

For SPHEREx, the middle shield operates near 150 K during the mission with a large view factor to the warmer outer shield and nearby small polymer parts and closeouts, so some accumulation is expected as long as water remains in the source components. As the outer shield sources desiccate, the rate of water desorption decreases, and eventually the rate of sublimation outpaces accumulation on the

middle shield. By contrast, the telescope mirrors and inner Photon Shield operate at such low temperatures that, even in the vacuum of space, the sublimation rate is essentially negligible.

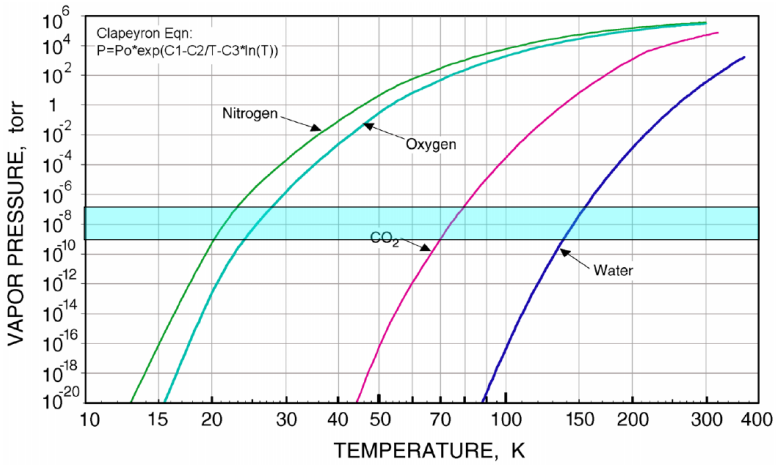

Figure 51 Vapor pressure of various contaminants based on the Clausius-Clapeyron equation. The approximate pressure in space at 650km is indicated with a blue box (R. G. Ross 2015)

The derivation of the emissivity of thin ice layers follows directly from the previous section, as it is essentially a thin-film optical problem. Given that the wavelengths of interest at temperatures below 200 K are several microns, any feasible ice layer will be much thinner than the wavelength of light. Fully modeling this phenomenon requires accounting for multiple re-reflections; however, Auguié has clearly documented the derivation (Auguié 2017).

A primary challenge in implementing this model was compiling the necessary n and k data for water ice across relevant temperature ranges. Multiple sources were combined to cover the broad wavelength and temperature band of interest, then carefully filtered and interpolated to produce a complete dataset (Warren and Brandt 2008) (Trotta 1996) (Grundy and Schmitt 1998) (Mastrapa, et al. 2009). The original data are shown in Figure 52 and the processed and interpolated results are presented in Figure 53. The n and k values of the underlying metal substrate were derived using the Drude equation described in the previous section.

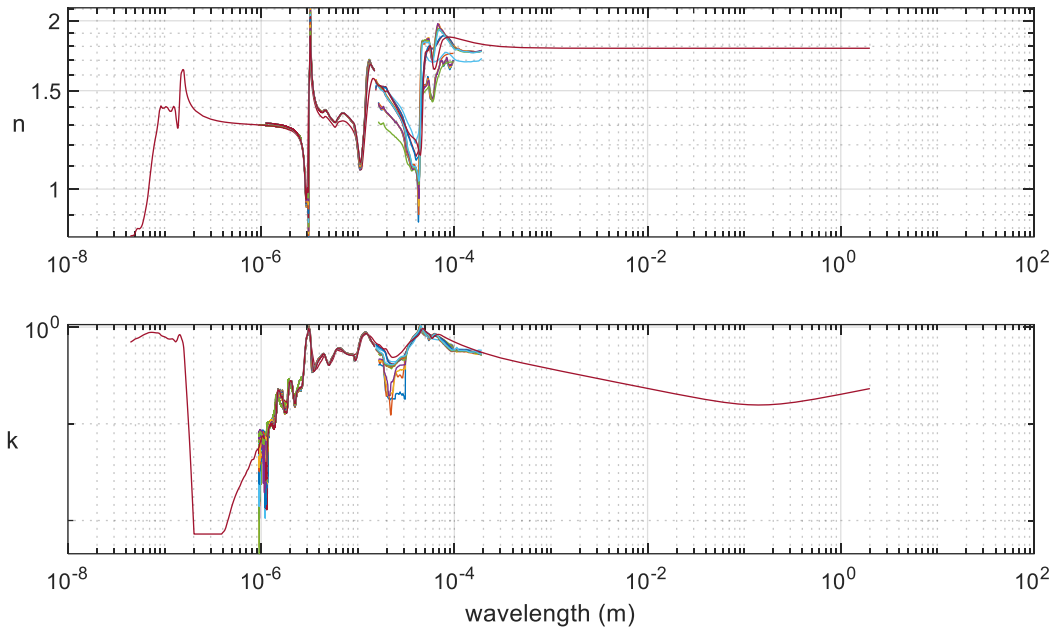

Figure 52 Temperature and wavelength dependent optical constant data for water ice, raw (Warren and Brandt 2008) (Trotta 1996) (Grundy and Schmitt 1998) (Mastrapa, et al. 2009)

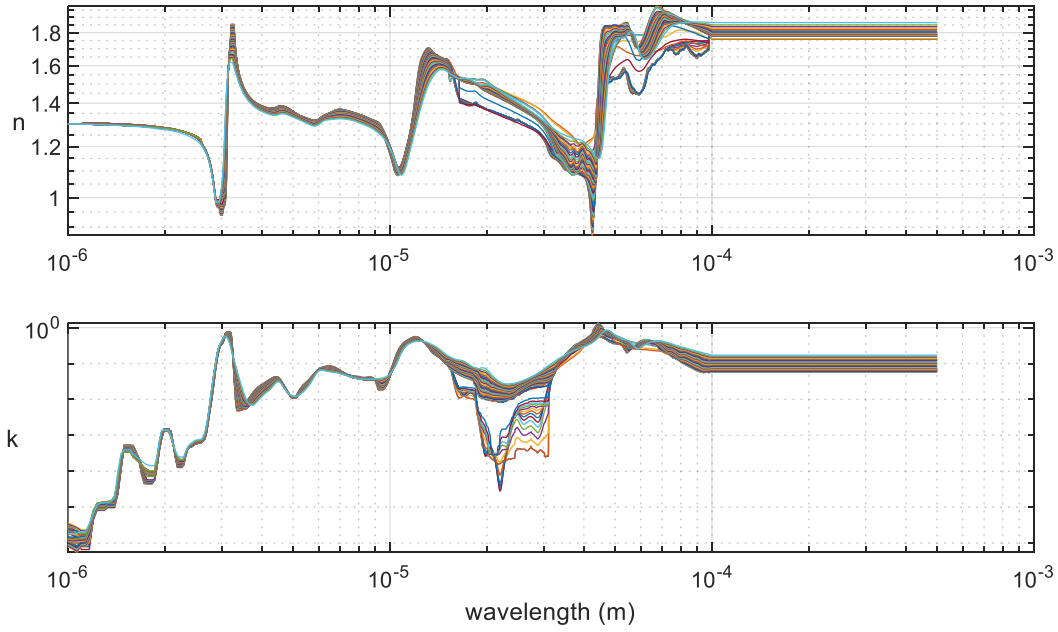

Figure 53 Temperature and wavelength dependent optical constant data for water ice from Figure 52, interpolated and smoothed across temperatures and wavelengths of interest.

Given the complexity of the equations, validation against measured data was essential. Viehmann measured the emissivity of polished stainless-steel samples with varying ice thicknesses at 70 K

(Viehmann and Eubanks 1971). This model is compared to the measured data in Figure 54 using relative emissivity, since the Drude model predicts lower emissivity than Viehmann measured at zero ice thickness, likely due to differences in alloy or surface preparation.

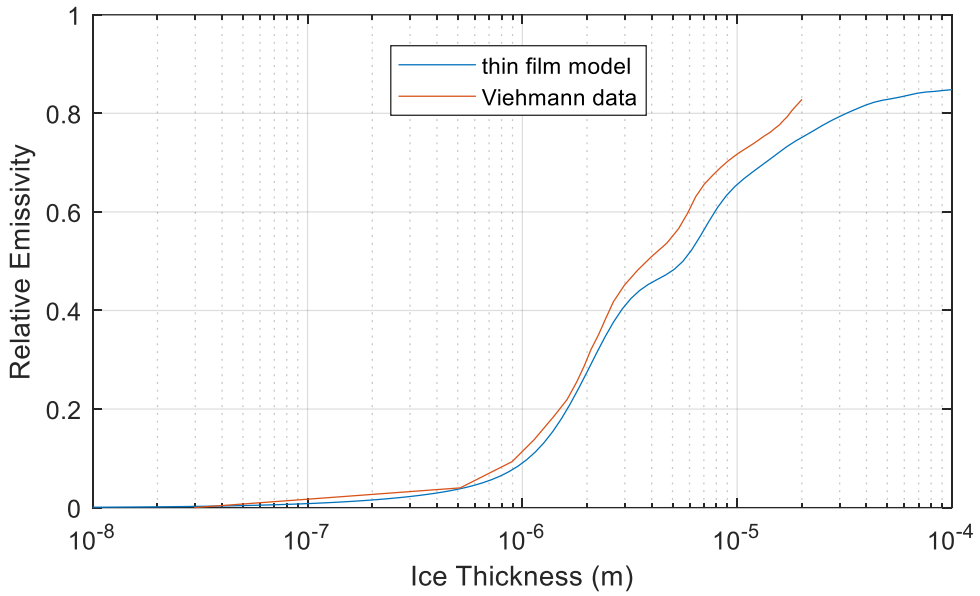

Figure 54 Relative emissivity increase vs ice thickness modelled at 70K vs Viehmann measured data at 70K (Viehmann and Eubanks 1971)

With the accuracy established, the relative emissivity increase versus ice thickness for various temperatures is shown in Figure 55**.** It is important to note the temperature dependence of the emissivity increase due to ice accumulation. At 45 K, 1 μm of ice results in an emissivity increase of only 0.016, compared to 0.04 at 150 K. This effect benefits SPHEREx, as the most sensitive thermal surfaces would require a very large ice accumulation to substantially impact performance. In later sections, there will be more discussion on the mitigations for ice accumulation.

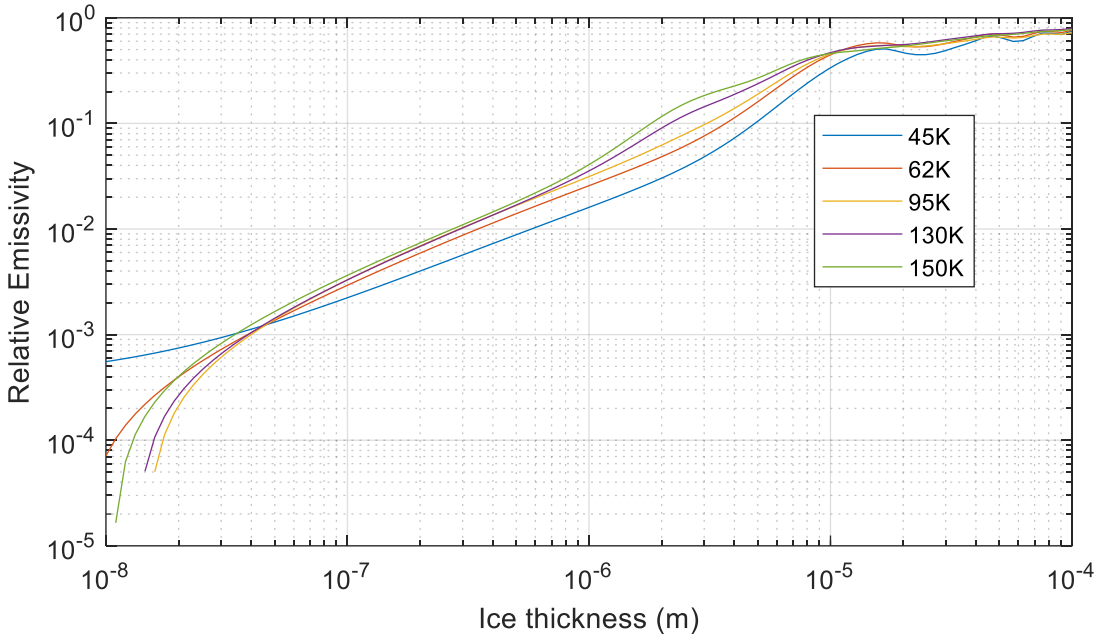

Figure 55 Modelled relative emissivity increase vs water ice thickness for various temperatures

3.5.2.4 Other degradation mechanisms

The white silicon (S-13G) paint can experience darkening due to ultraviolet (UV) exposure, which can be partially ameliorated by atomic oxygen (AO) cleaning. The Long Duration Exposure Facility (LDEF) experiment, launched in 1984 and operating for approximately six years, provides a wealth of data on both effects specifically for S-13G (Whitaker and Gregory 1992). The results of darkening on the leading edge (exposed to AO cleaning) and trailing edge (not exposed to AO cleaning) from the LDEF experiment are shown in Figure 56.

The original reference provides a power-law fit to the leading-edge data but gives limited information on the units of the fit (no clear time basis appeared to align with the plot). Therefore, the fit to the "S0069LE C92" sample was repeated in this work and is shown in equation 21, with t_m representing months of exposure and the output representing the change in absorptance. Note that for exposure times shorter than six months the change in absorptance is negligible; this fit is only valid for times greater than six months. An offset of 0.13 can be applied to align the fit with the farthest trailing-edge data and linearly interpolated to 0 change at 0 exposure.

$$\Delta\alpha = 0.0177\ln(t_m)^2 - 0.0263\ln(t_m) - 0.0055 \quad t_m > 6\ months \tag{21}$$

This power law was applied with the ~18,990 equivalent sun hours expected for the sun-facing side of SPHEREx by the end of the mission to predict a reduction in absorptivity of ~0.097 on the leading edge and ~0.216 on the trailing edge. No UV degradation is expected on the anti-sun side.

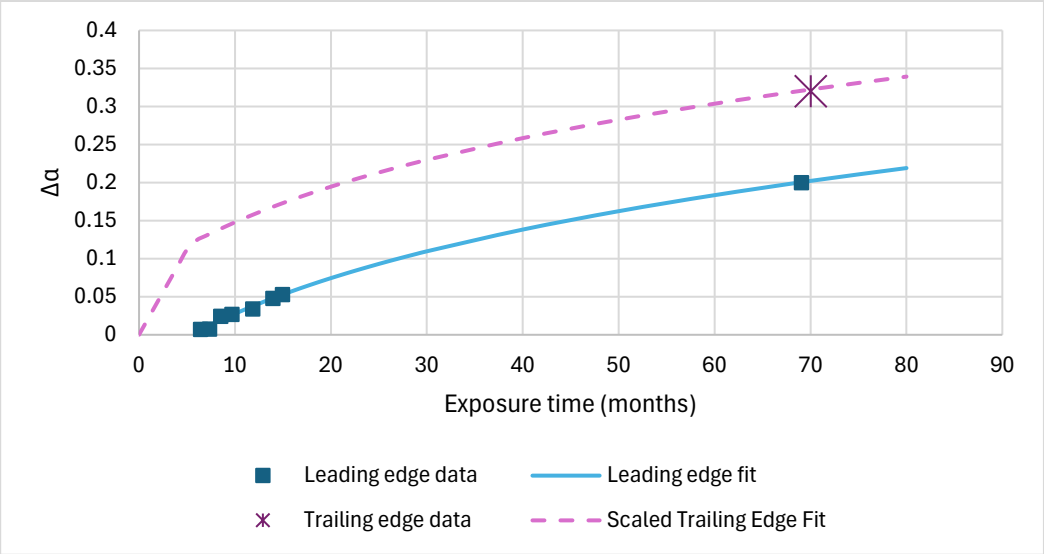

Figure 56 Solar absorptivity increase due to UV exposure for S13G paint in the ram and trailing edge directions (Whitaker and Gregory 1992)

It is important to note that the LDEF orbit was lower than SPHEREx's orbit, ranging from 465 km at the beginning of the mission to 325 km at the end, and thus experienced a higher AO fluence. To understand possible scaling to different fluences, another experiment on A276 paint was used. Figure 57 shows that even between 90° and 105° incidence—which represents a change of approximately two to four orders of magnitude in AO fluence—substantial AO cleaning still occurs. The LDEF experiment experienced on the order of 9×10^{21} atoms/cm² AO exposure, whereas SPHEREx expects 1.6×10^{18} to ~5.3×10^{20} atoms/cm². Given the orders-of-magnitude difference, no fluence scaling was applied; however, the lower potential AO cleaning will be a focus for on-orbit monitoring.

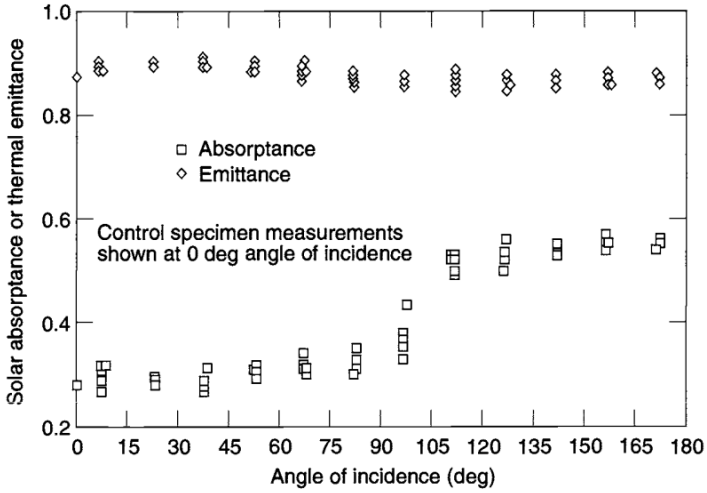

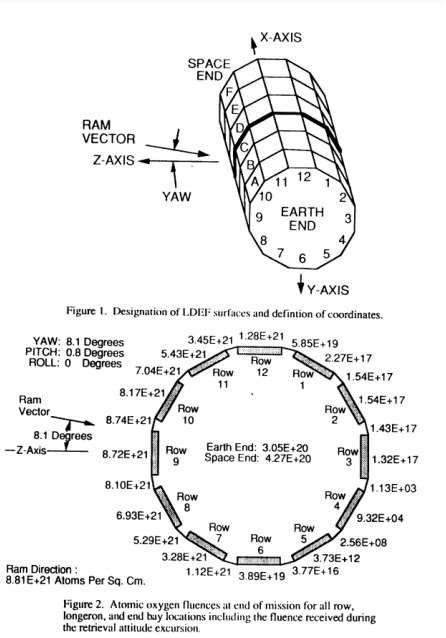

Figure 57 Solar absorptivity increase relative to atomic oxygen angle of incidence for A276 white paint (Donabedian, Spacecraft thermal control handbook, volume I: Fundamental Technologies 2002) (Whitaker and Gregory 1992)

A final source of degradation for the outer shields is molecular contamination. In particular, one of the torque rods located directly beneath a ram-facing outer shield panel is a potential source of silicone contamination, which according to Alred can substantially increase absorptivity (Alred and Soares 2001). Figure 58 shows the response to different film thicknesses and UV exposure. No data are available on how this contamination layer interacts with AO, but it could negate any AO cleaning that occurs.

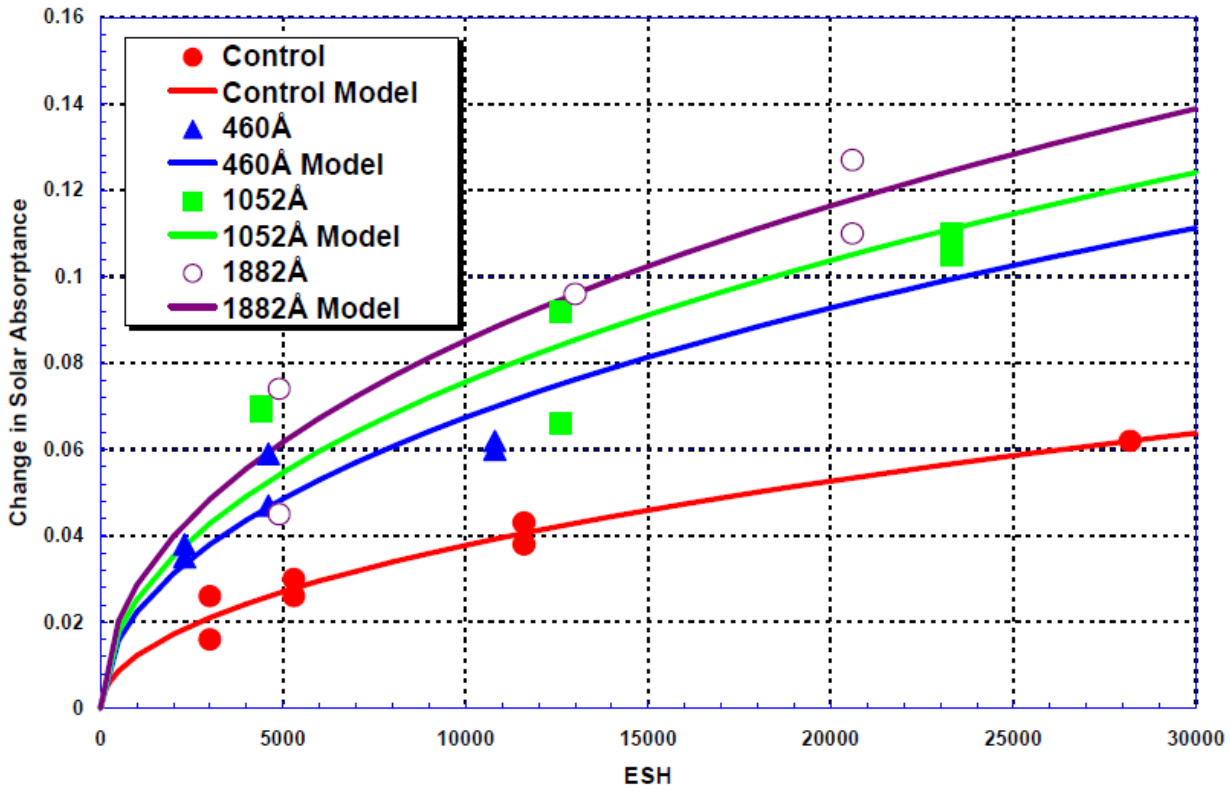

Figure 58 Solar absorptivity increase due to molecular contaminant films of varied thicknesses relative to Equivalent Sun Hour (ESH) exposure (Alred and Soares 2001)

Particulate contamination was also accounted for as a percent area coverage, assuming all particles are black and opaque. The derivation of particulate coverage is described in greater detail in Alred's paper (Alred, Martin, et al. 2022). The percent area coverage of each individual photon-shield region was derived from the top-aperture area of the photon shield. Particles "raining down" from the launch vehicle and other sources were assumed to be uniformly distributed over the upward-facing (even angled upward) surfaces of that region. While this assumption may not be entirely valid because some particles settle out, the analysis assumes that small particles dominate the distribution and become statically adhered to the surfaces they contact. Since each particle is assumed black and opaque, this coverage is directly converted into an emissivity knockdown. Table 8 presents the aperture area and percent coverage of each of the photon-shield/V-groove regions.

Table 8 Particulate percent coverage predicted from launch vehicle translated to effective emissivity knock down

	Percent coverage on aperture from cc analysis	Aperture area	Photon shield and V-groove combined area	Effective emissivity knock-down
Inner Photon shield/V-groove	0.5%	3.21	8.13	0.002
Middle Photon shield/V-groove	0.5%	1.86	10.67	0.0009
Outer Photon shield/V-groove	0.5%	2.75	13.92	.001

A final source of possible degradation is MMOD (micro-meteorite and orbital debris) management. Analysis was conducted by an orbital debris engineer and yielded an approximate "coverage" of impacts on any surface in the ram direction. If the precent coverage of MMOD impacts is translated directly to an emissivity increase, it results in an increase of ~0.0037.

3.5.3 Mass alignment

Although mass does not influence "steady-state" results, it is critical for transient analyses. Simplified thermal model representations inevitably overestimate or underestimate mass. To address this, a detailed audit of as-measured masses was conducted on a per-component or component-group basis to determine effective density multipliers. This alignment was performed at the critical design review (CDR) phase and was not revisited until after launch. As a result, the mass used for pre-launch predictions and cooldown analyses was slightly higher—and therefore more conservative (predicting slower cooldown)—than the actual mass.

Once on orbit, the mass was adjusted to align with the most accurate estimate of the total mass. The main discrepancy was in the telescope, which was approximately 8.5 kg (~10%) heavier in the thermal model than in reality, with the remainder of the discrepancy distributed among the photon shields and V-grooves. Several direct measurements of individual component masses contributed to this analysis, but no measurement of the fully assembled payload with all components present simultaneously was available, hence the "estimate." The final adjusted in-flight model mass remains slightly off because large bulk adjustments were applied and some small components were left unadjusted.

The total rolled-up thermal model mass of the payload is presented in Table 9**.**

Table 9 Total SPHEREx Payload mass roll up (excludes Spacecraft Bus)

Mass used for pre-launch predictions (kg)	Most accurate estimate from system rollup (kg)	Post launch tuned Mass (kg)
253.3634	240.38	241.39

3.6 Model Checks

3.6.1 Component connections

Verification of conductive connections was performed using a “kicker” run that sequentially elevates the temperature of each component relative to the others. Each resulting temperature contour was manually examined to ensure that heat spread as expected and that no unintended thermal shorts existed between components. In general, secondary checks of these connections were performed when evaluating solution results by examining system heat maps. All “kicker” runs are presented in Appendix B

3.6.2 Numerical Convergence

Before presenting results, basic numerical model checkouts were required to ensure accuracy and stability.

3.6.2.1 Thermal solution convergence criteria

The first step was to ensure that the convergence criteria were adequate to capture the physics of the model while still achieving reasonable solution times. For steady-state runs in Thermal Desktop, the main convergence controls are the maximum allowable temperature change for arithmetic nodes (ARLXCA; diffusion nodes are converted to arithmetic nodes at run time for steady-state runs), the nodal-level energy balance (EBALNA), and the system-level energy balance. For transient runs, there is an additional parameter: the maximum allowable temperature change for diffusion nodes (DARLXCA). Energy-balance criteria are not applied in transient runs (since, if energy were perfectly balanced, there would be no temperature change at all). The system-level energy balance was not emphasized due to the large differences in load among SPHEREx regions.

To improve solution speed, different values for these parameters were applied to the “warm” components (spacecraft bus and outer shield/V-grooves) and the “cryo” components (all colder elements). All of these parameters were swept, and the resulting SWIR and MWIR control heat as well as the photon-shield temperatures were evaluated; these results are shown in Appendix C. The final values selected are presented in Table 10.

A value of zero for EBALNA disables the nodal energy-balance check and instead focuses on temperature stability. Later, an end-to-end run-to-run stability check will be presented to verify that these convergence criteria, coupled with the radiation calculations, are adequate.

Table 10 Thermal desktop convergence criteria used for steady state and transient solutions

ARLXCA and DRLXCA Cryo (temperature convergence criteria)	ARLXCA and DRLXCA warm (temperature convergence criteria)	EBALNA Cryo (nodal energy convergence criteria)	EBALNA Warm (nodal energy convergence criteria)
0.001	0.001	0 (disabled)	0 (disabled)

3.6.2.2 Radiation – Surface to Surface

As previously discussed, Thermal Desktop uses a Monte Carlo ray-trace analysis to determine the coupling between surfaces. The main control parameters for this analysis are:

1. Maximum number of rays shot. The analysis begins with an initial batch of rays and increases the number until this threshold is reached.
2. Allowable error. Once the estimated error falls below this value, no additional rays are shot.
3. Energy cutoff fraction. This parameter controls ray bounces; once a re-reflected ray falls below this fraction of its initial energy, it is truncated (no longer reflected).
4. Bij cutoff fraction. Below this fraction, Bij (the effective node-to-node view factor) radiation conductors are truncated. This can be used together with a constraint enforcing that the total view factor sum for each node equals one, which allows additional Bij values to be shot if this criterion is not met. For SPHEREx, the Bij cutoff fraction was used alone because sensitivity studies showed it could achieve accurate results in a reasonable time without enforcing the sum-to-one

constraint. This parameter is particularly important in ground tests, where very small views from a hot surface to a cryogenic surface can represent large loads on the cryogenic surface.

Two sets of radiation-analysis groupings were used: one for ground testing and one for in-orbit conditions. Radiation analysis in Thermal Desktop can be made much more efficient if components that have no possible view to each other are placed in separate analysis groups. For example, the telescope has no view of the outer photon shield in space and can therefore be placed in a separate group, eliminating the need to compute view factors to the outer photon shield. However, this grouping is not valid during ground tests (such as the observatory thermal-vacuum test), because every component can have a view to every other component via chamber reflections.

For the ground-test configuration, only two groupings were used: one external and one internal. The internal group included components inside the spacecraft bus or the internal surfaces of strut tubes. The external group included all other components—essentially anything not inside an enclosed volume. Given the sensitivity of the innermost cryogenic regions to radiation, it was determined that two million rays were required for these components. Within a single radiation group, the number of rays can be adjusted by component, though other control parameters such as error criteria are global to the group. Consequently, successively fewer rays were shot for warmer regions: approximately 100,000 rays for the region between the inner and middle photon shields and between the outer and middle shields, and only 50,000 rays for the room-temperature regions. The same run was repeated multiple times with a new random seed in the radiation calculations to assess numerical run-to-run stability. The stability of SWIR and MWIR heat loads and temperatures is shown in Figure 59**.** The goal was to ensure that the error was much less than the temperature or heat load of interest, with a threshold of <1% error—approximately <1 mW for the MWIR region and <2.5 mW for the SWIR region.

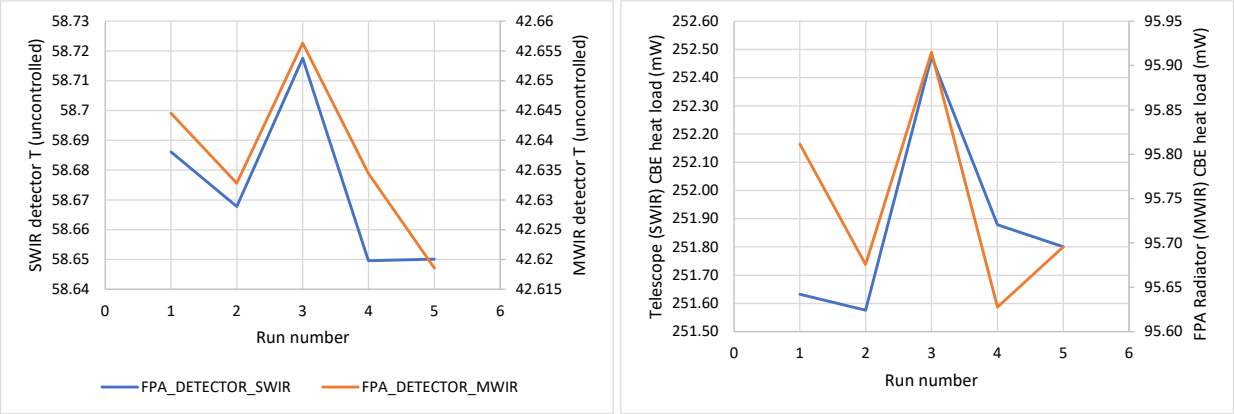

Figure 59 (Left) base uncontrolled run to run temperature stability. (Right) run to run heat load stability.

For the flight configuration, the internal group remained unchanged, but the external group was split into four groups:

1. Spacecraft bus and exterior of the outer photon shield
2. Between outer and middle shields
3. Between middle and inner shields
4. Inside the inner shield

This splitting enabled finer tuning of the numbers of rays shot and error criteria. The specific sensitivity studies used to determine the appropriate parameters are presented in Appendix D. The final in-flight values for the radiation analysis are shown in Table 11. The run-to-run stability of the in-flight model is shown in Figure 60. This study clearly demonstrates that controlling the radiation groupings can dramatically reduce the total number of rays required to achieve an accurate result.

Table 11 Key Monte Carlo radiation solution parameters used for the in-flight model

Region	Max Rays	Error	Energy Cutoff Fraction	Bij Cutoff Fraction
Internal	100000	1	0.1	1E-5
Spacecraft and outer shield	50000	0.1	0.1	1E-4
Outer/Mid	100000	0.1	0.1	1E-6
Mid/Inner	100000	0.1	0.01	1E-5
Inner/telescope	500000	0.1	0.01	1E-6

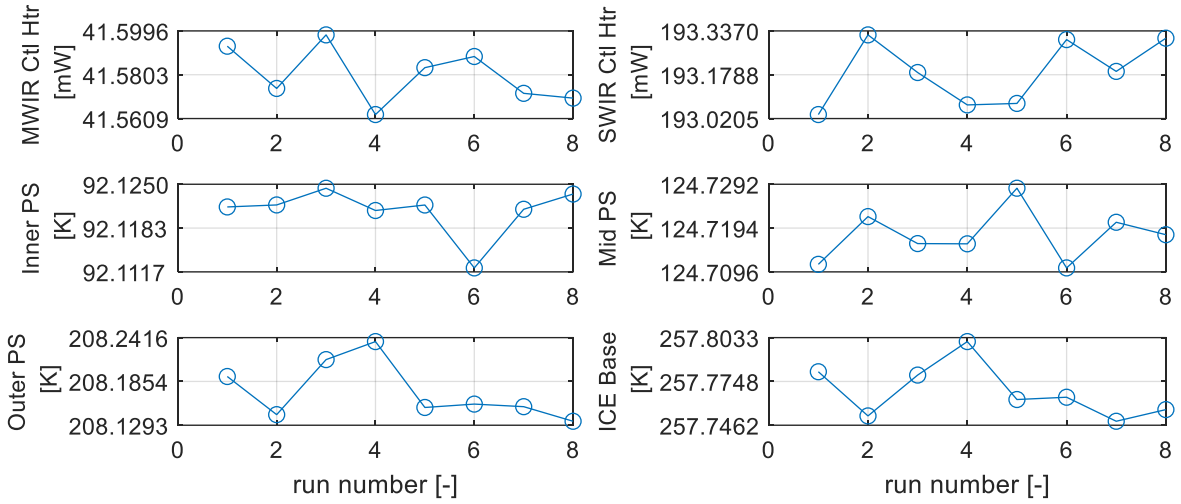

Figure 60 Run-to-Run solution stability of in-flight model

3.6.2.1 Radiation – Environmental loads

The analysis approach for environmental loads also employed a Monte Carlo ray-trace to determine the view from the surface of the Earth or Moon to various spacecraft components. The same groupings used for the surface-to-surface radiation calculations were applied to the environmental-load calculations. Earlier model iterations, including those used for the pre-launch predictions, employed a single radiation group for all external surfaces and therefore required a very large number of rays. These earlier models used the same per-region breakdown as the surface-to-surface calculations (2 million rays for the inner region, 100,000 rays between photon-shield regions, and 50,000 rays for the external bus region).

For the flight on-orbit model, the same zones used for the surface-to-surface radiation solution were adopted. Sensitivity studies were repeated to determine the per-zone parameters presented in Table 12**,** with full parametric studies provided in Appendix D.

An additional parameter important for environmental-load calculations is the number of orbital positions. Thermal Desktop computes the environmental loads for each orbital position specified by the user and then either time-averages these for a steady-state case or interpolates between them for a transient case. It is essential to verify that an adequate number of orbital positions are used to represent the variations in albedo and Earth infrared, as well as the changing shadow due to non-zero beta angles

(Sun not aligned) or mean local time of ascending node (MLTAN) not equal to 0°. Based on the results shown in Figure 61 and Figure 62, twelve or more positions were determined to be sufficient to capture the orbital-physics effects for both zenith- and inertially-pointed orbits.

Table 12 Key Monte Carlo environmental load solution parameters used for the in-flight model

Region	Max Rays	Error	Energy Cutoff Fraction	Bij Cutoff Fraction
Spacecraft and outer shield	50000	0.1	0.1	1E-4
Outer/Mid	100000	0.1	0.1	1E-6
Mid/Inner	100000	0.1	0.01	1E-5
Inner/telescope	200000	0.1	0.01	1E-6

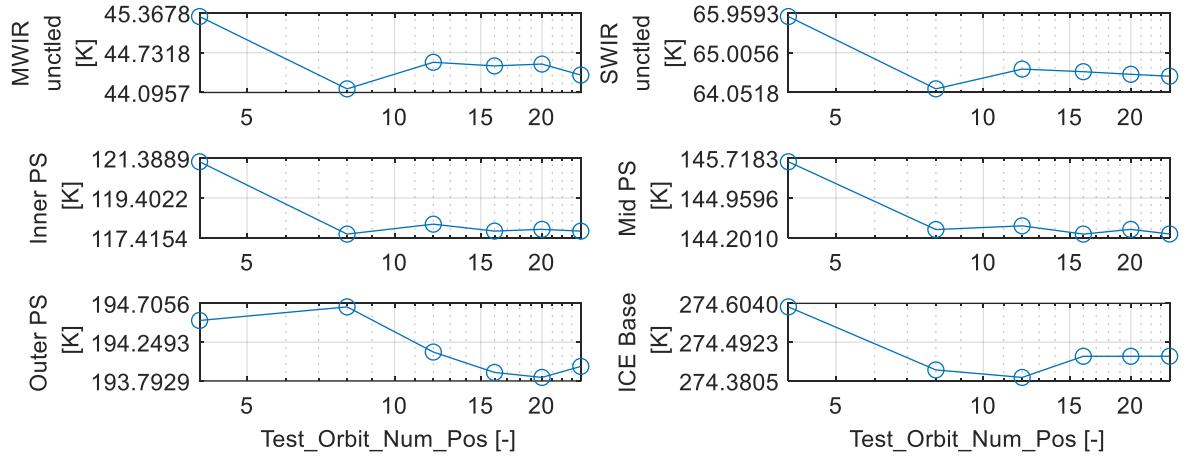

Figure 61 Key temperature and heat load responses to varied number of orbital positions for Zenith orbit

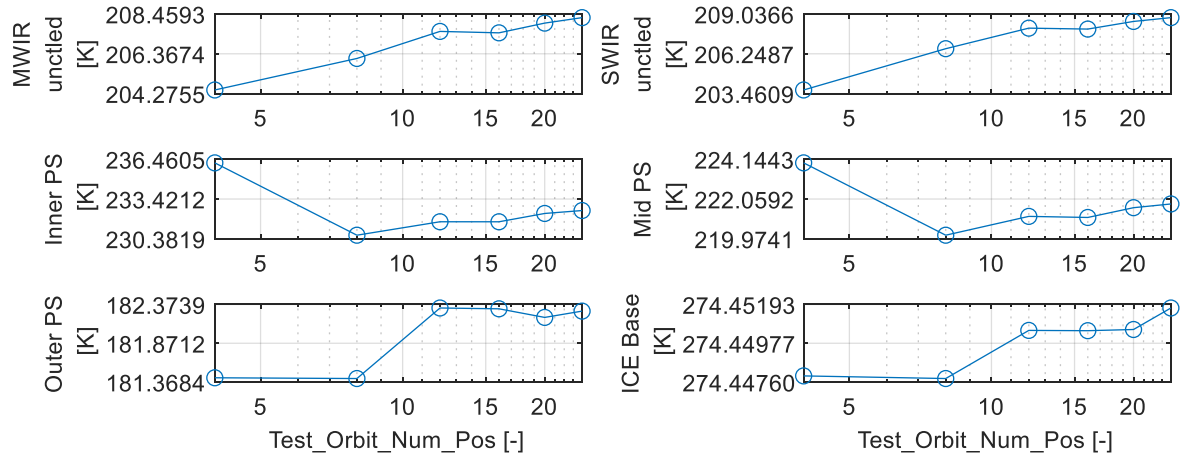

Figure 62 Key temperature and heat load responses to varied number of orbital positions for Inertial orbit

3.6.3 Sensitivity Studies

Given time and computational-resource constraints, it was not feasible to vary every single parameter in the model. Instead, focus was placed on a series of "heavy hitters," and sensitivities to those parameters were conducted. Every parameter considered to have high uncertainty or high impact was varied within reasonable bounds. This approach proved particularly useful for identifying non-linear effects, such as the impact of tip-over angle. In some cases, a single offset value was used—for example, the photon-shield emissivity—which could be scaled to determine the impacts of contamination or damage. Usually, the total load or change in load served as the figure of merit; in some cases, however, the baseline uncontrolled temperatures were used instead. In total, hundreds of cases were run to conduct these sensitivity studies. While all of them cannot be shown in this report, they ensured a robust and well-understood thermal design. The key sensitivity studies and their top-level findings are summarized as follows:

1. Photon-Shield and V-Groove Surface Emissivity (Figure 63): This study showed the relative impact of each individual surface's emissivity when increased by 0.1 from the beginning-of-life value. The system is highly coupled but not always in an intuitive manner. For example, the inner emissivity of the outer photon shield had more impact than that of the middle photon shield, despite being further removed from the sensitive internal cryogenic regions. Some surfaces even improved performance when their emissivity increased. This result demonstrated that increasing the emissivity of all surfaces together may not have as large an impact as Increasing any one surface individually. This analysis also informed a sensitivity matrix of various temperature responses to changes in emissivity, which was later used to tune the flight model on orbit shown in Table 13.
2. Photon-Shield and V-Groove Surface Specularity (Figure 64): This analysis used an approach similar to the emissivity sensitivity study, reducing each surface's specularity by 0.1 from its beginning-of-life value. As with emissivity, different surface specularity values exhibited varying levels of impact.

3. Photon-Shield Transmissivity (Figure 65): This study assessed the relative impacts of unclosed-out gaps by modifying the photon-shield transmissivity and translating that to an effective hole size based on the shields' areas. While this is a "broad-brush" approach—since the transmissivity property blends radiation penetration across the whole shield rather than modeling point-source specular bounces—it nevertheless provided a good relative relationship. The results showed that a large number of penetrations would be required to appreciably affect MWIR or SWIR performance.
4. Sensitivity to Tip-Over Angle (Figure 66): This study examined rotation about the x-axis (Sun axis) to quantify the relative impact of increased Earth loading on the cryogenic regions. The results are expressed in terms of steady-state detector base temperatures. The curve remains relatively flat until the MWIR radiator or telescope becomes illuminated, after which the temperature rises until the requirement limits are no longer met.
5. Sensitivity to Telescope-Strut Radius (Figure 67): The bipod radius was increased relative to the baseline of 0.03 m to support design trades. Other conductive links, such as V-groove supports and MWIR radiator supports, could be directly scaled linearly from their baseline values. However, the main struts also function as radiators, and increasing their cross section by increasing the radius does not yield a one-to-one relationship. For example, the approximate total bipod load into the telescope was 350 mW (including conductive and radiative coupling) for the baseline case; increasing the radius from 0.03 m to 0.035 m (a 36% increase in cross section) resulted in only a 23% increase in the total load.

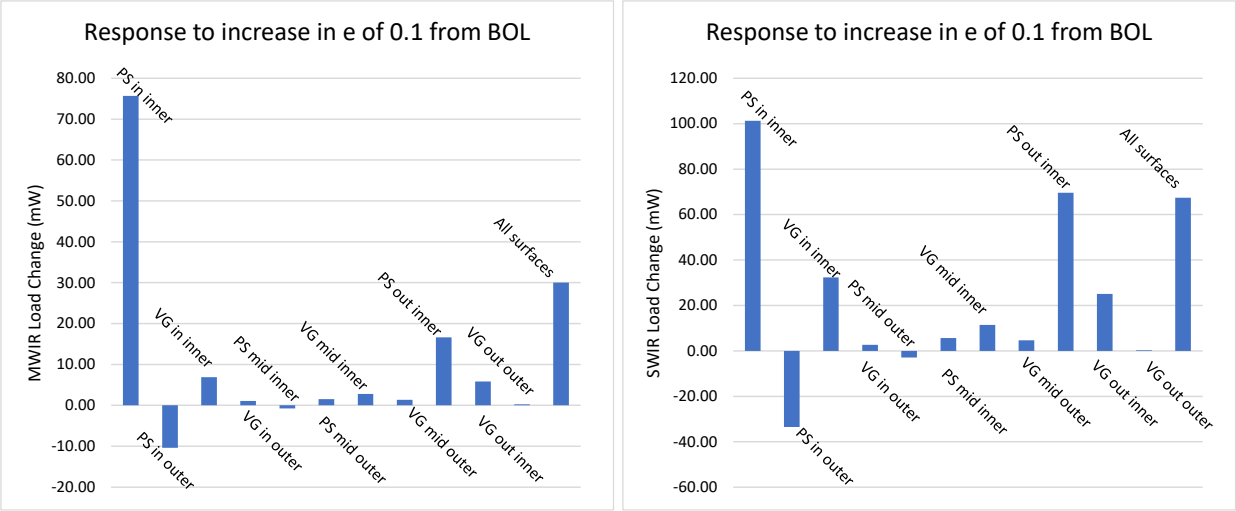

Figure 63 Margin sensitivity to varied emissivity of each surface respectively and all together. (Left) MWIR margin. (Right) SWIR margin.

Table 13 Sensitivity matrix of Photon Shield/V-groove to changes in emissivity

surface with change in e of 0.1	PS/VG in ave ΔT (K)	PS/VG mid ave ΔT (K)	PS/VG out ave ΔT (K)
PS in inner	-18.7058	-0.6047	0.0051
PS in outer	-14.9061	-0.3588	0.0060
VG in inner	-4.0807	-0.1291	-0.0034
VG in outer	1.3146	-0.0314	-0.0010
PS mid inner	-1.0000	-24.9277	-0.0671
PS mid outer	1.0344	3.7773	0.0414
VG mid inner	1.1003	-2.9218	-0.0226
VG mid outer	1.2783	7.2234	-0.0799
PS out inner	8.8688	38.0674	-3.6165
VG out inner	2.3773	7.2509	-2.4191
VG out outer	0.0921	0.1037	0.2689
all surfaces	-3.6204	17.7198	-1.1684

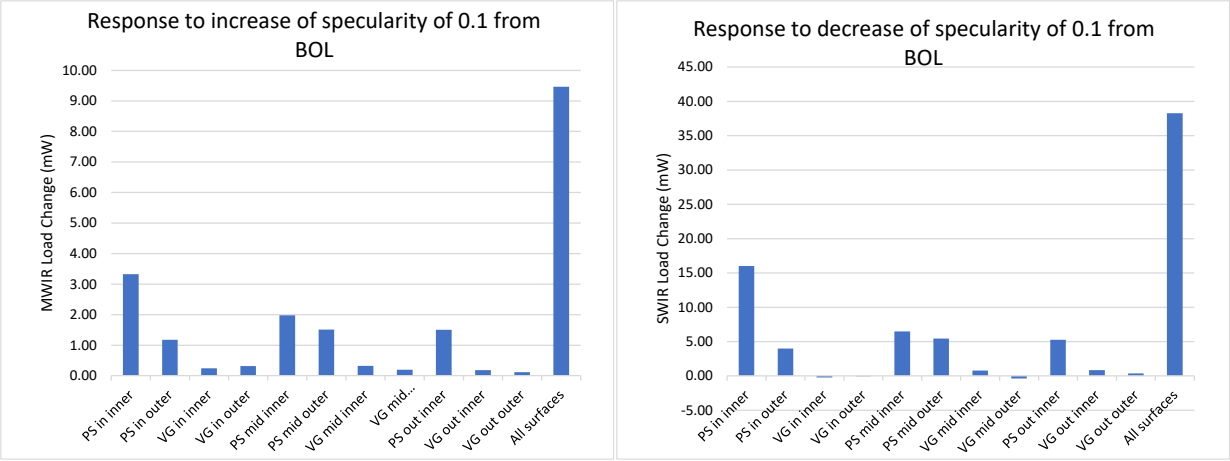

Figure 64 Sensitivity to specularity increase of 0.1: (left) MWIR load change (right) SWIR load change

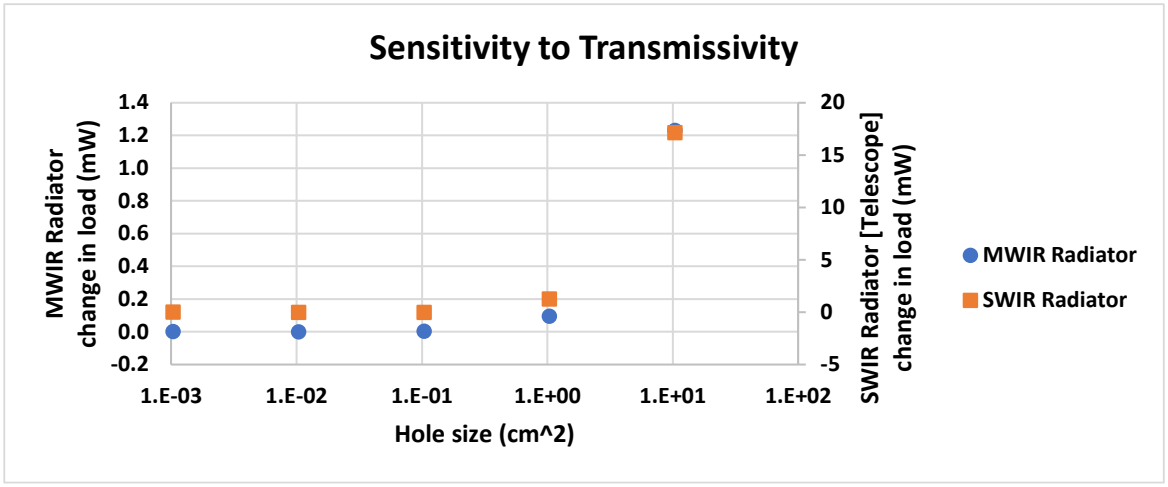

Figure 65 Sensitivity to Photon Shield transmissivity; MWIR and SWIR change in load vs effective hole size

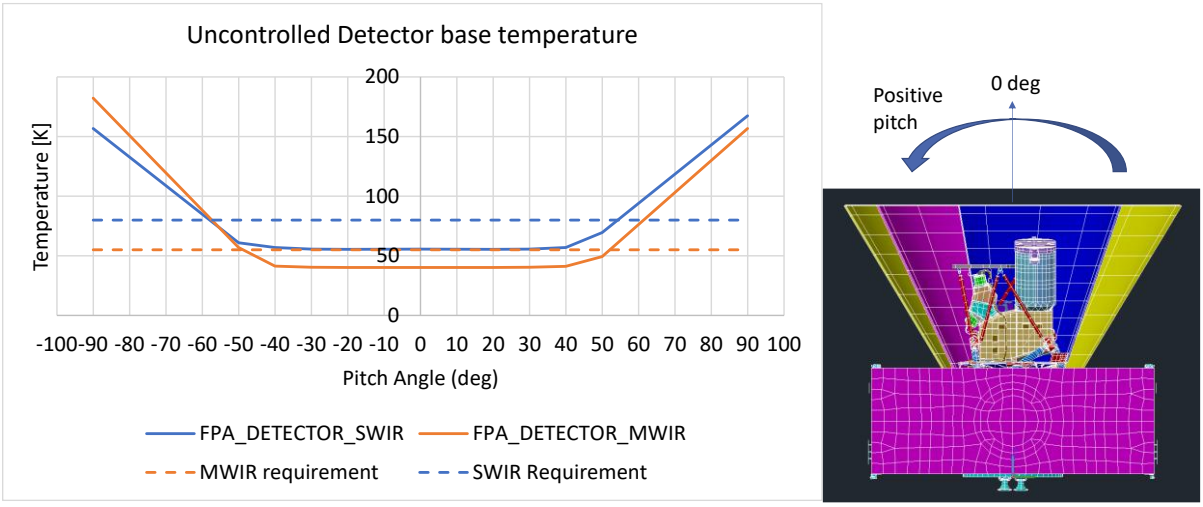

Figure 66 Sensitivity to spacecraft pitch: (left) minimum detector temperature vs pitch angle (right) direction of pitch

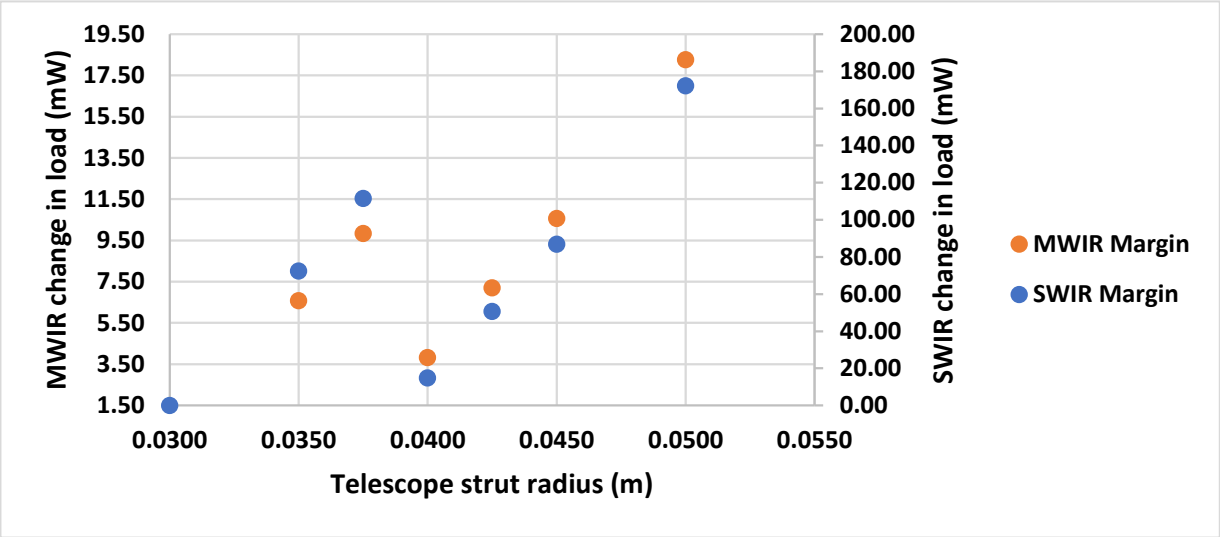

Figure 67 Sensitivity to strut radius; Strut radius in meters vs MWIR and SWIR load change

3.7 STOP

A secondary interaction of the thermal system was its interface with the structural model to generate STOP (structural–thermal–optical) results. For SPHEREx, this analysis focused on telescope-optic deformations and pointing stability/accuracy. The telescope-optic deformation analysis was performed internally by Ball Aerospace (now BAe). The input from this work to the Ball analysis consisted of accurate bounding environments and boundary conditions.

The thermal-subsystem analysis was performed at JPL and leveraged the same bounding environments to determine the relative boresight changes between conditions. The only additional thermal work required for this analysis was mapping the temperatures produced for thermal performance into a structural model. This mapping was carried out within Thermal Desktop: the structural model was read in, and Thermal Desktop linearly interpolated the temperatures from the thermal nodes to the structural nodes, producing a data file that could be read into the structural-analysis tool (Siemens NASTRAN in this case).

Because the structural model contained millions of nodes, care had to be taken to avoid discontinuities and mis-mapping of temperatures. An example of the differences between the two models is shown in

Figure 68. To prevent mis-mapping, the nodes of the two models were grouped into corresponding temperature zones (e.g., outer photon shield and V-groove). Thermal nodes were only mapped to structural nodes within the same group, even if a closer thermal node existed in a different group. This approach was especially important in tight areas separated by vacuum gaps smaller than the thermal-model node spacing.

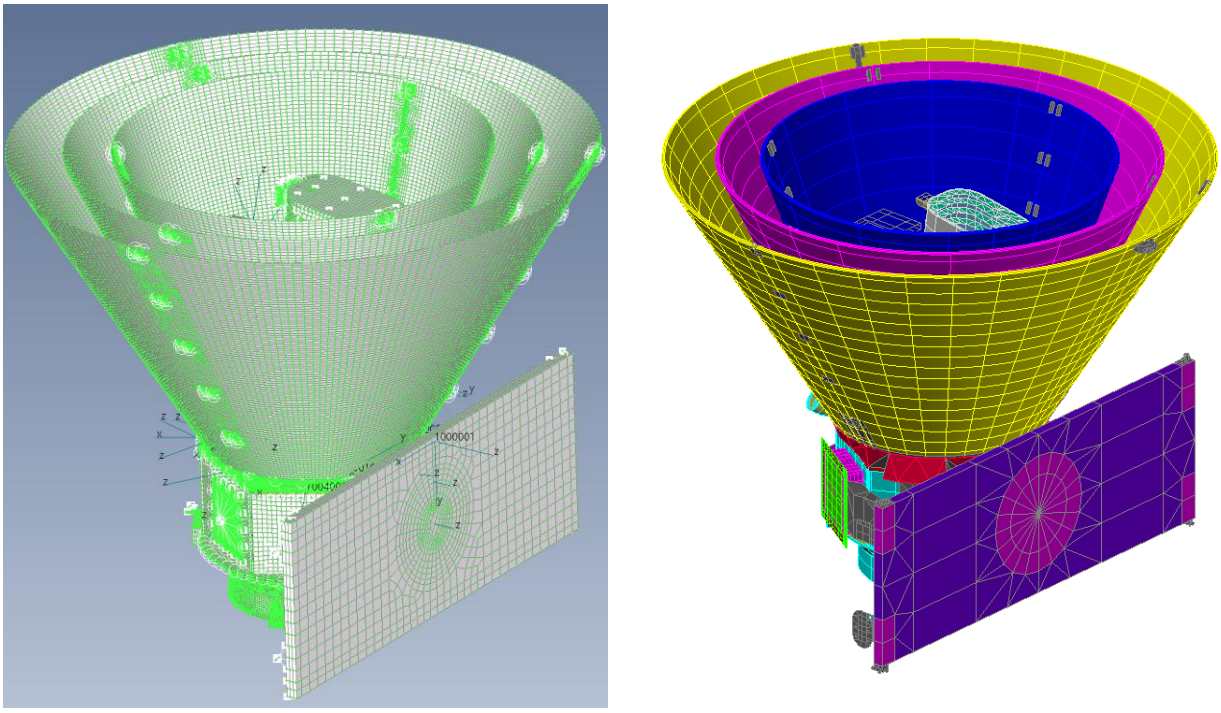

Figure 68 Comparison of mesh density of structural FEM (left) to thermal model (right)

3.8 Operational considerations

3.8.1 Contamination Management

As discussed in the optical-properties section 3.5.2.3, ice and other contaminants can interfere with both science and thermal performance. To mitigate this, SPHEREx implemented a “controlled cooldown,” which used decontamination heaters to bias the temperature of the optics above that of the surrounding telescope. As water desorbed from the telescope paint, it migrated to the coldest surface in the enclosed telescope, which, under this scheme, remained the telescope paint surface rather than the optics. This temperature bias was held until the telescope fell below 150 K, at which point the ice in the paint became immobilized (Alred, Moore, et al., Designing a Decontamination Solution for the Low-

Earth-Orbit, Cryogenic SPHEREx Mission 2021) (Alred, Moore, et al., Modeling contaminant outgassing and free molecular transport processes for the cryogenic SPHEREx observatory 2024).

To reduce the number of heater channels, all of the mirror heaters and the beam-splitter heater were wired in parallel on one heater circuit. This required a very accurate estimate of the power needed for each optic, since each heater circuit required a different resistance to achieve the desired power. Each mirror contained three heater elements wired in parallel to distribute heat more evenly. The resistances used for each heater are presented in Table 14

Table 14 Optic and detector decontamination circuit specifications

Circuit	element	Resistors used	Circuit resistance including leads (ohm)	Max power (100% duty cycle) at min bus voltage (29.25V) [W]	Max power (100% duty cycle) at max bus voltage (32.4V) [W]
MWIR	MWIR	1x100ohm	106.47	8.03	9.85
SWIR	SWIR	1X350ohm	OL*	0	0
Optics	Beam splitter	1x5K ohm	90.22	9.48	11.63
	PM	3x750 ohm ||			
	SM	3x1 Kohm ||			
	TM	3x750 ohm ||			
			Total (max avail 73W)	17.51	21.48

The heater circuit employed a simple bang–bang control with a dynamic setpoint based on the maximum telescope-sensor temperature versus the minimum optic-sensor temperature, with an additional bias applied for sensor inaccuracy and placement relative to actual maxima and minima. The reference temperatures and algorithm description are provided in Table 15**,** and the predicted performance of this approach is shown in Figure 69. A brief period occurs at the beginning of cooldown in which the MWIR heater does not have sufficient power to overcome the radiator's cooling power; the low mass of the radiator causes it to cool more quickly than the telescope. This condition was deemed acceptable because the temperatures remain above 175 K in the water band.

Table 15 Decontamination controlled cooldown algorithm, reference sensors and on/off setpoints

Htr Circuit	Ref sensors for TEL	Ref sensors for OPT	Ctrl active temp range	Set Point[3]	
				On	Off
MWIR FPA Prim[1]	TS_TEL_HS_1_ENG; TS_TEL_HS_2_ENG; TS_TEL_HS_3_ENG; TS_TEL_HS_4_ENG; TS_TEL_BAF_1_ENG; TS_TEL_BAF_2_ENG	TS_MW_IF_P_ENG; TS_MW_IF_R_ENG	200K> Min(TEL) && Max(TEL) >150K	Min(OPT)< (Max(TEL)+3K)	Min(OPT)> (Max(TEL)+5K)
MWIR FPA Red[1]	TS_TEL_HS_1_ENG; TS_TEL_HS_2_ENG; TS_TEL_HS_3_ENG; TS_TEL_HS_4_ENG; TS_TEL_BAF_1_ENG; TS_TEL_BAF_2_ENG	TS_MW_IF_P_ENG; TS_MW_IF_R_ENG	200K> Min(TEL) && Max(TEL) >150K	Min(OPT)< (Max(TEL)+3K)	Min(OPT)> (Max(TEL)+5K)
SWIR	TS_TEL_HS_1_ENG; TS_TEL_HS_2_ENG; TS_TEL_HS_3_ENG; TS_TEL_HS_4_ENG; TS_TEL_BAF_1_ENG; TS_TEL_BAF_2_ENG	TS_SW_IF_ENG	200K> Min(TEL) && Max(TEL) >150K	Min(OPT)< (Max(TEL)+3K)	Min(OPT)> (Max(TEL)+5K)
Optics	TS_TEL_HS_1_ENG; TS_TEL_HS_2_ENG; TS_TEL_HS_3_ENG; TS_TEL_HS_4_ENG; TS_TEL_BAF_1_ENG; TS_TEL_BAF_2_ENG	TS_BS_ENG; TS_PM_ENG; TS_SM_ENG; TS_TM_ENG	200K> Min(TEL) && Max(TEL) >150K	Min(OPT)< (Max(TEL)+3K)	Min(OPT)> (Max(TEL)+5K)

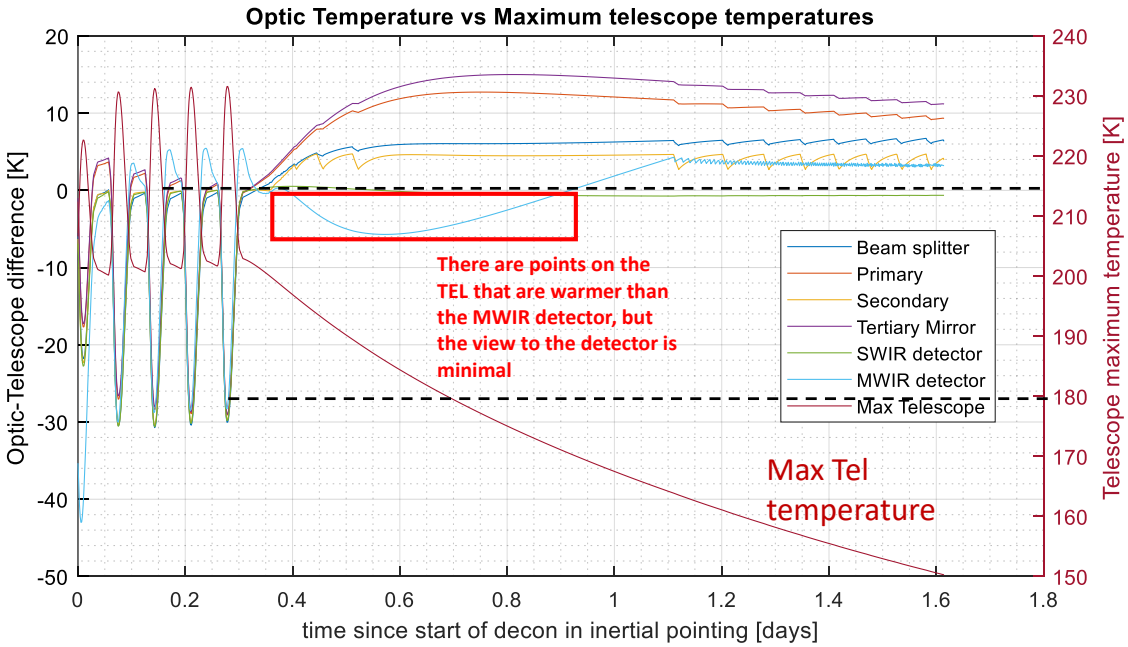

Figure 69 Pre-flight predicted controlled cooldown decontamination performance

During testing, two decontamination heaters failed: the only heater for the SWIR detector and the primary heater for the MWIR detector (the redundant MWIR heater remains functional). The SWIR detector, cooled by the telescope, naturally lags the contamination source due to its thermal capacitance. The MWIR detector, however, cools much faster than the telescope and becomes the coldest point for contamination accumulation. Given the heater failures, an alternative decontamination strategy was developed. This strategy exploits the same factors that cause the MWIR to cool quickly (its low mass and high emissivity-to-area ratio) to preferentially warm the MWIR radiator and detector.

Under this contingency procedure, the telescope is allowed to cool well below the water band (~110 K) before the spacecraft briefly slews toward Earth, allowing the MWIR radiator to be illuminated by Earth infrared radiation and warmed above the water band while the telescope mass keeps it cold. The telescope paint then becomes the receiver to recapture and retain the water desorbed by the MWIR radiator. Once the MWIR warms above ~170 K, the spacecraft slews back to zenith pointing, and the MWIR rapidly cools again. As long as the telescope remains below 150 K, it does not become a new source for redepositing contamination on the MWIR detector. The modeled performance of this contingency procedure is shown in Figure 70**.**

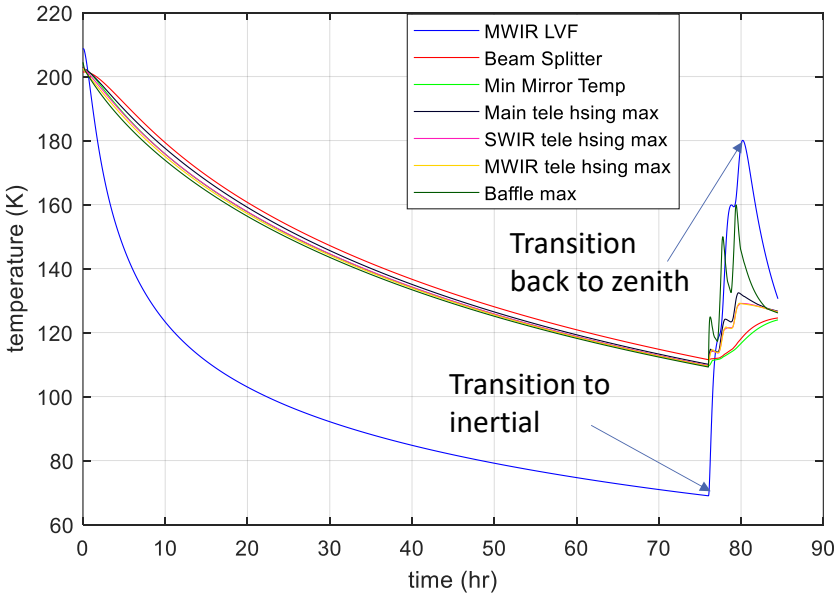

Figure 70 Modelled performance of pointing contingency procedure for failed MWIR decontamination heater

For the sub-150 K photon shields, heaters were not an option. If on-orbit performance degrades to the point of affecting mission science, the spacecraft can be oriented in inertial pointing. This results in the photon shields pointing toward Earth for part of the orbit, where Earth infrared is sufficient to raise the average temperature to ~200 K and desorb the accumulated water. Alred's (2024) paper discusses the expected contamination accumulation on the photon shields. Essentially, the only appreciable accumulation is on the inner surface of the inner photon shield, which is expected to cool faster than the telescope, particularly during the controlled-cooldown decontamination, and adsorb much of the water shed from the telescope paint.

However, because the relationship between temperature and desorption/adsorption is non-linear, these analysis results should be interpreted with caution. Figure 71 shows the approximate temperature ranges of components under steady-state operations, with a sizeable amount of composite and polymeric material above 140 K and with a view to colder surfaces. For conservatism, a substantial ice-accumulation allowance was applied to the outer surfaces of the inner and middle shield/V-grooves for end-of-life estimates. Specifically, an accumulation of approximately 0.2 μm of ice, corresponding to an emissivity increase of about 0.007, was allocated on these surfaces. This assumption represents a worst-case scenario in which all water absorbed in the bipods and V-groove close-outs is completely desorbed and deposited as a uniform layer over the respective regions of the photon shields.

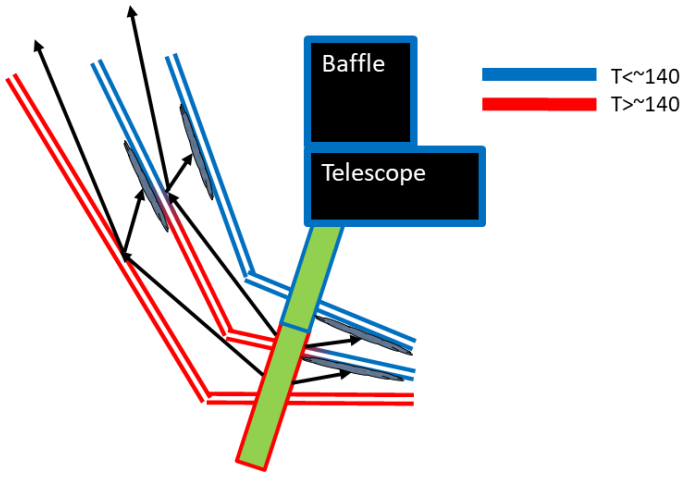

Figure 71 Schematic of temperatures and contamination path for Photon Shield and V-groove contamination

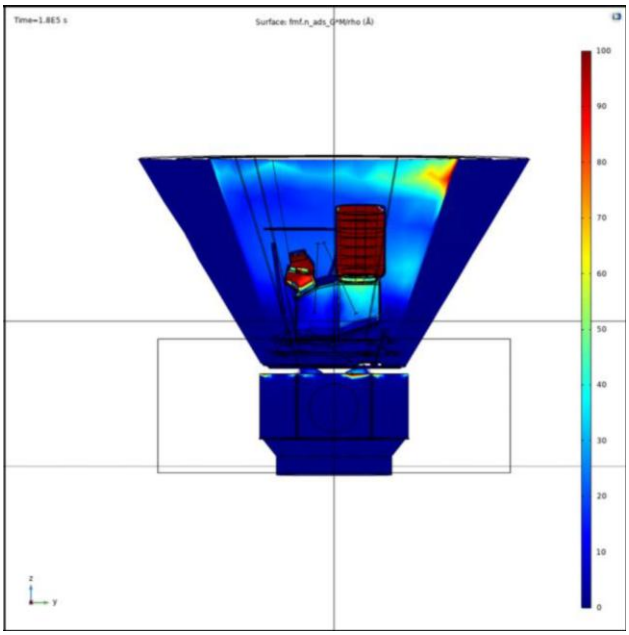

Figure 72 Pre-flight Water accumulation at end of cooldown. The color scale is 0-100 Å .

3.8.2 Temperature control

Precise temperature control is critical to meeting the extremely tight temperature stability requirements on the detectors of 0.67uK average slope over 150s, 2mk pk-pk over 8 min, 100mK pk-pk over 6 months, and 200mK pk-pk over 1 year.

SPHEREx regulates detector temperature using high-accuracy Lakeshore Cernox CX-1080 sensors. Sensor measurements feed a Kalman-filtered control loop that drives a miniature Vishay VPR-220Z precision-foil resistor used as the control heater. The control point is located on the detector side of the thermal strap that couples the detector assembly to its radiating surfaces, ensuring the loop directly controls the detector thermal node and rejects strap-side disturbances.

The dominant disturbance source is environmental load variation during spacecraft slews—incident on a dedicated radiator for the MWIR focal plane and on the telescope structure for the SWIR focal plane. Internal dissipation is negligible: saturating every pixel deposits ~20 nJ per 100 s exposure (~0.2 nW). Given an effective detector-assembly heat capacity of ~20 J/K (mass is ~.564kg of primarily molybdenum or TZM-titanium–zirconium–molybdenum with ~95% molybdenum), the corresponding temperature rise is ~1 nK per exposure ($\Delta T \approx Q/C$), allowing internal load variation to be ignored. In

practice, achievable detector stability is well approximated by the uncontrolled redundant sensor co-located with the control sensor on the detector side of the strap.

The heater and sensor locations were informed by detailed modelling of the PID control in Thermal Desktop. The simulation even went so far as to include heater and sensor quantization and simulate the resistance measurement noise and translate it to temperature for the Cernox sensors used. MicroKelvin level control was demonstrated with the proposed control loop design. However, with such tight requirements, a laboratory demonstration was required.

A "cryo-surrogate" of the FPAs was built to simulate the approximate capacitances and conductances of the FPA, and control was shown with demonstration electronics. The results are shown in Figure 73. Given the multiple hours of meeting the short-term stability, given availability control authority on the heaters the long term stability will be met. This is addressed by ensuring the absolute change in load across the mission is less than the capacity of the heater control loops.

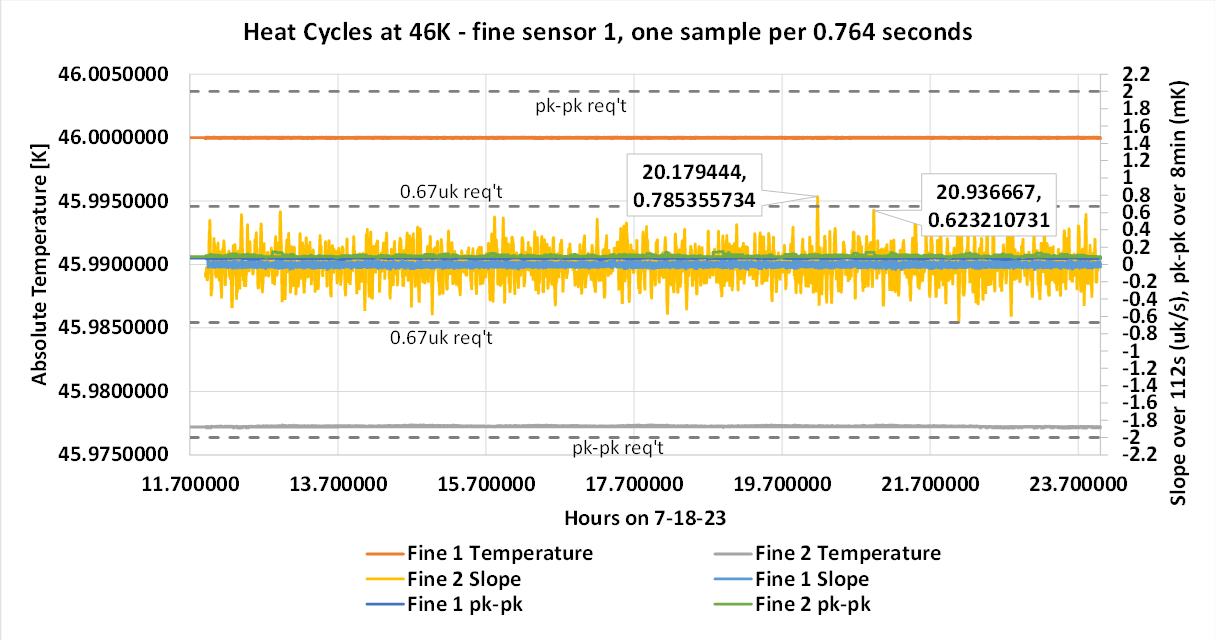

Figure 73 Results of FPA temperature control testing. Fine control sensors are plotted in response to a simulated cycling heat load based on predicted flight loads

3.9 System level test verifications

Initially, a stand-alone thermal-system performance test was planned. This test would have included 10–40 K targets for each successive radiative region to simulate the space environment and

would have enabled verification of both conductive and radiative coupling. However, it was descoped due to budget and schedule constraints. Consequently, the results of multiple test configurations were pieced together, requiring considerable effort to justify the overall model correlation.

3.9.1 FPA verification

The first measured validation of the thermal model was performed at the FPA level. This test was conducted on a “qualification model” that was thermally and mechanically equivalent to the flight unit but contained only one operational detector. A pulse-tube cryocooler was used to cool the detector to the expected flight conditions, and the boundary conditions were varied across five thermal-balance points. No significant changes were required for the FPA model; instead, several adjustments—multiplication factors between 0.8 and 1.2 on conductances and capacitances—were applied to account for model simplifications, material uncertainties, and as-manufactured/assembled tolerances.

Correlating the model slightly increased the thermal margin, but the most significant outcome was verification of the detector-dissipated power, even though only one of the three detectors was active. The thermal rise from activating the detector, relative to the thermal rise from known heater powers, was used to calibrate the dissipation downward from 8 mW to 6 mW per detector, thereby reducing the total load for each detector array by 6 mW (3×8 mW vs. 3×6 mW). The results of this correlation are presented in Table 16, with the greatest difference less than 0.25 K and the average difference only about 10 mK.

Table 16 FPA thermal model correlation results. Shown are absolute differences between modelled and measured in K.

Component\balance point	TB0	TB1	TB2	TB3	TB4
Top of thermal strap	NA	0.001	-0.029	-0.035	-0.028
Bottom of thermal strap	NA	0.016	-0.013	-0.023	-0.016
Cable bracket	0.1	-0.19	0.243	0.148	0.127
Mid support ring	0.028	-0.136	0.047	-0.049	-0.051
Mosiac plate	0.007	-0.008	-0.039	-0.072	-0.059
Tele IF Ring	0.022	-0.221	0.007	-0.108	-0.112
Tele IF Sim	0.012	0.003	-0.009	-0.029	-0.028
average T difference		-0.01076	max T difference		0.243

3.9.2 Instrument level verification

Instrument level testing was conducted at Caltech in what was called the KASI test, since the chamber was provided by the Korea Astronomy and Space Science Institute (KASI). This had two, 2-stage PT820 cryocoolers to cool an outer shroud heat intercept to 135K and an inner shroud to 60K-45K depending on the configuration. The primary goal of this test was optical calibration, but thermal balance testing was a secondary objective. The telescope, FPA radiator and Inner V-Groove were all cooled by the inner shroud, while the Middle V-Groove was cooled by the outer shroud. All of these components had separate control heaters at their interfaces. All cold interfaces between the chamber and instrument used flexible thermal straps to prevent differential thermal stresses, and the gaps between V-grooves and respective shrouds were closed out with single layer VDA Kapton insulation. The Outer V-Groove was not cooled and both the top and bottom were exposed to the room temperature chamber walls. The Photon Shields were not included in this test. There were two modes of this test. A “dark mode” for spectral calibration, in which a chamber extension and Winston cone were added to the front of the chamber; and an “optical mode”, for focus calibration, that had a sapphire vacuum window with its inner surface coated in gold and a cold stop on the inner shroud with gold coating on the exterior face. Most thermal balance cases were conducted in the “optical mode” configuration shown in Figure 74.

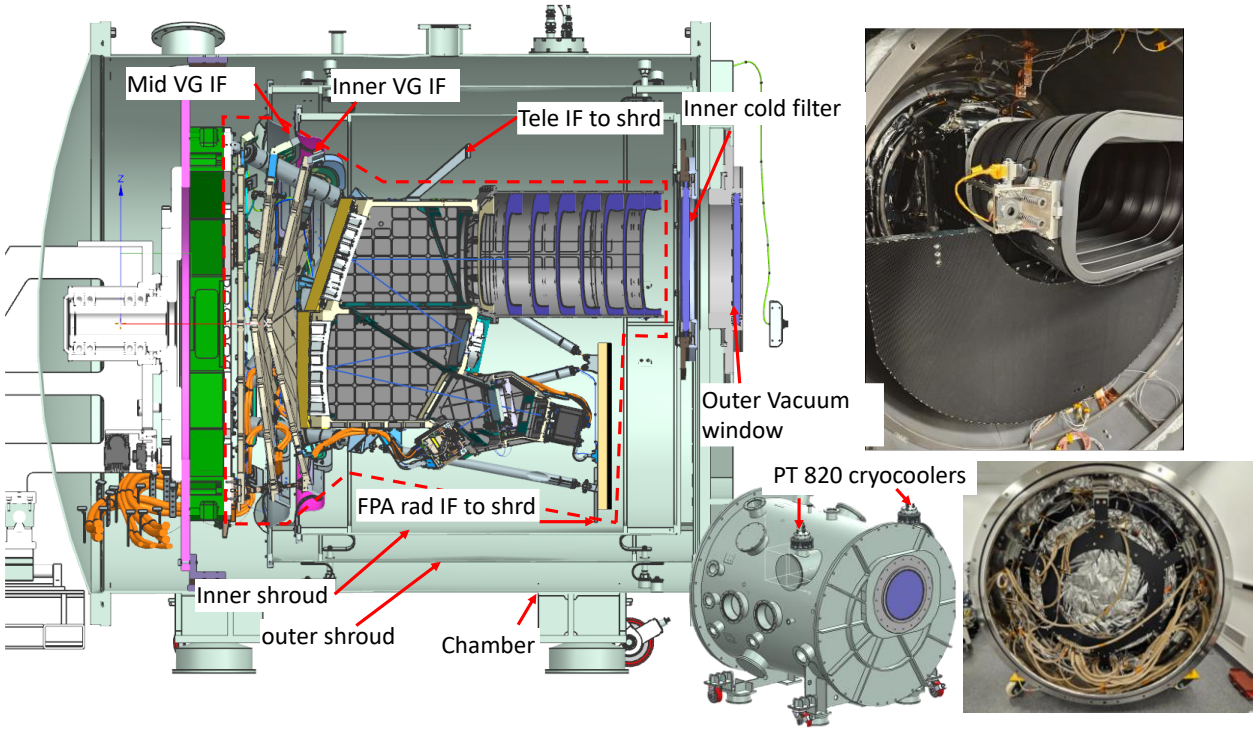

Figure 74 (Left) section view of KASI chamber with major components indicated. A red dashed line delineates the SPHEREx instrument. (lower center) exterior view with cryocoolers. (Upper Right) front view of FPA radiator and telescope baffle in chamber. (lower right) back closeouts of V-grooves.

The cryocoolers were initially modelled as temperature dependent negative heat flows to simulate real performance on cooldown. Initial predicted cooldown using this approach had reasonable agreement between modelled and measured temperatures. However, digging into steady state performance uncovered several issues. Namely, a very large temperature imbalance was measured between the two cryocoolers, indicating either very poorly controlled conductive interfaces or a thermal short. Examining the chamber construction revealed that both were likely issues. Rather than a diffusion bonded, soldered, or welded thermal straps, large stacks of copper foil were simply clamped at the interfaces. Additionally, these very stiff straps were less than 1mm from the room temperature chamber wall with compressed blankets in the gap. The attachments for the FPA radiator and telescope to the inner shroud were also clamped foils. The clamped foil method is both much less effective and extremely variable in performance depending on oxidation layers and clamping force. The chamber arrived pre-assembled from Korea and Caltech lacked the equipment to fully disassemble nor was schedule available to do so. Given that the chamber reached the temperature required for optical testing, corrections were not pursued.

Other issues included, uncertain internal sensor mounting, both in terms of location and mounting method, uncertainties on the optical window coating and emissivity, multilayer insulation (MLI) blanket performance, and quality of Al1100 alloy used for the shrouds.

In general, the configuration itself made thermal correlation difficult, since the FPA radiator, Telescope, and Inner V-Groove, which are thermally isolated from each other in the flight configuration, were all attached to the same thermal sink. This is akin to trying to determine the precise resistance of a 1Mohm resistor while it's wired in parallel with a 1ohm resistor, it is possible but requires careful thought. Two approaches were used to compensate for this uncertainty. The first was to minimize the control volume. For the thermal model, rather than trying to understand the performance and coupling of the cryocoolers, a single trustworthy temperature sensor was selected for each shroud and the cryocoolers were allowed to provide the heat required to match that temperature to the measured temperature. The conductor to provide the cooling to each side was scaled to match the apparent load imbalance measured. This removed the uncertainty in the exact cooling power of the cryocoolers and their conductance to the chamber. Unfortunately, this prevented accurate cooldown comparisons, since the chamber mass is a significant contributor to the overall cooldown time and controlling with this method would provide an unrealistic cooling capacity of the cryocoolers to match the measured cooldown. The second method was to refine the assessment criteria and goals. Since the temperatures were controlled at the interfaces to the instrument, assessing temperatures did not provide enough accuracy. Rather, the measured heater power used to achieve this control could be compared to the modelled heater power. The allowable deviation of this heater power was then based on maintaining adequate margin for flight. To ensure the minimum JPL margin of 25%, this difference threshold was +/-109mW for the MWIR/FPA radiator control and +/-343mW for the SWIR/Telescope.

There were 9 thermal balance points selected. The extremely long time-constants of the chamber and instrument required exponential fits to be applied to the data for each balance point. Two balance points were not used due to a change in the cooling direction which prevented accurate fitting with this method.

For correlation, initially an optimization routine was employed to iterate on uncertain variables in the model and minimize the difference between modelled and measured temperatures. This failed completely, resulting in worse predictions than the initial unchanged model. Instead, manual tweaks were made to variables based on hand calculations and engineering judgement for several iterations. As will be discussed in the observatory TVAC correlation, eventually a sensitivity matrix was generated for both the KASI test and observatory TVAC configuration and further refinements were made simultaneously.

The result of correlation is shown in Table 17. The accuracy goals of the MWIR and SWIR heaters were reached. There were two cases highlighted that show high uncertainty for the Inner V-Groove and Middle V-Groove. As will be discussed further with the observatory TVAC, that there may be additional ice accumulation not represented on the Middle V-Groove. This accumulation would be much worse in the KASI test than in the observatory given the closer proximity of MLI to the Middle V-Groove surface. Thus, using the same optical property for both tests could explain this discrepancy.

Table 17 KASI model correlation result with the 7 balance points used

	Absolute difference							**Percent difference**						
Component\Balance point	TB1	TB2	TB3	TB4	TB5	TB8	TB9	TB1	TB2	TB3	TB4	TB5	TB8	TB9
MWIR detector T (K)	0.28	-0.03	-0.06	-0.07	-0.06	-0.03	-0.04	0.47%	-0.05%	-0.08%	-0.10%	-0.08%	-0.05%	-0.06%
MWIR radiator T (K)	0.31	0.06	0.02	0.01	0.02	0.04	0.03	0.52%	0.10%	0.04%	0.02%	0.03%	0.06%	0.05%
SWIR detector T (K)	-0.29	-0.06	-0.03	-0.01	-0.02	-0.10	-0.08	-0.48%	-0.10%	-0.05%	-0.02%	-0.04%	-0.15%	-0.13%
Telescope Baffle T (K)	-0.33	-0.07	-0.12	-0.02	-0.02	-0.07	-0.04	-0.55%	-0.11%	-0.19%	-0.04%	-0.04%	-0.11%	-0.06%
Telescope T (K)	-0.31	-0.10	-0.05	-0.01	0.02	-0.09	-0.08	-0.50%	-0.15%	-0.08%	-0.01%	0.03%	-0.14%	-0.12%
Inner V-Groove T (K)	-0.35	-0.60	-0.58	-0.56	-0.93	-0.97	-0.90	-0.33%	-0.54%	-0.53%	-0.51%	-0.81%	-0.85%	-0.79%
Middle V-Groove T (K)	0.25	0.33	0.29	0.30	0.28	0.17	0.20	0.14%	0.19%	0.16%	0.17%	0.16%	0.09%	0.11%
Outer V-Groove 1 T (K)	-0.14	-0.04	-0.06	-0.13	-0.22	0.10	0.60	-0.05%	-0.01%	-0.02%	-0.05%	-0.08%	0.04%	0.22%
MWIR htr (mW)	0.00	11.80	13.03	7.69	-29.42	2.53	8.13	0.00%	7.44%	2.16%	0.66%	-2.62%	1.01%	3.35%
Telescope htr (mW)	0.00	20.25	-11.1	-0.66	11.54	-11.93	6.98	0.00%	4.96%	-3.26%	-0.29%	12.19%	-2.85%	1.78%
Inner V-Groove htr (mW)	0.00	-11.3	-12.6	-11.2	-143.6	-24.50	24.27	0.00%	-3.92%	-5.32%	-6.21%	-18.6%	-4.17%	6.58%
Mid V-groove htr (mW)	0.00	-16.2	2.96	10.10	38.75	13.98	-1318	0.00%	-3.40%	0.65%	2.31%	10.49%	1.89%	-35.2%
max tele/MWIR heater absolute difference						29.42 mW		max T % diff		0.85%	max IVG/MVG heater % diff			35.2%

One other important outcome of the KASI testing was to improve the correlation of the optic mounts to the Telescope in support of the on-orbit decontamination analysis for the Telescope. There are several uncertain interfaces between the mirrors and housing. Decontamination on SPHEREx is a

fundamentally transient process, so a precise understanding of both the conductance and capacity of the optical components is required. Figure 75 shows the good agreement achieved between the model vs measured temperatures in response to a step heat input.

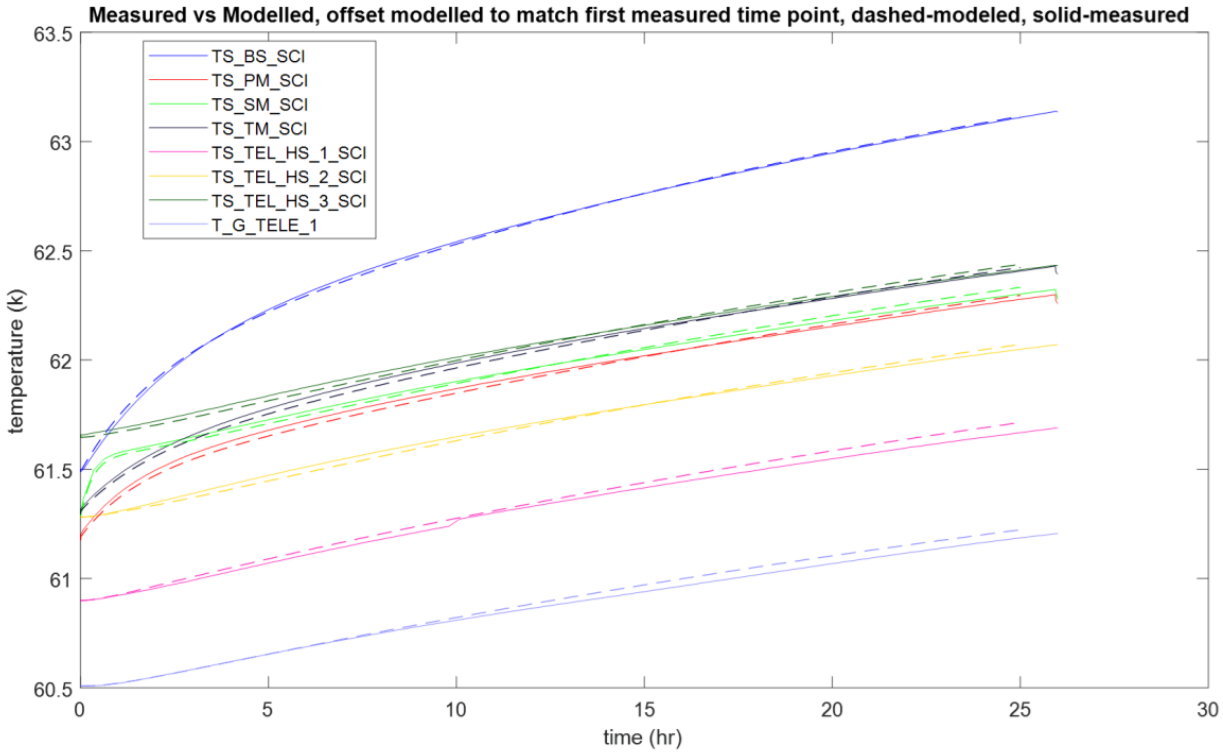

Figure 75 Comparison of modelled vs measured temperature responses of mirrors to a step input of heater power from decontamination heaters.

3.9.3 Observatory TVAC

The Observatory TVAC test, conducted at BAe in the "Titan" chamber, was primarily a verification of the radiative interfaces. The full SPHEREx observatory was placed inside a Liquid Nitrogen cooled shroud capable of reaching ~83K. The nominally room temperature spacecraft bus was held warm by a large trolly at 10C and radiative heater panels controlled to simulate hot and cold operational setpoints. The outer Photon Shields were held near their operating temperatures by heaters conductively mounted to handling holes and a large enveloping MLI blanket. The modelled temperatures and photos of the setup are shown in Figure 76.

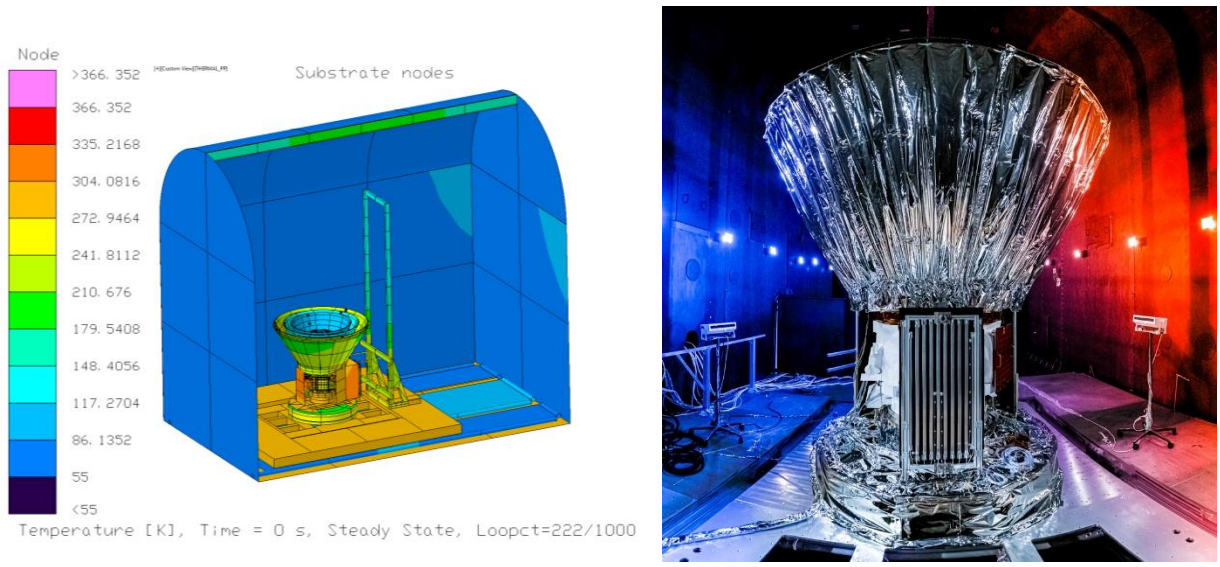

Figure 76 (Left) Overall observatory TVAC chamber layout and temperatures. (Right) Image of SPHEREx with outer Photon Shield blanket in TVAC chamber

This test was limited given that the shroud base temperature of 83K was much warmer than the predicted flight temperatures of the coldest regions. Additionally, there were no cooled radiative baffles to prevent cross talk between regions from chamber reflections. Even a very high emissivity shroud will reflect some portion of incident thermal radiation, and a small portion of room temperature radiation can be a very large load for sensitive cryogenic surfaces. This required attention to detail for both the physical representation of the chamber and the radiation analysis parameters.

For the correlation, a full sensitivity matrix was built for both the observatory TVAC configuration and KASI configuration and any adjustments were checked against both configurations. This matrix varied the emissivity of each of the optical surface and multipliers for some of the key conductive interfaces, such as the main telescope support struts and cables. The primary adjustments in the correlation were made on the optical properties of the Photon Shields and V-grooves. One area of interest is that the outer surface of the Middle V-Groove required a much higher emissivity than predicted. Beginning of life (no ice) optical properties were used for both TVAC and KASI. Given the vacuum pressure, the temperature of the Middle V-Groove, and its view to warm surfaces, it's likely that there was significant ice accumulation on this surface. Using this calibrated emissivity with additional on-orbit ice accumulation could be double counting for this knock down. However, certainty that this is ice or simply

high emissivity due to other effects is difficult to determine based on TVAC data alone. Further examination of this will be conducted with on-orbit data.

Since the only control heaters were at the outer shield boundary and the control power is more driven by the effectiveness of non-flight surrounding blankets, the accuracy goals for this test correlation were assessed in terms into temperatures. Using the measured T^4 of the chamber and instrument, the allowable heat load difference derived for KASI was translated to temperature accuracy requirements of 0.4K for the MWIR/FPA radiator region and 1.9K for the SWIR/Telescope region. There are only effectively two balance points, “hot” and “cold”, in this configuration, and an exponential fit extrapolation was required to extrapolate final temperatures. Unlike KASI, the cooldown curves could be compared. The results of the cooldown vs modelled are shown in Figure 77. There is a large difference in the cooldown results using room temperature vs cryo emissivity for the photon shields. The fact that these two curves essentially bound the cooldown, indicates that updating the radiation calculations based on temperature during the cooldown may be required for accurate results on orbit. Results of the correlation are shown in Table 18. The absolute accuracy of both the MWIR radiator and telescope are highlighted and met the goals of this correlation.

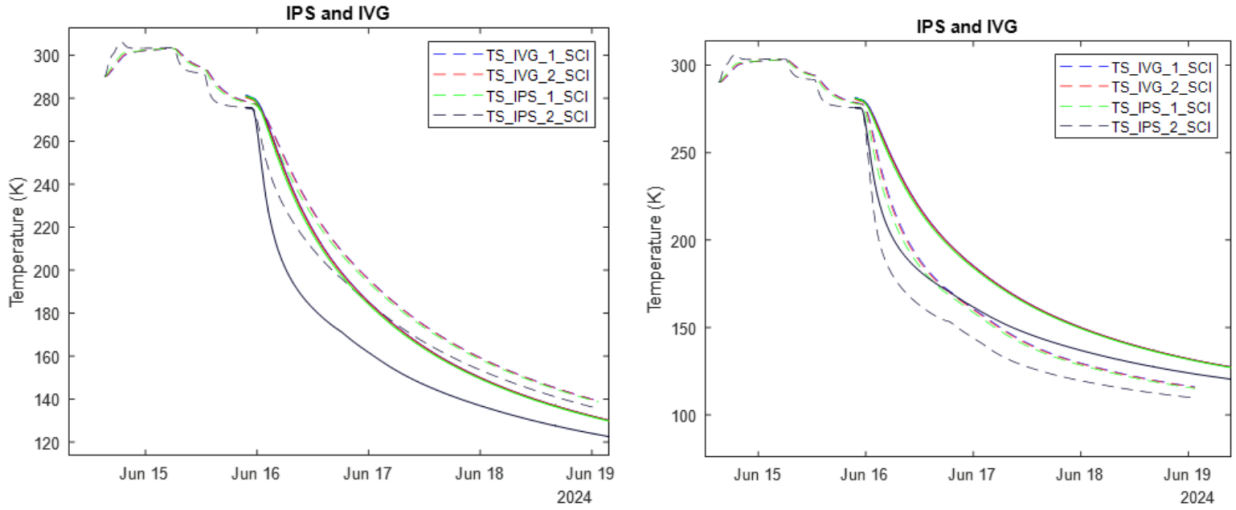

Figure 77 Predicted (dashed) vs measured (solid) cooldown of the inner Photon Shield. (Left) is with the cryogenic optical properties predicted for the final temperature, (Right) uses room temperature optical properties

Table 18 Observatory TVAC model correlation results

	Measured (K)		Modelled (K)		Absolute Diff (K)		% difference	
Component\test case	hot	cold	hot	cold	hot	cold	hot	cold
MWIR	91.45	90.65	91.22	90.47	0.22	0.18	0.2%	0.2%
MWIR radiator	91.29	90.52	91.03	90.29	0.26	0.23	0.3%	0.2%
SWIR	94.01	92.88	95.40	93.76	-1.39	-0.88	-1.5%	-0.9%
Telescope Baffle	93.60	92.61	94.94	93.36	-1.34	-0.75	-1.4%	-0.8%
Telescope	93.76	92.73	95.17	93.56	-1.41	-0.82	-1.5%	-0.9%
Inner V-Groove	108.07	104.60	110.51	104.33	-2.44	0.28	-2.3%	0.3%
Inner Photon Shield bottom	107.84	104.42	110.02	103.99	-2.18	0.43	-2.0%	0.4%
Inner Photon Shield top	104.26	101.62	107.75	102.41	-3.48	-0.79	-3.3%	-0.8%
Middle V-Groove	153.77	136.19	154.81	137.39	-1.04	-1.20	-0.7%	-0.9%
Middle Photon Shield bottom	153.01	135.67	153.28	136.50	-0.27	-0.82	-0.2%	-0.6%
Middle Photon Shield top	134.13	124.01	140.24	129.32	-6.11	-5.32	-4.6%	-4.3%
Outer V-Groove 1	278.69	225.94	284.36	224.25	-5.68	1.68	-2.0%	0.7%
Outer V-Groove 2	262.48	226.25	262.90	223.78	-0.43	2.48	-0.2%	1.1%
Outer Photon Shield bottom	293.47	224.27	291.29	222.20	2.18	2.07	0.7%	0.9%
Outer Photon Shield top	243.16	240.28	241.53	238.88	1.63	1.41	0.7%	0.6%

3.10 Pre-launch predictions

The top-level thermal margins for the best- and worst-case scenarios are presented in Table 19**.** These results were generated using the most recent iteration of the thermal model, incorporating the updates from model correlation discussed later. Values well above the desired 100% thermal margin demonstrate that robust thermal margins remained even at this late phase of the mission.

A heat map of the overall system is shown in Figure 78. This figure illustrates the relative magnitude of the different contributions to the overall load for each component. It does not depict every node-to-node exchange but instead sums nodes across multiple components to represent the overall heat exchange. This plot also serves as a key model-validation tool, as the spreadsheet that automatically generates it also performs a total-energy-balance check for each region. Any unexpected sources of heat load would be apparent in this energy balance.

Temperature contours of the base, uncontrolled temperatures are shown in Figure 79, which presents the minimum temperatures achievable by the SPHEREx thermal system for both beginning- and end-of-life conditions.

Table 19 SPHEREx best and worst case predicted heat loads and associated margin, highlighted values show the expected control authority on orbit in initial cooldown,

Case	MWIR detector base temp [K]	SWIR detector base temp [K]	MWIR control pwr for 45K [mW]	MWIR control pwr for 62K [mW]	FPA radiator (MWIR) CBE loads [mW]	Telescope Housing (SWIR) CBE loads [mW]	FPA radiator (MWIR) max lift at 55K [mW]	Telescope Housing (SWIR) max lift at 80K [mW]	FPA radiator (MWIR) percent margin [%]	Telescope Housing (SWIR) percent margin [%]
Best case BOL	39.0	55.3	42.5	262.1	60.9	182.2	232.2	731.1	281.4%	301.1%
Worst case EOL	41.9	60.4	11.4	125.4	79.2	256.9	232.0	730.7	192.8%	184.4%

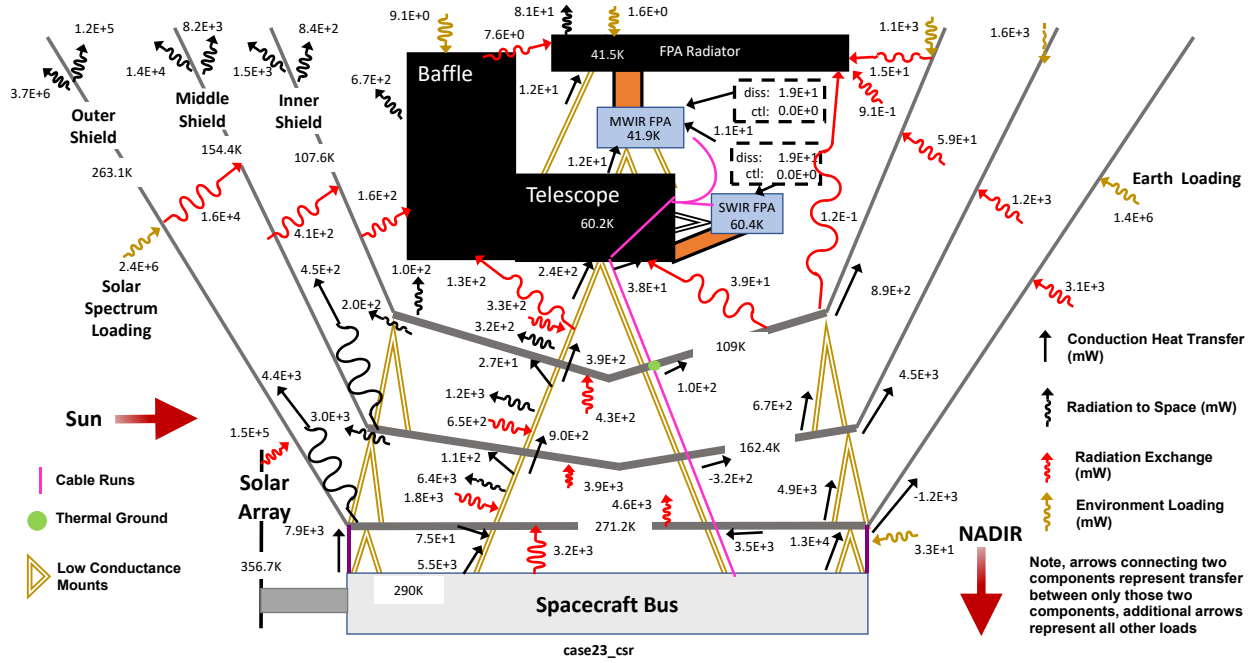

Figure 78 SPHEREx worse case/end of life (case 23) full observatory heat map

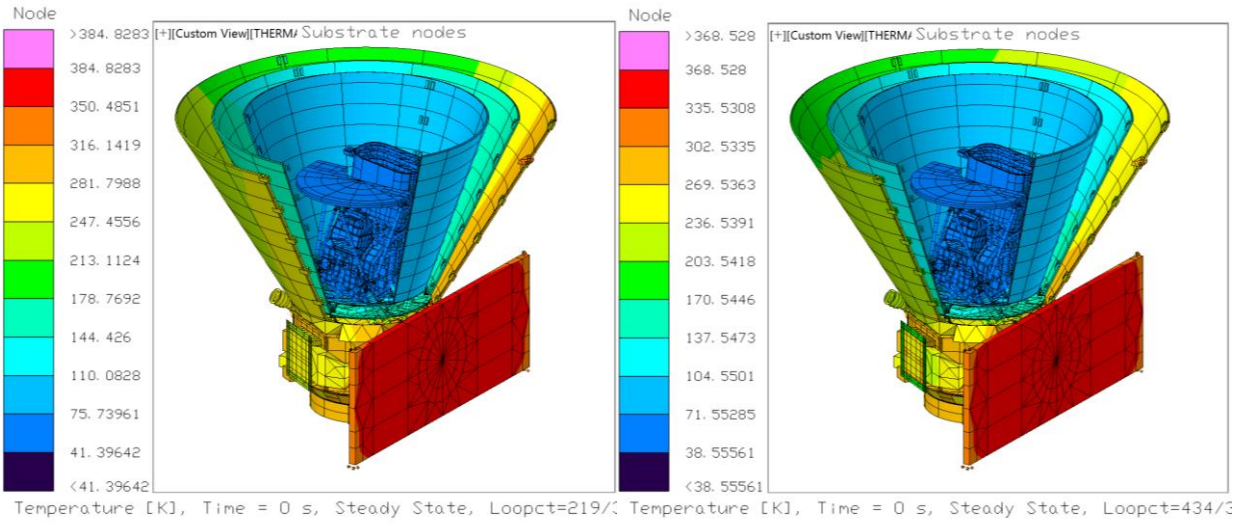

Figure 79 (Left) Best case/beginning of life (case 2) uncontrolled temperature contours. (Right) worst case / end of life (case 23) uncontrolled temperature contours. Photon Shield sections hidden to show internals.

The cooldown from launch to final operations proceeded through several discrete phases and key events that affected the thermal profile. The planned full cooldown is shown in with numbered indicators corresponding to Table 20

Immediately after tip-off from the launch vehicle, SPHEREx entered an inertial-pointing state. The high Earth-infrared loading kept all payload components between 200 K and 250 K, with the apparent noise in the plot representing orbital temperature variations. During several days of in-orbit checkout of basic communication and spacecraft systems, the payload outgassed water and other contaminants at these higher temperatures.

Following this checkout and decontamination period, the spacecraft slewed to an anti-velocity pointing configuration (Z-axis opposite to the orbital-velocity vector) to deploy the telescope cover, causing temperatures to begin cooling slightly. This was followed by another period of inertial pointing with the decontamination heaters active and the cover removed. When the spacecraft transitioned to zenith pointing, the cryogenic components began a controlled cooldown with the decontamination heaters supplying power to maintain optical components above the surrounding temperatures.

After the telescope cooled below 150 K, the decontamination heaters were deactivated and the MWIR and SWIR components naturally cooled to their planned setpoint temperatures of 45 K (MWIR)

and 62 K (SWIR). The FPA temperature-control loop was activated before reaching the base temperatures and intercepted the cooldown at the setpoint values.

Because the actual in-orbit checkouts could take longer than planned, and because the time required to reach quasi–steady-state temperatures in inertial pointing is neither critical nor slow, the key metric is the time from the spacecraft's slew to zenith pointing until the SWIR reached its setpoint temperature. Pre-launch analysis predicted this to take 13.7 days.

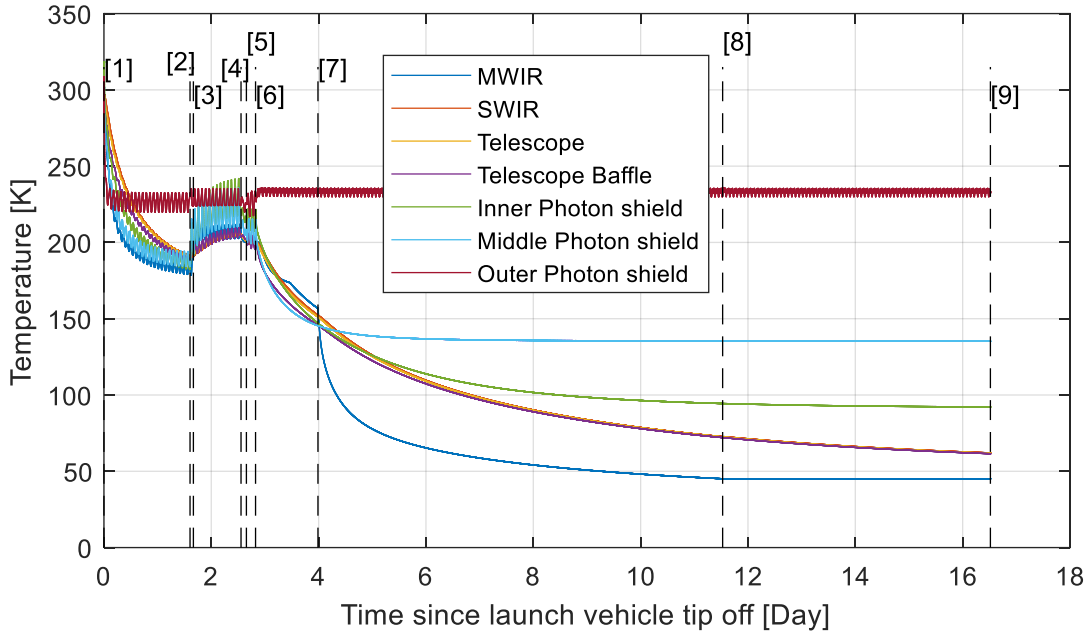

Figure 80 SPHEREx pre-flight predicted in orbit cooldown from launch vehicle tip off

Table 20 Key thermal events planned for on orbit operations, numbers align with Figure 80

#	Description	time (days)
1	After tip off achieve AcqSun Attitude within a few minutes. Note AcqSun maintains a 15˚ angle between +X and the sun line (inertial pointing)	0.00
2	Slew to Inertially-Fixed attitude (similar to AcqSun) but tipped closer to sun (+X to Sun is ~7˚, to support decon heater usage)	1.60
3	Decon Heaters Enabled	1.67
4	Slew to near Anti-Ram for cover deploy	2.55
5	Slew back to Inertially-Fixed attitude (similar to AcqSun)	2.65
6	Slew to near Zenith (+X to Sun is ~7˚, to support decon heater usage)	2.83
7	Decon complete, cooldown to detector control temperatures	3.99
8	MWIR lands at control temp	11.53
9	SWIR lands at control temp	16.52

The results of structural deformation and compliance with requirements are presented in Table 21 and Table 22. A model-uncertainty-factor (MUF) multiplier was applied to the results. Only rotation about the y-axis slightly exceeded requirements, but this deviation was absorbed by the system-level margin held rather than pursuing an expensive active thermal control strategy to mitigate it.

Table 21 full mission duration predicted rotations and maximum change in rotation due to thermo-structural deformation.

Mission duration rotational changes	Rx [arcsec]	Ry [arcsec]	Rz [arcsec]
Max Rotation	-148.48	-87.33	-6.55
Min Rotation	-154.38	-107.72	-12.32
Max Change (CBE)	5.89	20.38	5.76
MUF x1.1	6.48	22.42	6.34
Requirement on change in rotation	8	18.60	19.80
Margin (%)	19	-20.54	67.97

Table 22 Transient (150s, short exposure duration) maximum change in rotation due to thermo-structural deformation

Max across orbit x1.1 MUF				Avg across orbit x1.1 MUF			Margin on Max across orbit			Margin on Average across orbit		
Case	dRx - 150s [arcsec]	dRy - 150s [arcsec]	dRz -150s [arcsec]	dRx - 150s [arcsec]	dRy - 150s [arcsec]	dRz - 150s [arcsec]	dRx 150s [%]	dRy 150s [%]	dRz 150s [%]	dRx 150s [%]	dRy 150s [%]	dRz 150s [%]
101	5.6E-02	5.9E-02	1.7E-02	1.5E-02	1.7E-02	6.3E-03	60.1	80.4	96.6	89.5	94.4	98.7
102	6.6E-02	1.8E-01	5.1E-02	2.0E-02	8.1E-02	2.2E-02	53.0	41.6	89.9	85.7	73.0	95.5
104	4.9E-02	9.4E-02	2.9E-02	2.4E-02	4.6E-02	1.4E-02	65.3	68.7	94.1	83.0	84.6	97.3
requirement	0.14	0.3	0.5	0.14	0.3	0.5						

4 On-orbit performance and correlation

Prior to launch, and in the preceding sections of this work, much of the focus was on bounding the thermal-system performance to ensure that minimum functional requirements would be met. A “best-estimate” on-orbit performance was produced by leveraging test correlations, but the emphasis remained on bounding the problem. Once on-orbit performance was established, however, the focus shifted toward generating the most accurate predictions of performance rather than simply bounding it.

This higher-fidelity analysis proved advantageous because the very small variations in loads experienced on orbit made a high-accuracy model essential for understanding discrepancies between modeled and measured values and for diagnosing potential degradation mechanisms. This exercise is valuable not only for the SPHEREx mission but also for future missions, where better understanding of disconnects between ground testing and on-orbit behavior can improve predictions and clarify degradation mechanisms in passive cryogenic systems.

4.1 In Orbit Checkout (IOC)

Before presenting the modeled-versus-measured performance and correlation, the actual events from post-launch through the commissioning phase, ending with the start of the survey, are summarized to provide context. From a thermal perspective, SPHEREx was a success. The SWIR reached its setpoint temperature in less time than predicted (13 days from zenith pointing) with a healthy margin that could be allocated to addressing other unexpected aspects of the survey.

As of September 2025, the final control heat required to hold the MWIR at 45 K and the SWIR at 62 K is approximately 46.3 mW and 213.9 mW, respectively (with some orbital and seasonal variation). The cooldown is shown in Figure 81 with a corresponding list of “thermal-centric” events in Table 23. Data for several components begins on March 17, 2025, when the instrument control electronics were powered on.

The initial cooldown during inertial pointing is shown in Figure 82), illustrating the orbital oscillations as Earth and deep space alternately filled the view of the sensitive cryogenic components.

Figure 82 also shows the activation of the decontamination heaters, which are active only when an optic falls below 200 K, flattening the bottom of the MWIR oscillation. The slew to anti-velocity pointing to eject the telescope cover is shown as well, with the inset displaying the extremely slight thermal signature of the ejection itself.

For the brief inertial-pointing period before transitioning to zenith pointing, the absence of the cover reduced the oscillation amplitude on the MWIR while greatly increasing the temperature oscillations of the telescope baffle. In addition to ADC telemetry, this provided confirmation that the telescope cover had successfully deployed, since the detectors were not turned on for several days.

The final focus plot, shown in Figure 83**,** presents the decontamination performance. The heater sizing was adequate, and even the MWIR interface remained biased above the telescope for the entire cooldown. The pre-launch analysis that indicated it might dip below the telescope at the beginning of cooldown was based on a lower bus voltage than the actual on-orbit value.

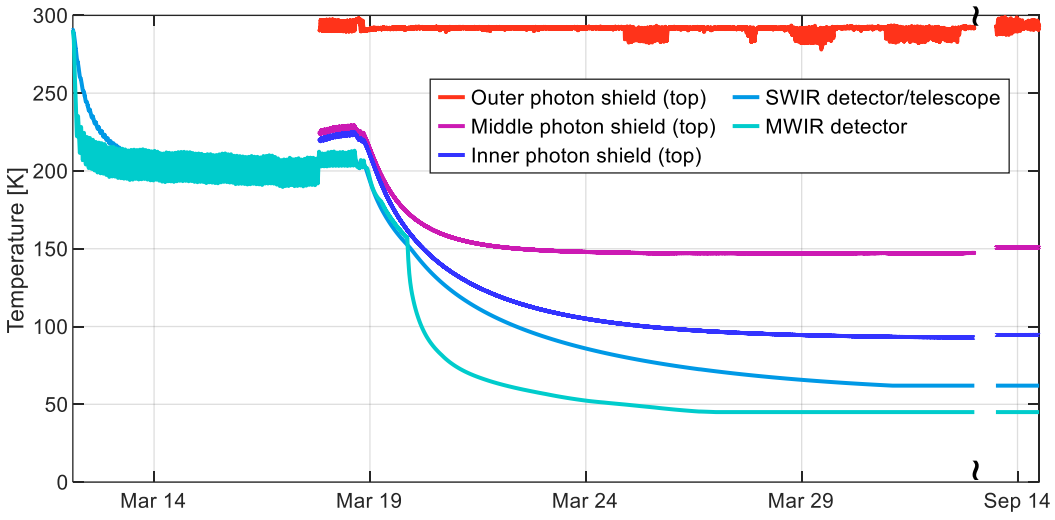

Figure 81 In-Flight cooldown from launch vehicle tip off

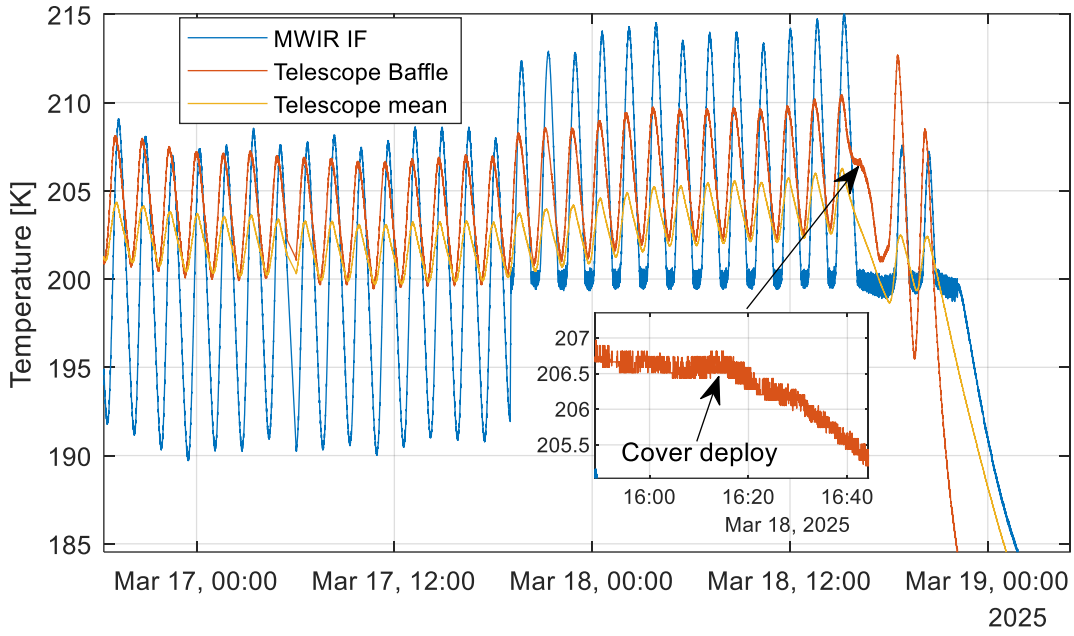

Figure 82 In-flight inertial pointing stability in acquire sun, transition to point state with decontamination heater activation, and telescope cover deploy

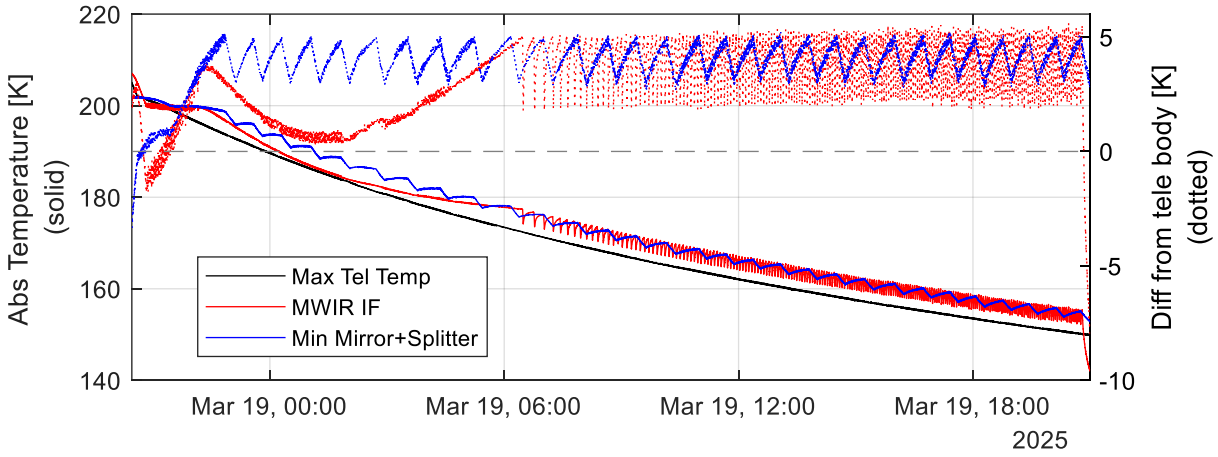

Figure 83 In-flight decontamination algorithm performance

Table 23 Listing of all thermal-centric events in In Orbit Checkout (IOC)

Date UTC	Event description	elapsed time (days)
3/12/25 2:50	telemetry recording begins	0.00
3/12/25 2:55	Tipoff	0.00
3/12/25 6:23	Decon heaters disabled	0.14
3/17/25 18:19	Transition to point state	5.64
3/17/25 19:01	Decon heaters enabled	5.67
3/17/25 7:59	CEB power on	5.21
3/18/25 15:25	Transition to anti velocity for cover deploy	6.52
3/18/25 16:14	Telescope Cover deploy	6.56
3/18/25 9:28	ROB power on (detectors off)	6.27
3/18/25 17:55	Transition to inertial point state post deploy	6.63
3/18/25 20:28	Transition to point standby (zenith)	6.73
3/19/25 21:00	Decon complete (below active temp)	7.75
3/20/25 18:10	Decon heaters disabled	8.64
3/23/25 8:41	MWIR requirement temperature reached	11.24
3/24/25 21:32	Slew performance assessment start	12.78
3/24/25 23:05	SWIR requirement temperature reached	12.84
3/25/25 21:45	Slew performance assessment end	13.78
3/25/25 22:39	CEB/ROB board temperature control on : ROB -7.5C and 5C CEB -11.5C and -2.5C	13.82
3/26/25 15:05	FPAs On	14.51
3/26/25 15:54	Start of CPTOBS	14.54
3/26/25 16:55	End of CPTOBS	14.58
3/26/25 18:19	CEB/ROB board temps updated. ROB 5C and 12C; CEB 0C and 7C	14.64
3/27/25 0:16	MWIR at setpoint temperature	14.89
3/27/25 17:07	Practice Survey 1 start	15.59
3/27/25 22:17	Practice Survey 1 end	15.81
3/28/25 17:36	Survey diagnostics start	16.61
3/28/25 20:10	CEB/ROB board temps updated. ROB B at 9C and 16C, All other ROBs at 8C and 15C; CEB 10C and 17C	16.72
3/29/25 17:41	Survey diagnostics end	17.62
3/30/25 22:40	Practice Survey 2 start	18.82
3/31/25 2:29	SWIR at setpoint temperature	18.98
4/1/25 15:26	Practice Survey 2 end	20.52
4/2/25 12:41	Moonshine start	21.41
4/6/25 8:32	Moonshine end	25.23
4/7/25 22:30	Practice Survey 3 start	26.82
4/8/25 22:55	Practice Survey 3 end	27.83
4/9/25 17:10	Earthshine 1 start	28.59
4/10/25 12:53	Earthshine 1 end	29.42
4/22/25 23:56	Earthshine 2 start	41.88
4/24/25 16:52	Earthshine 2 end	43.58
5/1/25 12:15	Survey starts	50.39

4.1.1 Initial on orbit vs modelled

Shortly after launch, telemetry became available from the limited set of sensors read out by the spacecraft. This included ten sensors on the telescope but only one sensor on the MWIR radiator interface

with the FPA and one on the inner V-groove. No additional sensor information was available for the other photon-shield layers until the instrument electronics were activated later.

Immediate comparisons between modeled and measured data were performed using the available telemetry. As shown in Figure 84, the pre-launch model prediction was significantly off for both the MWIR radiator and the telescope in the initial “acquire-Sun” state but agreed more closely in the later “point” state, which was skewed more toward the Sun. In flight, considerably more time was spent in the initial acquire-Sun state while issues with other spacecraft systems were addressed. Operationally, this had no negative implications, but it provided valuable data for informing model changes to improve the accuracy of the cooldown phase and to generate early estimates of the final thermal-system performance.

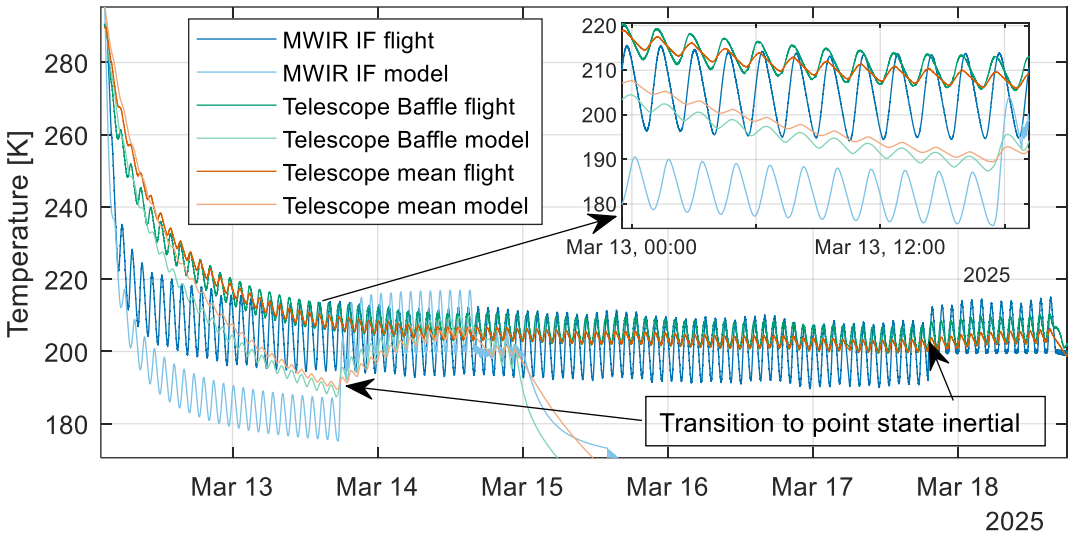

Figure 84 Initial in-flight vs modelled cooldown for key temperatures in inertial pointing

4.1.1.1 Environmental load updates

The first area suspected to cause a disconnect was the environmental loads. The latitude-dependent albedo used in the pre-launch model was based on a JPL internal document and a decades-old paper with very coarse spatial resolution. This limitation was especially relevant during the “knee season” of March, when substantial polar ice remains yet is no longer in polar night, reflecting a considerable amount of sunlight. Additionally, ice coverage differs appreciably from that of past decades.

A better data source was therefore employed to generate a much finer latitude-dependent albedo. The Earth infrared (IR) component was considered less suspect because it exhibits weaker latitude dependence and because even 1–2 °C changes in the average surface temperature have relatively little impact on the overall Earth IR to space. Data from the CERES (Clouds and the Earth's Radiant Energy System) instrument provided top-of-atmosphere (TOA) total flux incoming from the Sun, reflected shortwave flux, and emitted longwave flux. The albedo at any given point was derived as the ratio of reflected shortwave radiation to the total incoming solar flux. CERES data can be queried for "clear-sky" or "all-sky" conditions to infer the effects of cloud cover. Because clouds do impact the effective albedo perceived by a spacecraft, the all-sky data were used but averaged monthly to filter out abnormally heavy cloud cover. This produced a latitude–longitude grid of effective albedo. (Kato, et al. 2025)

Near the latitudes at which polar night begins, the data became somewhat jittery, so filtering and extrapolation were applied simply to make interpolation more stable. Functionally, this does not affect results, as these regions are in perpetual (or nearly perpetual) night and thus reflect little sunlight. Given that the primary focus of the thermal performance is long-term behavior—and that building a specific orbit for the longitudinal track would require significant effort—the grid was averaged across longitude for each latitude to generate a latitude-dependent average albedo for each month. The monthly average latitude-dependent Earth IR was extracted from the Earth-radiation budgets (Stephens, Campbell and Haar 1981). Both the albedo and IR values can then be further interpolated to a specific date of interest. Appendix F shows the latitude–longitude gridded plots of albedo and the averaged latitude-dependent albedo and Earth IR produced by this method.

At the beginning of the mission, a tool to transfer the spacecraft pointing quaternions into a Thermal Desktop vector set had not yet been developed. Consequently, the original Keplerian orbit was used with the updated latitude-dependent albedo and Earth IR. Additionally, the initial temperatures were updated to match those measured shortly after tip-off. Because the only available photon-shield/V-groove sensor was on the inner V-groove, its temperature was used as a proxy for the middle and outer shields as well.

The updated cooldown with the new environmental loads is shown in Figure 85. A slight phase lag is visible due to the pointing not being perfectly inertial, which also explains the small temperature differences. However, the fact that a simple update of the environmental loads brought the modeled and measured data into close agreement strongly indicates that nothing was severely amiss in the model.

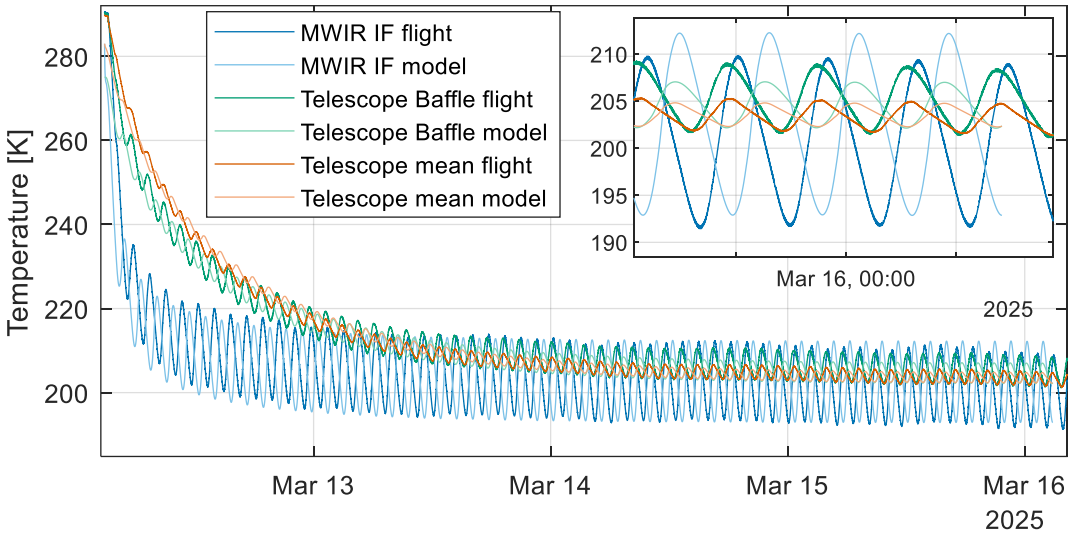

Figure 85 Corrected environmental loads, in-flight vs modelled key temperatures

4.1.2 Zenith cooldown modelled vs measured

Given that updating the environmental loads during inertial pointing essentially resolved any serious modeled-versus-measured discrepancies, the original pre-launch cooldown prediction was not updated. This decision was based on the fact that the pointing during cooldown allows essentially no Earthshine into the sensitive cryogenic regions, so an updated environment would not have significantly affected the predicted cooldown. This assumption was validated by the close agreement between modeled and measured cooldown shown in Figure 86**.**

The full cooldown from the start of zenith pointing until the SWIR reached its final setpoint of 62 K took 13.02 days versus the predicted 13.7 days. The slight difference can be attributed to the mass discrepancy already discussed. Because this discrepancy was not identified until after the cooldown was completed, there was no need to repeat the very long simulation required for the cooldown prediction once it had already been completed.

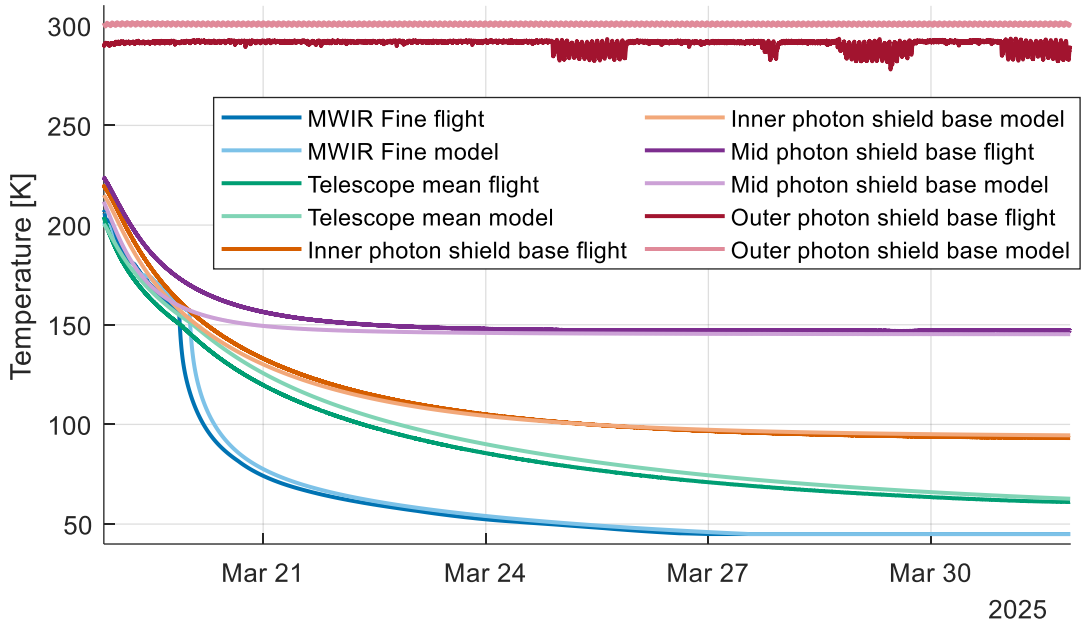

Figure 86 In-flight vs modelled cooldown from transition to Zenith pointing to final detector setpoints

4.1.3 Final landing at temperature and expanded earth keep out requirements

After reaching the setpoint temperatures, additional time was required for the heater power to equilibrate and for internal gradients to stabilize. During this stabilization period, practice surveys and checkout tests—including an Earthshine-avoidance test—were conducted. The Earthshine test was of particular importance to thermal performance because it tipped the spacecraft well beyond the planned limits, including full illumination of the MWIR FPA radiator. The temperature control during the initial equilibration and Earthshine test is shown in Figure 87**.** Tight temperature control was maintained even throughout the Earthshine measurements.

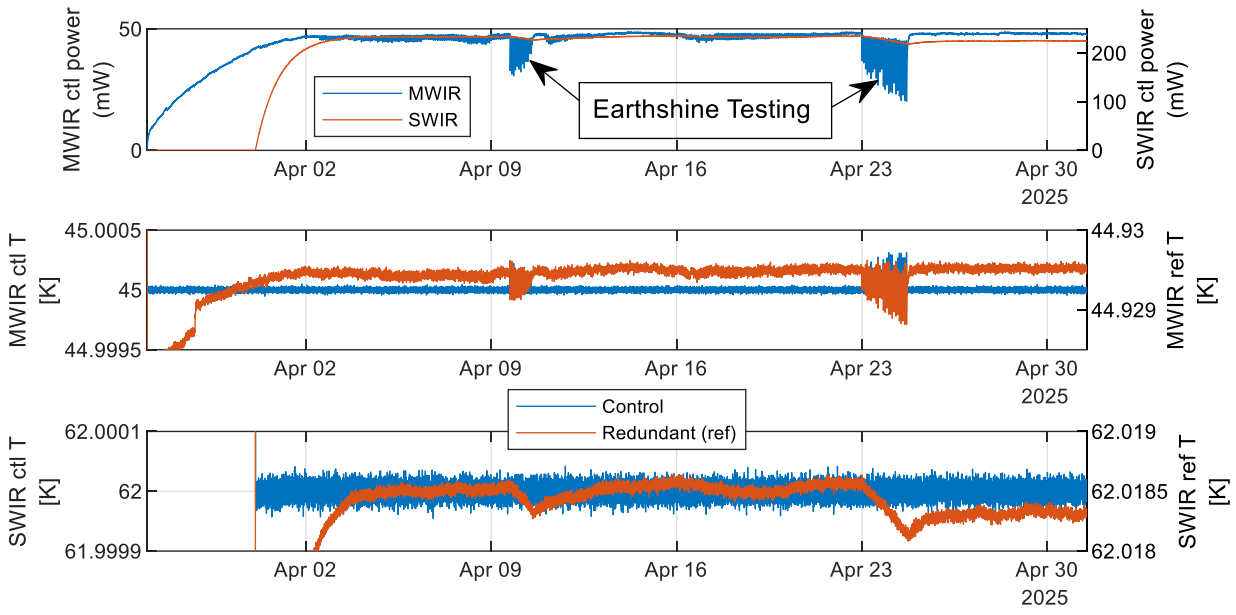

Figure 87 In-flight detector temperature stabilization and earthshine measurements pre-survey start

At the start of In-Orbit Commissioning (IOC), the Earth-avoidance limit was set at 40° Z-zenith (38° in the survey-planning software plus 2° of margin). However, findings during instrument checkout revealed that a phenomenon called “shuttle glow” was producing a high background level and interfering with observations. This phenomenon, first observed on the Shuttle *Columbia*, is highly correlated with ram angle (Murad 1998). Consequently, the survey required a new strategy that tipped much further back anti-ram, exceeding the Earth-limits for which the photon shields were designed. This resulted in direct illumination of the baffle and, in some extreme cases, a very small area of the MWIR radiator.

At this decision point, the model had not yet been fully correlated; however, the accuracy of the pre-launch modeling—combined with results from the Earthshine testing, which had already tipped far beyond the original keep-out-zone requirements—and the very healthy thermal margins allowed a rapid determination that this change was acceptable from a thermal perspective. This change was implemented prior to survey start.

The temperature control for the most challenging “Max Moon Exposure” orbit is shown in Figure 88 compared to the ground-test data, and the entire survey up to the time of publication with the expanded

earth keep-out-zone is shown in Figure 89. The key metric is the average slope of an exposure, taken from the redundant, non-controlled sensor. This shows only a very brief and slight exceedance even with the expanded survey limits. The long-term stability requirements were satisfied by orders of magnitude. Comparing the ground test with the most challenging orbit demonstrates that the cryo-surrogate approach and the derived loads applied in that test were very effective for flight.

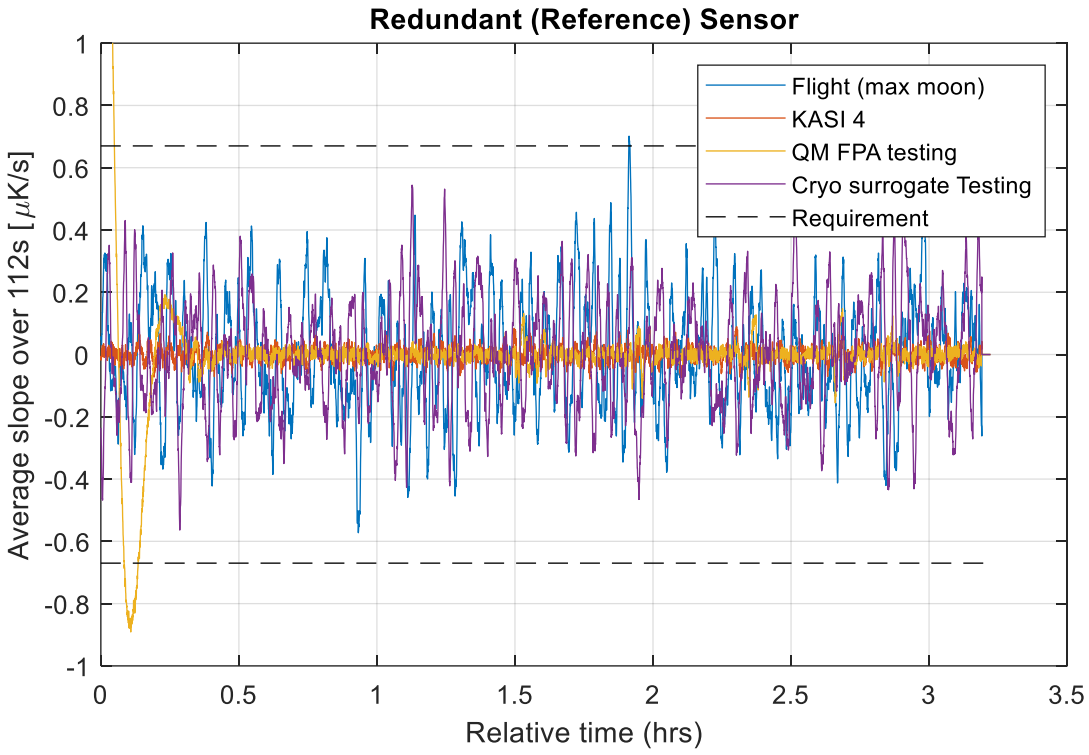

Figure 88 FPA temperature control performance in flight vs ground test

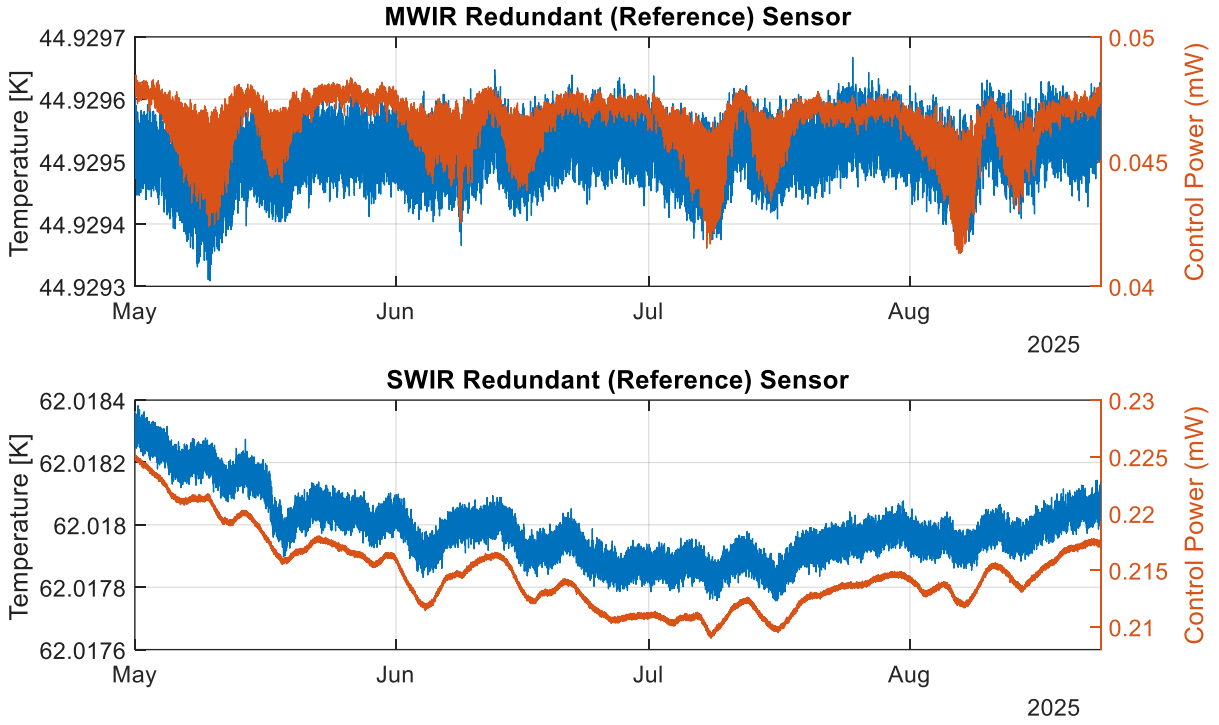

Figure 89 FPA temperature control performance over the mission to date

4.2 Long term orbital trends

For a spacecraft that slews rapidly and frequently, it can be difficult to determine whether a dip in heater power or a drift in temperatures arises from a thermal-system issue or simply from spacecraft movements. Thermal Desktop runs can evaluate overall performance and large-scale trends but are intractable to execute for every minute of the orbit. To address this, a unique approach was developed in this work: a simple model of the heat loads on the critical cryogenic components. Two tools were created to track the expected variation in environmental loads versus the measured variation.

4.2.1 Simple geometric environmental load estimator

The first tool is a simple geometry-based model that ingests relevant vectors from telemetry and calculates the effective view factor from a Z^+ patch to Earth, Sun, and Moon for each minute of the mission. It does so using the vectors for the Sun and body (Earth or Moon) in the spacecraft-centered frame.

The case for the Moon is relatively straightforward. Using the phase angle between the Moon and the Sun (equation 22), an illumination fraction can be derived (equation 23). The illuminated-side and dark-side temperatures are then T^4-averaged using this illumination fraction (equation 24) to produce the effective blackbody temperature for lunar IR loading. The view factor from the Moon to the spacecraft can be simplified to the Z-component of the spacecraft-to-Moon vector multiplied by the squared distance ratio, which corresponds to the cosine of the angle between the Z-axis and the Moon. This culminates in the total lunar IR load shown in equation 25, where ε_{moon} is the emissivity of the Moon and σ is the Stefan–Boltzmann constant.

$$\mathrm{Cos}(\alpha) = -u_{sc2sun} \cdot u_{sc2moon} \tag{22}$$

$$f = \frac{1 + \cos(\alpha)}{2} \tag{23}$$

$$T_{eff,moon} = \left(f * T_{day}^4 + (1 - f) * T_{night}^4 \right)^{\frac{1}{4}} \tag{24}$$

$$HL_{moon,IR} = e_{moon} * \sigma * T_{eff,moon}^4 * \left(\frac{R_{moon}}{Dist_{SC,moon}} \right)^2 * u_{sc2moon,Z} \tag{25}$$

For lunar albedo, a Lambertian phase function (equation 26) with the same α as defined above was used, in conjunction with the solar constant (S_0=1361 W m^{-2}), lunar albedo (a=0.12), and the same view factor as used in the IR loading to derive the lunar albedo loading (equation 27).

$$\Phi = \frac{\left(sin(\alpha) + (\pi - \alpha) .* cos(\alpha) \right)}{\pi} \tag{26}$$

$$HL_{moon,IR} = s0 * a * \Phi * \left(\frac{R_{moon}}{Dist_{SC,moon}} \right)^2 * u_{sc2moon,Z} \tag{27}$$

The Earth loading is somewhat more complex. Because Earth-limb contributions are significant, a simple view factor as computed for the Moon cannot be used. Instead, a tiny-disk quadrature is employed in which a number of "rays" are shot in successive rings. If they intersect the planet, the "hit" is accumulated to generate a view factor. Though the code for this numerical quadrature is longer, the equation itself for Earth IR is simple, shown in equation 28, where E_{IR} is treated as a constant 237 W m^{-2} on both the illuminated and shadowed sides due to atmospheric effects.

$$HL_{moon,IR} = E_{IR} * F \tag{28}$$

Earth albedo employs the same Lambertian approach as shown in equation 26 for the lunar case, except that α is now a function of the spacecraft-to-Sun and spacecraft-to-Earth vectors (equation 29).

$$\mathrm{Cos}(\alpha) = \mathrm{acos}\,(-u_{sc2sun} \cdot u_{sc2earth}) \tag{29}$$

An additional improvement was to interpolate from the higher-accuracy seasonal and latitude-dependent Earth IR and albedo derived earlier in section 4.1.1.1.

This tool does not account for the emissivity or shading of various components; it simply calculates the load in W m^{-2} on the Z^+ surface at the top of the photon shields. As such, it is only useful for relative trends and for indicating whether those trends are driven by orientation or by other effects (such as contamination accumulation).

4.2.2 Thermal desktop ray trace environmental load estimator

The second tool relied on Thermal Desktop but not to run a full thermal solution at each time step. Instead, it built a set of vectors spanning all possible spacecraft pointings for Earth, Sun, and Moon. A matrix of all combinations of Earth/Sun and Moon/Sun geometries was generated, and Thermal Desktop was used to perform a Monte Carlo ray trace of the environmental loads for each pointing. The resulting loads for each component of interest were then extracted.

This approach inherently accounted for shadowing by other components, reflected light from adjacent surfaces, and the emissivity of individual surfaces. Because the number of individual ray-trace solutions required in Thermal Desktop scales as $n_{earth/moon} \times n_{sun}$, the vector set was minimized. This was achieved by using an irregular grid in spherical coordinates with higher density around geometries of interest (such as the angles at which Earthshine first illuminates the baffle or the FPA radiator). The input vectors used to construct this grid are shown in Figure 90**.**

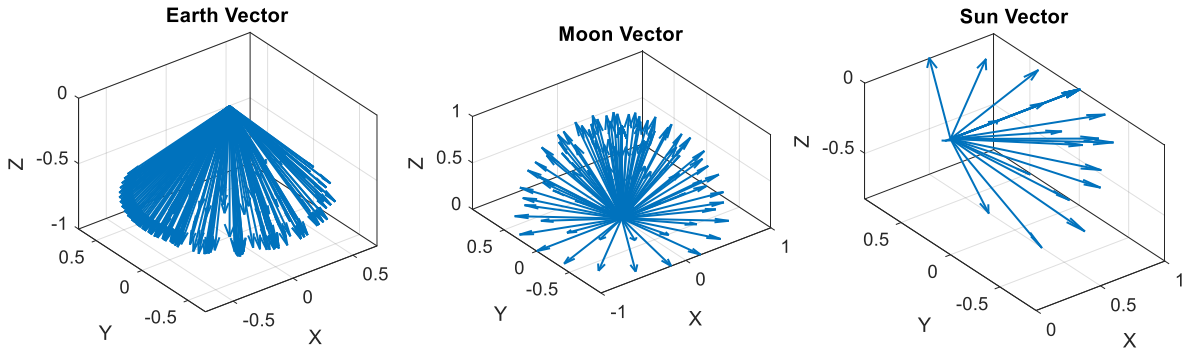

Figure 90 Vectors used to calculate effective environmental load interpolation table

The resulting six-dimensional table (x, y, z for Earth or Moon, and Sun) initially proved difficult to interpolate stably. Two techniques were therefore implemented. First, because the vectors lie on a unit sphere, they were expressed in spherical coordinates (ϕ azimuth and θ polar) for Sun and Earth/Moon, reducing the dimensionality to four. Second, the data were regridded to a much finer mesh in ϕ–θ space. This required several iterations to refine. The final method interpolated each ring of ϕ to a regular, dense spacing for the existing θ values, after which two-dimensional interpolation filled additional θ values. An example of this regridding is shown for the inner photon-shield Earth IR and albedo data in Figure 91. The dots represent the input data. Note that θ is the angle to +Z; the first illumination of the inner surface of the inner photon shield occurs at the Earth-limb angle of the SPHEREx orbit (658km) which is ~24.7 degrees (which is $180–24.7\approx155.3°$ in this convention). This is consistent with the start of the slope increase at that point.

The plateau at the top of the curve Is nonphysical—the load continues to increase to a maximum at 0°, but in normal operations this is well beyond allowable pointing and was not included in the input data. To maintain well-behaved interpolation, the extrapolated data were set to the last available values. If

required for future mission planning, the approach can be extended to encompass any angle. All key component surface plots for both Earth and Moon loading are shown in Appendix F.

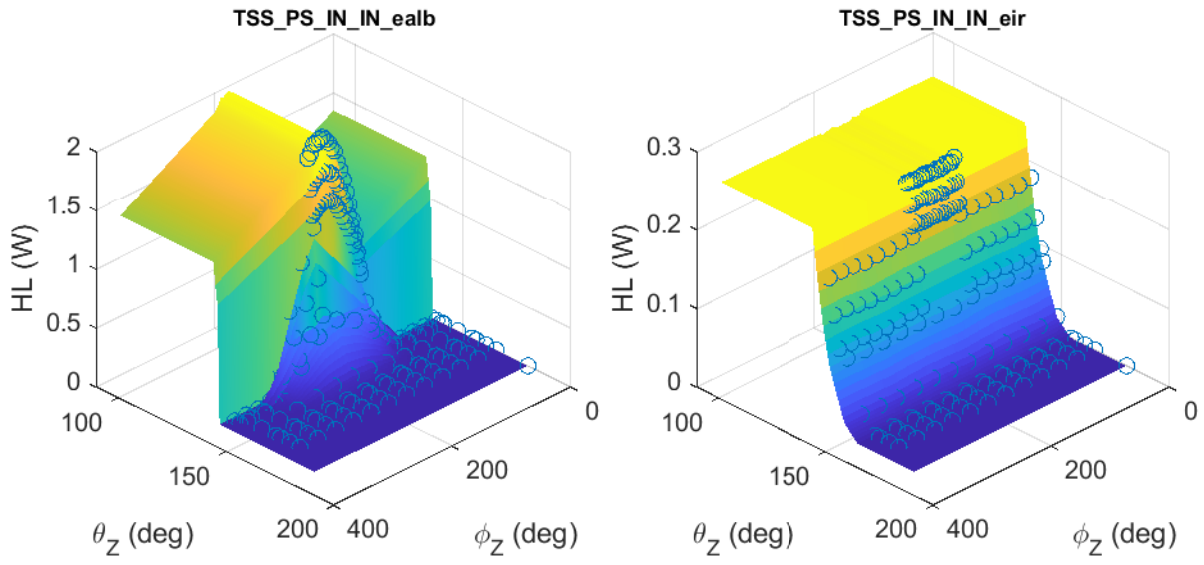

Figure 91 Surface plots of effective environmental load vs spherical coordinate angles: (left) earth IR; (right) earth reflected sunlight (albedo)

After the Earth/Moon grids were regularized and densified, the effective load on various components could be interpolated for the actual mission vectors. This was done in two steps:

1. Determining the output values for the Earth or Moon for all nearest Sun vectors to the actual Sun vector.
2. Using Delaunay triangulation between those values based on relative position to the Sun vectors.

A fallback was added near the pole (x-axis in the Sun case), applying a Gaussian blend based on distances to avoid numerical issues with Delaunay triangulation. Finally, the interpolated values of Earth IR and albedo loads were scaled from the constant values used in Thermal Desktop to the seasonal and latitude-dependent values derived earlier.

In general, this approach did not include more static parasitic loads (such as those from support struts) and so could be derived directly from orientation and date. This made it suitable for predictive use with the survey plan. For retrospective analysis of already-logged data, the effective loading of the inner photon shield/V-groove was also included. The view factor from the inner shields to the SWIR and

MWIR radiators was extracted and effective loading derived using this fixed value (which includes emissivity) and the temperatures of the shields and SWIR/MWIR radiators. This accounted for natural variation in inner-shield/V-groove temperatures resulting from pure environmental-load changes. Increased coupling due to changing emissivity on the shields would manifest as changes in the difference between predicted and measured heat load. When predicting future loading, the inner-shield temperature variations can be estimated from the Thermal Desktop load estimator; however, for analyzing past data to tease out real degradation in performance, using the measured temperature directly provided a more accurate approach.

Because this process involved a number of time-consuming (~33 hours to run all ray traces) and difficult-to-visualize steps—from vector generation and analysis in Thermal Desktop to regridding to final interpolation—a simple check model was built. A perfectly black disk with Z^+ orientation identical to SPHEREx's Z^+ surface was run through the pipeline. In theory, this should produce a profile similar to the geometric model discussed in the previous section. Figure 92 shows the results of the two models compared. This produced a good validation of the approach.

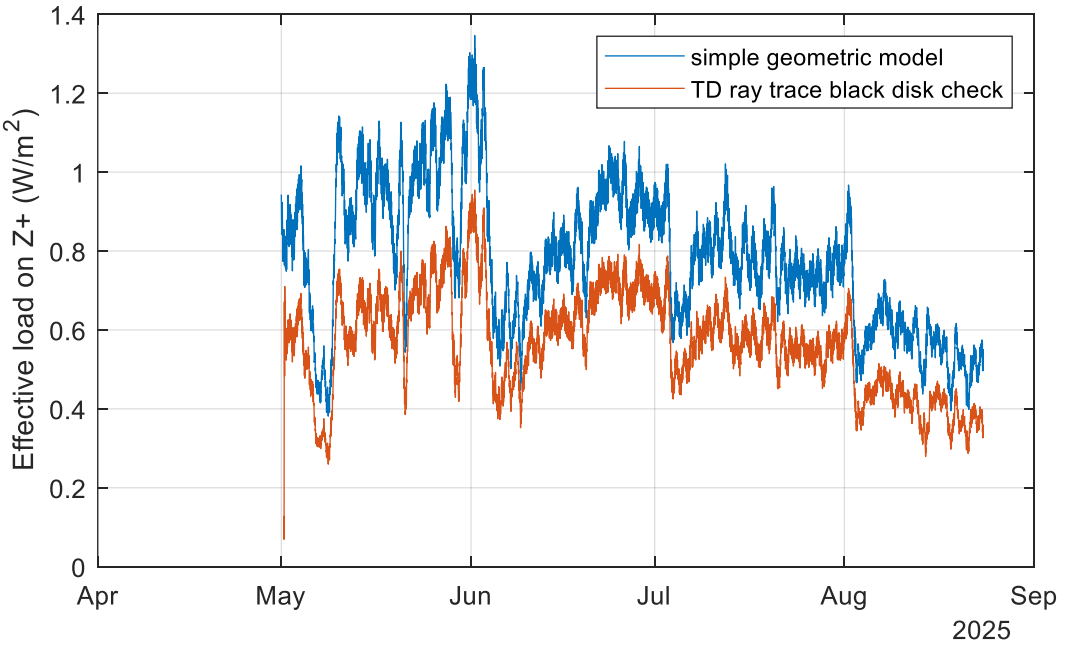

Figure 92 Effective total earth (IR and reflected solar) environmental load on a black disk using the thermal desktop load estimator and simple geometric model. A moving average of 1000 points was used to smooth the data for easier comparison

A comparison of the two methods to the actual heater-power variation is shown in Figure 93. Several conclusions are apparent. The Thermal Desktop–derived effective loading as a function of input vectors is quite accurate in terms of relative loading; it captures both short-term features and long-term trends with much higher absolute and relative accuracy. The simple model explains the long-term and overall trends but does not reproduce many of the smaller features and nuances. This is expected because it does not include component shading or the varying emissivity of surfaces (for example, the baffle and MWIR radiator are recessed), but it provides a good, rapid sanity check. The imprint of various orientations and seasonal variation of environmental loads is visible.

Both the Thermal Desktop ray-trace model and the simple geometric model outputs were filtered with a moving average. This has physical meaning because neither accounts for the time constant of the components being heated. If the telescope and MWIR region were each perfect thermal lumps, the time constants defined by equation 30 would be ~10000 min for the telescope and ~950 min for the MWIR radiator. In reality, both are fairly thin shells dissipating radiation to space, so only a small fraction participates in the plant model of the respective FPA control loops. Manual iteration found that a moving mean of ~90 min for the MWIR region and ~2000 min for the telescope/SWIR region yielded similar short-timescale excursions while exposing the long trends.

$$\tau = m * \frac{c_p}{4 * \epsilon * \sigma * A * T_{eq}^3} \tag{30}$$

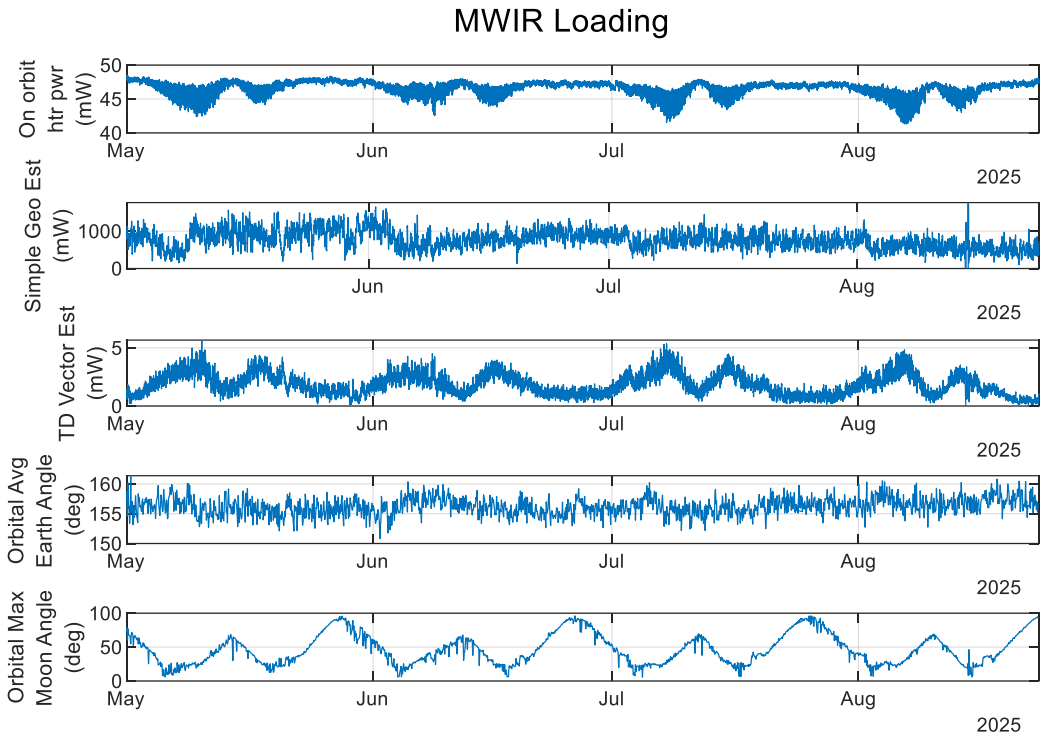

Figure 93 Estimates of environmental loads from simple geometry model and TD vector model vs actual in-flight heater power and average Earth/Moon vectors for MWIR

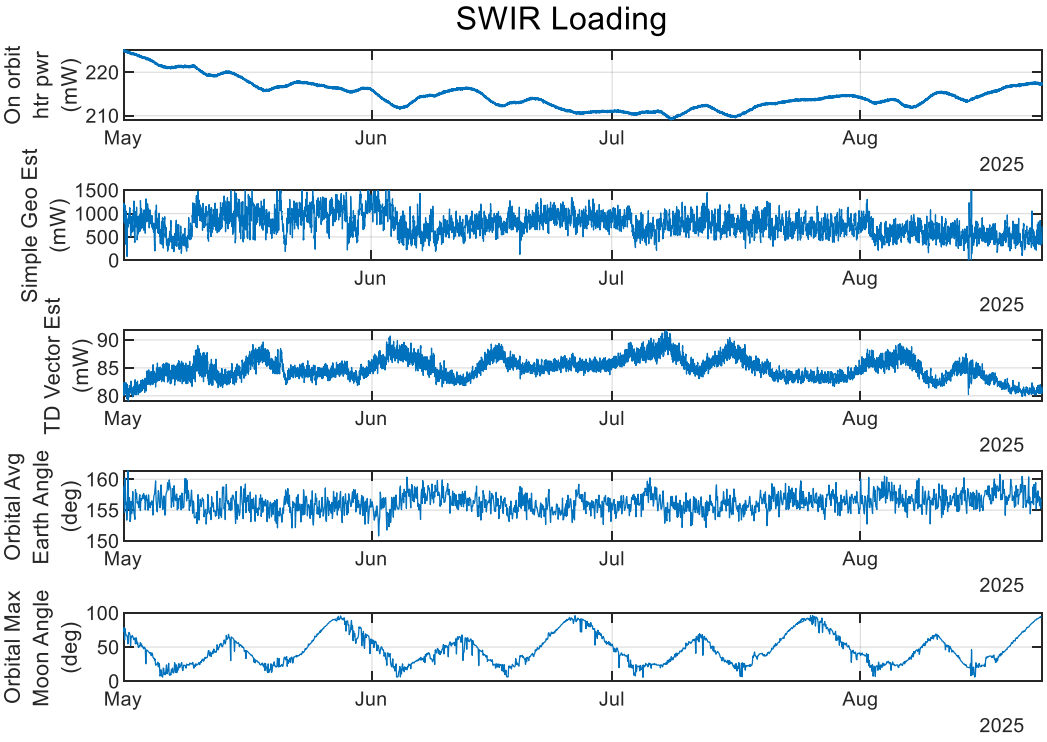

Figure 94 Estimates of environmental loads from simple geometry model and TD vector model vs actual in-flight heater power and average Earth/Moon vectors for SWIR

4.2.3 Trending assessment

With this tool, the seasonal dependence of albedo could be revisited. As previously discussed, the albedo used was the last 5-year average on a per-month basis. The CERES data release is typically a few months behind the current date (as of writing in August 2025, the most recent month available was June 2025). However, the May–June portion of on-orbit data provided actual monthly albedo averages for comparison. Figure 95shows the difference in predicted loads when using the last 5-year average versus only the last year. As can be seen, the difference is negligible. During the times when there is a large difference in albedo (for example, at the South Pole in winter), the cryogenic components have very little exposure. This validates the "average of last 5 years" approach and indicates that the overall accuracy and finer latitude steps, not necessarily climatological accuracy, are the true source of improved accuracy when using the CERES data.

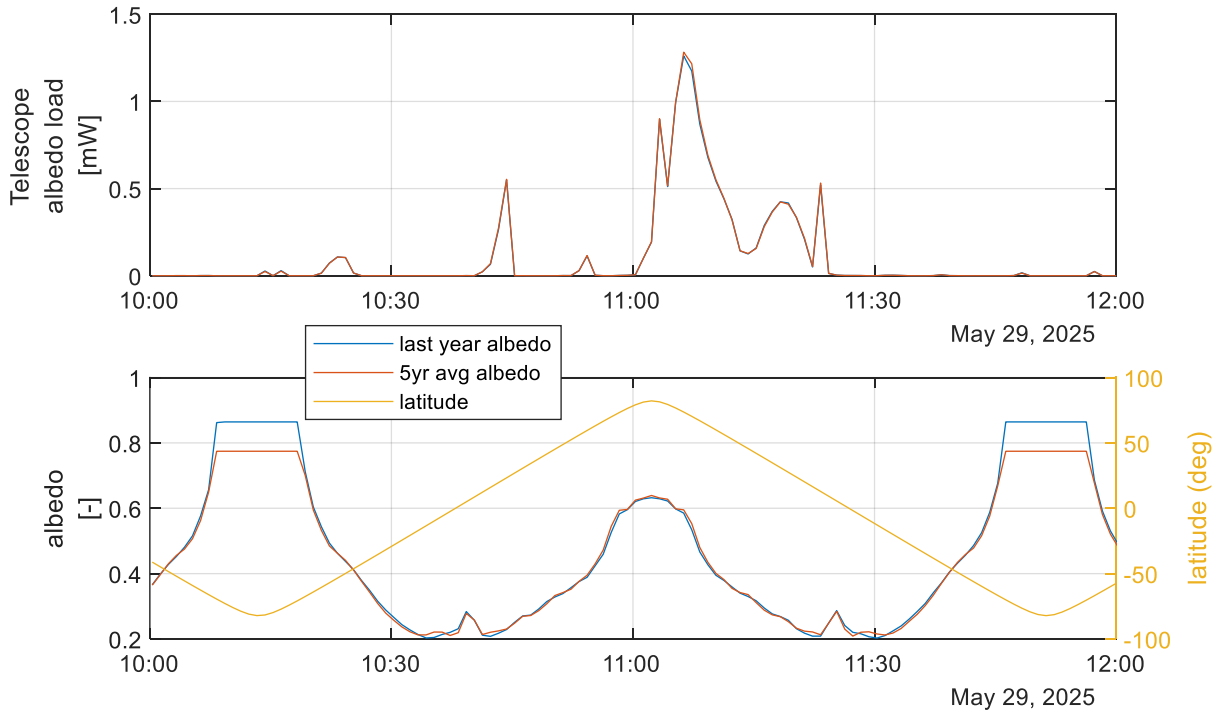

Figure 95 Comparison of different average durations to values of albedo from CERES data

The most useful outcome of the more advanced Thermal Desktop model was the ability to predict accurate relative heat loads. The model does not account for nearly static loads due to conduction. The

relative heat load (difference from the value at the start of the survey) is plotted in Figure 96 for MWIR and Figure 97 for SWIR. The relative change from the start of the mission between modeled and measured data agrees very closely and tracks well with seasonal and orientation changes. However, the long-term trend of the difference between these two values reveals a slight increase over the mission to date. The SWIR appears to have stabilized, whereas the MWIR is more difficult to assess because of variations in lunar load. This finding confirms that there is some small amount of degradation of thermal performance.

The plausible mechanisms for the overall increased loads on the SWIR and MWIR stages include ice accumulation, micrometeorite impacts on the inner surfaces of the photon shields, and darkening of the outer-shield paint due to UV exposure. Examining the photon-shield temperatures in Figure 98 (absolute) and Figure 99 (relative change over the mission) shows that all of the photon shields are slowly increasing in temperature. This could be due to thermal "bleed-through" from the warmer stages—for example, degradation of only the outer-shield paint would increase its temperature, which in turn warms the middle shield, which in turn warms the inner shield.

However, the loads change by orders of magnitude from one stage to the next, the temperature change should also be attenuated. Each stage is instead experiencing similar temperature changes, indicating some intrinsic degradation at each stage. Revisiting the sensitivity study on the effect of emissivity on photon-shield temperature narrows down the location and type of degradation. Micrometeorite damage is unlikely because it would impinge only on the inner surfaces of the shields, for which increased emissivity actually lowers the temperature. Given the very long residence time of any ice accumulated at the middle and inner shields, ice is not likely to have quickly accumulated at the beginning of the mission (before survey start) and then substantially reduced based on contamination modeling. Thus, ice and emissivity on the inner/middle shield is likely increasing over this time span.

Only specific surfaces, the outer surface of the inner V-groove and the outer surfaces of both the middle photon shield and V-groove, are expected to accumulate ice because of their temperature ranges and proximity to potential contaminant sources. The outer-shield UV degradation is a well-understood

phenomenon and was discussed earlier, accounting for the outer shield's behavior. This trending establishes the direction of investigation when correlating model degradation over long time spans.

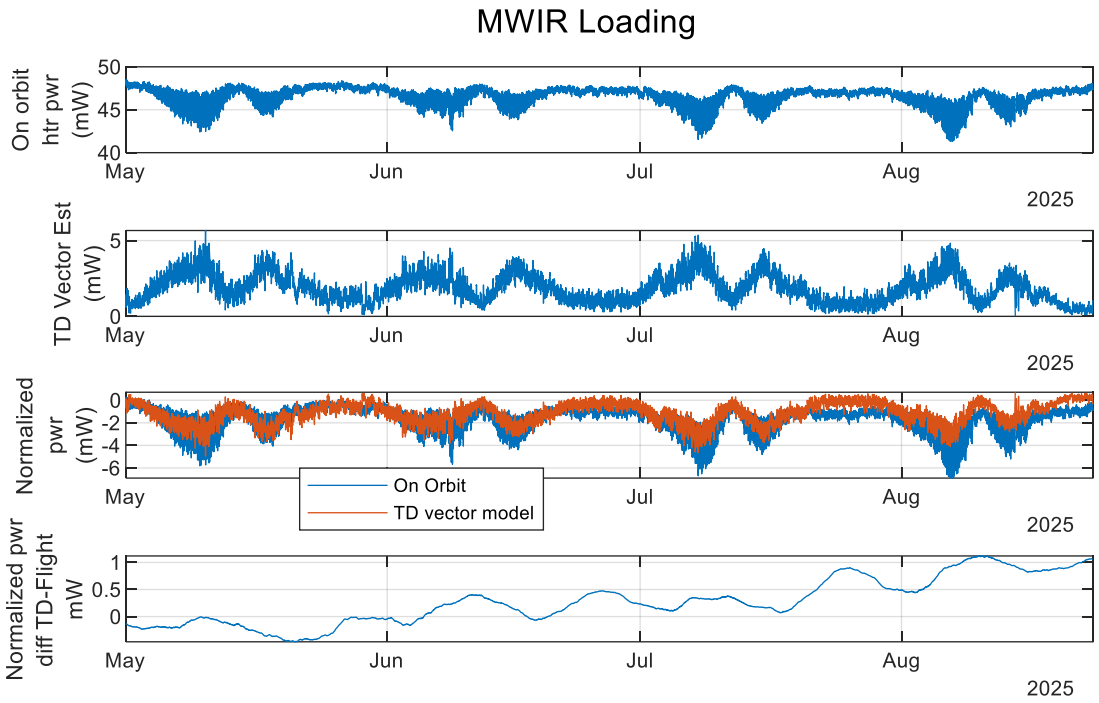

Figure 96 Comparison predicted TD vector model to actual on orbit heater power relative to start of survey for MWIR

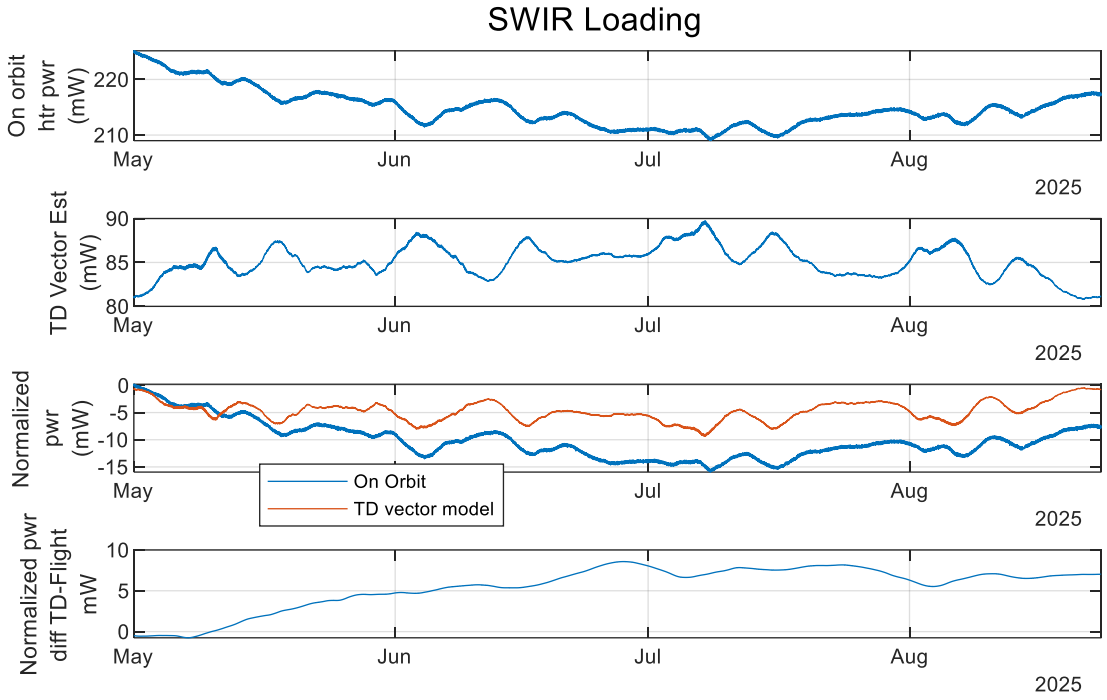

Figure 97 Comparison predicted TD vector model to actual on orbit heater power relative to start of survey for SWIR

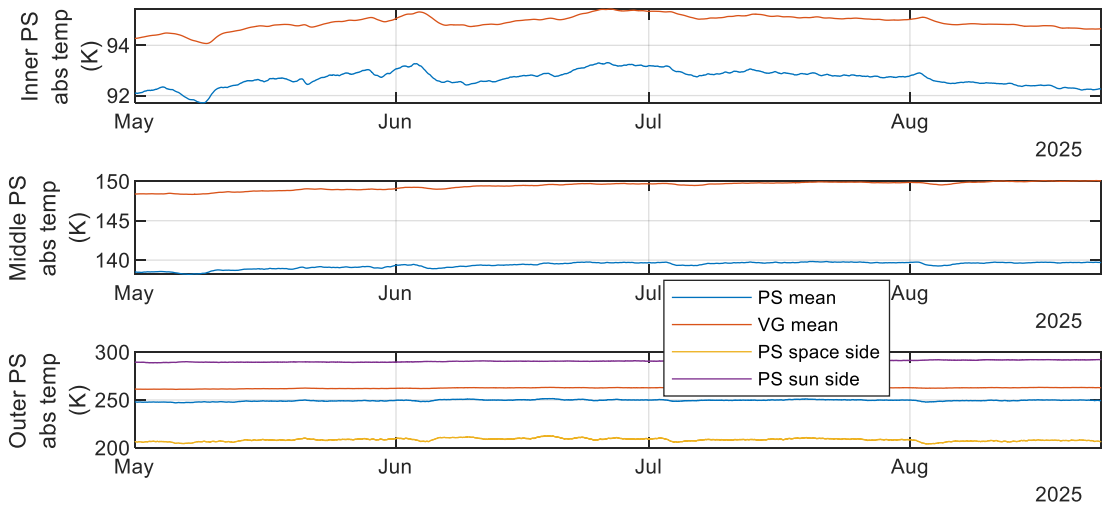

Figure 98 In-flight long-term trending of photon shield and V-groove temperatures

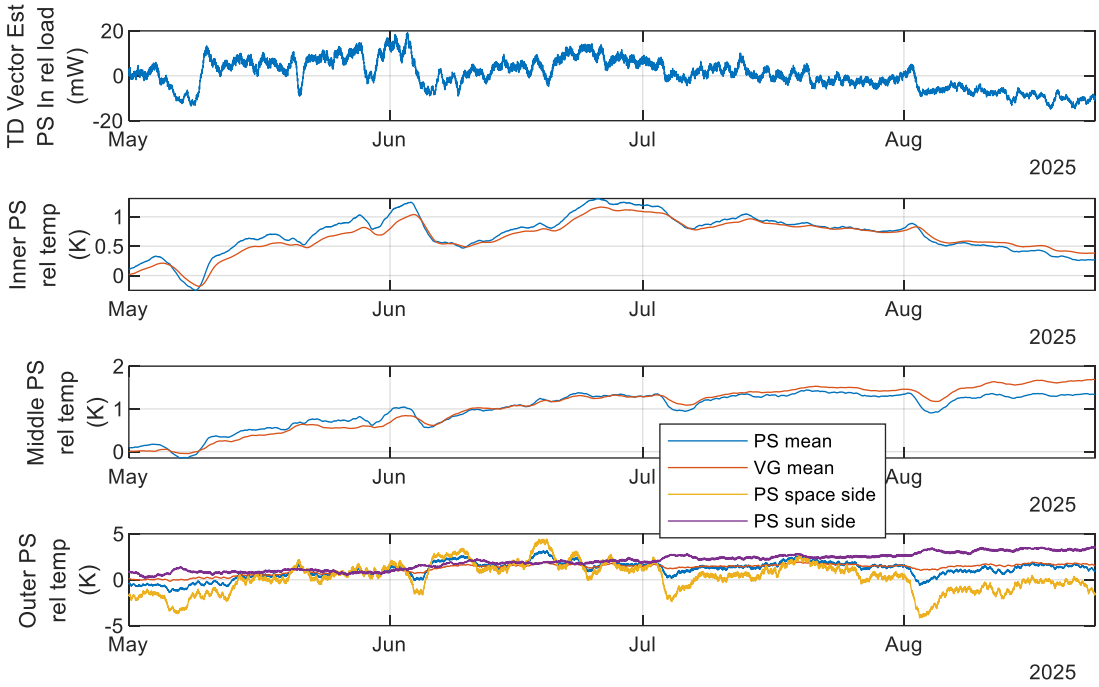

Figure 99 In-flight long-term trending of photon shield and V-groove temperatures relative to start of survey

4.3 On orbit correlation

Based on on-orbit performance, model correlation was performed. The primary objectives of this correlation were (a) to explain any discrepancies between predicted and actual performance and (b) to produce a model that could be used for future flight operational planning, such as an extended mission phase or expanded operational parameters.

4.3.1 Balance point selection and orbit generation

In general, six balance points were selected for steady-state correlation. These points spanned times with high Moon load and low Moon load before survey start (with a more quiescent slew pattern), at the beginning of the survey, and at the end of the survey. The balance temperatures and heater powers were taken as the average of 10 orbital averages (a ~97-minute orbit gives close to the ~2000-minute effective time constant observed in the environmental-load comparison in the previous section). Averaging over longer time spans risked blurring the effects of Moon exposure and other long-term survey pointing artifacts.

A single orbital average was not sufficient because significant orbit-to-orbit variation exists, particularly in the outer-shield regions, and the thermal inertia from previous orbits can skew results. The actual orbit vectors generated for Thermal Desktop environmental-load computation were based on a single orbit, not an averaged orbit. Averaging the per-orbit positions was considered, but this would have washed out peaks caused by large slews. Especially near the Moon, most orbits contained at least a few large slews that did not occur at the same point in the orbit; averaging would therefore have eliminated these peaks. Instead, a representative single orbit was selected for each time.

Figure 100 shows the full profile of MWIR and SWIR heater powers and associated Moon-Z and Earth-Z angles, with the balance points highlighted. Table 24 lists the balance points and provides brief descriptions. The relevant Earth, Moon, and Sun orbital vectors were then extracted for each of these times.

Because a full Monte Carlo solution was required for each position, care was taken to minimize the number of positions while still capturing the shape of the maneuvers. A peak-finding algorithm in MATLAB was used to select the critical points. The latitude-dependent albedo and Earth IR were interpolated based on the date of each balance point and mapped to the time basis required for the planet/Sun vector input to Thermal Desktop. Appendix G shows the relative Earth and Moon angles for each position used, demonstrating that the full shape of the cross-orbit slews was captured.

For orbits with very low Moon exposure (maximum Moon-to-Z angle >75° and thus no illumination of the telescope or FPA radiator), Moonshine was not included in the analysis. For the orbits in which Moonshine was included, it was only included for the region inside the inner photon shield.

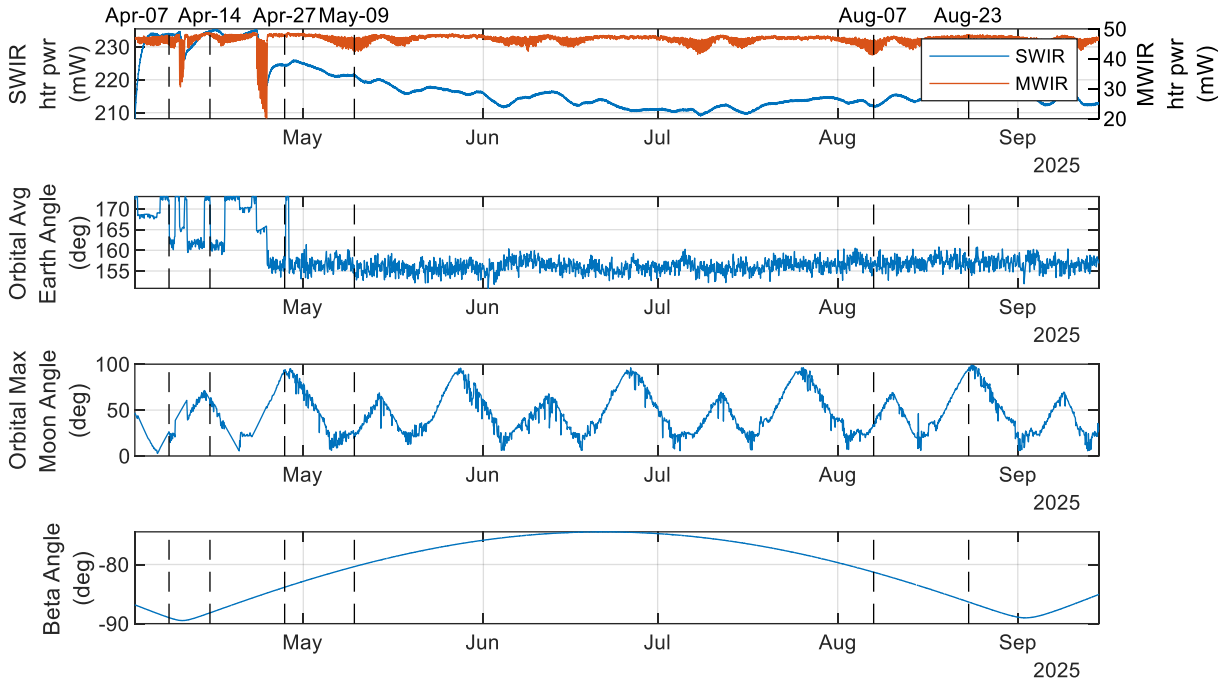

Figure 100 Balance points selected for model correlation and comparison

Table 24 Balance points selected for model correlation and comparison with descriptions and dates

Date	Description
4/7/2025 21:16	Beginning of mission, min slews, max moon exposure
4/14/2025 22:22	Beginning of mission, min slews, min moon exposure
4/27/2025 19:00	Beginning of mission, survey-like slews, min moon exposure *Reference orbit for correlation BOL
5/9/2025 18:45	Beginning of mission, survey slews, max moon exposure
8/7/2025 4:28	Latest in mission, survey slews, max moon exposure
8/23/2025 13:00	Latest in mission, survey slews, min moon exposure *Reference orbit for correlation some degradation

Given the very long timescales involved and the well-behaved FPA thermal control, there was no need for a precisely correlated transient model. Furthermore, because no two orbits are truly identical, it would be difficult to establish initial conditions for a transient comparison (the start and end points of any given orbit assessed would differ). Accomplishing this would require computing the environmental loads for many orbits in series to remove effective drift, which would drive the analysis time into weeks. Consequently, this was not performed post-launch.

4.3.2 In-flight steady state vs modelled

Before embarking on model correlation, it is important to establish the starting point. The closest orbit to that used for the pre-flight predictions is the 14 April 2025 balance point. The orbit used for the "Case 2" best-case beginning-of-life analysis closely matches this orbit. A comparison of the key temperatures between the uncorrelated pre-flight model and the actual in-flight measurements is shown in Table 25.

Although the absolute values of the control heat may initially appear large, they are in milliwatts and represent only the control heat applied in addition to the parasitic loads. The model estimated total load (including control heat) of the MWIR stage was ~106 mW and ~713 mW for the SWIR stage. This corresponds to percent errors of only 5.5 % for the MWIR and 3.9 % for the SWIR, an excellent starting point for correlation.

Table 25 Initial pre-launch to in-flight comparison of key steady state temperatures and heat loads

	Flight 4-14-25	Modelled case 2 BOL	Abs Difference	% difference
MWIR control heat (mW)	234.54	262.10	-27.56	-10.52%
SWIR control heat (mW)	48.32	42.50	5.82	13.69%
MWIR primary fine control T [K]	45.00	45.00	0.00	0.01%
MWIR radiator T [K]	44.66	44.72	-0.06	-0.14%
Telescope Baffle T [K]	60.30	60.01	0.30	0.49%
Telescope Housing T [K]	60.57	60.44	0.14	0.22%
SWIR primary fine control T [K]	62.00	61.99	0.01	0.02%
Inner photon shield top T [K]	88.29	90.78	-2.49	-2.74%
Inner photon shield bottom T [K]	92.89	93.10	-0.21	-0.23%
Inner V-groove 2 T [K]	93.14	93.37	-0.23	-0.25%
Inner V-groove 1 T [K]	93.22	93.62	-0.40	-0.43%
Middle photon shield top T [K]	127.24	129.17	-1.93	-1.50%
Middle photon shield bottom T [K]	147.94	143.25	4.69	3.27%
Middle V-groove 2 T [K]	147.38	142.75	4.63	3.24%
Middle V-groove 1 T [K]	148.42	144.30	4.12	2.86%
Outer photon shield top T [K]	209.09	201.24	7.85	3.90%
Outer photon shield bottom T [K]	292.66	297.90	-5.25	-1.76%
Outer V-groove 2 T [K]	250.07	241.16	8.90	3.69%
Outer V-groove 1 T [K]	275.23	275.92	-0.69	-0.25%

If the overestimate of the SWIR control power is conservatively applied as a "loss of margin" to the absolute worst-case end-of-life scenario (noting that on-orbit operations show the average orientation

is nowhere near the worst-case orbit and trending shows much less degradation and ice accumulation than budgeted), it results in an initial decrease of ~27.6 % margin (from 184.4 % down to 156.8 %), with another 44.5 % drop from the beginning of mission to the lowest control heat in the first six months. This still leaves a substantial 148 % margin at the time of publication, without harvesting the additional conservatism of assessing margin only against the telescope housing as the radiating surface and excluding the baffle.

For the MWIR detector, on-orbit results actually improved the margin since the predictions expected a 5.8 mW lower heater power at 45 K. This added 23 % margin, and accounting for a 23.9 % drop to the minimum on-orbit control power (occurring in maximum moonshine) leaves 192.1 % margin. All of this is assessed against the CBE loads from a pathological orbit with very conservative ice accumulation and outer-shield degradation. In reality, the orbit and degradation are closer to the more benign best-case BOL results, in which there was a predicted margin of 281.4 % for the MWIR and 301.1 % for the SWIR. Following the same application of the inaccuracy of the prediction and the measured on-orbit degradation leaves 280 % margin for the MWIR and 225 % margin for the SWIR.

It should be noted that these margins are against requirement temperatures of 55 K (MWIR) and 80 K (SWIR), not the nominal 45 K and 62 K detector setpoints.

4.3.3 Model improvements

Before solving for parameters with high inherent uncertainty, all previous modeling assumptions were systematically rechecked. Several obvious updates and omissions were identified, as described below. Many of these adjustments were discovered in the course of correlation, but are treated separately here because they were not uncertain values in themselves. Rather, they were parameters or representations that had either been excluded (intentionally or inadvertently). The correlation process focused on estimating values that could not be inferred directly from physics or ground testing, such as the effective emissivity of the photon shields after launch contamination, ice accumulation, or surface damage.

4.3.3.1 Photon Shield Conductivity

A detailed model had been generated early in the project to determine the effective conductivity of the honeycomb core. However, on orbit, the observed temperature gradients across the shields were much larger than expected. This discrepancy prompted an audit of the assumptions used in the honeycomb-core derivation. Two issues were identified:

- First, each ribbon layer comprising the honeycomb had been assumed welded to its neighbors, whereas in reality they were bonded.
- Second, the incorrect ratio of high-purity alloy had been used in the submodel to derive conductivity. The specification states 5% nominal and 4% minimum high-purity cladding thickness, but only 1% had been used in the earlier detailed honeycomb model—a human error caused by referencing emails rather than the actual specification.

In addition to correcting the composition issues in the submodel, internal radiation was included, and the model size was expanded both laterally and through the thickness. Instead of cutting at the plane of symmetry, the full through-thickness section was represented with both facesheets included. This was necessary to fully capture the internal radiative exchange.

Furthermore, the heat applied in the model to measure the “effective conductivity” was scaled with temperature to maintain a relatively constant temperature difference across the sample. Because there remained some uncertainty in the specification regarding the percentage of high-purity alloy, several percentages—4%, 5%, and 6% of the total thickness—were tested. The results are shown in Figure 101. Although a slight bump in conductivity appeared at lower temperatures due to the increased conductivity of high-purity aluminum, the effect was minor, and the nominal 5% value was deemed acceptable.

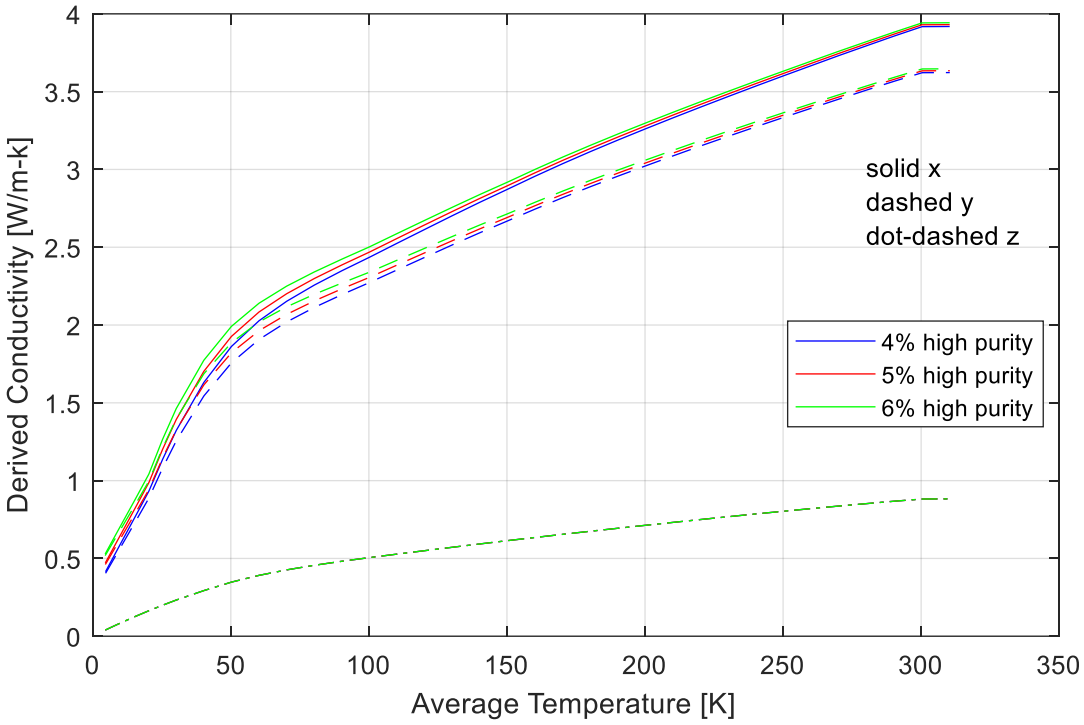

Figure 101 Updated Photon Shield honeycomb core modelled effective conductivity

Additionally, doublers had been added to reinforce the honeycomb layup in regions of higher stress. These consisted of 0.02-inch-thick sheets of the same alloy as the 0.008-inch-thick primary facesheet. They were incorporated into the thermal model as additional thickness in the regions specified by the photon-shield drawings.

4.3.3.2 Improved nodalization

As with the honeycomb-core analysis, nodalization sensitivities had been conducted early in the program. However, as the model evolved, these checks were not repeated because of model-size and solution-time limitations. Components such as the telescope already contained several thousand nodes, and increasing their density was not a simple option.

The key nodalization checks were therefore performed on components most likely to experience large thermal gradients. The telescope and FPA radiator themselves do not show large gradients, but the photon shields, telescope support struts, and FPA-radiator support struts do. The FPA internal supports

were not rechecked because a detailed FPA correlation test had already been conducted and the model had been adjusted with multipliers to account for any nodalization inaccuracies.

Two metrics were used to assess nodalization: (1) the FPA control-heater power required to hold the desired setpoints of 45 K (MWIR) and 62 K (SWIR) and (2) the relative temperature gradients across each component. A representative flight orbit with untuned optical properties was used, so absolute heater powers were interpreted only in a relative sense. For the strut nodalization, only the control-heater power was compared.

The assumption was that additional nodes would improve accuracy but at diminishing returns. Node density was therefore increased until the key metrics changed negligibly. Although no absolute cut-off was used, the target criteria were temperature changes of <0.1 K for cryogenic components and <0.5 K for room-temperature components, and heat-load changes of <0.25 mW for the MWIR loop and <1 mW for the SWIR loop. Some intrinsic uncertainty from the radiation/temperature solution (discussed in Section 3.6.2) was recognized. Temperature contours were also generated and are provided in Appendix H.

Results are summarized in the tables below.

Table 26 Outer Photon Shield nodalization comparison

Metrics\nodes	392 nodes (initial)	1566 nodes	2437 nodes
MWIR control heat (mW)	39.1	39.3	39.2
SWIR control heat (mW)	190.8	192.6	193.6
Outer Photon Shield base sensor (OPS_1) (K)	296.9	304.9	304.5
Outer Photon Shield top sensor (OPS_2) (K)	207.0	206.4	206.2

Table 27 Middle Photon Shield nodalization comparison

Metrics\nodes	336 nodes (initial)	486 nodes
MWIR control heat (mW)	39.2	38.7
SWIR control heat (mW)	192.6	191.0
Middle Photon Shield base sensor (MPS_1) (K)	148.9	150.0
Middle Photon Shield top sensor (MPS_2) (K)	132.1	132.3

Table 28 Inner Photon Shield nodalization comparison

Metrics\nodes	332 nodes (initial)	632 nodes
MWIR control heat (mW)	38.7	38.8
SWIR control heat (mW)	191.0	190.4
Inner Photon Shield base sensor (IPS_1) (K)	94.3	94.4
Inner Photon Shield top sensor (IPS_2) (K)	91.4	91.4

Table 29 Telescope support struts nodalization comparison

Metrics\nodes	316 nodes initial	652 nodes	1032 nodes
MWIR control heat (mW)	38.7	38.6	38.7
SWIR control heat (mW)	191.0	197.8	197.2

Table 30 FPA radiator support struts nodalization comparison

Metrics\nodes	184 nodes initial	238 nodes	274 nodes
MWIR control heat (mW)	38.7	39.4	39.5
SWIR control heat (mW)	197.8	197.2	196.8

Based on these results, the outer photon shield was increased to 1,566 nodes, the middle shield to 486 nodes, and the inner shield left at 332 nodes. For the support struts, node counts were doubled for both the telescope-support struts and the FPA-radiator struts to 652 and 238 nodes, respectively.

4.3.3.3 Additional adjustments

Several other refinements were implemented during the post-launch model review and correlation. These adjustments did not stem from parameter uncertainty per se but from conservative or outdated assumptions made during the pre-launch phase:

MWIR radiator bipods: In the aggregate material definition, the vacuum-deposited aluminum (VDA) layer had originally been modeled at a very conservative 1,000 Å (1×10^{-4} % of the cross section), whereas most VDA coatings range from roughly 30–500 Å. This thickness was reduced to 100 Å (1×10^{-5} % of the cross section). In addition, VDA Kapton can have a relatively low effective residual resistivity ratio (RRR) (R. G. Ross 2015). Therefore, the Kapton material property was changed from RRR = 100 to Al 6061 (typical RRR < 50). This adjustment alone represented a few milliwatts of power

on the MWIR stage, demonstrating the importance of correctly accounting for even seemingly minor effects.

Mass corrections: As discussed earlier, some component masses were never updated to the most accurate values before launch. These were corrected post-launch, although the impact on key analyses was small because most were steady-state assessments.

Outer V-grooves: A late-stage change order in manufacturing substituted aluminum alloy 6061 for the originally planned 7075. Because these two alloys have a significant difference in thermal conductivity, the model was updated accordingly.

FPA radiator: The emissivity of the FPA radiator was changed from a single grey value to an angularly dependent formulation. The normal emittance at 0° incidence was taken from theory as 0.99, a cosine shaped curve as tuned to achieve desired total hemispherical emittance of 0.95, resulting in 0.91 at 90° incidence. This approach can be further correlated in the future to account for knock-downs due to visible bolt heads, bent cells, or other geometric details.

4.3.4 Correlation

It is important to remember that, when correlating complex, multi-variable coupled models, there can be more than one solution that satisfies the available data. The correlation presented here is one such solution. It is based on reasonable assumptions and physically defensible adjustments, but another combination of parameter values could produce similar results. Nevertheless, the close agreement of the correlated model with flight data, together with the physical reasoning behind each adjustment, provides strong evidence that the solution adopted was appropriate for the goals of this mission.

The primary focus of the correlation was on the emissivities of the photon shields and V-grooves, which are both highly uncertain and have a large impact on the cryogenic stages. Several other components with high uncertainty were also adjusted:

Cables: The stainless-steel cross-section measured during harness testing had not been applied in the pre-launch model (retained for conservatism) and was finally updated for correlation. The effective

radial conductance of the harnesses remained an uncertain quantity. Because the cables are modeled as 2-D surfaces, some finite radial “insulator” must be specified; otherwise there would be an unrealistic coupling to external radiative surfaces. The initial value was simply the cable radius, but this also implicitly represents contact between internal conductors, packing tightness, and tie-downs (parameters that can vary widely). These were treated as free parameters within reasonable bounds, since the outer-surface view to space was poorly characterized in ground tests and their combined effect was never fully isolated.

Bus adjustments: The spacecraft bus model is managed by BAe, but the payload thermal model needed to represent the significant conductive and radiative coupling between the outer photon shield/V-grooves and the solar array and top deck. Because proprietary details of the spacecraft internals were unavailable and BAe resources could not be allocated to refine the model, broad adjustments were made based on available telemetry and photographs; for example, tweaking key conductances, surface-finish knockdowns, and solar array active area. These coarse adjustments inevitably reduced the accuracy of deeper bus internals, but the objective was simply to bring the bus interfaces with the payload into agreement with measured values. An unexplained gradient across the bus interface remained that could not be corrected with reasonable parameter changes, indicating internal features that require future re-evaluation. This discrepancy slightly influenced outer V-groove temperatures but kept average values within acceptable limits.

Final emissivity correlation: The free parameters adjusted were the inner and outer emissivities of each photon shield and V-groove, as well as the top-edge emissivity. A multiplier factor was also applied to the telescope emissivity because numerous assumptions and estimates had been made for coverage knockdowns due to bonded-on hardware, unpainted areas, and cabling. In an ideal workflow, these parameters would be treated as design variables in an optimization routine to converge model and measured data automatically. However, after a forced Windows 11 upgrade, the Dynamic SINDA analysis routine could no longer run long enough to complete a solution without interruption. Dynamic SINDA was also needed for temperature- and wavelength-dependent radiation calculations, which likewise could

not be finalized. Fortunately, after the model accuracy improvements and updated environmental loads described earlier, the starting point was already close to flight data, and manual tuning sufficed to achieve a satisfactory match.

Table 31 thru Table 36 compare the final correlated model to the flight data for each of the selected balance points. The correlated model does not yet include any degradation effects (addressed in the following section), so some divergence later in the mission is expected. The top outer-shield sensor (OPS-2) is highly susceptible to environmental loads and can vary by as much as 3 K between a single-orbit and a five-orbit average. Consequently, any discrepancy between this sensor and the steady-state model output reflects orbital variability rather than a model deficiency.

The reference flight data also may not represent a true steady state. Ie the loads on the cryogenic stages are very small compared with the telescope's overall heat capacity, it can take weeks for a given orientation/orbit combination to reach full equilibrium, something that never occurs during normal operations. Care was taken when selecting the balance points to minimize this effect, but it cannot be completely avoided.

Overall, the agreement between the correlated model and the flight data is very good. Across all mission cases (including end-of-life cases so far), the percentage difference of the MWIR and SWIR control heat remains consistently below 10 %, and below 5 % for many cases. As discussed earlier, this discrepancy represents a much smaller fraction of the total load into each stage. The temperatures (excluding the outer shield) are within 2 % error, with only one outlier of 2.9 % on the inner photon-shield temperature in one of the beginning-of-mission, maximum-moon-exposure cases. These maximum-moon-exposure regions are particularly difficult to claim as steady state because the large and variable slews required to compensate for moon avoidance on the telescope boresight drive non-steady thermal behavior. The other parameter that was not explored is the photon shield inner region surface absorptivity, particularly on the tops of photon shields. This may affect the susceptibility to changing orbits and orientations.

Table 31 Comparison in-flight to correlated model: 7-Apr-2025 21:16 – Beginning of mission, min slews, max moon exposure

	Flight	Modelled no degrade	Abs Difference	% Difference
SWIR control heat (mW)	233.82	220.18	-13.64	-5.8%
MWIR control heat (mW)	46.43	44.83	-1.61	-3.5%
MWIR primary fine control T [K]	45.00	45.00	0.00	0.0%
MWIR radiator T [K]	44.67	44.72	0.05	0.1%
Telescope Baffle T [K]	60.31	60.25	-0.06	-0.1%
Telescope Housing 1 T [K]	60.58	60.69	0.11	0.2%
SWIR primary fine control T [K]	62.00	62.00	0.00	0.0%
Inner photon shield top T [K]	88.13	87.10	-1.03	-1.2%
Inner photon shield bottom T [K]	92.72	91.31	-1.41	-1.5%
Inner V-groove 2 T [K]	92.96	91.49	-1.47	-1.6%
Inner V-groove 1 T [K]	93.04	91.70	-1.34	-1.4%
Middle photon shield top T [K]	127.06	127.07	0.02	0.0%
Middle photon shield bottom T [K]	147.72	148.10	0.37	0.3%
Middle V-groove 2 T [K]	147.18	147.39	0.21	0.1%
Middle V-groove 1 T [K]	148.21	148.59	0.38	0.3%
Outer photon shield top T [K]	209.39	204.61	-4.78	-2.3%
Outer photon shield bottom T [K]	292.47	293.92	1.44	0.5%
Outer V-groove 2 T [K]	250.05	250.04	0.00	0.0%
Outer V-groove 1 T [K]	275.09	276.75	1.65	0.6%

Table 32 Comparison in-flight to correlated model: 14-Apr-2025 22:22 – Beginning of mission, min slews, min moon exposure

	Flight	Modelled no degrade	Abs Difference	% Difference
SWIR control heat (mW)	234.54	222.22	-12.32	-5.3%
MWIR control heat (mW)	48.32	47.31	-1.01	-2.1%
MWIR primary fine control T [K]	45.00	45.00	0.00	0.0%
MWIR radiator T [K]	44.66	44.71	0.05	0.1%
Telescope Baffle T [K]	60.30	60.23	-0.07	-0.1%
Telescope Housing 1 T [K]	60.57	60.68	0.10	0.2%
SWIR primary fine control T [K]	62.00	62.00	0.00	0.0%
Inner photon shield top T [K]	88.29	87.11	-1.18	-1.3%
Inner photon shield bottom T [K]	92.89	91.34	-1.56	-1.7%
Inner V-groove 2 T [K]	93.14	91.51	-1.63	-1.7%
Inner V-groove 1 T [K]	93.22	91.73	-1.49	-1.6%
Middle photon shield top T [K]	127.24	127.24	0.01	0.0%
Middle photon shield bottom T [K]	147.94	148.21	0.27	0.2%
Middle V-groove 2 T [K]	147.38	147.52	0.14	0.1%
Middle V-groove 1 T [K]	148.42	148.72	0.30	0.2%
Outer photon shield top T [K]	209.09	206.32	-2.78	-1.3%
Outer photon shield bottom T [K]	292.66	293.63	0.97	0.3%
Outer V-groove 2 T [K]	250.07	250.46	0.39	0.2%
Outer V-groove 1 T [K]	275.23	276.77	1.54	0.6%

Table 33 Comparison in-flight to correlated model: 27-Apr-2025 19:00 -Beginning of mission, survey-like slews, min moon exposure *Reference orbit for correlation BOL

	Flight	Modelled no degrade	Abs Difference	% Difference
SWIR control heat (mW)	224.47	223.06	-1.41	-0.6%
MWIR control heat (mW)	47.88	47.05	-0.83	-1.7%
MWIR primary fine control T [K]	45.00	45.00	0.00	0.0%
MWIR radiator T [K]	44.66	44.71	0.05	0.1%
Telescope Baffle T [K]	60.35	60.24	-0.12	-0.2%
Telescope Housing 1 T [K]	60.62	60.68	0.06	0.1%
SWIR primary fine control T [K]	62.00	62.00	0.00	0.0%
Inner photon shield top T [K]	90.13	90.24	0.11	0.1%
Inner photon shield bottom T [K]	94.03	93.70	-0.34	-0.4%
Inner V-groove 2 T [K]	94.28	93.87	-0.41	-0.4%
Inner V-groove 1 T [K]	94.34	94.06	-0.29	-0.3%
Middle photon shield top T [K]	128.39	127.99	-0.40	-0.3%
Middle photon shield bottom T [K]	148.32	148.18	-0.14	-0.1%
Middle V-groove 2 T [K]	147.86	147.60	-0.26	-0.2%
Middle V-groove 1 T [K]	148.75	148.66	-0.10	-0.1%
Outer photon shield top T [K]	206.39	200.12	-6.27	-3.0%
Outer photon shield bottom T [K]	288.91	289.21	0.29	0.1%
Outer V-groove 2 T [K]	249.61	248.90	-0.71	-0.3%
Outer V-groove 1 T [K]	272.76	273.52	0.77	0.3%

Table 34 Comparison in-flight to correlated model: 09-May-2025 18:45 – Beginning of mission, survey slews, max moon exposure

	Flight	Modelled no degrade	Abs Difference	% Difference
SWIR control heat (mW)	221.41	205.02	-16.39	-7.4%
MWIR control heat (mW)	45.18	42.82	-2.36	-5.2%
MWIR primary fine control T [K]	45.00	45.00	0.00	0.0%
MWIR radiator T [K]	44.67	44.72	0.05	0.1%
Telescope Baffle T [K]	60.37	60.34	-0.04	-0.1%
Telescope Housing 1 T [K]	60.64	60.77	0.13	0.2%
SWIR primary fine control T [K]	62.00	62.00	0.00	0.0%
Inner photon shield top T [K]	89.79	92.39	2.60	2.9%
Inner photon shield bottom T [K]	93.79	95.16	1.37	1.5%
Inner V-groove 2 T [K]	94.04	95.36	1.32	1.4%
Inner V-groove 1 T [K]	94.11	95.52	1.41	1.5%
Middle photon shield top T [K]	128.35	129.57	1.22	1.0%
Middle photon shield bottom T [K]	148.45	148.81	0.36	0.2%
Middle V-groove 2 T [K]	147.96	148.33	0.37	0.2%
Middle V-groove 1 T [K]	148.87	149.28	0.41	0.3%
Outer photon shield top T [K]	206.83	206.33	-0.50	-0.2%
Outer photon shield bottom T [K]	289.50	289.43	-0.07	0.0%
Outer V-groove 2 T [K]	249.78	250.58	0.80	0.3%
Outer V-groove 1 T [K]	273.14	273.86	0.71	0.3%

Table 35 Comparison in-flight to correlated model: 07-Aug-2025 04:28 – Latest in mission, survey slews, max moon exposure
*Reference orbit for correlation some degradation

	Flight	Modelled no degrade	Abs Difference	% Difference
SWIR control heat (mW)	212.09	215.79	3.70	1.7%
MWIR control heat (mW)	43.94	43.27	-0.68	-1.5%
MWIR primary fine control T [K]	45.00	45.00	0.00	0.0%
MWIR radiator T [K]	44.67	44.72	0.05	0.1%
Telescope Baffle T [K]	60.42	60.28	-0.14	-0.2%
Telescope Housing 1 T [K]	60.68	60.72	0.03	0.1%
SWIR primary fine control T [K]	62.00	62.00	0.00	0.0%
Inner photon shield top T [K]	90.50	90.56	0.06	0.1%
Inner photon shield bottom T [K]	94.55	93.72	-0.83	-0.9%
Inner V-groove 2 T [K]	94.80	93.92	-0.88	-0.9%
Inner V-groove 1 T [K]	94.87	94.09	-0.77	-0.8%
Middle photon shield top T [K]	129.20	128.77	-0.43	-0.3%
Middle photon shield bottom T [K]	149.97	148.28	-1.69	-1.1%
Middle V-groove 2 T [K]	149.31	147.80	-1.51	-1.0%
Middle V-groove 1 T [K]	150.33	148.76	-1.57	-1.0%
Outer photon shield top T [K]	206.70	206.47	-0.24	-0.1%
Outer photon shield bottom T [K]	291.53	288.30	-3.23	-1.1%
Outer V-groove 2 T [K]	250.65	250.18	-0.47	-0.2%
Outer V-groove 1 T [K]	274.74	273.15	-1.59	-0.6%

Table 36 Comparison in-flight to correlated model: 23-Aug-2025 13:00 – Latest in mission, survey slews, min moon exposure

	Flight	Modelled no degrade	Abs Difference	% Difference
SWIR control heat (mW)	217.39	228.52	11.13	5.1%
MWIR control heat (mW)	47.66	47.51	-0.16	-0.3%
MWIR primary fine control T [K]	45.00	45.00	0.00	0.0%
MWIR radiator T [K]	44.66	44.71	0.05	0.1%
Telescope Baffle T [K]	60.39	60.21	-0.18	-0.3%
Telescope Housing 1 T [K]	60.66	60.65	-0.01	0.0%
SWIR primary fine control T [K]	62.00	62.00	0.00	0.0%
Inner photon shield top T [K]	90.18	89.43	-0.75	-0.8%
Inner photon shield bottom T [K]	94.37	92.96	-1.41	-1.5%
Inner V-groove 2 T [K]	94.62	93.14	-1.48	-1.6%
Inner V-groove 1 T [K]	94.69	93.33	-1.36	-1.4%
Middle photon shield top T [K]	129.18	127.87	-1.31	-1.0%
Middle photon shield bottom T [K]	150.27	148.00	-2.27	-1.5%
Middle V-groove 2 T [K]	149.56	147.45	-2.11	-1.4%
Middle V-groove 1 T [K]	150.61	148.46	-2.15	-1.4%
Outer photon shield top T [K]	205.84	201.33	-4.51	-2.2%
Outer photon shield bottom T [K]	292.18	288.69	-3.50	-1.2%
Outer V-groove 2 T [K]	250.56	249.09	-1.47	-0.6%
Outer V-groove 1 T [K]	275.06	272.99	-2.07	-0.8%

4.3.5 Derivation of degradation zones from correlated model

After the initial beginning-of-life (BOL) correlation, the model was re-correlated at a later point in the mission (23 August 2025) with minimal moonshine in order to provide a clean comparison to the BOL balance point used for correlation (27 April 2025, 19:00). This later point is not referred to as “end of life” (EOL), since SPHEREx continues to operate on orbit with many months of survey remaining. In this re-correlation, only the surfaces with expected degradation—the outer surface of the middle shield and the sun-facing outer shield—were modified. Based on the LDEF results and the accumulated Equivalent Sun Hours (ESH) to date, the ram side of the outer shield is not expected to show an appreciable increase in absorptivity, whereas the anti-ram side is expected to exhibit an increase of approximately 0.12. The 100 Å layer of ice predicted to accumulate on the inner surface of the inner shield corresponds to effectively no measurable increase in emissivity, and the very conservative ice assumption of 0.2um accumulation was not applied initially.

Table 37 compares the prediction for the 23 August 2025 and 27 April 2025, 19:00 balance points with no degradation, the pre-launch degradation assumptions (which is only due to increase in outer shield absorptivity), and the correlated degraded emissivity at the same point. Given the very small variations in heat load and temperature, the key metric is the difference between the BOL and post-degradation conditions. A further “difference-of-differences” comparison between the flight deltas and the modelled deltas is provided as a measure of the model’s relative accuracy. The outer-shield absorptivity was not adjusted beyond the 0.12 increase discussed above, as the average temperatures of the lower outer-shield and V-groove sensors already matched the model closely.

The key surface optical properties that produce these results are summarized in Table 38. These include: (i) the “theoretical best” derived from the scaled Drude model based on the surface temperature and hot-side balance temperature; (ii) the pre-launch observatory TVAC-correlated values; (iii) the flight BOL-correlated values; and (iv) the flight post-degradation-correlated values. During correlation, the inner photon-shield surface was divided into upper and lower regions to capture local effects; however,

both regions ultimately used the same value of emissivity. The results indicate that some amount of ice or contamination was present during the observatory TVAC testing on which the pre-launch values were based, and that comparable accumulations occurred on orbit primarily during the cooldown phase, as expected. During the survey, no additional accumulation has been evident, and some surfaces have even shown reductions in emissivity, suggesting that ice sublimation is occurring faster than accumulation. This behavior is consistent with expectations that most contamination occurs initially, followed by a very slow reduction over the mission. No evidence has been observed of MMOD damage increasing emissivity on the inner surfaces of the inner photon shield.

Although this solution may not be unique, the strong physical rationale for the degradation pattern lends it credibility. During the correlation process, several other combinations of emissivity increases on different surfaces were tested; however, each alternative produced imbalances in other key parameters, such as temperature gradients or the distribution of heat-load inaccuracies, making them less plausible than the adopted solution.

Table 37 Comparison of key temperature and heat load differences BOL to later in mission, no degradation, pre-launch degradation, and correlated degradation

	Flight BOL	Flight 6mo		Model BOL ref	Model 6 mo no degradation			Model 6 mo predicted degradation			Model 6 mo correlated degradation		
	'27-Apr-2025 19:00'	23-Aug-2025 13:00'	diff BOL - EOL	'27-Apr-2025 19:00'	23-Aug-2025 13:00'	diff BOL - 6mo	diff of diff	23-Aug-2025 13:00'	diff BOL - 6mo	diff of diff	23-Aug-2025 13:00'	diff BOL - 6mo	diff of diff
SWIR control heat (mW)	224.47	217.39	-7.08	223.06	228.52	5.46	12.54	220.36	-2.70	4.39	219.21	-3.85	3.23
MWIR control heat (mW)	47.88	47.66	-0.21	47.05	47.51	0.46	0.67	47.27	0.22	0.43	47.05	0.00	0.21
MWIR primary fine control T [K]	45.00	45.00	0.00	45.00	45.00	0.00	0.00	45.00	0.00	0.00	45.00	0.00	0.00
MWIR radiator T [K]	44.66	44.66	0.00	44.71	44.71	0.00	0.00	44.71	0.00	0.00	44.71	0.00	0.00
Telescope Housing 1 T [K]	60.62	60.66	0.03	60.68	60.65	-0.03	-0.06	60.69	0.01	-0.02	60.70	0.02	-0.01
SWIR primary fine control T [K]	62.00	62.00	0.00	62.00	62.00	0.00	0.00	62.00	0.00	0.00	62.00	0.00	0.00
Inner photon shield top T [K]	90.13	90.18	0.06	90.24	89.43	-0.81	-0.86	90.12	-0.11	-0.17	90.44	0.20	0.14
Inner photon shield bottom T [K]	94.03	94.37	0.34	93.70	92.96	-0.74	-1.08	93.77	0.08	-0.26	93.97	0.28	-0.06
Inner Vgroove 2 T [K]	94.28	94.62	0.34	93.87	93.14	-0.73	-1.07	93.96	0.09	-0.25	94.15	0.28	-0.06
Inner Vgroove 1 T [K]	94.34	94.69	0.35	94.06	93.33	-0.73	-1.08	94.15	0.10	-0.25	94.34	0.28	-0.06
Middle photon shield top T [K]	128.39	129.18	0.79	127.99	127.87	-0.12	-0.91	129.26	1.27	0.48	129.04	1.05	0.26
Middle photon shield bottom T [K]	148.32	150.27	1.95	148.18	148.00	-0.17	-2.13	150.54	2.37	0.41	150.03	1.85	-0.10
Middle Vgroove 2 T [K]	147.86	149.56	1.70	147.60	147.45	-0.15	-1.85	149.72	2.12	0.42	149.18	1.58	-0.12
Middle Vgroove 1 T [K]	148.75	150.61	1.86	148.66	148.46	-0.20	-2.06	150.80	2.14	0.28	150.26	1.60	-0.26
Outer photon shield top T [K]	206.39	205.84	-0.55	200.12	201.33	1.22	1.76	201.30	1.18	1.73	201.31	1.19	1.74
Outer photon shield bottom T [K]	288.91	292.18	3.27	289.21	288.69	-0.52	-3.79	292.87	3.66	0.40	292.88	3.67	0.40
Outer Vgroove 2 T [K]	249.61	250.56	0.95	248.90	249.09	0.19	-0.76	249.76	0.86	-0.09	249.78	0.88	-0.07
Outer Vgroove 1 T [K]	272.76	275.06	2.31	273.52	272.99	-0.53	-2.84	274.44	0.92	-1.38	274.46	0.93	-1.37

Table 38 Comparison of key optical properties to later in mission, no degradation, and correlated degradation. Highlighted are values that changed

	Theory surf temp	Theory hot side balance	Pre-launch	BOL correlation	Degraded
MWIR FPA radiator	0.974	0.982	0.953	0.99@90o 0.91@0o 0.95 hemi	0.99@90o 0.91@0o 0.95 hemi
telescope baffle main	0.842	0.861	0.821	0.821	0.821
telescope baffle clamshell edges	0.842	0.861	0.766	0.766	0.766
telescope MWIR housing	0.842	0.861	0.805	0.805	0.805
telescope SWIR housing	0.842	0.861	0.797	0.797	0.797
telescope housing main	0.842	0.861	0.841	0.841	0.841
telescope side panel edges	0.842	0.861	0.726	0.726	0.726
Inner Photon Shield inner surface top	0.007	0.007	0.011	0.005	0.005
Inner Photon Shield inner surface bottom	0.007	0.007	0.011	0.005	0.005
Inner Photon Shield outer surface	0.007	0.010	0.017	0.023	0.020
Inner V-groove inner surface	0.016	0.016	0.014	0.016	0.016
Inner V-groove outer surface	0.007	0.010	0.032	0.040	0.036
Middle Photon Shield inner surface	0.010	0.010	0.025	0.012	0.012
Middle Photon Shield outer surface	0.010	0.016	0.046	0.038	0.038
Middle V-groove inner surface	0.020	0.020	0.014	0.020	0.020
Middle V-groove outer surface	0.010	0.016	0.051	0.040	0.035
Outer Photon Shield inner surface	0.027	0.027	0.027	0.025	0.025
Outer V-groove inner surface	0.027	0.027	0.035	0.033	0.033
Outer V-groove outer surface (MLI)	0.030	0.030	0.055	0.040	0.04

Surface-degradation values are shown in Table 39. By applying the ice-thickness-to-emissivity model to the relative changes in emissivity, an estimated ice-layer thickness can be inferred. The emissivity changes and corresponding “ice thickness” are also shown relative to the theoretical “worst-case” hot-side balance. This comparison indicates either that the theoretical emissivity was underestimated or that ice accumulated during cooldown for both TVAC and flight cooldown, the latter being far more likely. The apparent “negative” ice accumulation between the theoretical emissivity and the correlated BOL values reflects conservative assumptions used in the Drude model rather than true sublimation losses; this conservatism is advantageous for mission planning.

Table 39 Apparent ice accumulation derived from emissivity changes of photon shield and V-groove surfaces

	change in e from hot side theory	inferred ice accumulation during cooldown (um)	change in e	inferred ice accumulation from start of survey (um)
Inner Photon Shield inner surface top	-0.002	-0.08	0.000	0.000
Inner Photon Shield inner surface bottom	-0.002	-0.08	0.000	0.000
Inner Photon Shield outer surface	0.013	0.39	-0.003	-0.092
Inner V-groove inner surface	0.000	-0.02	0.000	0.000
Inner V-groove outer surface	0.030	0.96	-0.004	-0.119
Middle Photon Shield inner surface	0.002	0.07	0.000	0.000
Middle Photon Shield outer surface	0.022	0.68	0.000	0.000
Middle V-groove inner surface	0.000	0.02	0.000	0.000
Middle V-groove outer surface	0.024	0.75	-0.005	-0.146
Outer Photon Shield inner surface	-0.002	-0.07	0.000	0.000
Outer V-groove inner surface	0.006	0.16	0.000	0.000
Outer V-groove outer surface (MLI)	0.010	0.29	0.000	0.000

Long-term trending now shows little additional degradation, indicating that the water-ice source is essentially depleted and that the outer-shield absorptivity increase has reached equilibrium with atomic-oxygen scrubbing. For the remainder of the mission, the available thermal-control authority may actually improve, depending on seasonal conditions and survey-plan orientations.

5 Conclusions and work to go

SPHEREx is, to public knowledge, currently the coldest passively cooled instrument operating in low-Earth orbit. As of this writing, the observatory is six months into its 26-month survey of the cosmos. Its thermal performance has exceeded expectations and continues to operate without issue, while accommodating survey pointings beyond those originally planned. The thermal model not only predicted on-orbit performance with high accuracy but was further refined using flight data to inform future operations.

From a thermal-engineering perspective, the most important successes of SPHEREx are the lessons learned and the tools developed to inform future very-low-temperature cryogenic missions. This project has expanded the envelope of what is considered feasible to achieve entirely passively in low-

Earth orbit. Some lessons are “wish-list” items for tests that should have been conducted; others are things that were done correctly. The top points are:

1. **Conduct the most accurate ground and thermal-balance testing possible.**

   This is a given but bears repeating. SPHEREx never had an opportunity to perform a full thermal-balance test to near operating temperature. Even the tests that were conducted suffered from limited accuracy, instrumentation, and understanding of the chamber itself. Careful setup and checkout of the facility can remove many of these uncertainties.

2. **Prioritize subcomponent testing.**

   SPHEREx did this fairly well with, for example, the composite-conductance test and the paint-emissivity test. But during correlation, when trying to understand photon-shield gradients, the effective conductance still came into question—illustrating the value of more extensive subcomponent testing.

3. **Neglect nothing without a reason.**

   In passive cryogenic systems, every single detail needs a physical justification for inclusion or omission—be it a hand calculation, a detailed physical model, or a test. Often, measured data in the specific range or material needed is sparse and budgets are tight for direct measurement, but sound physics and traceable assumptions are indispensable.

4. **Understand sensitivities to everything.**

   While it is important to understand “worst-worst” cases for requirements compliance, there are often times when another subsystem or the science could benefit greatly from a very slight change. Understanding environmental bounds and keeping estimates up-to-date enables faster, better system-level decisions.

5. **Model the entire system as one.**

   Aerospace projects tend to draw strict interface boundaries between systems. Some level of partitioning is inevitable, but cryogenic systems are especially sensitive to cross-coupling. For example, knowing how the bus gradient leads to the outer V-groove gradient, which leads to the

middle shield gradient, is critical. Even if a full-fidelity model is not built on both sides of an interface, the engineer must understand the simplifications and the variability of key values.

6. **Minimize the size of the core modeling team.**

   With more intellectual interfaces, details get missed. Today's computational tools and automation (including AI) allow fewer engineers to model larger, more complex systems. This does introduce single-point-failure risk, but that can be mitigated by thorough documentation (such as this thesis) and periodic independent deep-dive reviews by experts familiar with the tools.

With respect to the objectives laid out in the original dissertation plan, the only objective not completed was the execution of full temperature-dependent radiation calculations. This was prevented by issues with tool interaction under Windows 11 and institutional antivirus software—an opportunity still open to further hone the understanding of ice formation and to run a temperature-dependent cooldown.

And the mission is not yet done. Moving forward, flight data will continue to be monitored for unexpected behavior and trended against the tools described in this thesis. Long-term degradation is far less than the worst-case pre-launch predictions and appears to have stabilized, but evidence of continued degradation will be monitored and recorded for future missions.

Ad astra per aspera.

6 References

Ade, Peter A. R., Nabila Aghanim, Monique Arnaud, Mark Ashdown, J. Aumont, C. Baccigalupi, M. Baker, et al. 2011. "Planck early results. II. The thermal performance of Planck." *Astronomy & Astrophysics* (EDP sciences) 536: A2.

Alred, John M., Bradley D. Moore, Sara Susca, Konstantin I. Penanen, Valentina Ricchiuti, Jennifer M. Rocca, and Carlos E. Soares. 2021. "Designing a Decontamination Solution for the Low-Earth-Orbit, Cryogenic SPHEREx Mission." *2021 IEEE Aerospace Conference (50100).* 1–8.

Alred, John M., Bradley D. Moore, Sara Susca, Valentina Ricchiuti, Jennifer M. Rocca, and Carlos E. Soares. 2024. "Modeling contaminant outgassing and free molecular transport processes for the cryogenic SPHEREx observatory." *AIP Conference Proceedings.*

Alred, John M., Maxwell G. Martin, William A. Hoey, Phil Korngut, Jennifer M. Rocca, and Carlos E. Soares. 2022. "Particle contamination launch redistribution and effects on the low-earth-orbit infrared SPHEREx telescope." *Space Systems Contamination: Prediction, Control, and Performance 2022.* 261–271.

Alred, John W., and Carlos Soares. 2001. "Solar absorptivity as a function of spacecraft external contamination." *INTERNATIONAL SAMPE TECHNICAL CONFERENCE.* 1581–1584.

2017. "AMS-QQ-A-250/5: Aluminum Alloy Alclad Sheet and Plate." *AMS-QQ-A-250/5: Aluminum Alloy Alclad Sheet and Plate.* https://www.sae.org/standards/content/amsqqa250/5c/.

Ansys. 2025. "Thermal Desktop User's Manual." https://www.crtech.com/guides-and-manuals.

Arenberg, J., J. Flynn, A. Cohen, R. Lynch, and J. Cooper. 2016. "Status of the JWST sunshield and spacecraft." *Space Telescopes and Instrumentation 2016: Optical, Infrared, and Millimeter Wave* (SPIE) 9904: 20–33.

Auguié, Baptiste. 2017. "Fresnel formulae." *Fresnel formulae.* March. https://nano-optics.ac.nz/planar/articles/fresnel.html.

Bard, Steven. 1984. "Advanced passive radiator for spaceborne cryogenic cooling." *Journal of Spacecraft and Rockets* 21: 150–155.

Bell, Doug, Tim Panczak, and Dan Green. 2014. "Non-Grey and Temperature Dependent Radiation Analysis Methods." *Thermal and Fluids Analysis Workshop (TFAWS) 2014, Short Course.* NASA.

Bhandari, Pradeep, Bradley Moore, Douglas Bolton, and Asad Aboobaker. 2020. "Design and Analysis of V-Groove Passive Cryogenic Radiators for Spaceborne Telescopes & Instruments."

Boggess, Nancy W., John C. Mather, R. Weiss, Charles L. Bennett, ESe al Cheng, E. Dwek, S. Gulkis, et al. 1992. "The COBE mission-Its design and performance two years after launch." *Astrophysical Journal, Part 1 (ISSN 0004-637X), vol. 397, no. 2, p. 420-429.* 397: 420–429.

Bradley, Peter E., Ray Radebaugh, and others. 2013. "Properties of selected materials at cryogenic temperatures." *NIST Publ* 680.

Cao, Changyong, Frank J. De Luccia, Xiaoxiong Xiong, Robert Wolfe, and Fuzhong Weng. 2013. "Early on-orbit performance of the visible infrared imaging radiometer suite onboard the Suomi National Polar-Orbiting Partnership (S-NPP) satellite." *IEEE Transactions on Geoscience and Remote Sensing* (IEEE) 52: 1142–1156.

Chang. 2002. "Molecular contamination effects on the thermal emittance of highly reflective surfaces at cryogenic temperatures." *Proc. SPIE 4774.*

Chen, W., I. McKinley, and B. Moore. 2024. "Selection Considerations Between Active Cryocoolers and Passive Radiative Coolers for Space Instrument Applications."

Clawson, James F. unpublished. "D-8160 Thermal Environments." Tech. rep., Jet Propulsion Laboratory (JPL).

Collaudin, B., and N. Rando. 2000. "Cryogenics in space: a review of the missions and of the technologies." *Cryogenics* (Elsevier) 40: 797–819.

Crill, Brendan P., Michael Werner, Rachel Akeson, Matthew Ashby, Lindsey Bleem, James J. Bock, Sean Bryan, et al. 2020. "SPHEREx: NASA's near-infrared spectrophotometric all-sky survey." *Space Telescopes and Instrumentation 2020: Optical, Infrared, and Millimeter Wave.* 61–77.

DiPirro, Michael, J. Tuttle, Edgar R. Canavan, and Peter John Shirron. 2012. "Use of cold radiometers in several thermal/vacuum tests." *AIP Conference Proceedings.* 1513–1518.

Donabedian, Martin. 2002. *Spacecraft thermal control handbook, volume I: Fundamental Technologies.* American Institute of Aeronautics and Astronautics, Inc.

—. 2004. *Spacecraft thermal control handbook, volume II: cryogenics.* American Institute of Aeronautics and Astronautics, Inc.

ESA. 2024. *Planck.* Accessed October 20, 2024. https://sci.esa.int/web/planck/ .

Fellini, Ryan A., and Yury L. Kropp. 2008. "James Webb space telescope sunshield: Challenges in analysis of gossamer structures." *Technology Review Journal* 16: 17–44.

Frolec, Jiří, Tomáš Králík, Věra Musilová, Pavel Hanzelka, Aleš Srnka, and Josef Jelínek. 2019. "A database of metallic materials emissivities and absorptivities for cryogenics." *Cryogenics* (Elsevier) 97: 85–99.

Gilberd, P W. 1982. "The anomalous skin effect and the optical properties of metals." *J. Phys. F: Met. Phys.* 12: 1845-60.

Glazer, Stuart D., Kimberly D. Brown, Theodore J. Michalek, and Walter C. Ancarrow. 2003. "WMAP observatory thermal design and on-orbit thermal performance." *SAE transactions* (JSTOR) 92–102.

Golden, J. L. 1992. "Results of Examination of the A276 White and Z306 Black Thermal Control Paint Discs Flown on LDEF." Edited by Arlene S. Levine. *LDEF — 69 Months in Space: First Post-Retrieval Symposium.* 975–987.

Grundy, W. M., and B. Schmitt. 1998. "The temperature-dependent near-infrared absorption spectrum of hexagonal H_2O ice." *Journal of Geophysical Research: Planets* 103: 25809–25822. doi:10.1029/98JE00738.

Howell, John R., M. Pinar Mengüç, Kyle Daun, and Robert Siegel. 2020. *Thermal radiation heat transfer.* CRC press.

Hulett, R., and C. Zierman. 1970. "Staged radiator design for low temperature spacecraft applications." *5th Thermophysics Conference.* 854.

Hust, J. 1984. *Thermal Conductivity of glass fiber-epoxy support bands.* NBSIR 84-3003, NIST.

Jahnke, Knud. 2024. "Euclid successfully de-iced, gains 15% sensitivity." *Euclid successfully de-iced, gains 15% sensitivity.* March. https://www.euclid-ec.org/euclid-successfully-de-iced-gains-15-sensitivity/.

JPL/Caltech. n.d. *AIRS: Atmospheric Infrared Sounder.* Accessed October 20, 2024. https://airs.jpl.nasa.gov/mission/airs-project-instrument-suite/airs/thermal-system/.

—. 2024. *SPHEREx.* Accessed 10 20, 2024. https://spherex.caltech.edu/.

Kato, Seiji, Norman G. Loeb, Fred G. Rose, David R. Doelling, David A. Rutan, T. E. Caldwell, Lin Yu, and Robert A. Weller. 2025. "CERES EBAF Edition 4.2: Surface and Top-of-Atmosphere Flux Data." *CERES EBAF Edition 4.2: Surface and Top-of-Atmosphere Flux Data.* June. https://ceres.larc.nasa.gov/data/.

Kauder, Lonny. 2005. "Spacecraft Thermal Control Coatings References." NASA Technical Publication, National Aeronautics and Space Administration (NASA), Washington, D.C. https://ntrs.nasa.gov/citations/20070014757.

Klein, S.A. 2022. *EES.* September 22. https://fchartsoftware.com/.

Korngut, Phillip M., James J. Bock, Rachel Akeson, Matthew Ashby, Lindsey Bleem, Justin Boland, Douglas Bolton, et al. 2018. "SPHEREx: an all-sky NIR spectral survey." *Space Telescopes and Instrumentation 2018: Optical, Infrared, and Millimeter Wave.* 576–586.

Krause, Keith Stuart, Stuart F. Biggar, Kurtis J. Thome, Jim Eagen, and Dave Kenyon. 2002. "On-orbit radiometric calibration using a solar diffuser." *Earth Observing Systems VI.* 135–145.

Kulkarni, MR, and R Brady. 1997. "A model of global thermal conductivity in laminated carbon/carbon composites." *Composites Science and Technology* 277-285.

L3Harris. 2020. Accessed October 20, 2024. https://www.l3harris.com/sites/default/files/2020-11/l3harris-cris-sell-sheet-sas.pdf.

Mainzer, Amy, J. Bauer, R. M. Cutri, T. Grav, J. Masiero, R. Beck, P. Clarkson, et al. 2014. "Initial performance of the NEOWISE reactivation mission." *The Astrophysical Journal* (IOP Publishing) 792: 30.

Mangan, T. P., J. M. C. Plane, and B. J. Murray. 2021. "The phase of water ice which forms in cold clouds in the mesospheres of Mars, Venus, and Earth." *Journal of Geophysical Research: Planets* (Wiley Online Library) 126: e2020JE006796.

Mastrapa, R. M., S. A. Sandford, T. L. Roush, D. P. Cruikshank, and C. M. Dalle Ore. 2009. "Optical constants of amorphous and crystalline H2O-ice: 2.5–22 μm (4000–455 cm- 1) optical constants of H2O-ice." *The Astrophysical Journal* (IOP Publishing) 701: 1347.

Modest, Michael F, and Mazumder Sandip. 2021. *Radiative heat transfer.* Academic press.

Modest, Michael F., and Sandip Mazumder. 2021. *Radiative heat transfer.* Academic press.

Morgante, G. I. A. N. L. U. C. A., Luca Terenzi, L. Desjonqueres, P. Eccleston, G. Bishop, A. Caldwell, M. Crook, et al. 2022. "The thermal architecture of the ESA ARIEL payload at the end of phase B1." *Experimental Astronomy* (Springer) 53: 905–944.

Murad, Edmond. 1998. "The shuttle glow phenomenon." *Annual review of physical chemistry* (Annual Reviews 4139 El Camino Way, PO Box 10139, Palo Alto, CA 94303-0139, USA) 49: 73–98.

Pilbratt, G. L., J. R. Riedinger, T. Passvogel, G. Crone, D. Doyle, U. Gageur, A. M. Heras, et al. 2010. "Herschel Space Observatory-An ESA facility for far-infrared and submillimetre astronomy." *Astronomy & Astrophysics* (EDP Sciences) 518: L1.

Regan, Michael W., and Louis E. Bergeron. 2020. "Zero dark current in H2RG detectors: it is all multiplexer glow." *Journal of Astronomical Telescopes, Instruments, and Systems* (Society of Photo-Optical Instrumentation Engineers) 6: 016001–016001.

Ross Jr, Ronald G. 2004. "Estimation of thermal conduction loads for structural supports of cryogenic spacecraft assemblies." *Cryogenics* (Elsevier) 44: 421–424.

Ross Jr, Ronald G. 2016. "Refrigeration systems for achieving cryogenic temperatures." In *Low temperature materials and mechanisms*, 127–200. CRC Press.

Ross, R. G. 2015. "Estimation of In-Space Emittance (IR absorptance) Increase of MIRI Refrigerant Lines over Time." *Unpublished Work.*

Ross, Ronald. 2007. "Aerospace Coolers: A 50-Year Quest for Long-Life Cryogenic Cooling in Space." In *Cryogenic Engineering: Fifty Years of Progress*, by Klaus Timmerhaus and Richard Reed, 225-284. New York: Springer.

Schirmer, M., K. Thürmer, B. Bras, M. Cropper, J. Martin-Fleitas, Y. Goueffon, R. Kohley, et al. 2023. "Euclid preparation: XXIX. Water ice in spacecraft Part I: The physics of ice formation and contamination." *Astronomy & Astrophysics* (EDP Sciences) 675: A142. doi:10.1051/0004-6361/202346635.

Schmitt, Bernard, Philippe Bollard, Damien Albert, and Lydie Bonal. 2012. "SSHADE/GhoSST: “Grenoble astropHysics and planetOlogy Solid Spectroscopy and Thermodynamics” database." *SSHADE/GhoSST: “Grenoble astropHysics and planetOlogy Solid Spectroscopy and Thermodynamics” database.* doi:10.26302/SSHADE/GHOSST.

Sparrow, E. M., L. U. Albers, and E. R. G. Eckert. 1962. "Thermal radiation characteristics of cylindrical enclosures."

Stephens, G. L., G. G. Campbell, and T.H. Vonder Haar. 1981. "Earth radiation budgets." *Journal of Geophysical Research: Oceans* (Wiley Online Library) 86: 9739–9760.

Trotta, F. 1996. "Détermination des constantes optiques de glaces dans l'IR moyen et lointain – Application aux grains du milieu interstellaire et des enveloppes circumstellaires." Ph.D. thesis, Université Joseph Fourier, Grenoble, France, 220.

Tuttle, J, E Canavan, and A Jahromi. 2017. "Cryogenic thermal conductivity measurements on candidate materials for space missions." *Cryogenics 88* 36-43.

Tuttle, J, E Canavan, M DiPirro, Li X, and P Knollenberg. 2014. "The total hemispheric emissivity of painted aluminum honeycomb at cryogenic temperatures." *Advances in Cryogenic Engineering AIP Conf. Proc. 1573.* 590-596.

Viehmann, Walter, and Alfred G. Eubanks. 1971. *Effects of surface contamination on the Infrared emissivity and visible-light scattering of highly reflective surfaces at cryogenic temperatures.* National Aeronautics and Space Administration.

Volz, S. M., and M. J. DiPirro. 1992. "Anomalous on-orbit behaviour of the NASA Cosmic Background Explorer (COBE) Dewar." *Cryogenics* (Elsevier) 32: 77–84.

Warren, Stephen G., and Richard E. Brandt. 2008. "Optical constants of ice from the ultraviolet to the microwave: A revised compilation." *Journal of Geophysical Research: Atmospheres* (Wiley Online Library) 113.

Whitaker, A, and J Gregory. 1992. "LDEF Materials Results for Spacecraft Applications." *NASA Conference Publication 3251.* Huntsville: University of Alabama in Huntsville.

Wikipedia contributors. 2025. "Drude model." *Drude model.*

Appendix A: List and locations of sensors and heaters

Sensor Name	Measure Temp Range	Vendor	Type	P/N	Required Accuracy [K]	Required Stability over mission [K]
TS_MW_RAD_SCI	30K-330K	Lakeshore	Cernox	CX-1080-CU	+/-0.5	+/-0.02
TS_MW_IF_P_ENG	30K-330K	Rosemount	PRT	0118MM2000A EACAB	30K-140K +/- 5K 140K-210K +/- 2.5K 210K-330K +/- 5K	+/-0.1
TS_MW_IF_R_ENG	30K-330K	Rosemount	PRT	0118MM2000A EACAB	30K-140K +/- 5K 140K-210K +/- 2.5K 210K-330K +/- 5K	+/-0.1
TS_MW_CRS_P_SCI	30K-330K	Lakeshore	Cernox	CX-1080-CU	+/-0.5	+/-0.02
TS_MW_CRS_R_SCI	30K-330K	Lakeshore	Cernox	CX-1080-CU	+/-0.5	+/-0.02
TS_MW_FINE_P_SCI	30K-330K	Lakeshore	Cernox	CX-1080-CU	+/-0.5	+/-0.02
TS_MW_FINE_R_SCI	30K-330K	Lakeshore	Cernox	CX-1080-CU	+/-0.5	+/-0.02
TS_SW_IF_ENG	30K-330K	Rosemount	PRT	0118MM2000A EACAB	30K-140K +/- 5K 140K-210K +/- 2.5K 210K-330K +/- 5K	+/-0.1
TS_SW_CRS_P_SCI	30K-330K	Lakeshore	Cernox	CX-1080-CU	+/-0.5	+/-0.02
TS_SW_CRS_R_SCI	30K-330K	Lakeshore	Cernox	CX-1080-CU	+/-0.5	+/-0.02
TS_SW_FINE_P_SCI	30K-330K	Lakeshore	Cernox	CX-1080-CU	+/-0.5	+/-0.02
TS_SW_FINE_R_SCI	30K-330K	Lakeshore	Cernox	CX-1080-CU	+/-0.5	+/-0.02
TS_BS_ENG	30K-330K	Rosemount	PRT	0118MM2000A EACAB	30K-140K +/- 5K 140K-210K +/- 2.5K 210K-330K +/- 5K	+/-0.1
TS_BS_SCI	30K-330K	Lakeshore	Cernox	CX-1080-CU	+/-0.5	+/-0.02
TS_PM_ENG	30K-330K	Rosemount	PRT	0118MM2000A EACAB	30K-140K +/- 5K 140K-210K +/- 2.5K 210K-330K +/- 5K	+/-0.1
TS_PM_SCI	30K-330K	Lakeshore	Cernox	CX-1080-CU	+/-0.5	+/-0.02
TS_SM_ENG	30K-330K	Rosemount	PRT	0118MM2000A EACAB	30K-140K +/- 5K 140K-210K +/- 2.5K 210K-330K +/- 5K	+/-0.1
TS_SM_SCI	30K-330K	Lakeshore	Cernox	CX-1080-CU	+/-0.5	+/-0.02
TS_TM_ENG	30K-330K	Rosemount	PRT	0118MM2000A EACAB	30K-140K +/- 5K 140K-210K +/- 2.5K 210K-330K +/- 5K	+/-0.1
TS_TM_SCI	30K-330K	Lakeshore	Cernox	CX-1080-CU	+/-0.5	+/-0.02
TS_TEL_HS_1_ENG	30K-330K	Rosemount	PRT	0118MM2000A EACAB	30K-140K +/- 5K 140K-210K +/- 2.5K 210K-330K +/- 5K	+/-0.1
TS_TEL_HS_2_ENG	30K-330K	Rosemount	PRT	0118MM2000A EACAB	30K-140K +/- 5K 140K-210K +/- 2.5K 210K-330K +/- 5K	+/-0.1
TS_TEL_HS_3_ENG	30K-330K	Rosemount	PRT	0118MM2000A EACAB	30K-140K +/- 5K 140K-210K +/- 2.5K 210K-330K +/- 5K	+/-0.1
TS_TEL_HS_4_ENG	30K-330K	Rosemount	PRT	0118MM2000A EACAB	30K-140K +/- 5K 140K-210K +/- 2.5K	+/-0.1

Sensor Name	Measure Temp Range	Vendor	Type	P/N	Required Accuracy [K]	Required Stability over mission [K]
					210K-330K +/- 5K	
TS_TEL_HS_1_SCI	30K-330K	Lakeshore	Cernox	CX-1080-CU	+/-0.5	+/-0.02
TS_TEL_HS_2_SCI	30K-330K	Lakeshore	Cernox	CX-1080-CU	+/-0.5	+/-0.02
TS_TEL_HS_3_SCI	30K-330K	Lakeshore	Cernox	CX-1080-CU	+/-0.5	+/-0.02
TS_TEL_BAF_1_ENG	30K-330K	Rosemount	PRT	0118MM2000AEACAB	30K-140K +/- 5K 140K-210K +/- 2.5K 210K-330K +/- 5K	+/-0.1
TS_TEL_BAF_2_ENG	30K-330K	Rosemount	PRT	0118MM2000AEACAB	30K-140K +/- 5K 140K-210K +/- 2.5K 210K-330K +/- 5K	+/-0.1
TS_TEL_BAF_SCI	30K-330K	Lakeshore	Cernox	CX-1080-CU	+/-0.5	+/-0.02
TS_IVG_ENG	30K-330K	Rosemount	PRT	0118MM2000AEACAB	30K-140K +/- 5K 140K-210K +/- 2.5K 210K-330K +/- 5K	+/-0.02
TS_IVG_1_SCI	30K-330K	Lakeshore	Cernox	CX-1080-CU	+/-0.5	+/-0.02
TS_IVG_2_SCI	30K-330K	Lakeshore	Cernox	CX-1080-CU	+/-0.5	+/-0.02
TS_IPS_1_SCI	30K-330K	Lakeshore	Cernox	CX-1080-CU	+/-0.5	+/-0.02
TS_IPS_2_SCI	30K-330K	Lakeshore	Cernox	CX-1080-CU	+/-0.5	+/-0.02
TS_MVG_1_SCI	80K-330K	Lakeshore	Cernox	CX-1080-CU	+/-0.5	+/-0.02
TS_MVG_2_SCI	80K-330K	Lakeshore	Cernox	CX-1080-CU	+/-0.5	+/-0.02
TS_MPS_1_SCI	80K-330K	Lakeshore	Cernox	CX-1080-CU	+/-0.5	+/-0.02
TS_MPS_2_SCI	80K-330K	Lakeshore	Cernox	CX-1080-CU	+/-0.5	+/-0.02
TS_OVG_1_SCI	200K-330K	Lakeshore	Cernox	CX-1080-CU-HT	+/-0.5	+/-0.02
TS_OVG_2_SCI	200K-330K	Lakeshore	Cernox	CX-1080-CU-HT	+/-0.5	+/-0.02
TS_OPS_1_SCI	200K-330K	Lakeshore	Cernox	CX-1080-CU-HT	+/-0.5	+/-0.02
TS_OPS_2_SCI	200K-330K	Lakeshore	Cernox	CX-1080-CU-HT	+/-0.5	+/-0.02

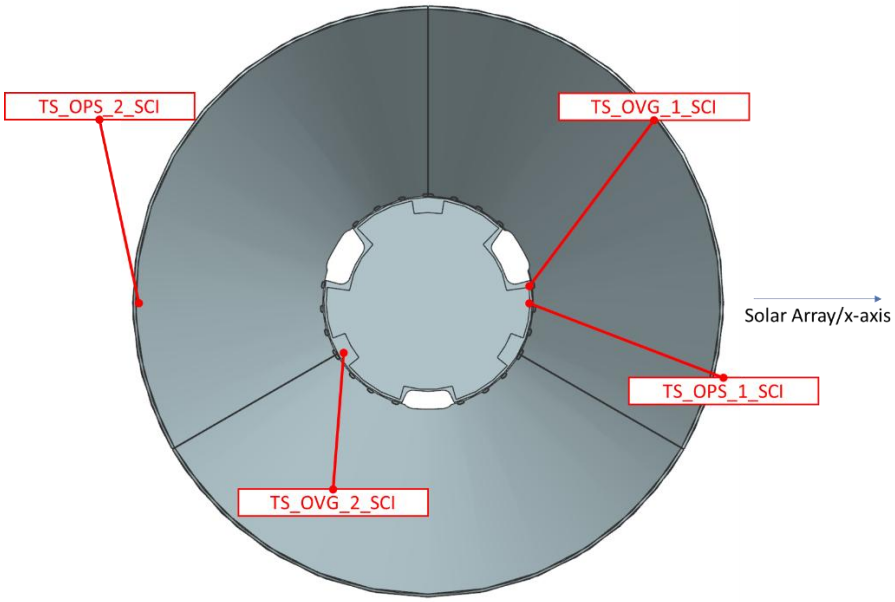

Figure 102 Outer photon shield temperature sensors

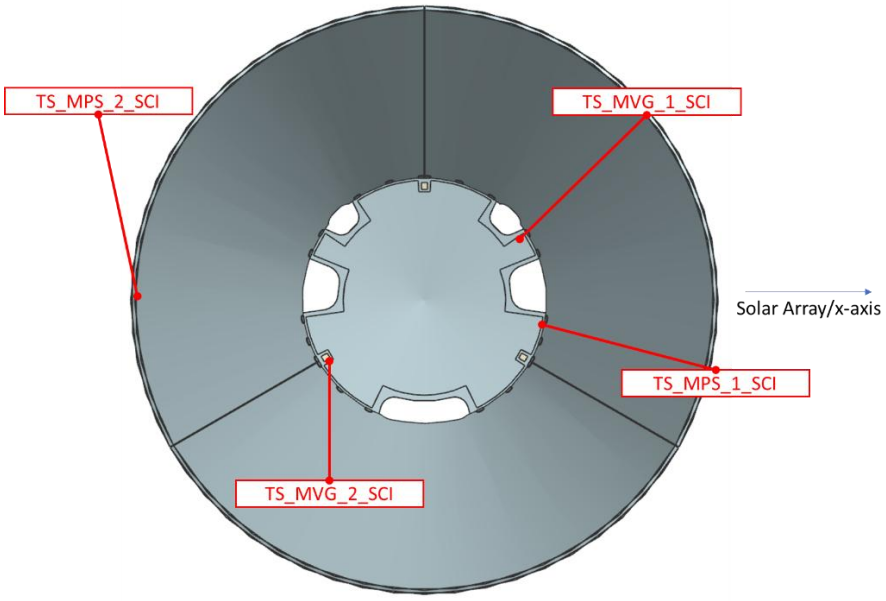

Figure 103 Middle photon shield temperature sensors

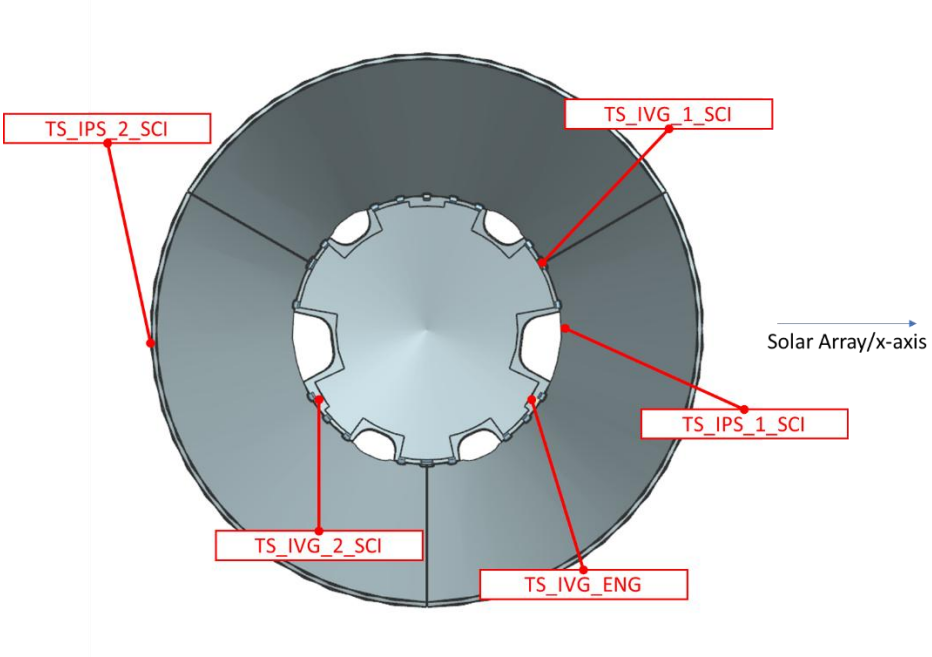

Figure 104 Inner photon shield temperature sensors

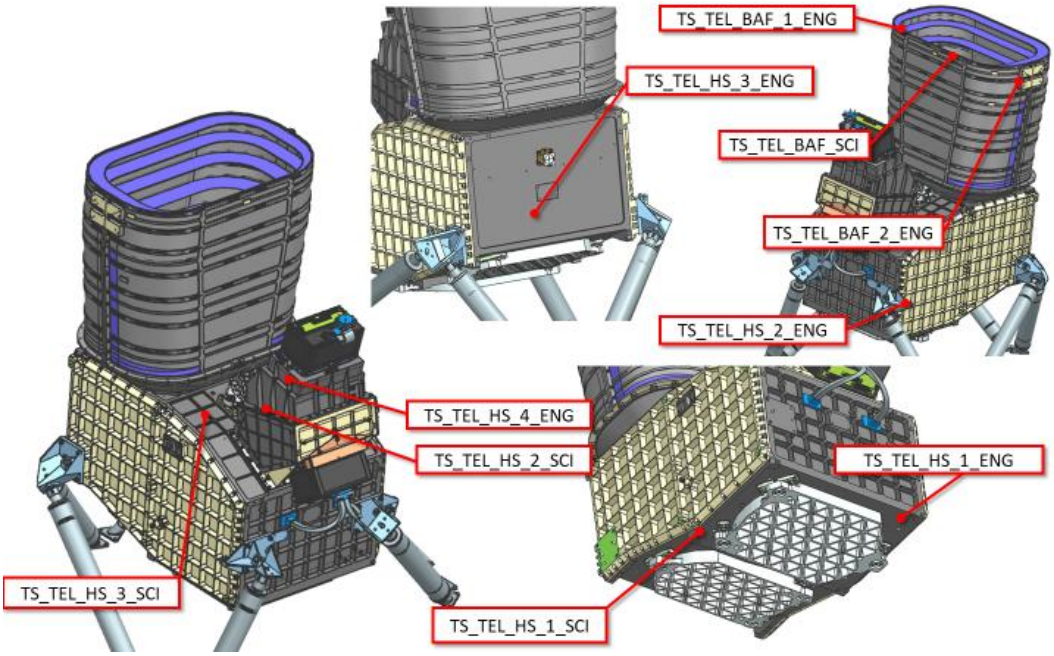

Figure 105 Housing and Baffle T-Sensors and Heaters

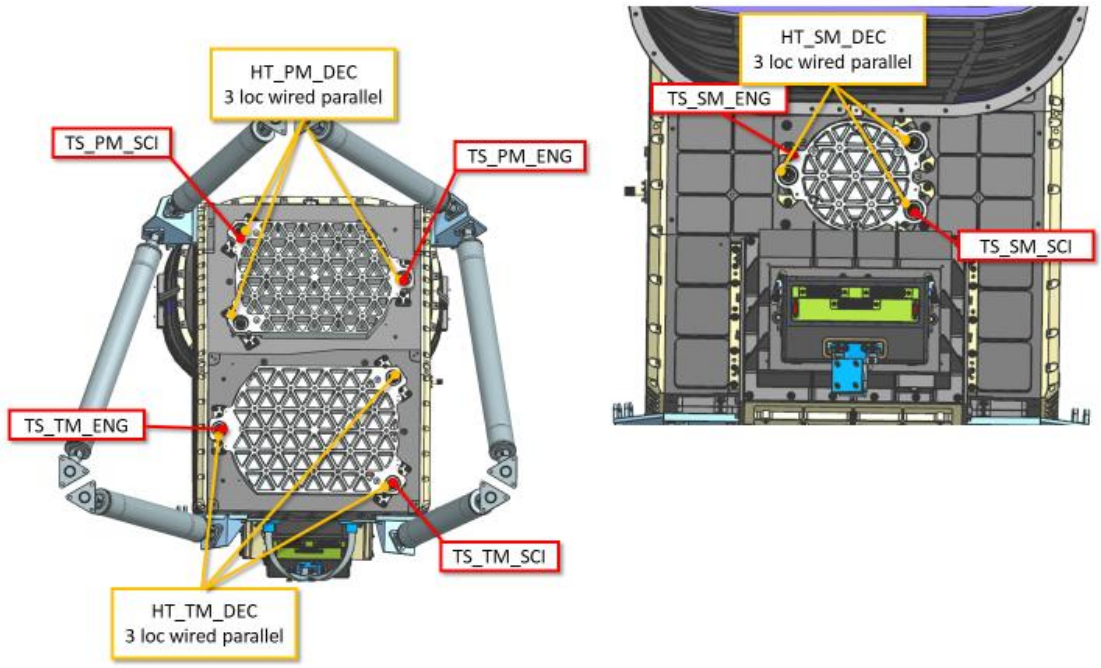

Figure 106 Housing and Baffle T-Sensors and Heaters

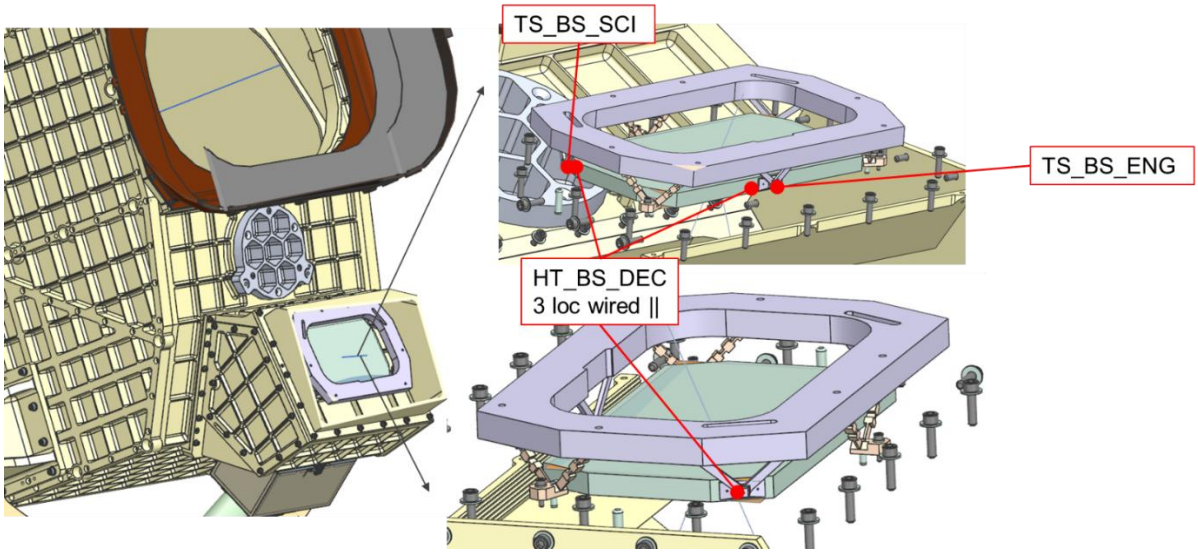

Figure 107 Beam Splitter Heater and T-Sensors

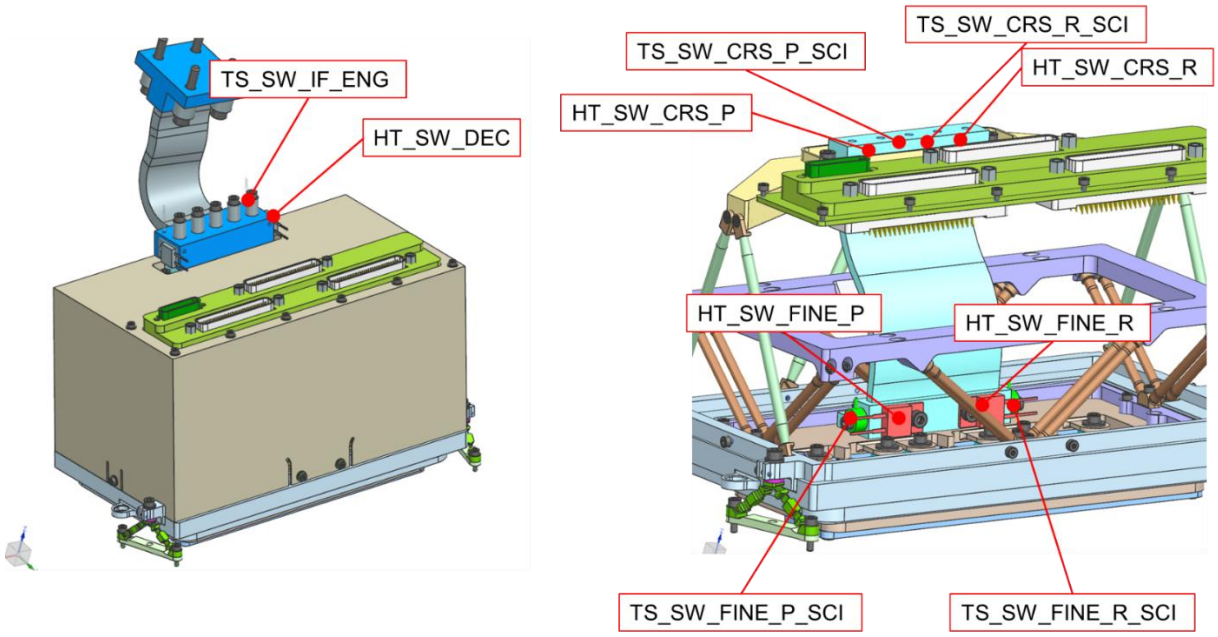

Figure 108 SWIR FPA Heaters and T-Sensors (note, the CAD is out of date, but the locations are approximately the same)

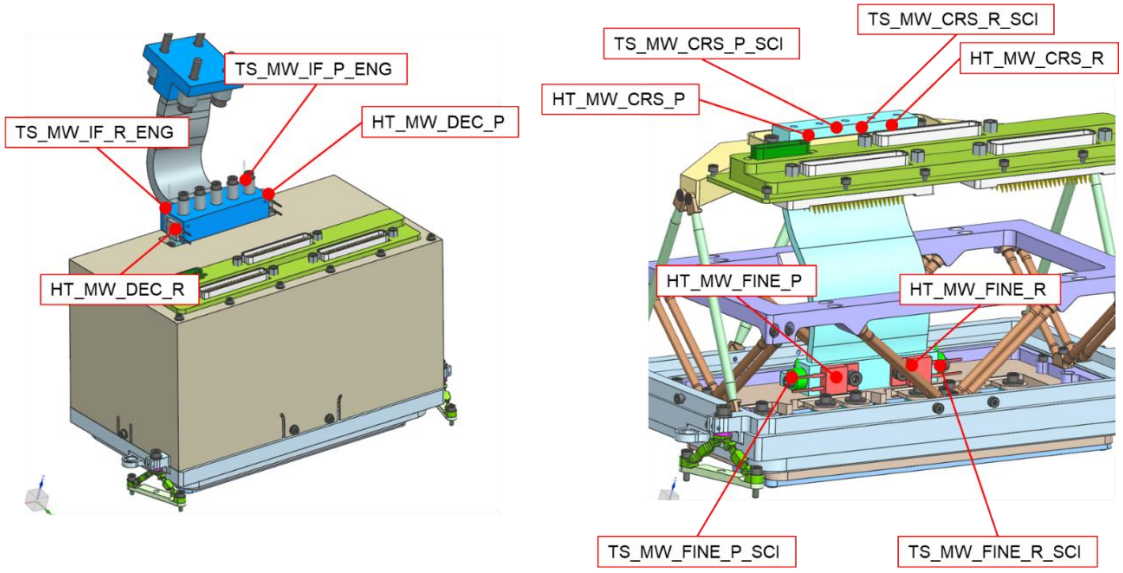

Figure 109 MWIR FPA Heaters and T-Sensors (note, the CAD is out of date, but the locations are approximately the same)

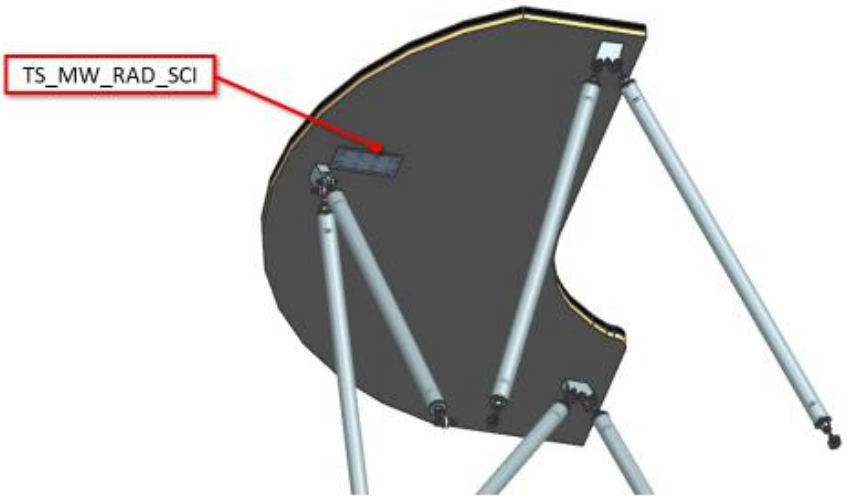

Figure 110 FPA Radiator temperature sensor

Appendix B: Kicker Runs

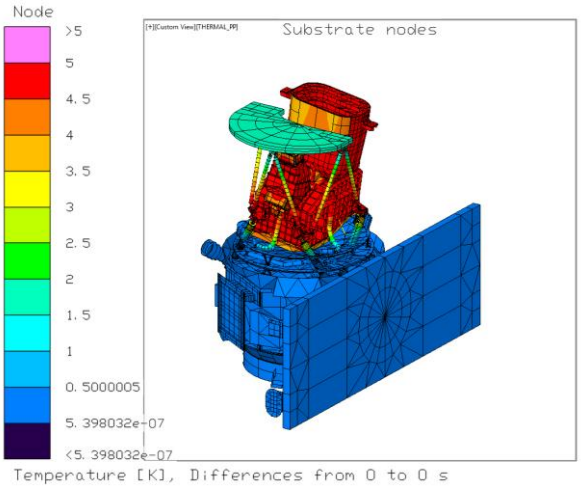

Figure 111 MWIR FPA interface - Kicker

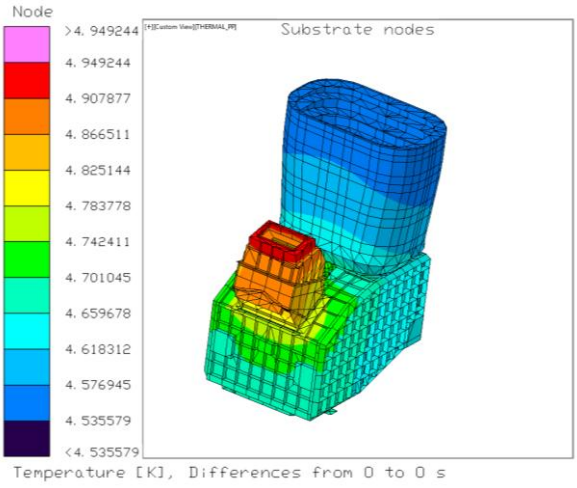

Figure 112 MWIR FPA interface zoom in - Kicker

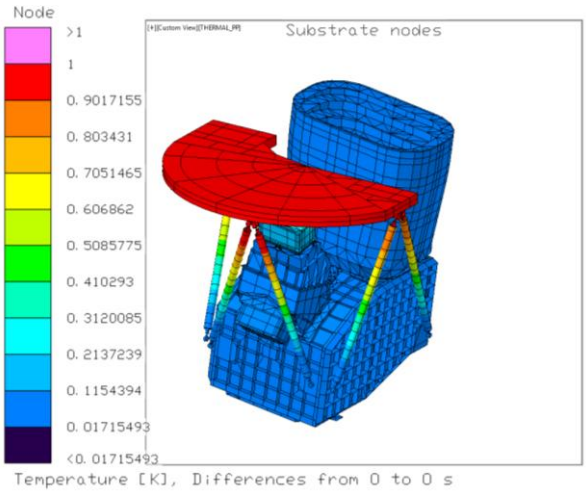

Figure 113 MWIR radiator - Kicker

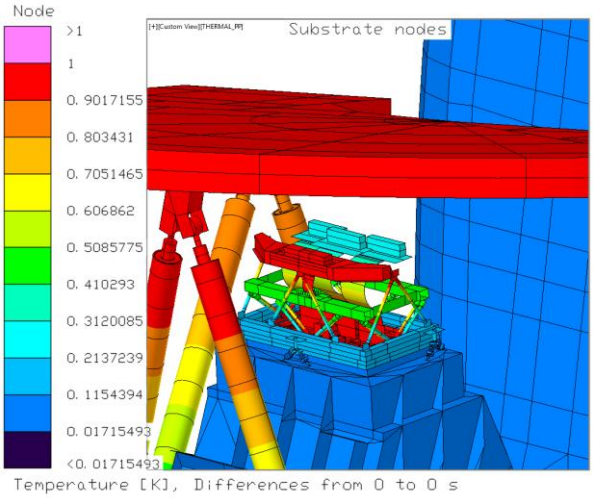

Figure 114 MWIR radiator zoom, enclosure removed - Kicker

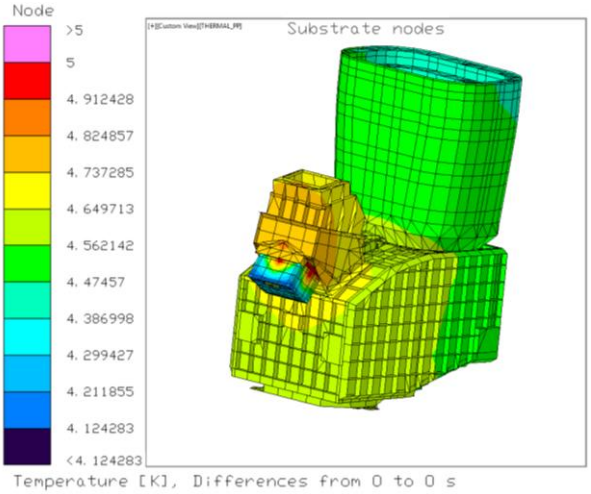

Figure 115 SWIR detector - Kicker

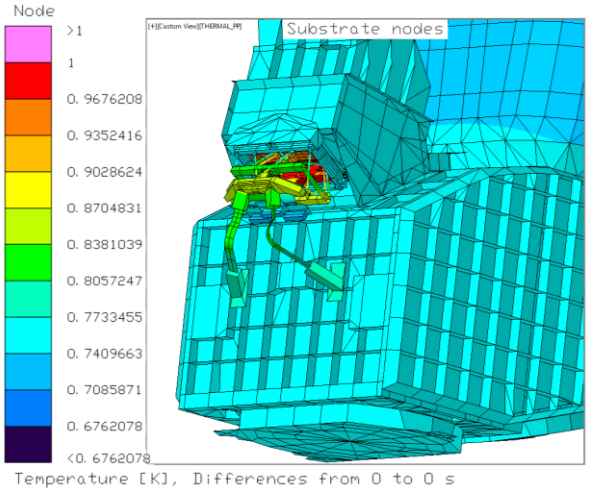

Figure 116 SWIR detector zoom, enclosure removed - Kicker

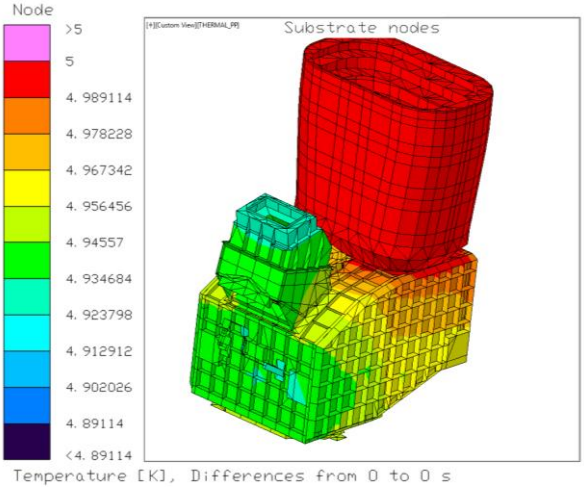

Figure 117 Telescope Baffle - Kicker

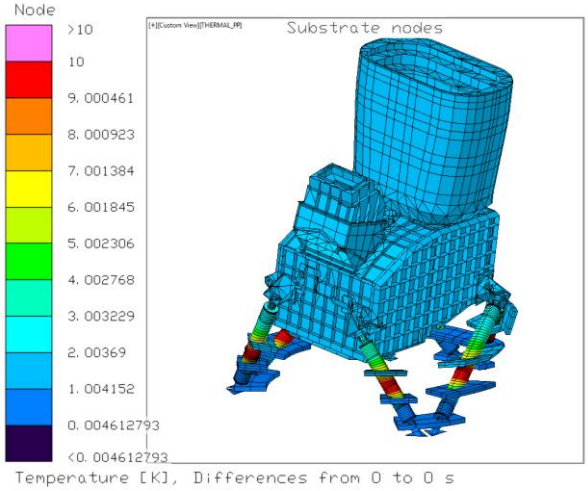

Figure 118 Telescope strut midspan - Kicker

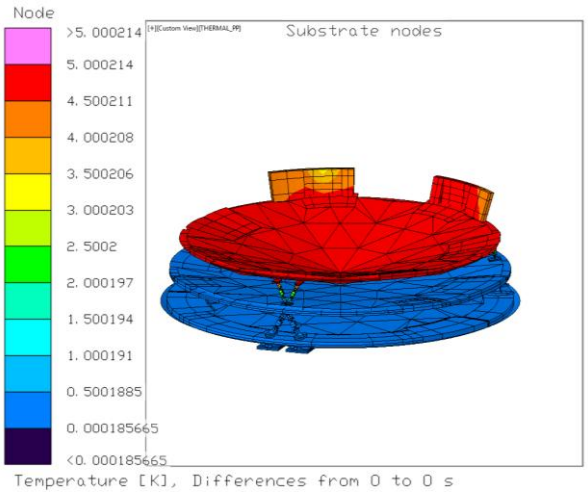

Figure 119 Inner V-groove - Kicker

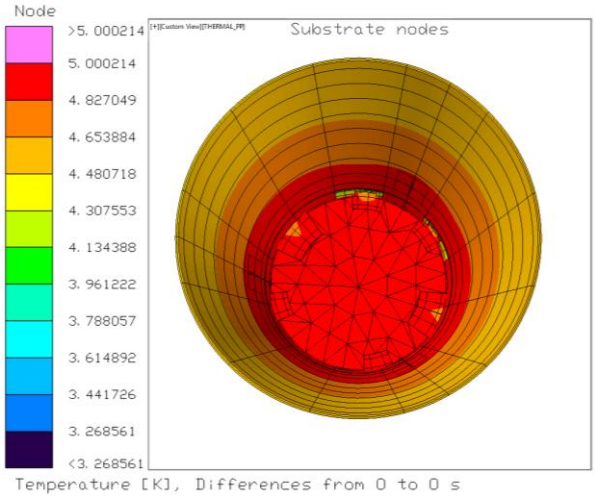

Figure 120 Inner V-groove with photon shield - Kicker

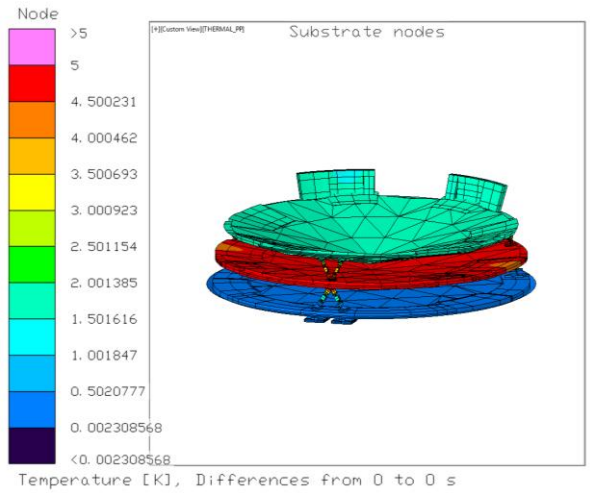

Figure 121 Middle V-groove - Kicker

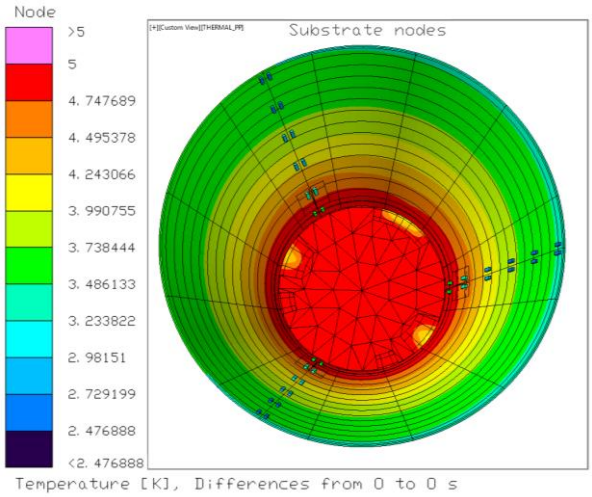

Figure 122 Middle V-groove with photon shield - Kicker

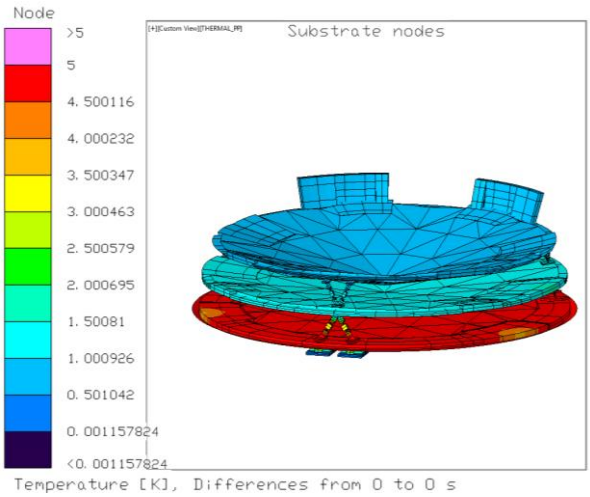

Figure 123 Outer V-groove - Kicker

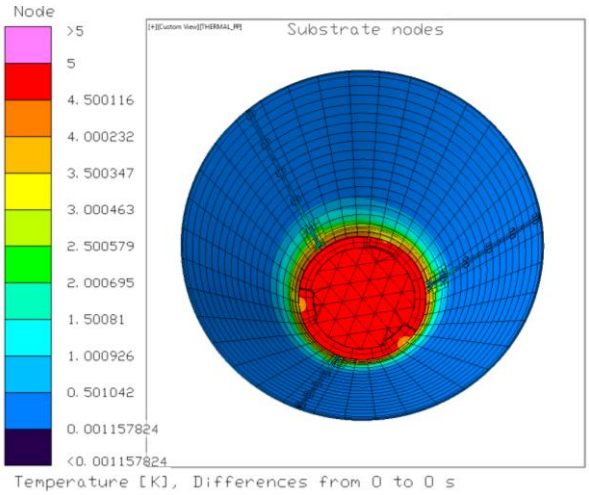

Figure 124 Outer V-groove with photon shield - Kicker

Appendix C: Convergence Criteria sensitivity

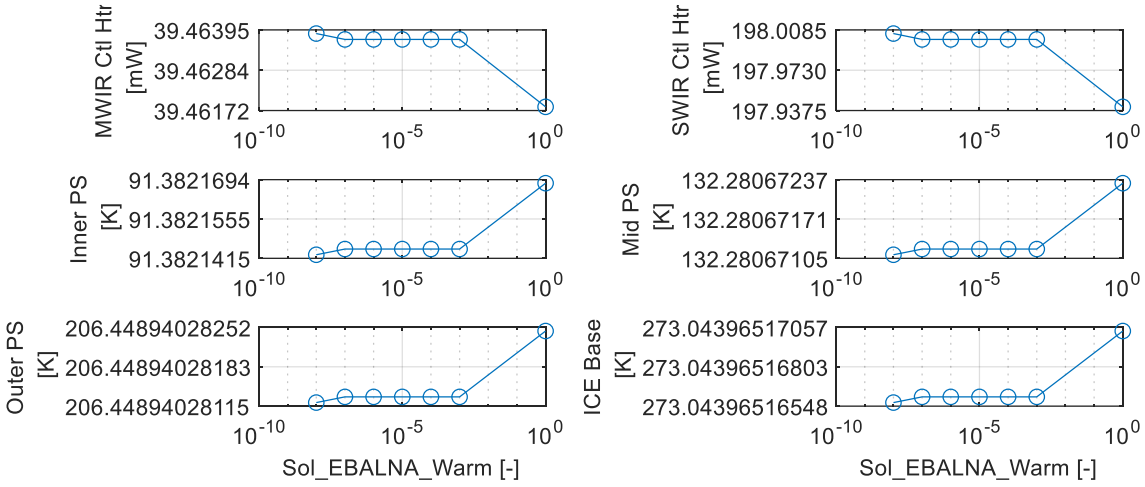

Figure 125 Convergence parametric study – EBALNA for warm regions

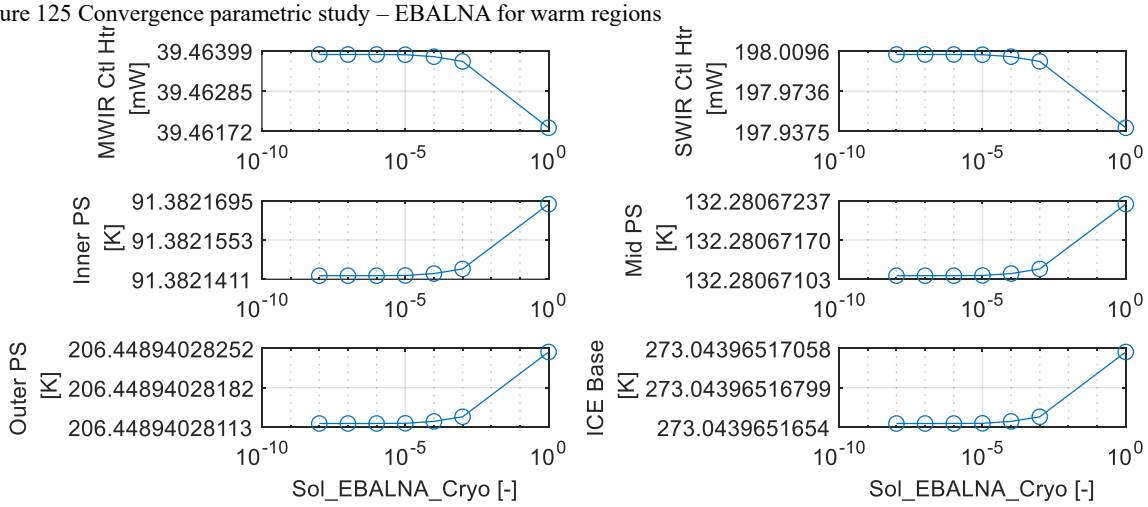

Figure 126 Convergence parametric study – EBALNA for cryo regions

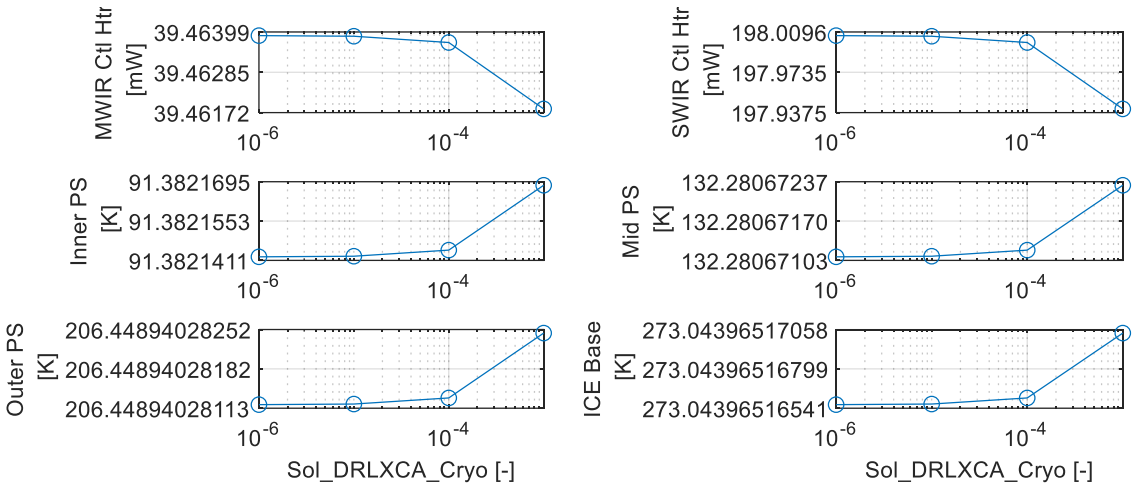

Figure 127 Convergence parametric study – DRLXCA for cryo regions

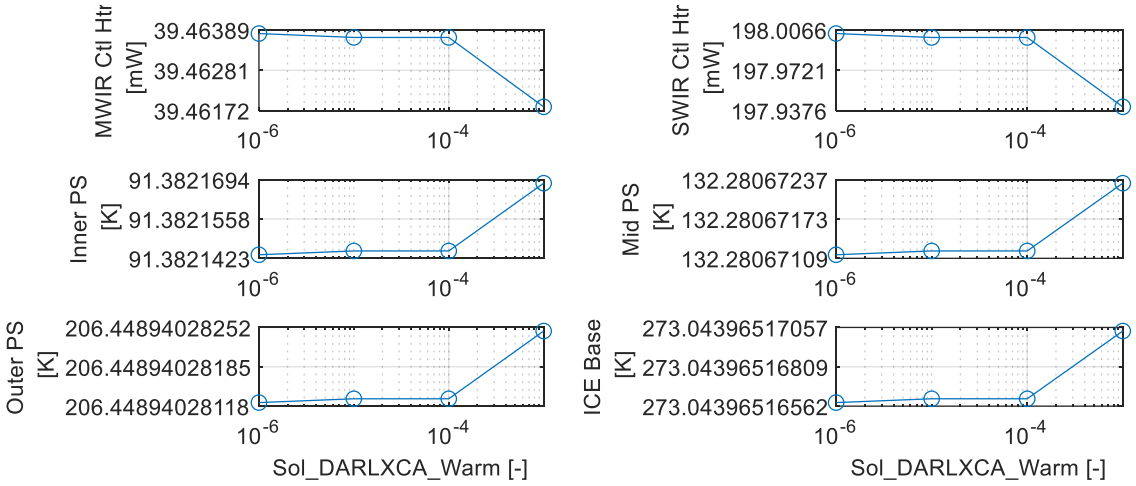

Figure 128 Convergence parametric study – DRLXCA for warm regions

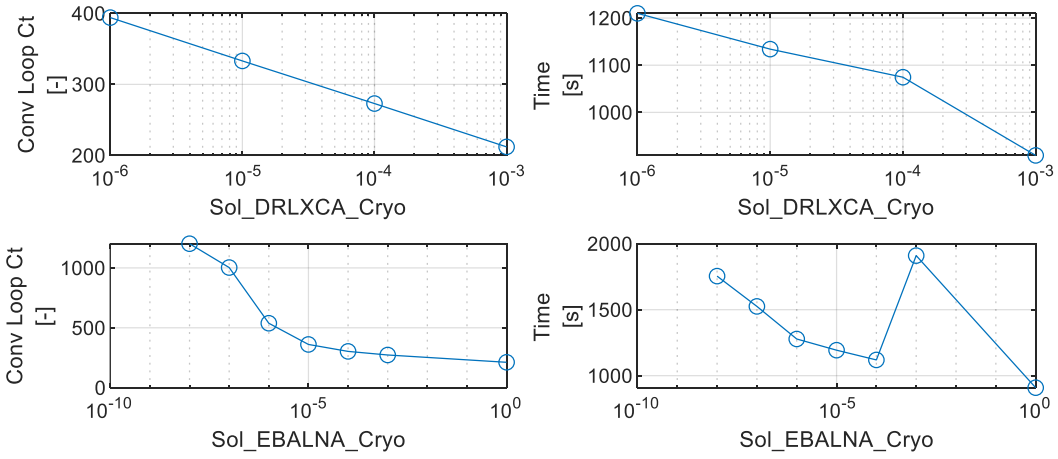

Figure 129 Convergence time and loops for varied EBALNA and DRLXCA for cryo regions

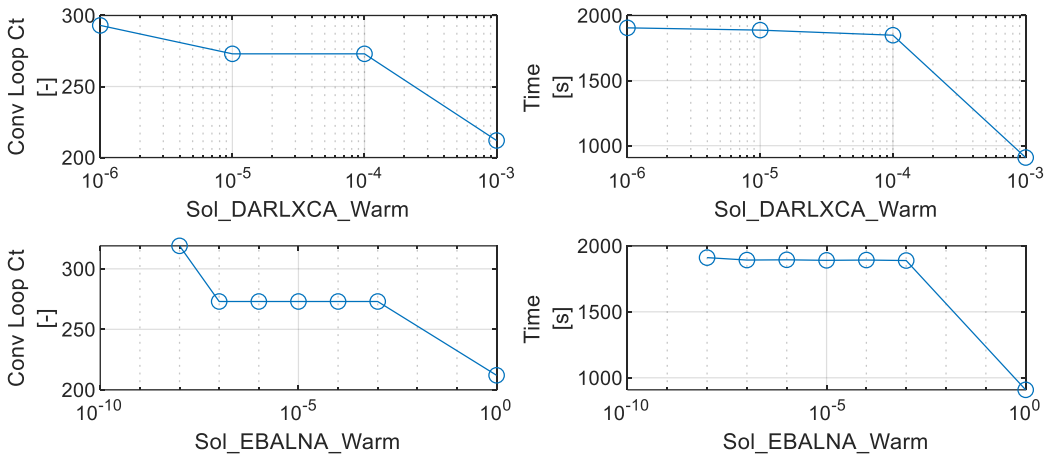

Figure 130 Convergence time and loops for varied EBALNA and DRLXCA for warm regions

Appendix D: Radiation parameter sensitivity

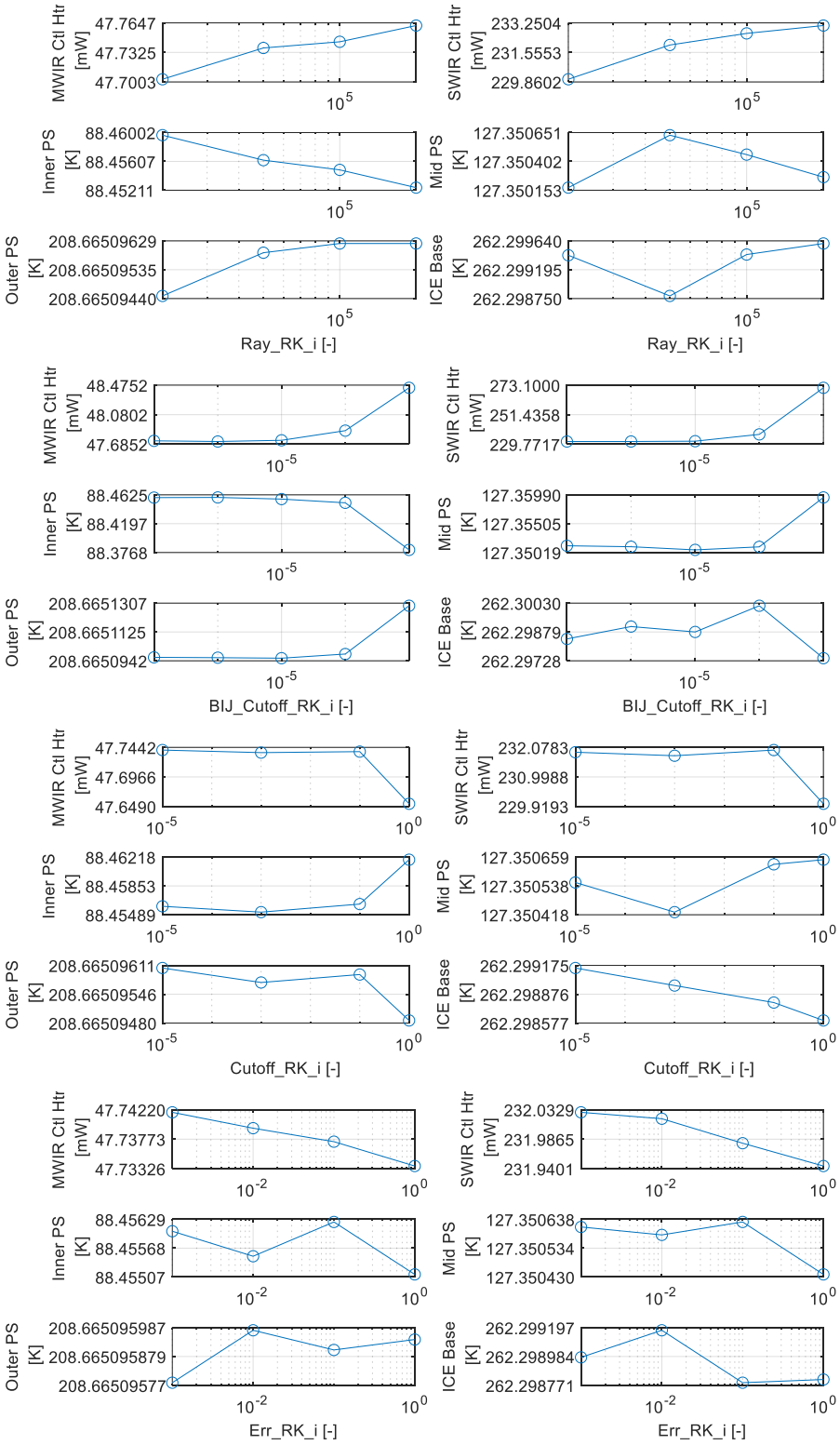

Figure 131 Internal region RadK parametric study

Note, there is a set of plots for each of the individual sun pointings (19 total), only 1 set of plots are shown here for reference

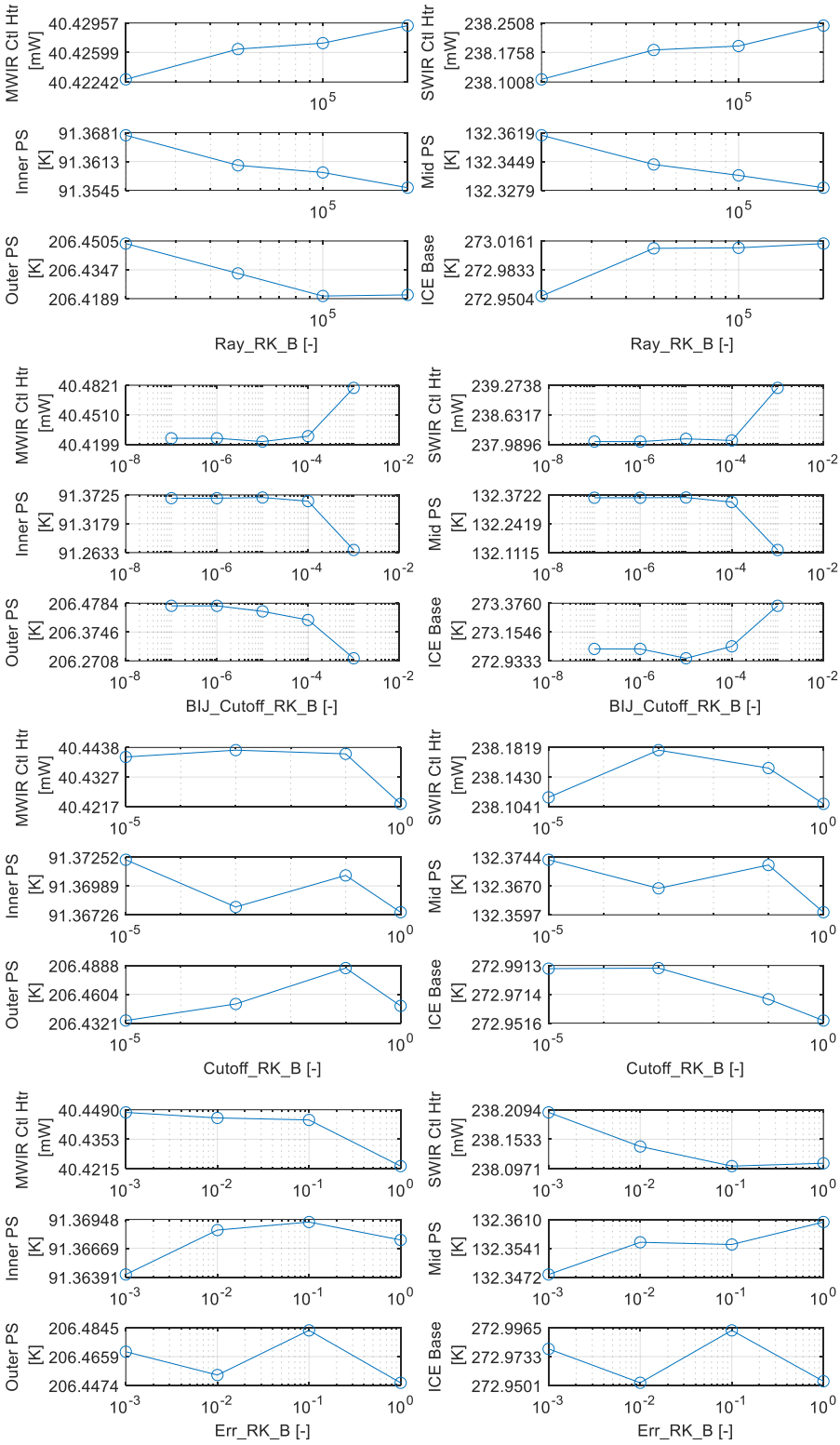

Figure 132 Bus external region RadK parametric study

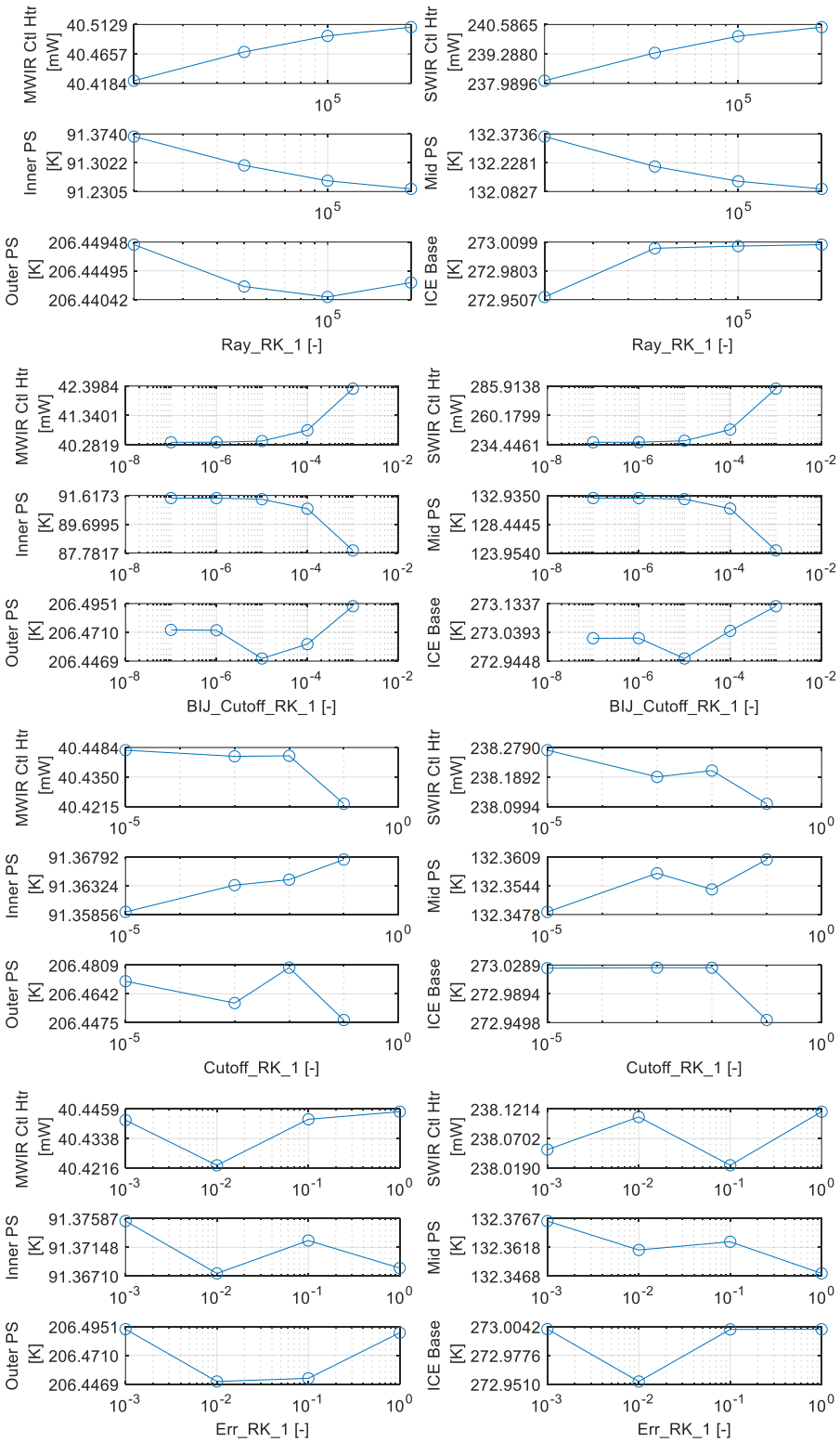

Figure 133 Outer/Mid region RadK parametric study

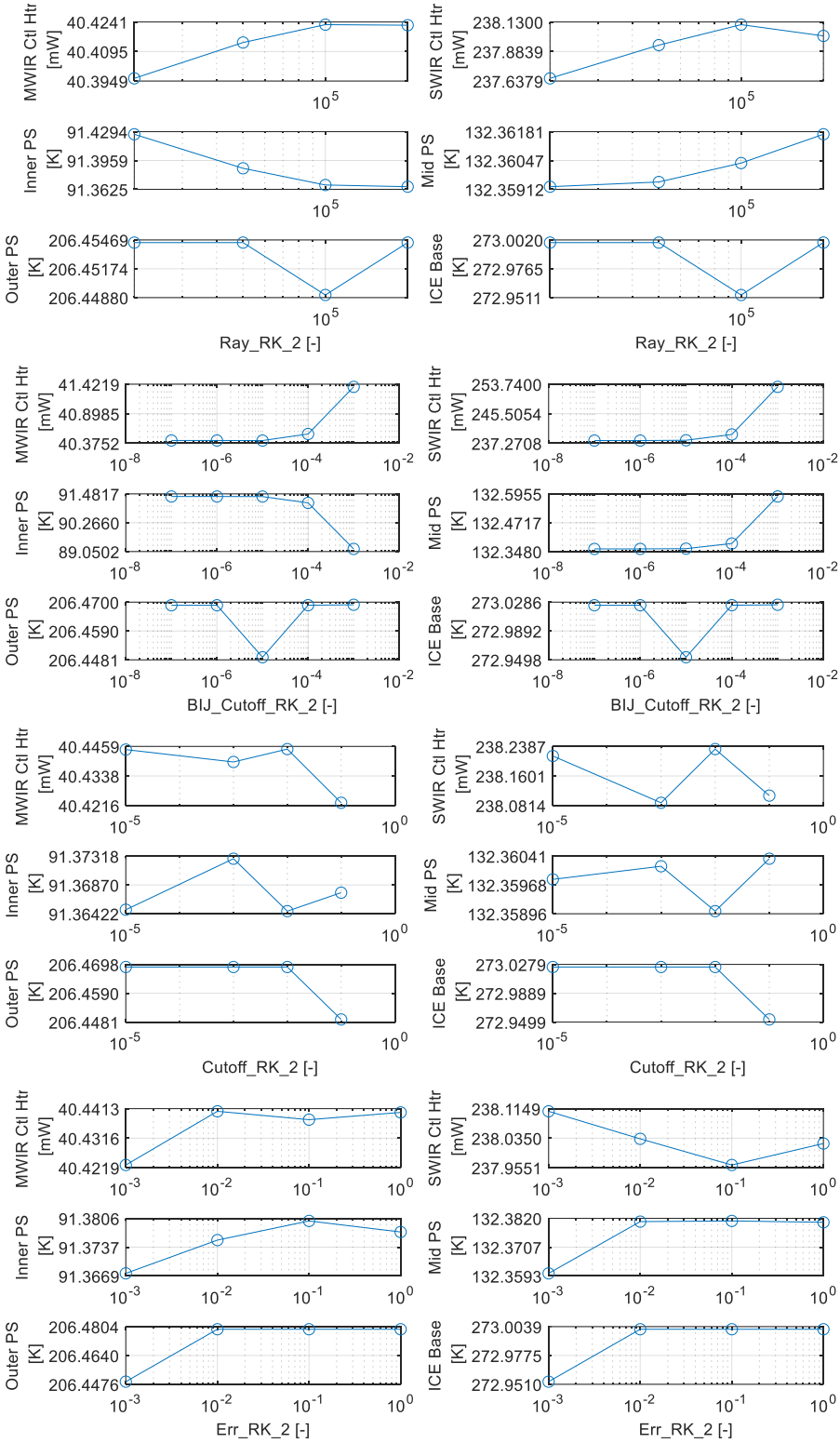

Figure 134 Mid/Inner region RadK parametric study

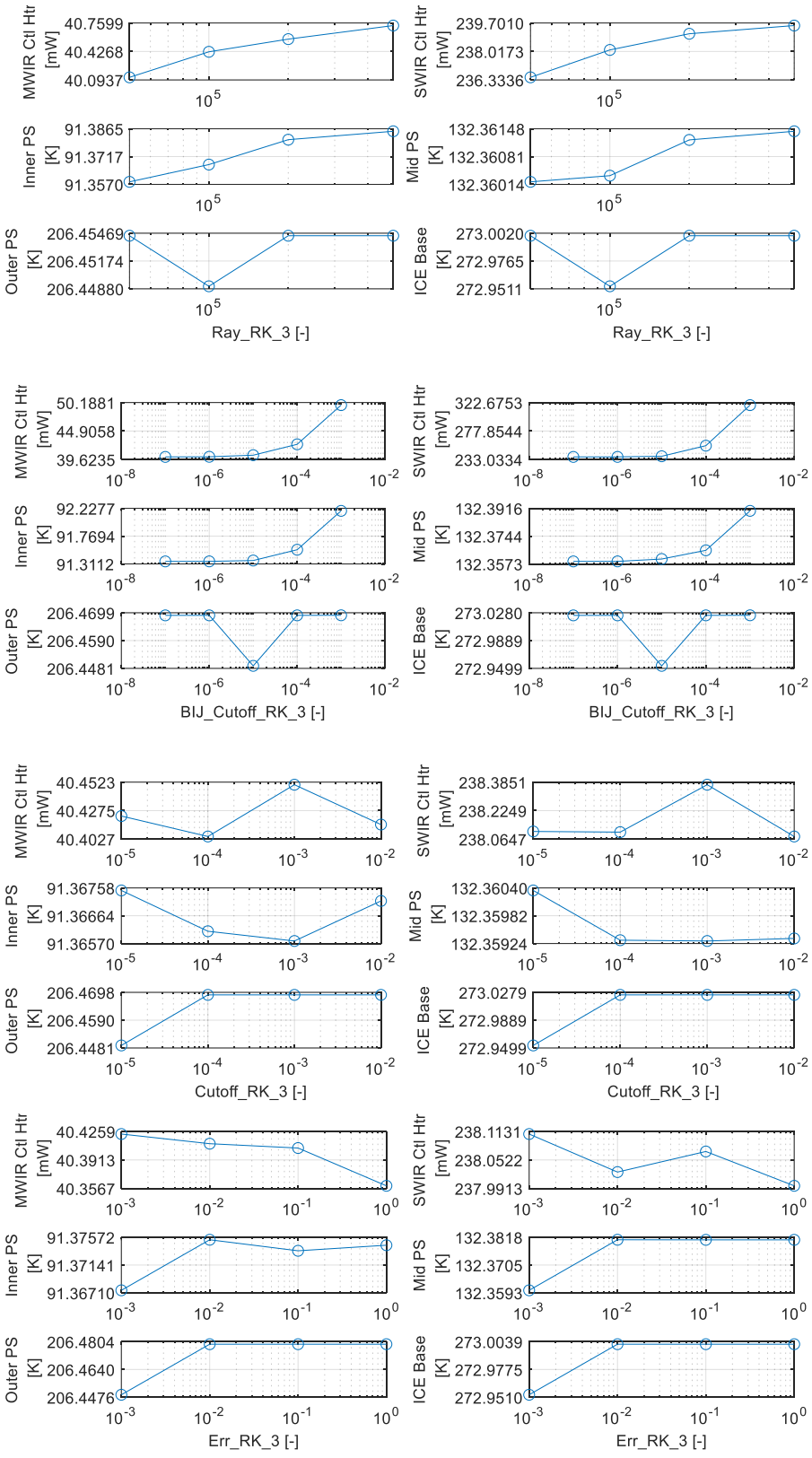

Figure 135 Inner/Telescope region RadK parametric study

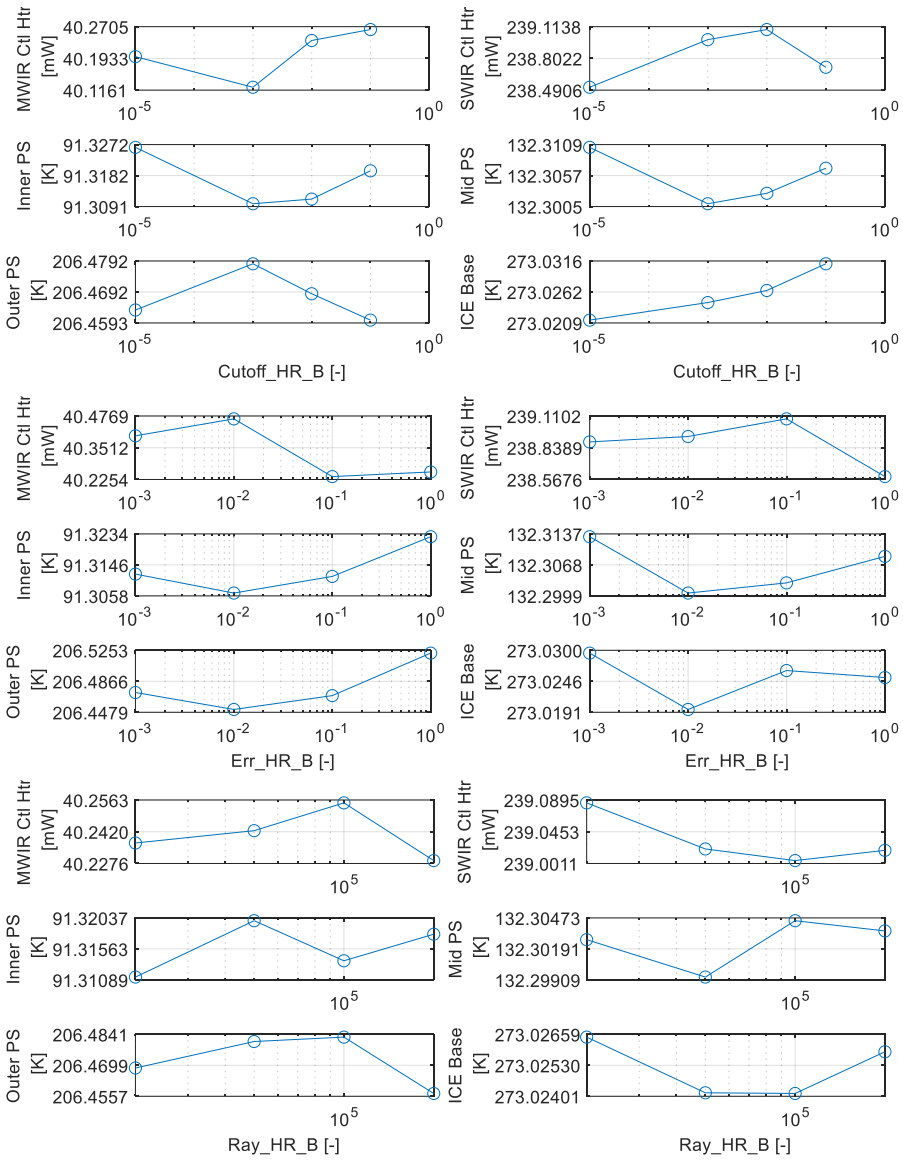

Figure 136 Bus external region heat rate parametric study

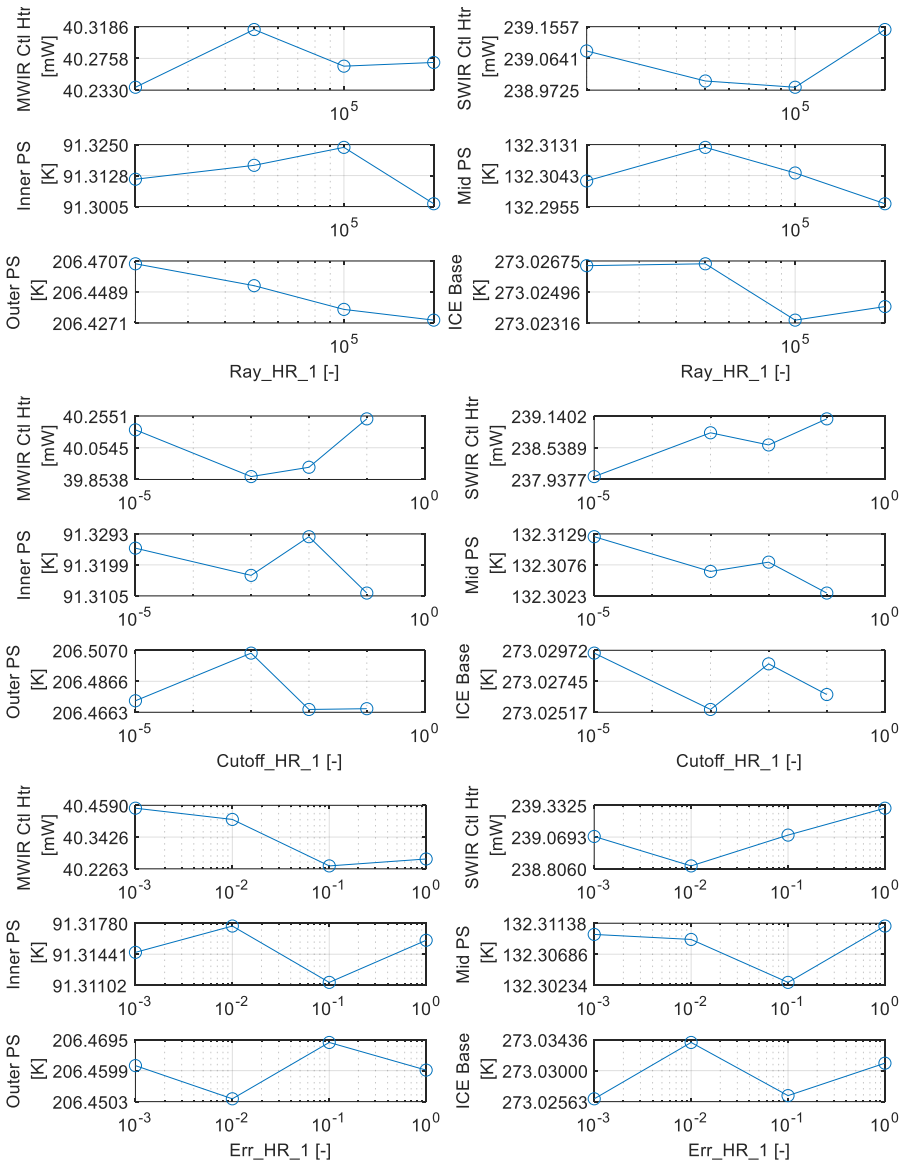

Figure 137 Outer/Mid region heat rate parametric study

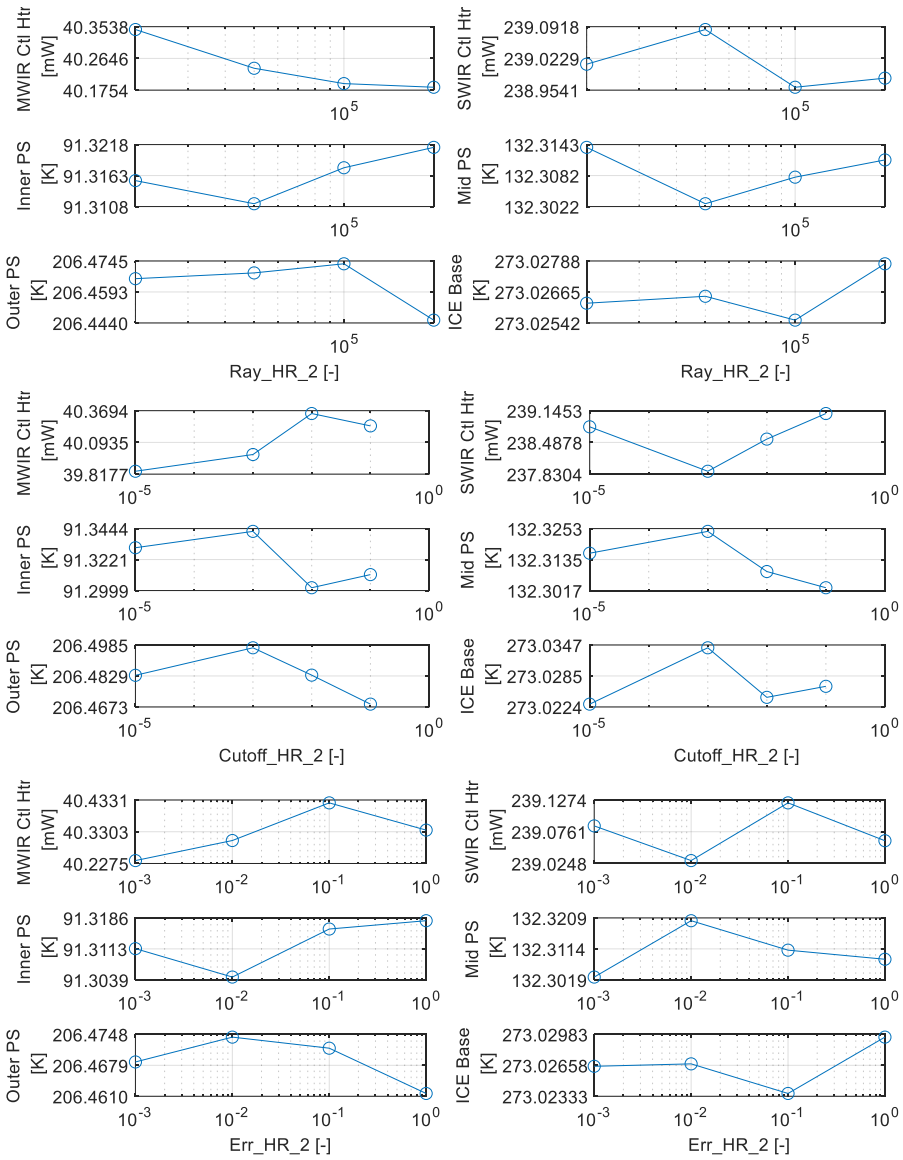

Figure 138 Mid/Inner region heat rate parametric study

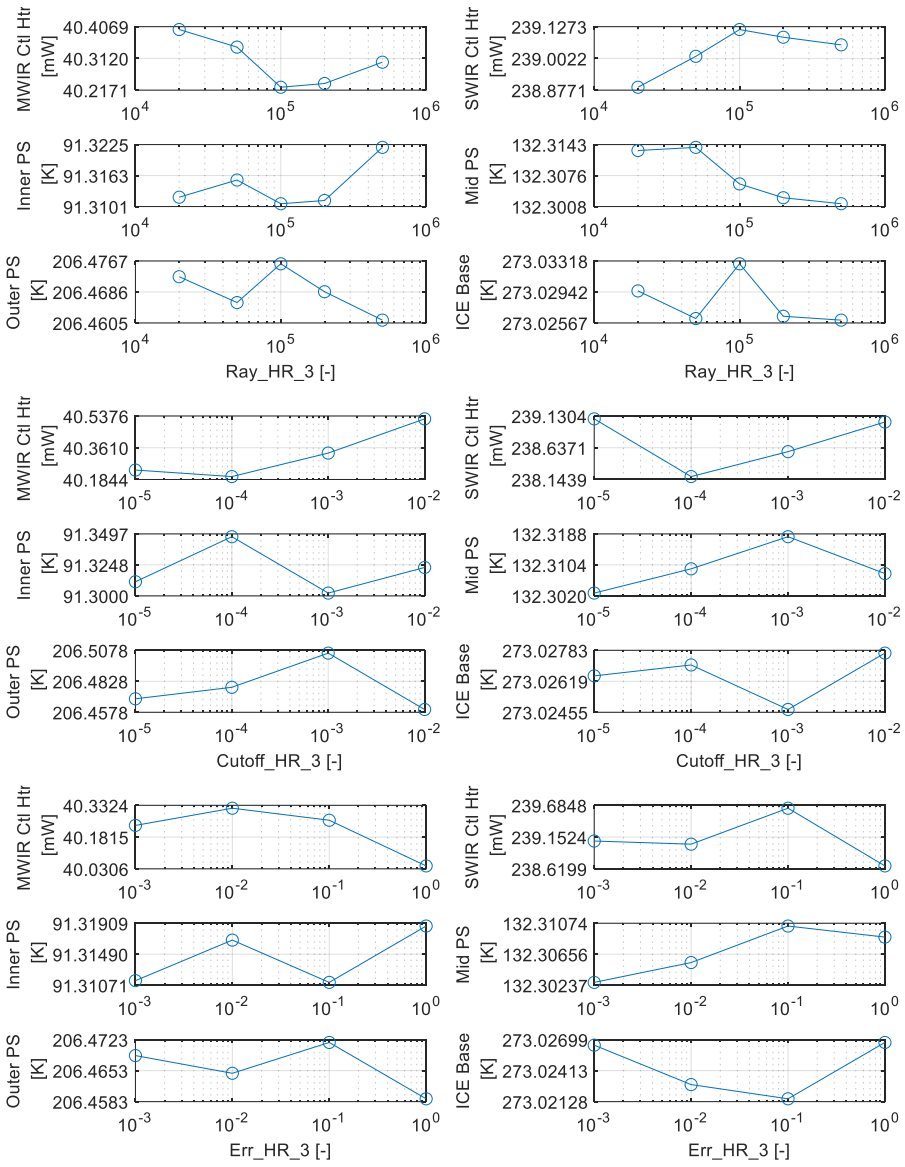

Figure 139 Inner/Telescope region heat rate parametric study

Appendix E: Environmental Loads

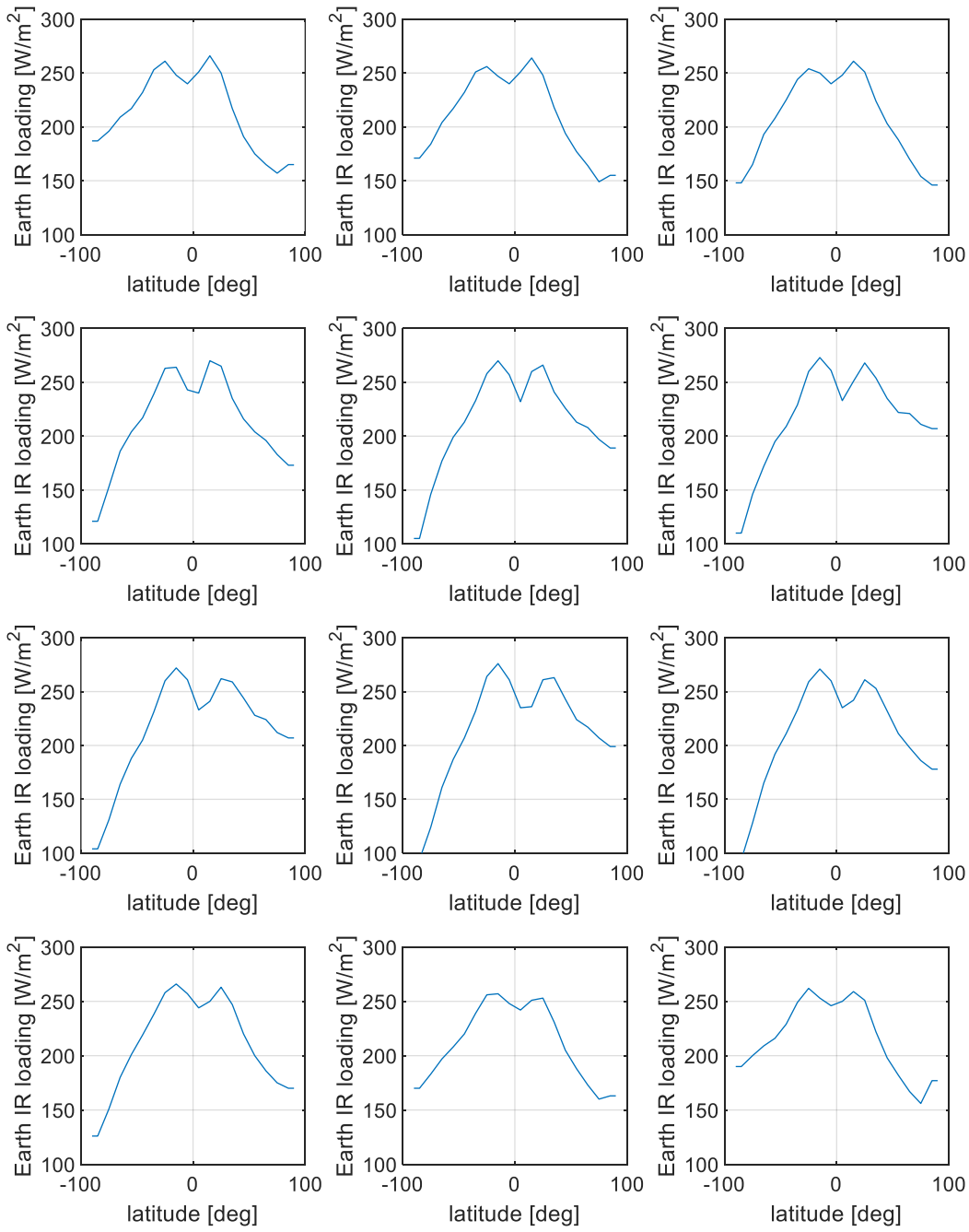

Figure 140 Latitude dependent Earth IR loading used per month

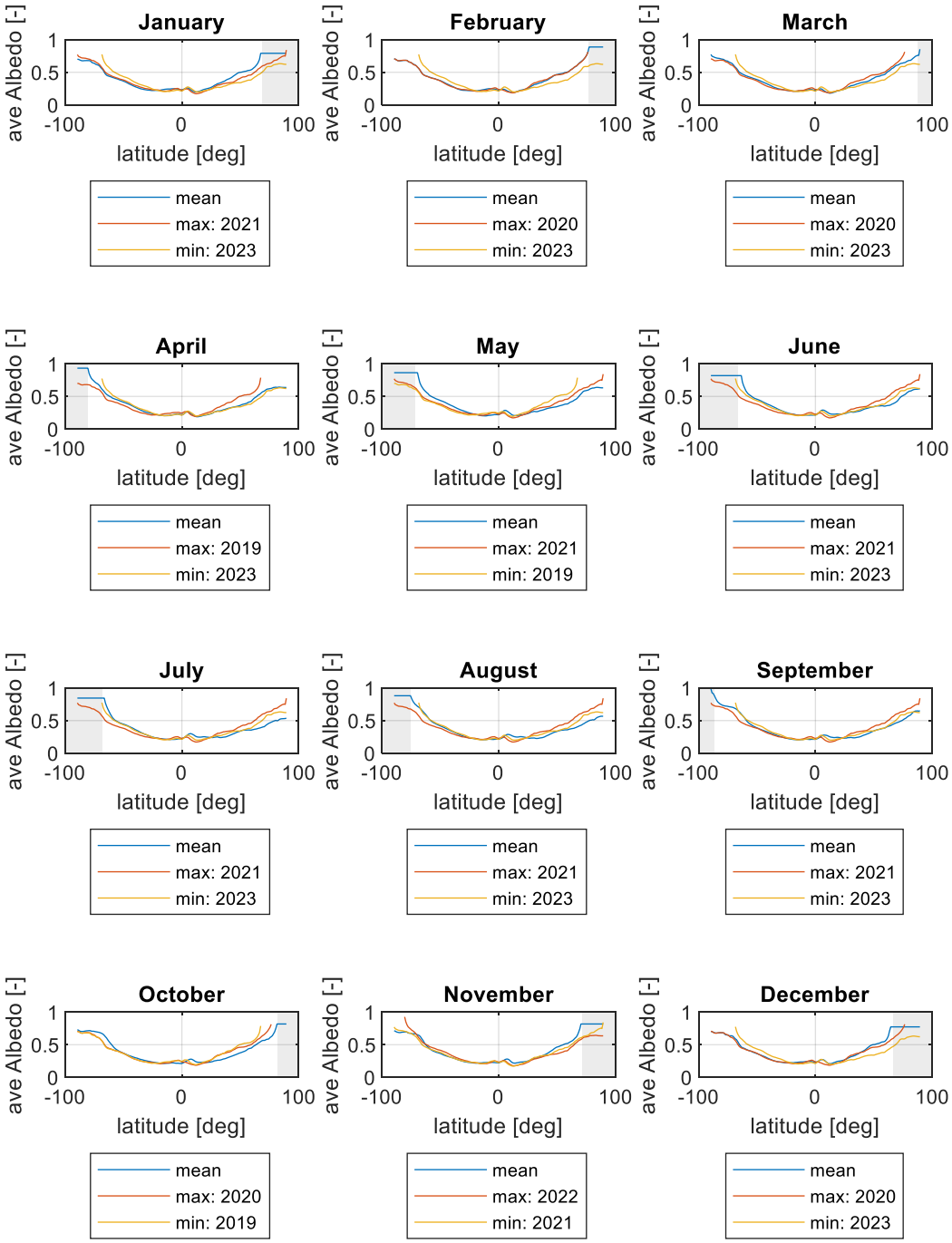

Figure 141 Latitude dependent Earth Albedo used per month, grey box denotes polar night for the given latitudes

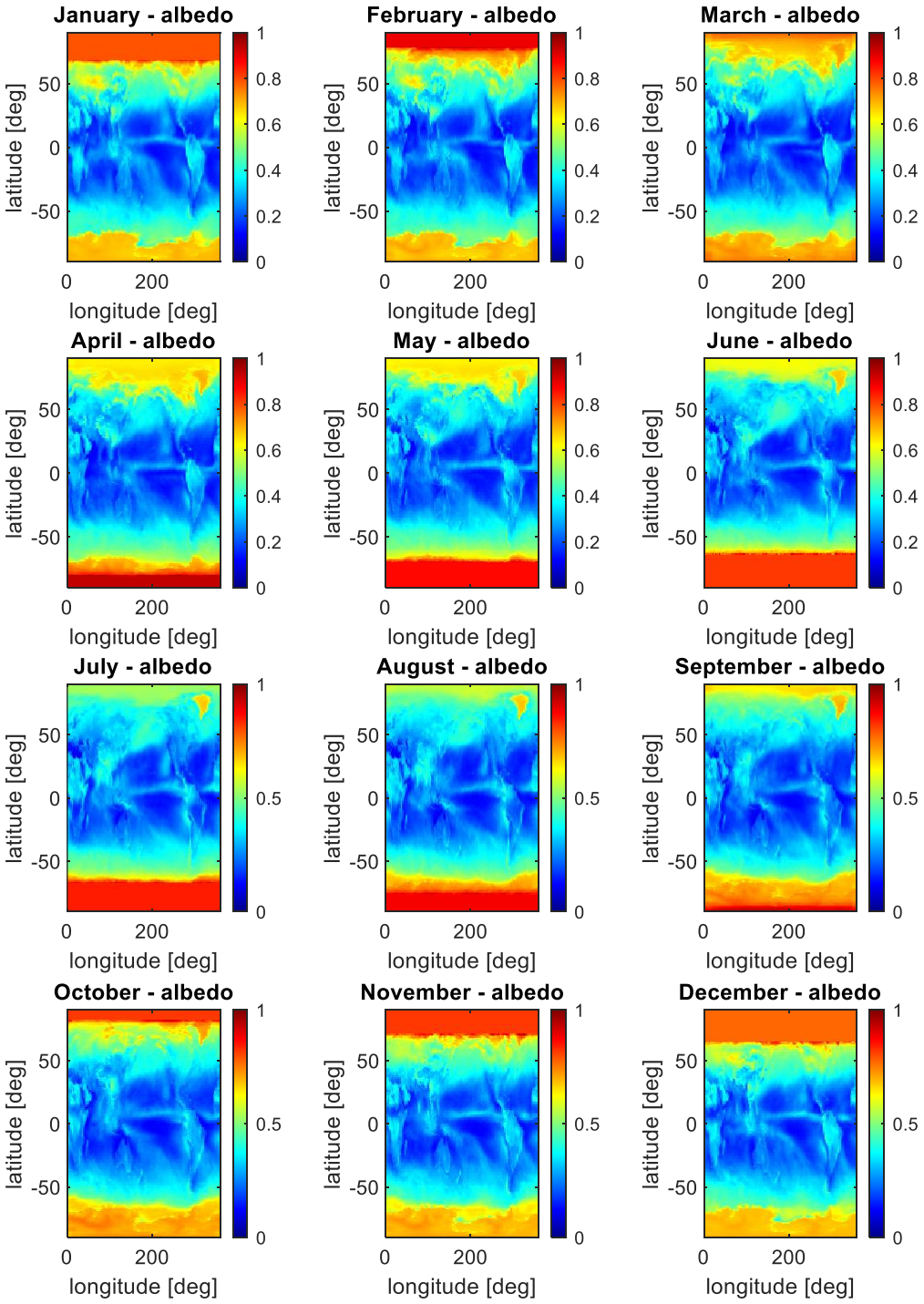

Figure 142 Regridded and smoothed albedo derived from CERES data, monthly average

Appendix F: Earth and moon gridded environmental load plots

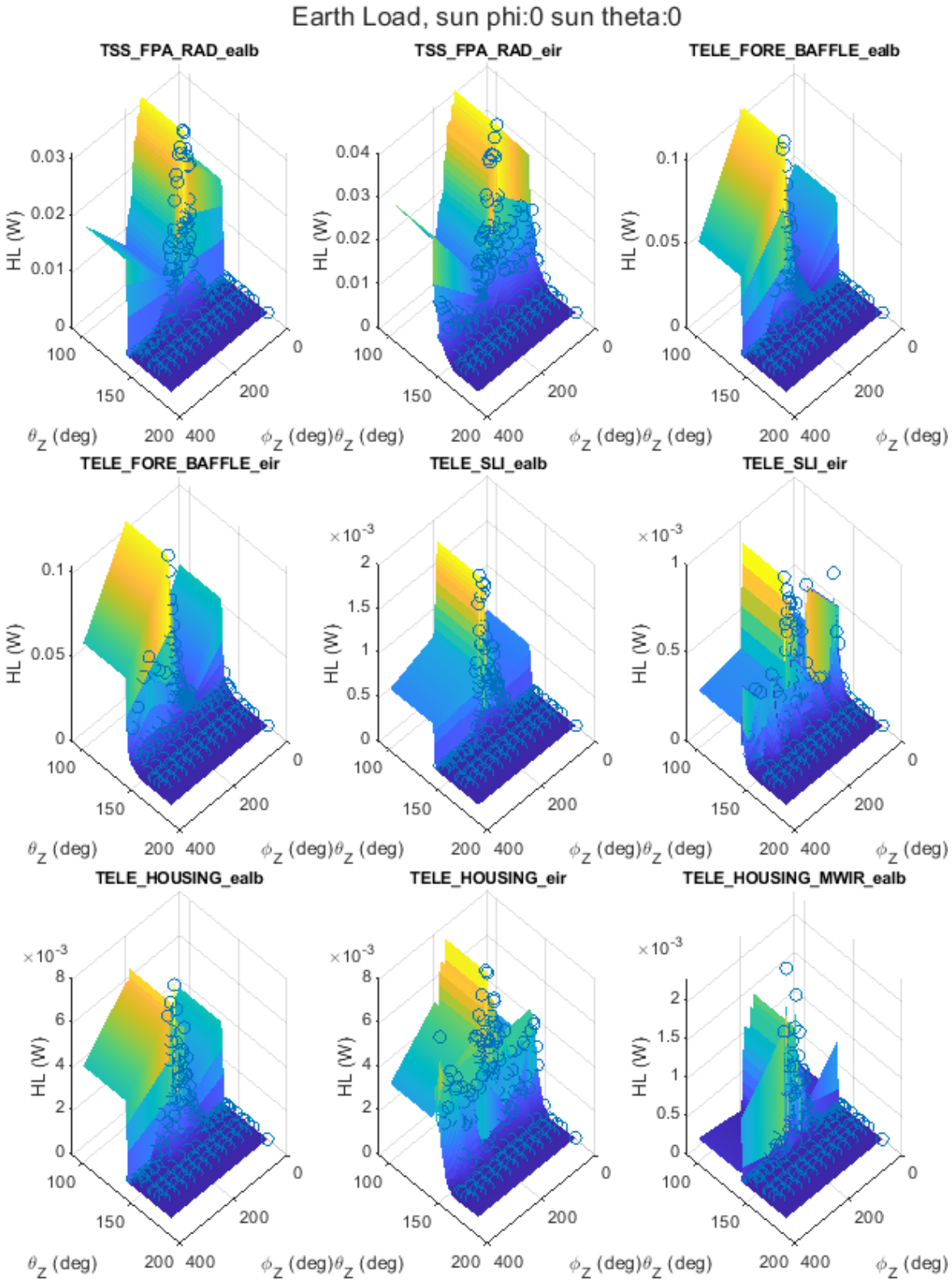

Figure 143 Surface plot of earth IR and Albedo loads for sun aligned to x axis in polar coordinates – set 1

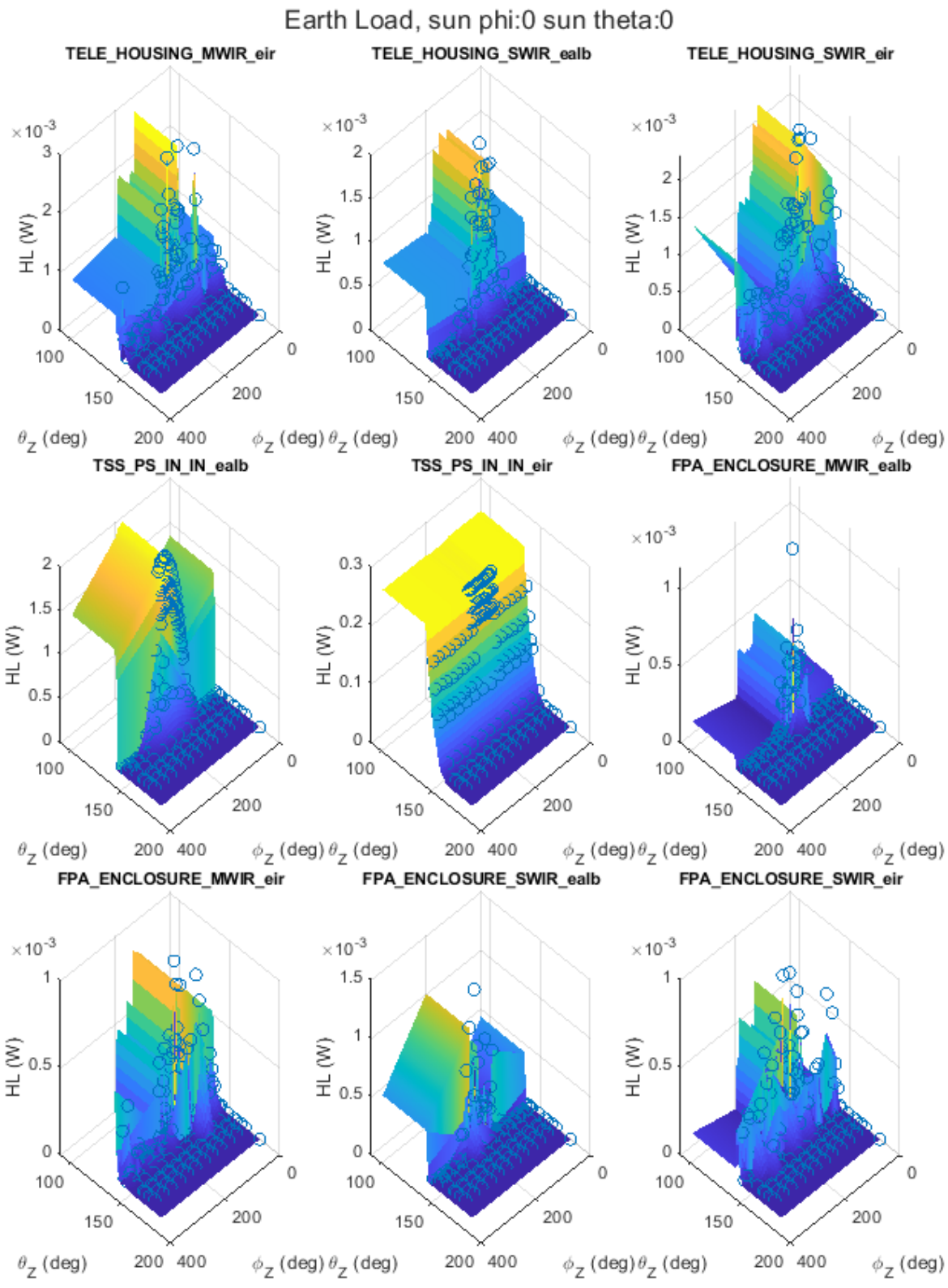

Figure 144 Surface plot of earth IR and Albedo loads for sun aligned to x axis in polar coordinates – set 2

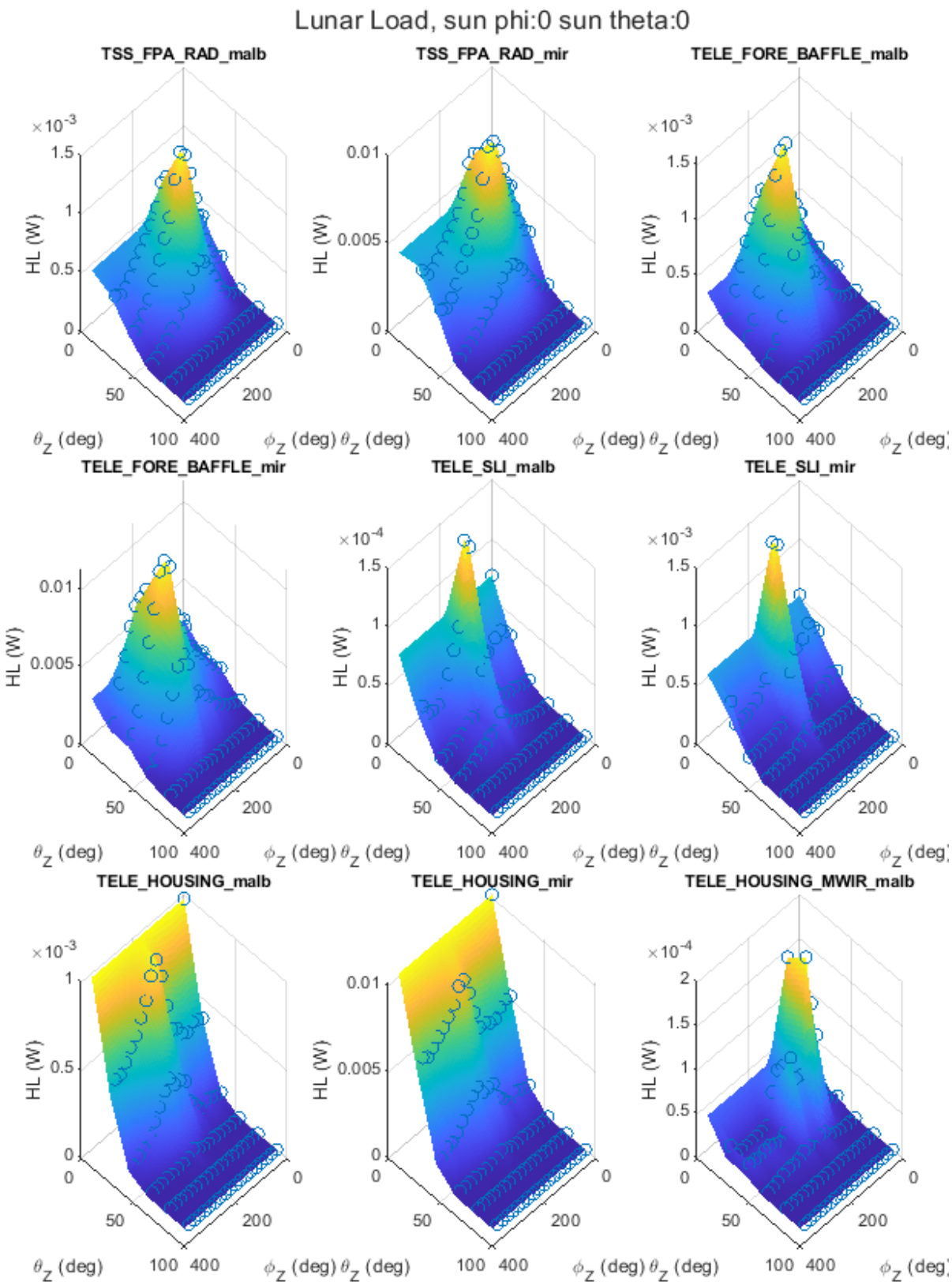

Figure 145 Surface plot of moon IR and Albedo loads for sun aligned to x axis in polar coordinates – set 1

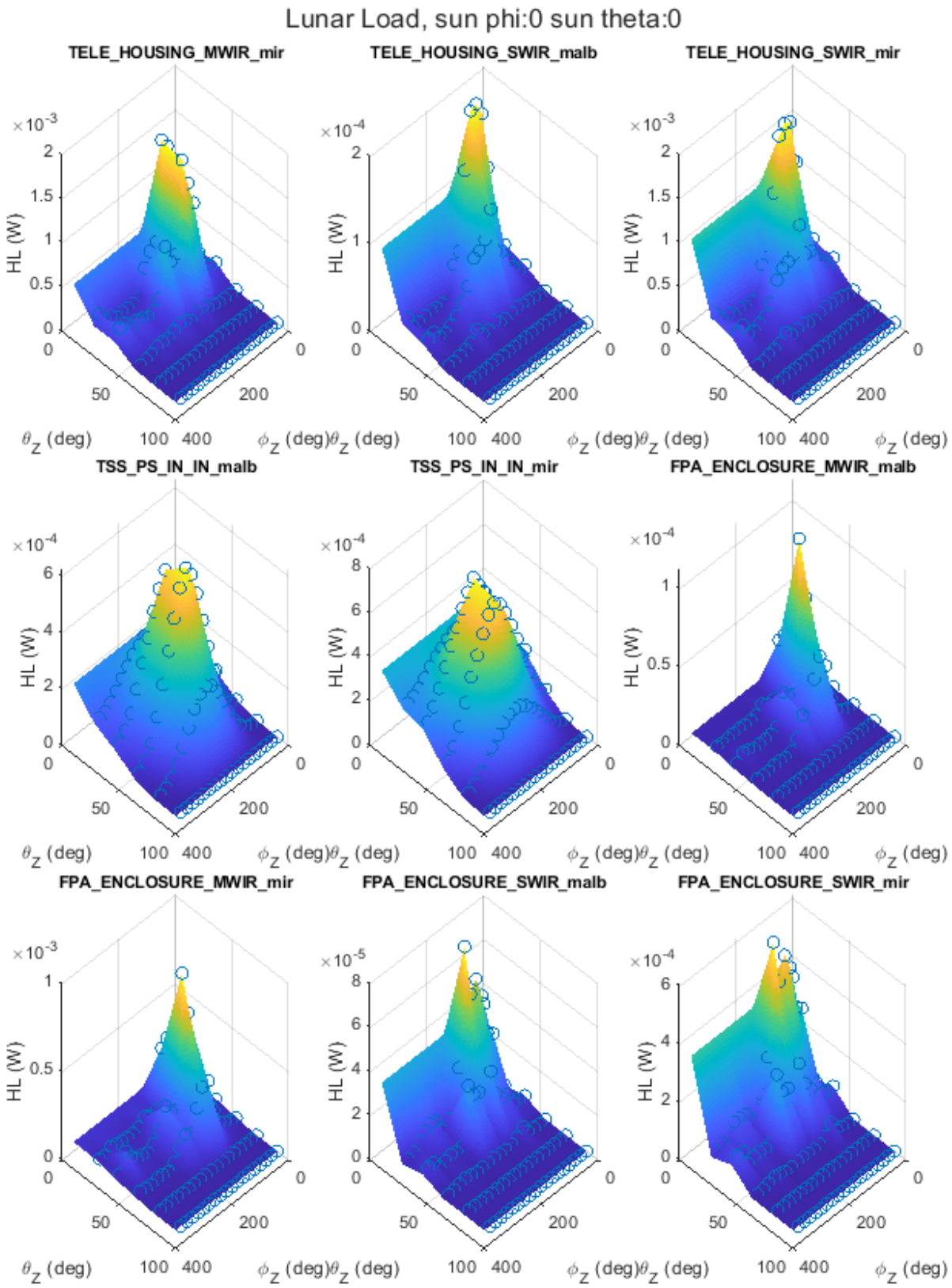

Figure 146 Surface plot of moon IR and Albedo loads for sun aligned to x axis in polar coordinates – set 2

Appendix G: Flight balance point orbit vectors

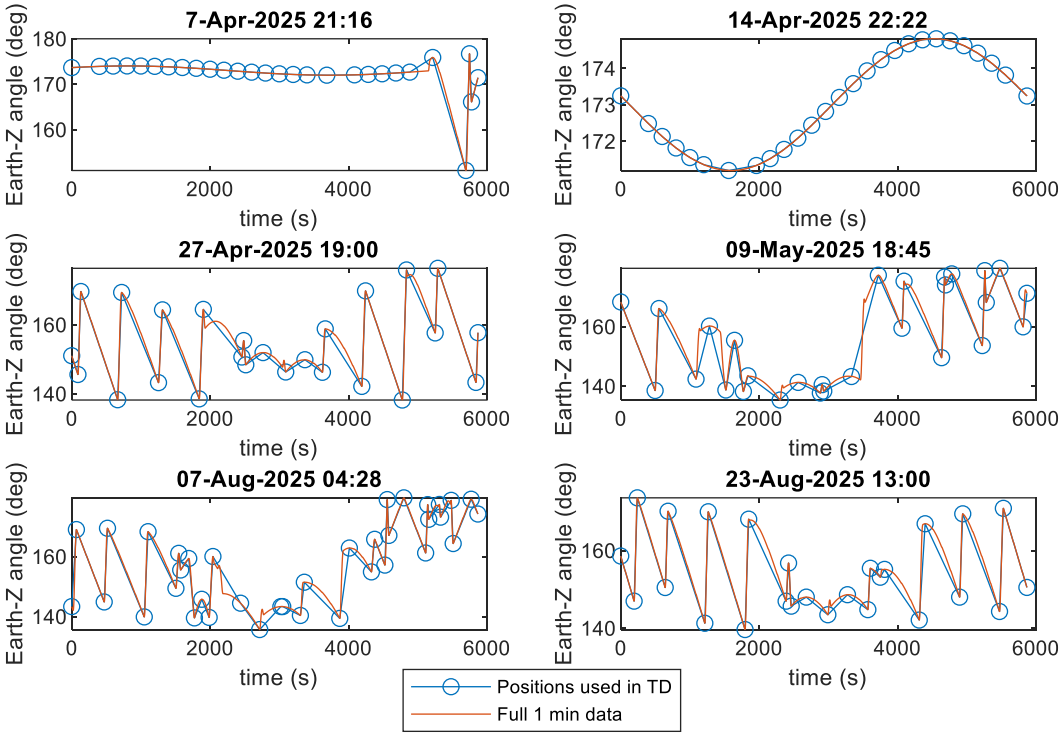

Figure 147 Extracted vectors for flight balance points – Earth angle

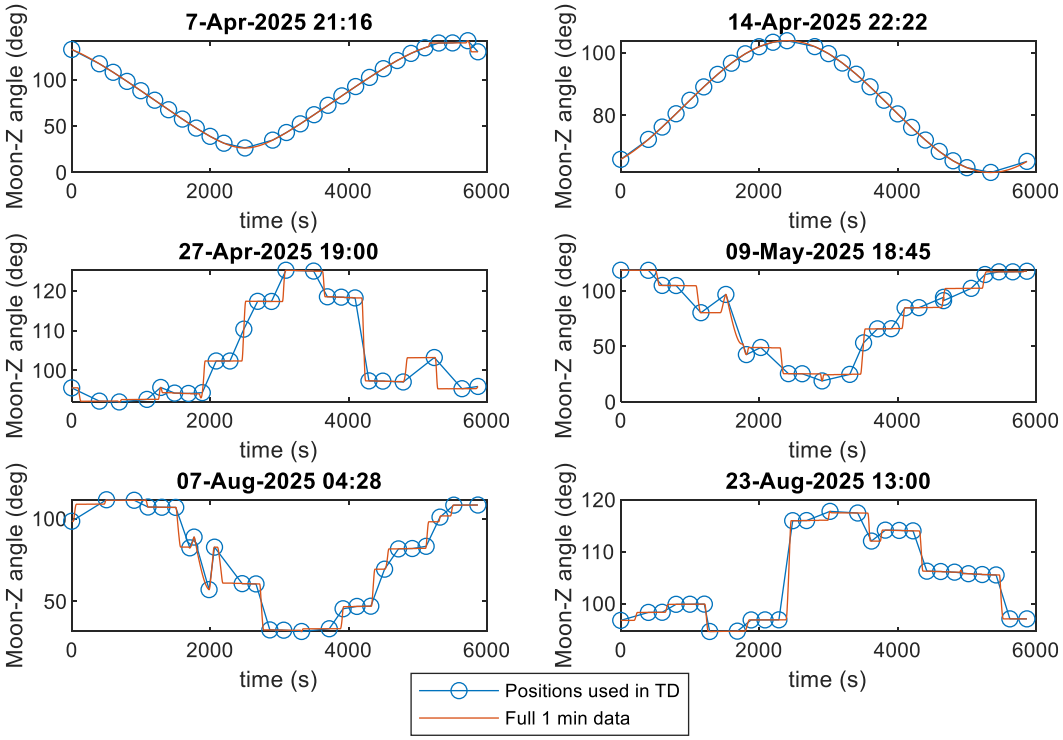

Figure 148 Extracted vectors for flight balance points – Moon Angle

Appendix H: Nodalization study temperature contours

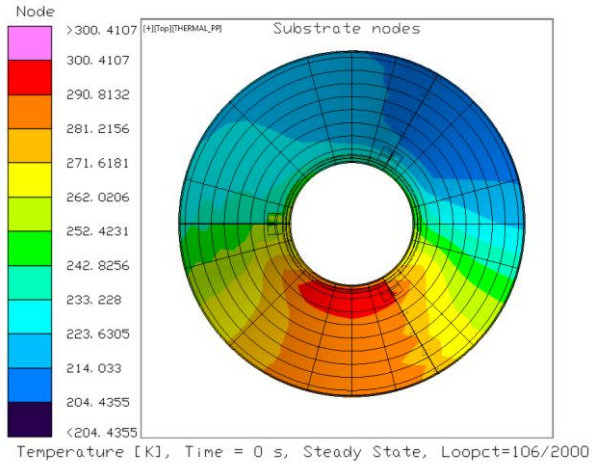

Figure 149 Outer shield nodalization initial

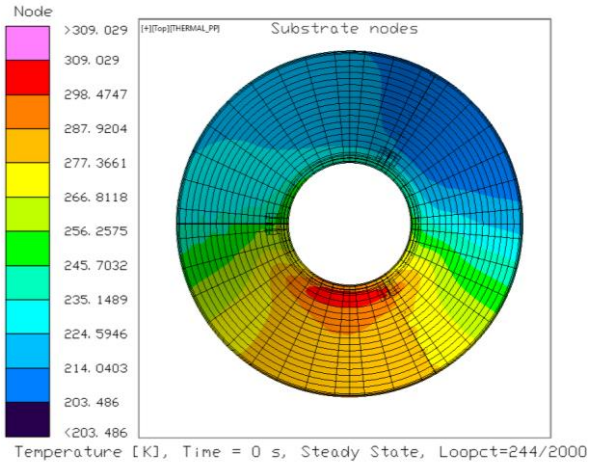

Figure 150 Outer shield nodalization 2

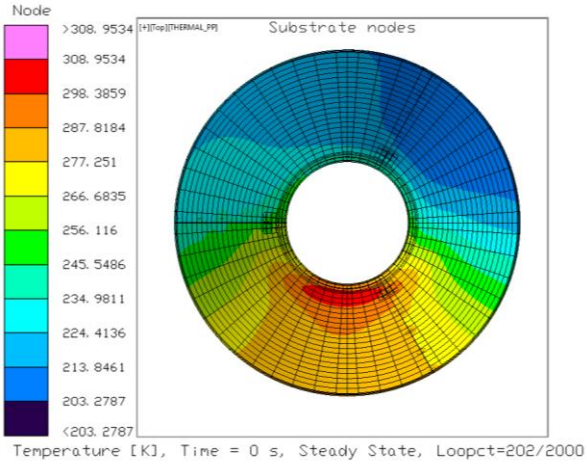

Figure 151 Outer shield nodalization 3

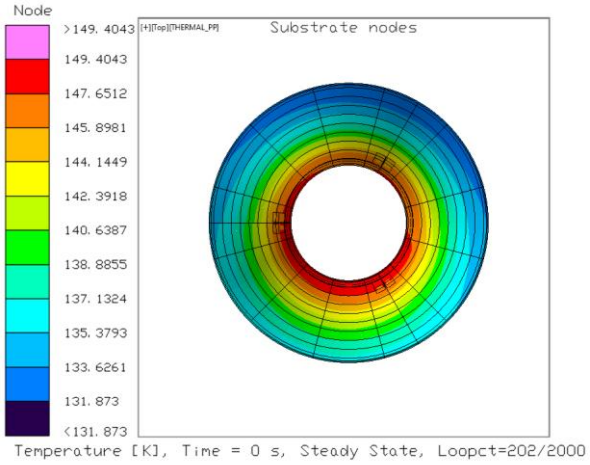

Figure 152 Middle shield nodalization initial

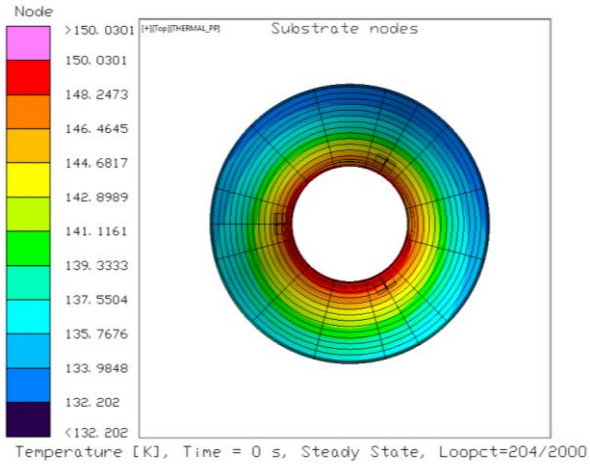

Figure 153 Middle shield nodalization 2

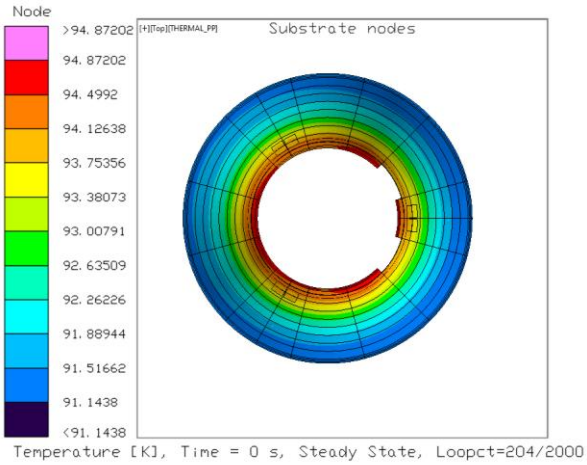

Figure 154 Inner shield nodalization initial

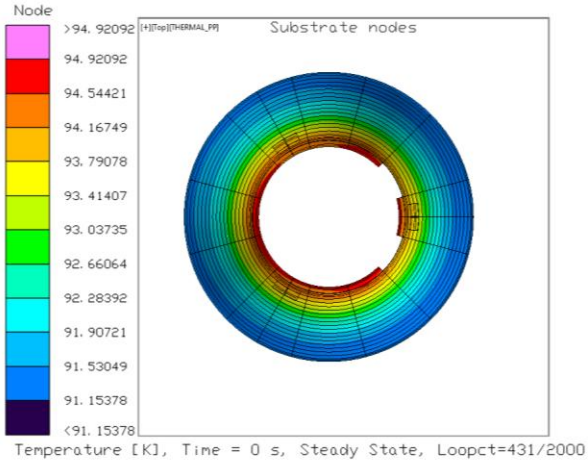

Figure 155 Inner shield nodalization 2

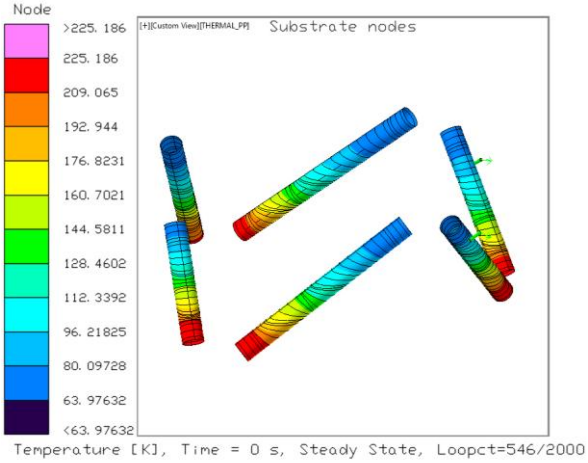

Figure 156 Telescope struts nodalization initial

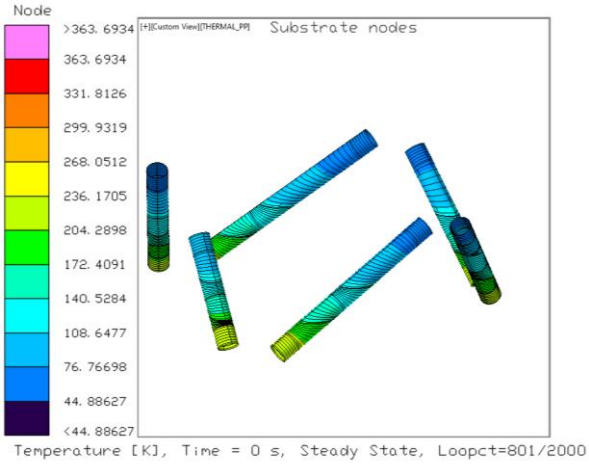

Figure 157 Telescope struts nodalization 2

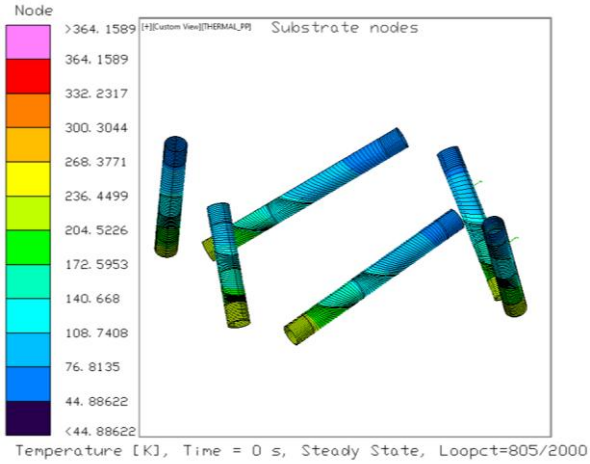

Figure 158 Telescope struts nodalization 3

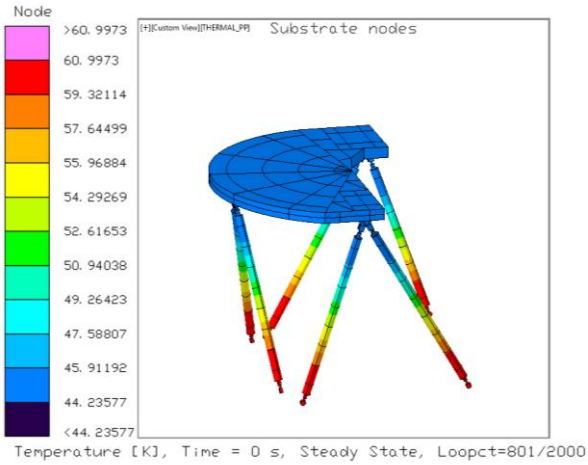

Figure 159 MWIR FPA radiator struts nodalization initial

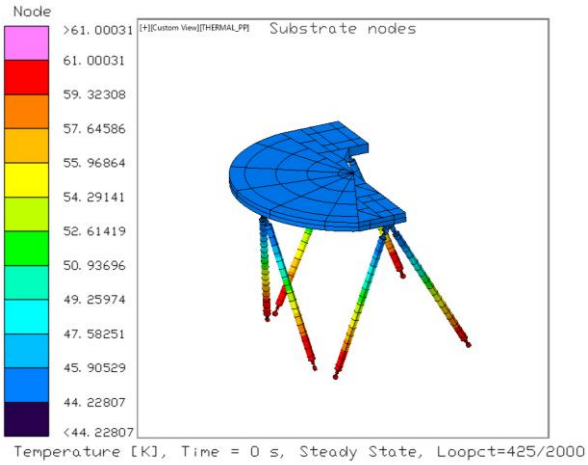

Figure 160 MWIR FPA radiator struts nodalization 2

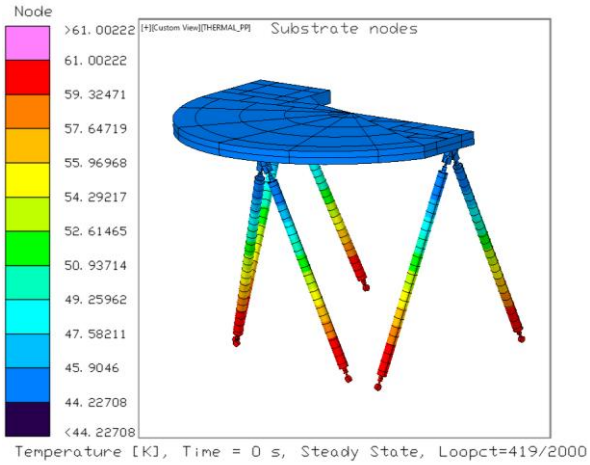

Figure 161 MWIR FPA radiator struts nodalization 3